Department of Mechanical Engineering

Interaction of non-metallic inclusions,microstructure, and fatigue loading with small crack growth in high-strength steels

Andrew Roiko

Aalto University

DOCTORAL DISSERTATIONS

Aalto University publication series
DOCTORAL DISSERTATIONS 191/2017
VTT SCIENCE 166

Interaction of non-metallic inclusions, microstructure, and fatigue loading with small crack growth in high-strength steels

Andrew Roiko

A doctoral dissertation completed for the degree of Doctor of Science (Technology) to be defended, with the permission of the Aalto University School of Engineering, at a public examination held at the lecture hall K216 of the school on 27 October 2017 at 12:00.

Aalto University
School of Engineering
Department of Mechanical Engineering
Engineering Materials

Supervising professor
Prof. Hannu Hänninen, Aalto University School of Engineering, Finland

Thesis advisor
Prof. Gary Marquis, Aalto University School of Engineering, Finland

Preliminary examiners
Prof. Arto Lehtovaara, Tampere University of Technology, Finland
Prof. emer. Gunnar Härkegård, Norwegian University of Science and Technology, Norway

Opponents
Prof. Gregory Glinka, University of Waterloo, Canada
Prof. Arto Lehtovaara, Tampere University of Technology, Finland

Aalto University publication series
DOCTORAL DISSERTATIONS 191/2017

VTT SCIENCE 166

ISBN 978-952-60-7649-2 (printed)
ISBN 978-952-60-7648-5 (pdf)
ISSN-L 1799-4934
ISSN 1799-4934 (printed)
ISSN 1799-4942 (pdf)
http://urn.fi/URN:ISBN:978-952-60-7648-5

ISBN 978-951-38-8579-3 (printed)
ISBN 978-951-38-8578-6 (pdf)
ISSN-L 2242-119X
ISSN 2242-119X (printed)
ISSN 2242-1203 (pdf)
http://urn.fi/URN:ISBN:978-951-38-8578-6

Unigrafia Oy
Helsinki 2017

Finland

441 697
Printed matter

Aalto University

Abstract

Aalto University, P.O. Box 11000, FI-00076 Aalto www.aalto.fi

Author
Andrew Roiko

Name of the doctoral dissertation
Interaction of non-metallic inclusions,
microstructure, and fatigue loading with small crack growth in high-strength steels

Publisher School of Engineering

Unit Department of Mechanical Engineering

Series Aalto University publication series DOCTORAL DISSERTATIONS 191/2017

Field of research Engineering Materials

Manuscript submitted 3 October 2017 **Date of the defence** 27 October 2017

Permission to publish granted (date) 21 August 2017 **Language** English

☐ **Monograph** ☒ **Article dissertation** ☐ **Essay dissertation**

Abstract

The increased demand and requirements for high-strength steels drives the need to better understand and predict the fatigue endurance and crack growth challenges related to their use in critical machine components. Non-metallic inclusions or defects in the steel become increasingly important as the hardness or strength of the steel increases. The distribution and the ability to predict the largest inclusion that causes failure is crucial for the proper and successful design and production of the components.

The extreme value distribution is effective in predicting the maximum inclusion in a volume of steel. The proper prediction and use of inclusion data gathered from polished specimen as well as differences in anisotropy are important to consider when gathering data for use in design and prediction of fatigue life or failure. The difference in non-metallic inclusions and the forging direction affects the distribution of the size of the inclusions as well as the fatigue endurance limit and its scatter of the steel. The extreme value distributions combined with the Murakami-Endo model are used as a design approach for fatigue failure for components with ultra-long fatigue lives and step loading. This design approach uses the master curve for Optically Dark Area (ODA) growth obtained by Murakami et al. and combines it with the prediction of the largest non-metallic inclusion along with the estimate of the fatigue life of the component.

The initiation and growth of small cracks from inclusions as well as small Focused Ion Beam (FIB) notches behave in a similar manner and show a strong tendency to follow the local microstructure. The effect of the local microstructure on the small fatigue crack growth is studied using FIB milling to create cross-sections of the microstructure. This showed that the microstructure is also linked to the formation of ODA around non-metallic inclusions in ultra-long fatigue. The behaviour of a small crack growing from notches in high cycle fatigue is studied by using high-speed microscopy and Rumul fatigue testing machines. The test results show that small cracks initiate and grow quickly in the beginning of the fatigue life after which they propagate slowly at a stress intensity range lower than the large crack growth threshold until it is reached.

Comparing different data results for different R-ratios shows that the parameter ΔK+ works well to compare the crack growth rate of small cracks in the studied quenched and tempered steel. For crack arrest the ΔK+ or Kmax thresholds are lower for cracks with higher compressive loading. Also test results showed that increasing only the compressive portion of loading can reinitiate arrested

Keywords Non-metallic inclusions, Small crack growth, fatigue

ISBN (printed) 978-952-60-7649-2 **ISBN (pdf)** 978-952-60-7648-5

ISSN-L 1799-4934 **ISSN (printed)** 1799-4934 **ISSN (pdf)** 1799-4942

Location of publisher Helsinki **Location of printing** Helsinki **Year** 2017

Pages 158 **urn** http://urn.fi/URN:ISBN:978-952-60-7648-5

Preface

It all began with a research proposal for clean steels and fatigue survival with material imperfections. The original research project, called FATE-DEFEX, was initiated with the cooperation between Industry partners, Aalto University (formerly known as Helsinki University of Technology (HUT)) and the Technical Research Centre of Finland VTT, along with the Finnish Funding Agency for Innovation (TEKES) overseeing and providing the majority of the funding for research. This 3 year project kicked off in 2008. Based on the body of work produced in this project and building upon it in two consecutive projects MACY and SCarFace (Short Crack and Fretting fatigue damage in mechanical engineering) (in the years 2011-2015) this thesis and the publications presented in it have been produced.

This thesis, like many human endeavors is one of work and perseverance that would not be possible without the supporting foundation of family, friends, and companions. I wish to thank first my supervisor Prof. Hannu Hänninen, who has made this all possible and offered me this opportunity. I would also wish to thank my work mentor, college and patient coauthor Jussi Solin, who provided me with an abundance of opportunity and guidance, and was so many countless times ready and willing to help. I would also like to thank Jouni Alhainen and Teemu Sarikka, as well as the staff of the Engineering Materials laboratory and VTT for their help. Special thanks are also in order to Prof. Yukitaka Murakami for his guidance and advice. His counsel and teaching have been important in my work. I also wish to thank all the researchers and staff I worked with at Kyushu University for their kind hospitality and support.

I wish to thank my wife Anna-Kaisa, for her unwavering support and love. I am grateful as well, for the support and encouragement from all my family and friends. Thank you all for the help in times of need, for it has made all the difference.

Espoo, October 3, 2017

Andrew Lauri Roiko

Contents

List of publications

This thesis is based on the following original publications which are referred to in the text as I–VI. The publications are reproduced with kind permission from the publishers.

I A. Roiko, H. Hänninen, H. Vuorikari, Anisotropic distribution of non-metallic inclusions in a forged steel roll and its influence on fatigue limit, International Journal of Fatigue, Volume 41, August 2012, Pages 158-167, ISSN 0142-1123

II A. Roiko, Y. Murakami, A design approach for components in ultralong fatigue life with step loading, International Journal of Fatigue, Volume 41, August 2012, Pages 140-149, ISSN 0142-1123

III A. Roiko, J. Solin, Measurement of small cracks initiating from inclusions, Focused Ion Beam notches and drilled holes, International Journal of Fatigue, Volume 62, May 2014, Pages 154-158, ISSN 0142-1123

IV A. Roiko, J. Solin, T. Sarikka, H. Hänninen, The paths of small fatigue cracks in high-strength steels initiated from inclusions and small defects, Accepted at: Materials Performance and Characterization on 21.4.2017

V A. Roiko, J. Solin, H. Hänninen, Behavior of small cracks under negative stress ratio fatigue loading, International Journal of Fatigue, Volume 104, 2017, Pages 379-388, ISSN 0142-1123

VI A. Cetin, A. Roiko, M. Lind, Towards proper sampling and statistical modelling of defects. Fatigue & Fracture of Engineering Materials & Structures, Volume 38, September 2015, Pages 1056-1065, ISSN 1460-2695

Author's contributions and original features

The experimental methods along with the analysis of the obtained data presented in this thesis for small crack growth at high and ultra-long cycle fatigue are used to better understand, measure and model small crack behaviour and growth with respect to loading, microstructure, and the defect or non-metallic inclusion distribution in high-strength steels. The following are the features believed to be original:

1. The author performed all the experimental as well as the majority of the data analyses of the experimental results which include the examination of the extreme value distribution of the inclusions located at the site of fatigue crack initiation on the fracture surface of the fatigue test bars. This is compared with the extreme value distribution of the inclusions found on polished specimen. The extreme value distribution of the non-metallic inclusions is used to predict the theoretical lower fatigue limit of the steel. The data obtained from the inclusion analyses and fatigue tests provided new results on the role of anisotropy in the extreme value distribution of inclusions in forged steel and the effect this has on the fatigue limit and scatter of the steel.

2. The author wrote a brief review of previous work on the origin and formation of Optically Dark Area (ODA) in ultra-long life fatigue. The author also contributed a new design approach, proposed for calculating the effects of different loading levels on ultra-long fatigue life using the ability to predict the presence of non-metallic inclusions in steels with extreme value methods combined with the master curve of ODA growth to determine the maximum threshold stress for ultra-long fatigue life using the $\sqrt{(area)}$ parameter model.

3. The author developed a specialized test method to study the initiation and growth of micro-cracks from small defects. This new method along with the majority of the analyses of the results performed by the author provided new and original data about the initiation and growth of small cracks from defects near the fatigue endurance limit.

4. The author used a new investigation method of FIB milling and imaging to investigate the connection between the microstructure and growth path of small cracks in high cycle fatigue. The general preferential growth direction and formation of ODA is linked to adjacent grain orientations and sub-grain structures such as martensite lath and packet orientation. Local martensite laths and packets in the microstructure surrounding a non-metallic inclusion give additional explanation to the formation and origin of the ODA which is an original and new result obtained by new and original methods.

5. The author tested and measured the growth of small cracks initiated from microscopic notches and loaded near the crack growth threshold under

varying stress ratios. These results of small crack growth under different negative stress ratios are unique and provide new insights into the interaction between small cracks, defects, and loading.

6. The experimental portion of the publication was the extent of the author's contribution to the publication.

List of abbreviations

ASTM	American Society for Testing Materials
EDS	Energy Dispersive X-ray Spectroscopy
FIB	Focused Ion Beam
FS	Fracture Surface
GCF	Giga Cycle Fatigue
GEV	Generalized Extreme Value
HCF	High Cycle Fatigue
HV	Vickers Hardness (kgf/mm^2)
LEFM	Linear Elastic Fracture Mechanics
LEVD	Largest Extreme Value Distribution
MML	Maximum Likelihood
MPa	Mega Pascal
ODA	Optically Dark Area
PDF	Probability Density Function
PS	Polished Specimen
QT	Quenched and Tempered
SEM	Scanning Electron Microscopy
UHCF	Ultra-High Cycle Fatigue

List of symbols

h_o	The average $\sqrt{area}$ of the maximum inclusion distribution obtained from the standard inspection area
$\sqrt{area_{max,j}}$	The maximum size of the largest inclusion determined for a standard inspection area S_o or volume V_o
$\sigma_w{}'$	The modified $\sqrt{area}$ model for ODA predicted lower bound fatigue limit
D_G	The standard deviation for the Gumbel distribution
$\sqrt{area}$	The square root projected area of an inclusion or defect on the plane normal to the stress
$\bar{\lambda}$	The mean of the Gumbel distribution
σ_a	The stress amplitude
σ_{max}	The maximum stress
σ_{min}	The minimum stress
σ_{wl}	The $\sqrt{area}$ model predicted lower bound fatigue limit
σ_{wu}	The predicted upper fatigue limit
ΔK_{ODA}	Stress intensity factor range for ODA
$\Delta\sigma_+$	The positive portion of the stress range
ΔK_{th}	Threshold stress intensity factor range
$\Delta\sigma$	The stress range
A	A parameter determined experimentally for predicting the largest inclusion
B	A parameter determined experimentally for predicting the largest inclusion
C	A constant used to calculate the fatigue limit
d_s	The standard deviation for the normal distribution
K_{max}	The maximum stress intensity factor
L	The calculated likelihood
n	The number of trials used for calculation of binomial probability
N_f	The number of stress cycles to failure

p	Binomal probability of an event
P_{conf}	The confidence of an unknown calculated probability
r	The number of failures for calculation of binomial probability
R	The stress ratio, $\sigma_{min}/\sigma_{max}$
R_o	Runout
S	Area of prediction (mm^2)
S_{max}	The maximum value of the stress amplitude
S_o	Standard inspection area (mm^2)
T	Return period
V	Volume of prediction (mm^3)
V_o	Standard control volume (mm^3)
V_s	Control volume for prospective fatigue failure (mm^3)
Y	Geometry correction factor
α	$0.226 + HV \times 10^{-4}$
ΔK_+	The positive portion of the stress intensity factor range
δ	Scale parameter used in extreme value theory
λ	Location parameter used in extreme value theory
σ	The stress acting on a specimen

1. Introduction

Machines that are used under demanding loads are commonly subject to fatigue failure. This failure is caused by the initiation and growth of small fatigue cracks from defects in the component that eventually result in the complete failure of the machine. This problem is examined here from three viewpoints: 1) the defect that initiates small crack growth (in steels generally a non-metallic inclusion), 2) the material surrounding the defect (in this case the microstructure), and 3) the effect of loading on initiation and small crack growth that makes up the majority of high and ultra-long cycle fatigue life.

Non-metallic inclusions are intrinsic to steel components. The cleanliness of the steel has been improved during the last 50 years due to the development of better production methods and technology that allow steel mills to minimize the impurities that result in defects and inclusions in the steel. The use and application of steels has also increased and the demands and design requirements have called for stronger and harder steels for lighter and more efficient machine components. This increase in the use of high-strength steels has resulted in the need for more specific and in-depth understanding of the challenges that are presented for harder and stronger steels. A general rule is: the higher the tensile strength the lower the ductility of the steel. This means that the size of defects or stress concentrators in the steel become more critical as the strength or hardness of the steel increases. This problem is seen in the correlation of the fatigue strength of steels to the hardness. Generally the fatigue strength of the steel increases until around 400 HV after which the scatter increases and the correlation is no longer valid.

Non-metallic inclusions can be of different types and sizes. The location, size and distribution of the non-metallic inclusions needs to be understood so that it is possible to predict for large components with large volumes the largest non-metallic inclusion conservatively. The theory that has been used to predict extremes (in this case maxima extremes) is called extreme value theory.

The research relating to small crack fatigue growth has been ongoing for many decades. The commonly referred Kitagawa-Takahashi diagram defines the basic relationship between small cracks that arrest and long cracks that behave according to

Linear Elastic Fracture Mechanics [1]. The application of linear elastic fracture mechanics to small cracks as well as studies about small crack growth were made by Smith in ref [2] and Taylor in ref [3] as well as many others [4-9]. The general conclusion is that this area is challenging and many researchers have concluded that there are certain intrinsic factors such as the relationship of the crack size to the microstructure that dominate this portion of the crack growth. The general understanding of the majority of the research is that the small cracks grow faster than long cracks and the explanation for this varies. Certainly there are differences in material as well as test methods, however the fact remains that the successful modelling of small crack growth is difficult and is also subject to many variables and interpretations.

One of the main reasons why small crack growth has been difficult to study is due to the lack of proper tools to perform reliable and repeatable measurements of very small cracks that are tested for very long fatigue lives. The in-situ high-speed optical microscopy combined with FIB notches and small drilled holes provides a novel as well as reliable and consistent method of measuring the growth of the small crack during long and continuous fatigue testing. Furthermore, the experimental setup used here provides a window into the behaviour of small cracks under large compressive fatigue loads in the high cycle fatigue regime. This type of testing gives insight as well as data about the effect of compressive stress on the behaviour of small cracks initiating and growing in many industrial machine components that use various surface hardening production methods to improve the fatigue life of the components.

1.1 Non-metallic inclusions in steel and fatigue endurance limit

The fatigue endurance limit of steels is calculated or estimated using different assumptions for the mechanism causing fatigue crack initiation. The steel can be defect free which would mean that a fatigue limit of this type of steel would be the upper limit, or as is generally the case a steel can have defects of varying sizes in its matrix which would result in a lower fatigue limit. The fatigue life or fatigue limit for steels is often studied with respect to the distribution of non-metallic inclusions in the steel. The connection between the distribution of defects in metallic materials and their fatigue properties has been discussed in many publications (see references: [10-33]). The general approach that has evolved to deal with this problem is based on the probabilistic modelling of the distribution of the inclusions. The occurrence of the largest inclusions in the steel is predicted by studying different cross-sections of steel and recording the sizes of the maximum inclusions found. Then by applying the theory of extreme values it is possible to predict the occurrence of the largest inclusion that will cause fatigue failure. The inclusion distribution model is then applied in a crack growth rate model which is used to calculate the distribution of cycles to failure or the decrease in the fatigue limit of the material. This kind of a predictive model is outlined in refs: [19] [20] [28].

1.1.1 Inclusion analysis

Non-metallic inclusions that occur in steels can be divided into two categories; indigenous and exogenous. Indigenous inclusions occur in steels as a result of the reactions that take place between the chemical compounds present in the steel as it cools and solidifies. The exogenous inclusions are inclusions that occur in steels due to the result of mechanical incorporation from the slag or other materials and impurities that the molten steel comes into contact with.

The forming of the indigenous inclusions happens by precipitation that is a result of the reactions occurring in the molten steel. The formation of these indigenous inclusions which are composed mostly of oxides and sulphides can be controlled by the use of additives to the steel, or by changes in the solubility during the cooling and solidification of the steel.

Exogenous inclusions are more variable in their occurrence and composition. Some of the main characteristics of these types of inclusions are greater size, increasing randomness in occurrence, irregular shapes and complexity in structure. The compositions of exogenous inclusions are typically oxides, which is due to the nature of the source of the inclusions such as the slag. [34]

During the production of wrought steel components there is a large degree of anisotropy that is produced depending on the amount of forging that is performed. The forging strengthens the component by refining the grain structure, but also can have an effect on the size distribution and direction of the non-metallic inclusions in the steel. This effect of anisotropy is studied in publication (I) and the difference in the sampling direction can be seen in the inclusion distribution. This effect is then reflected in the fatigue limit and its scatter. There is clearly a larger population of inclusions that are found when sampling perpendicular to the forging direction than parallel to the forging direction.

The data about the inclusions in the steel that is gathered from testing and analysis can be described using different types of distributions. Some of the typical parent distributions that are used are: normal, Poisson, binomial, exponential, and lognormal distributions. The method of extreme value analysis takes either the maximum or minimum values from the different types of original or parent distributions that were listed.

The largest inclusions found in steels can be considered to be the extreme maximum of the general population of inclusions. To choose which type of extreme distribution model to use the GEV, Fréchet, and Gumbel extreme value distributions were tested with a Kolmogorov–Smirnov test using the inclusion data. In publication (I) the best fit of these three was found to be the Gumbel distribution which is the extreme value distribution for the normal distribution. This extreme value distribution is given as follows:

$$P(X \leq x) = exp\left\{-exp\left(-\frac{x-\lambda}{\delta}\right)\right\} \quad (1)$$

where the values λ and δ are the location and scale parameters [32] [35]. For the Gumbel distribution the mean ($\bar{\lambda}$) is calculated as follows:

$$\bar{\lambda} = \lambda + \delta \cdot \gamma \quad (2)$$

where γ is calculated as:

$$\gamma = -\int_0^1 \left(\ln\left(\ln\left(\frac{1}{x}\right)\right)\right) dx \approx 0.57721 \quad (3)$$

The standard deviation (D_G) for the Gumbel distribution is:

$$D_G = \frac{\delta \cdot \pi}{\sqrt{6}} \quad (4)$$

The distribution parameters of a Gumbel distribution for the inclusion populations studied were estimated by using the Maximum Likelihood Method (MML). This method uses the probability density function to directly calculate the parameters of a distribution by calculating whether a certain probability distribution function can describe a set of data. The parameters of the probability distribution are fitted to maximize the likelihood which is calculated as follows:

$$L = \prod_{i=1}^{n} f(x_i) \quad (5)$$

In equation (5) the function $f(x_i)$ is the Probability Density Function (PDF). The Gumbel probability density function is given as:

$$f(x, \lambda, \delta) = \frac{1}{\delta} \cdot exp\left\{-\frac{(x-\lambda)}{\delta}\right\} \cdot exp\left\{-exp\left\{-\frac{(x-\lambda)}{\delta}\right\}\right\} \quad (6)$$

To estimate the parameters λ and δ of the distribution by MML method the logarithm of the MML is usually used for simplicity. This equation is called the log likelihood and is given as:

$$\ln(L) = \sum_{i=1}^{n} ln\{f(x_i)\} \quad (7)$$

The maximization of equation (7) is done with an iterative process. The two parameters λ and δ are manipulated to maximize ln(L) in equation (7). Once the maximum log likelihood ln(L) is known then the parameters λ and δ that produced the MML are the parameters that best fit the distribution according to MML method.

When the λ and δ maximum likelihood estimates for the Gumbel distribution are known these values are used to estimate the maximum size of the inclusion $\sqrt{area_{max}}$ with a return period T and it is given as:

$$x(T) = \lambda + \delta \cdot y \quad (8)$$

where y = -ln(-ln[(T-1)/T]) with the return period T being defined as V/V_o, where V_o is the inspection volume and V being the volume of the part for which the maximum inclusion is being predicted. In this case V_o is calculated as follows: $S_o \cdot h_o$, where h_o is the average $\sqrt{area}$ of the maximum inclusion distribution obtained from the inspection. The calculation of V for a test bar that is placed under rotating bending loading is considered to be the volume where the local stress is greater than 90% of the nominal stress. Murakami proposes in Ref. [28] the following volume: $V = 0.05\pi d^2 l$, where d is the diameter of the gauge length and *l* is its length for rotating bending fatigue test specimen used in publication (I).

1.2 The statistical aspects of fatigue for high-strength steels

The scatter in the fatigue strength of high-strength steels is mostly caused by the scatter of the size of the inclusions that are in the specimen [28]. The scatter in the size of the inclusions present in the steel is caused by two main factors. The first factor is the volume of steel that is in question, and the second is the distribution of the inclusion sizes in the steel.

The distribution of inclusion sizes has been researched and a method for inclusion rating based on extreme value statistics has been developed [36,37]. This method can also be found in the ASTM standard E 2283-03 and can be implemented as follows:

The maximum size $\sqrt{area_{max,j}}$ of the largest inclusion is determined for a standard inspection area S_o or volume V_o. This process is repeated n times and the resulting maximum inclusions are ranked as follows: $\sqrt{area_{max,1}} \leq \sqrt{area_{max,2}} \leq \cdots \leq \sqrt{area_{max,j}}$. The cumulative distribution function F_j(%) as well as the reduced variates y_j for the inclusion distribution are then calculated according to the following equations:

$$F_j = j \times 100/(n+1) \quad (9)$$

$$y_j = -ln\{-ln[j/(n+1)]\} \quad (10)$$

The maximum size $\sqrt{area_{max,j}}$ is then ploted according to the ranking that was done on a probability plot with the abscissa coordinates as $\sqrt{area_{max,j}}$ and the ordinate axis being either F_j or y_j. An example of this kind of a plot is shown in Figure 1.

As can be seen in Figure 1 the reduced variate plotted against the $\sqrt{area_{max,j}}$ has a linear relationship. This relationship can be used to predict for a larger volume of steel. The linear relationship can be written as follows:

$$\sqrt{area_{max}} = A \cdot y + B \quad (11)$$

where $y = -ln\{-ln[j/(n+1)]\}$. To predict the maximum inclusion in an area S or volume V we get: T = S/So or V/Vo and since we know that T=1/(1-F), so by using the previous equations we can write equation (11) as:

$$x(T) = B - A \cdot ln\{-ln[1 - 1/T]\} \quad (12)$$

This equation can be used to predict the largest inclusion in a given volume of steel. The parameters A and B are determined experimentally [28].

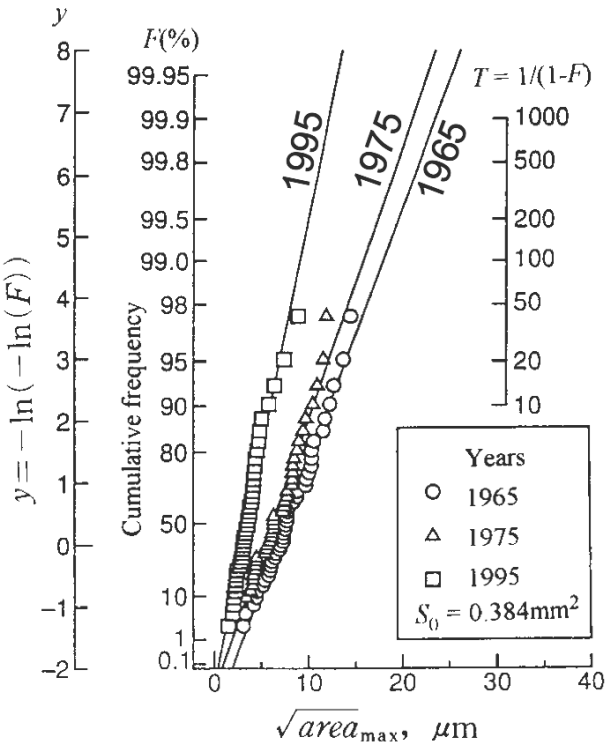

Figure 1. The results show the improvement in production quality for SAE52100 steel for different years with respect to the distribution of the maximum inclusions in the steel [28].

This standard method has been in use for many years, however there are improvements and changes that could be done to improve it. Some possible improvements are proposed in publication (VI).

1.3 Fatigue endurance limit prediction

The fatigue limit of steel is empirically estimated with fatigue tests. The staircase test method is used to estimate the fatigue limit of the steel. Two different methods are used for the analysis of test data. The first is the Maximum Likelihood Method (MML) that has been developed by Dixon and Mood for the staircase test [38], which uses the method of least squares to estimate the fatigue limit and its standard deviation from the data. The second method analyses the data with the binomial probability theory to estimate the fatigue limit of the steel. This method has been developed by Wallin [39].

1.3.1 Maximum likelihood analysis

The calculation of the fatigue endurance limit is done using a special case of the Maximum Likelihood Method, which is commonly called the method of least squares. This method is the minimization of the following equation which is called the sum of the squares:

$$\mathrm{S} = \sum_{i=1}^{n} \left(\frac{\mathrm{x_i} - \bar{\mathrm{x}}}{\mathrm{d}_s}\right)^2 \tag{13}$$

The average $\bar{\mathrm{x}}$ and the standard deviation d_s are assumed to be from the normal distribution and are fitted to the data so that equation (13) is minimized. This method has been developed by Dixon and Mood and is used for the analysis of the staircase test results. [38]

1.3.2 Binomial probability analysis

The results of the staircase test resemble a binomial distribution because the test specimen either fails at the stress level or it survives. The probability of having a certain number of failures at a certain stress level can be calculated according to the binomial theory as:

$$\mathrm{P}(X = r) = \binom{n}{r} \cdot p^r \cdot (1-p)^{n-r} \tag{14}$$

where

$$\binom{n}{r} = \frac{\mathrm{n!}}{\mathrm{r!(n-r)!}} \tag{15}$$

Equation (14) gives the discrete probability that there are (*r*) failures in (*n*) trials. In a staircase test the probability of the event *p* is not known. This probability can be calculated with a certain confidence (P_{conf}) with the following equation:

$$\mathrm{P}_{\mathrm{conf}}(p \leq x) = \frac{\int_{\mathrm{p}=0}^{\mathrm{x}} \binom{n}{r} \cdot p^{r} \cdot (1-p)^{n-r} \cdot \mathrm{dp}}{\int_{\mathrm{p}=0}^{1} \binom{n}{r} \cdot p^{r} \cdot (1-p)^{n-r} \cdot \mathrm{dp}} \quad (16)$$

The results can then be ranked according to binomial probability which starts at zero. The ranking gives the P_{conf} level of 5%, 50%, and 95 % for each stress level. [39,40]

1.3.3 The Murakami-Endo model

The Murakami-Endo Model predicts that when the location of the fracture origin is a small defect or non-metallic inclusion then the fatigue limit of the material can be determined by the Vickers hardness of the microstructure surrounding the non-metallic inclusion and the square root of the projected area $\left(\sqrt{area}\right)$ of the defect normal to the stress. [28]

The model treats the inclusions or defects that are smaller than $\sqrt{area} \leq 1000\ \mu m$ as small cracks and it has been tested to be valid for high-strength steels (HV ≥ 400). The general equation is given as:

$$\sigma_{wl} = C \cdot (HV + 120) / \left(\sqrt{area}\right)^{1/6} \quad (17)$$

where C is 1.43 for inclusions on the surface of a test specimen, 1.41 for inclusions in touch with the surface and 1.56 for inclusions underneath the surface. The σ_{wl} is the predicted fatigue limit (MPa), HV is the Vickers hardness of the matrix around the inclusion (kgf/mm^2), $\sqrt{area}$ is the square root projected area of the inclusion on the plane normal to the stress (µm). This method for calculating the lower fatigue limit has also been applied and used successfully for steels and metals with a micro hardness that is less than 400 HV. [28]

1.4 Small crack growth in high cycle fatigue

The study of small crack growth has been approached from different viewpoints. A general approach has been to examine the fatigue endurance limit with respect to the defect or size of the crack. This approach is schematically illustrated using the Kitagawa-Takahashi (KT) diagram shown in Figure 2. The x-axis is the size of the crack, and the y-axis is the threshold stress range. This graph shows that for the smallest cracks as the size approaches zero there is no longer any correlation between the stress range and crack size. This means that for many steels there is a part of the curve where the size of the crack will cause failure independent of the loading.

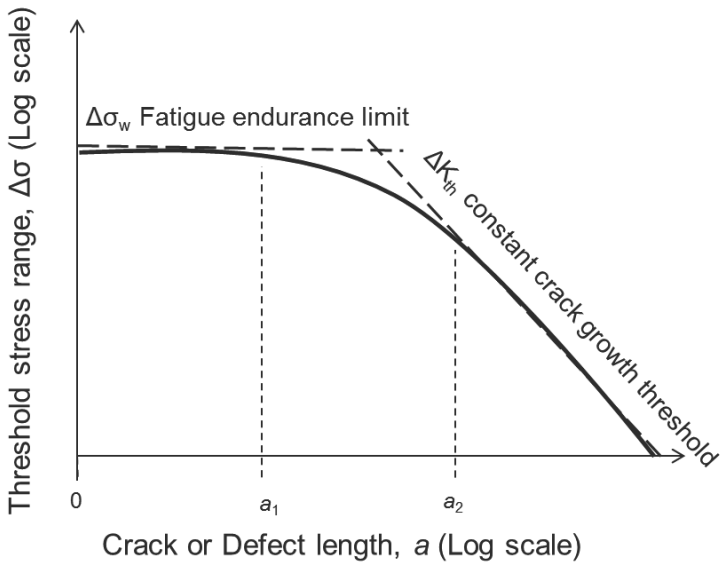

Figure 2. A schematic of the Kitagawa-Takahashi diagram. [1]

The KT diagram shows the fatigue endurance limit for small cracks and the fatigue crack growth threshold for long cracks. The existence of a fatigue endurance threshold can be interpreted to mean that below a certain size of defect or crack found in the material, in this case a_1, the material will fail if a stress range above the endurance limit is applied. An interpretation of these results was done by El Haddad et al. who proposed an intrinsic crack length ' *l* ' to be added to short cracks [41]. This publication offers a possible theoretical explanation to the short or small crack portion of the KT diagram, it does not however explain the phenomena itself, nor does the theory of an intrinsic crack length have any basis in the material itself.

Using the KT diagram assumes that there is actually a true threshold for fatigue endurance. This has usually been typically set at 10^7 fatigue cycles which is considered to be the runout limit for High Cycle Fatigue (HCF). With many machine components this amount of loading cycles is achieved early in the design life. This has led to more research into what is known as Ultra-High Cycle Fatigue (UHCF) or Giga Cycle Fatigue (GCF) which is fatigue cycles of more than 10^7 as well as up to and beyond 10^9 cycles. The KT diagram has to assume an endurance limit for the crack growth. If a higher number of cycles are assumed for an endurance limit it can be that this would also eliminate or reduce the small crack portion of the KT diagram.

1.4.1 Small crack growth and loading

The designer of machines or mechanical components that experience numerous loading cycles needs to understand the material response to the loads and possible defects or cracks that can grow or initiate fatigue cracks. This has given rise to many studies about small fatigue cracks and unique phenomena that occur in their initiation and growth. The effect of the compressive portion of the fatigue cycle on the behavior of small cracks is important for many industrial components that, for example, use various surface hardening treatments to improve their fatigue strength or endurance. Many fatigue improving treatments cause high compressive stresses on the component surface. This can prevent fatigue, but if not used properly, cause failure.

One important factor to consider is the impact of different mean stresses on the growth of small cracks. This area of research has been concentrated more on the positive portion of the R-ratio. In this study we observe what impact an increasing and large compressive loading ratio has on the initiation and growth of small cracks.

The general focus of most small crack growth research has been in the range of tension - tension loading ($R > 0$), symmetric loading at $R = -1$, and other researchers have studied also the initiation and arrest of short cracks from notches under fully compressive loading [5,42-50]. An interesting question is the amount of crack closure in small cracks because the original studies done on crack closure by Elber were performed on large cracks in soft metals [51,52]. More recently Silva studied the effect of compressive loading on crack growth. One of the main focuses of his research was the inability to explain some of the effects of compression on the crack growth in fatigue by crack closure [53]. The research showed that there is a significant effect of compressive loading on the crack growth and this varies from material to material. It was concluded that some intrinsic material properties should be incorporated into models that were previously developed [54]. A recent study demonstrated using finite element analysis that the largest effect of underloads or compressive loading was the reduction of retardation effects and acceleration of crack growth [55].

The focus on the effect of compressive loading on the growth of small fatigue cracks in the quenched and tempered steel is studied in publication (V). More specifically, the effect that the compressive part of loading has on the small cracks and their growth rates near and at the threshold for crack growth. The measurements are performed at the HCF regime and introducing very small surface notches, which can initiate cracks close to or even below the fatigue endurance limit ($N_f > 10^7$) of the specimen.

1.4.2 Small crack growth and microstructure

Fatigue crack initiation and growth from surface or subsurface non-metallic inclusions in high-strength steels is of importance in many industries. This has been the focus of many studies and, in particular, a book by Murakami [28]. Some studies have found that hydrogen trapped around non-metallic inclusions provides an explanation for a cause of failure in ultra-long fatigue life of high-strength steels [28,56-63]. However, there are yet questions about the characterization and prediction of initiation and growth of microstructurally small cracks from inclusions in high-strength steels. Some reserachers have shown other factors such as the fact that cracks grow in a vacuum inside the test specimen or changes in the microstrucure around the inclusion [64-66]. Other studies have used Focused Ion Beam (FIB) milling to create cross-sections, after which FIB imaging is used to make ion channeling contrast pictures of the microstructure [67- 73]. This imaging technique has been applied to small cracks in steels to study the profile in depth [68, 74]. Researchers have recently used the FIB tools to show how the size and crystal orientation of the grains affect the growth and direction of small cracks from notches and inclusions in steel [67,68,75,76]. These tools and techniques are used to study the role the martensite sub-grain microstructure has on the initiation and growth of small fatigue cracks in high-strength steels from inclusions and notches.

Non-metallic inclusions in steel promote subsurface crack initiation, which means that the direct observation of initiation and early growth of cracks is extremely challenging. One solution is to introduce FIB-milled semielliptical notches to simulate a case, where fatigue relevant inclusions are on the specimen surface, and so the path and growth of the small crack can be observed. The small cracks which have grown from the FIB notches can then be compared with the small cracks from non-metallic inclusions that failed at or near the endurance limit. In the past there have been various definitions used to define small cracks, however, for the purposes of this study we consider small cracks to be those that are less than around 1 mm in length.

1.4.3 ODA, inclusions, and small cracks

Research into the cause of ultra-long life fatigue failure in high-strength steels has revealed that fatigue crack initiation occurs at subsurface non-metallic inclusions. Next to these subsurface inclusions a dark area is observed that is called Optically Dark Area (ODA). The presence of an ODA is not observed on fracture surfaces of specimens with short fatigue lives. The appearance of the ODA next to subsurface inclusions has been researched and documented in the following references: [22,56-58,60,77-79]. The failure of test specimen at ultra-long fatigue lives (N_f >

10^7) and the effect caused by the size of the test specimen can be united by understanding the role that non-metallic inclusions play in causing fatigue failure in ultra-long fatigue.

To predict fatigue failure due to the presence and role of the ODA and its growth from non-metallic inclusions, the work in publication (II) reviews the research that has been performed by Murakami and his co-workers in references [58,59,61,62]. The results of these studies reveal that there are several factors that have to be considered. These factors are:

1) The growth of the ODA with respect to the fatigue life of the specimen and internal hydrogen in the specimen.
2) The statistical aspect of fatigue due to the difference in volumes tested and the distribution of the maximum inclusions in the steel.
3) The dependency of the threshold stress intensity factor range ΔK_{th} on crack size.

Publication (II) reviews these three main factors involved in ultra-long life fatigue failure in high-strength steels from internal inclusions viewpoint and proposes a fatigue design approach for ultra-long fatigue lives of high-strength steel components. This design approach incorporates the effect of the volume as well as the distribution of the inclusions in the steel, along with the growth of the ODA from the inclusions in ultra-long fatigue life regimes. This design approach is only meant to be used for ultra-long life fatigue failure in high-strength steels caused by subsurface non-metallic inclusions. This design approach does not take into consideration other factors in fatigue such as mean stress, environmental effects, surface effects or notch effects.

2. Aims of the study

The goal of this thesis is to focus on the interaction of the non-metallic inclusions with the microstructure and the fatigue loading with small cracks in high-strength steels. The experiments and analyses of the results approach this problem from three perspectives:

-What is the effect of the distribution and size of the non-metallic inclusions in the steel with respect to fatigue?
This is the perspective that is studied in publications: (I), (II), and (VI).

-What is the interaction of the microstructure, inclusions, and small fatigue cracks?
Using FIB milling and imaging this perspective is investigated in publication (IV).

-What is the interaction of small fatigue cracks, loading and defects?
The research on the growth of small cracks in high cycle fatigue is investigated with special high-speed microscopy combined with small FIB notches and drilled holes in publications: (III) and (V).

3. Material and experimental methods

3.1 Material properties

3.1.1 Rotating bending fatigue testing

The test bars studied in the fatigue tests were taken from an industrial forged steel roll. The approximate dimensions of the roll are around 1 m in diameter and 6 m long. The chemical composition of the steel is given in Table 1.

Table 1. The chemical composition (wt %) of the forged steel.

	C	*Mn*	*P*	*S*	*Cr*	*V*	*Mo*	*Si*
Weight %	0.61	0.50	0.005	0.005	1.34	0.08	0.26	0.23

The manufacturing process of the steel roll starts with the casting of a steel ingot, after which it is forged to a degree of deformation that ranges from 4 to 7. The forged steel is pre-machined after which it is quenched and tempered, and the surface is then induction hardened and machine finished. The microhardness of the steel test bars is 320 HV.

3.1.1 Axial fatigue testing

Different batches of two steel types were studied in publications (III) - (VI). One is a bearing steel of type 100Cr6 quenched and tempered at 180 ºC to hardness 720 HV (tensile strength 1630 MPa) and the other is a quenched and tempered 34CrNiMo6 steel with a hardness of 380 HV and with 1065 MPa and 1180 MPa yield and tensile strength, respectively. In publications (III, IV and VI) the 34CrNiMo6 QT steel is from the same production batch. For publication (V) the 34CrNiMo6 QT steel is from a separate production batch and has a slightly lower tensile and yield strength given in publication (V). From here on the steel studied in publications (III, IV, and VI) will be called 34CrNiMo6 QT(A) and the steel studied in publication (V) will be called 34CrNiMo6 QT(B).

EBSD images of the microstructure of these two steels are shown in Figure 3 and the chemical composition is given in Table 2. The average ferrite grain size is 2.2 µm for the 34CrNiMo6 QT steel and around 1.4 µm for the 100Cr6 bearing steel. The estimated prior austenite grain size for the two steels was around 30 µm for the 34CrNiMo6 QT(A) steel and around 7 µm for the 100Cr6 bearing steel.

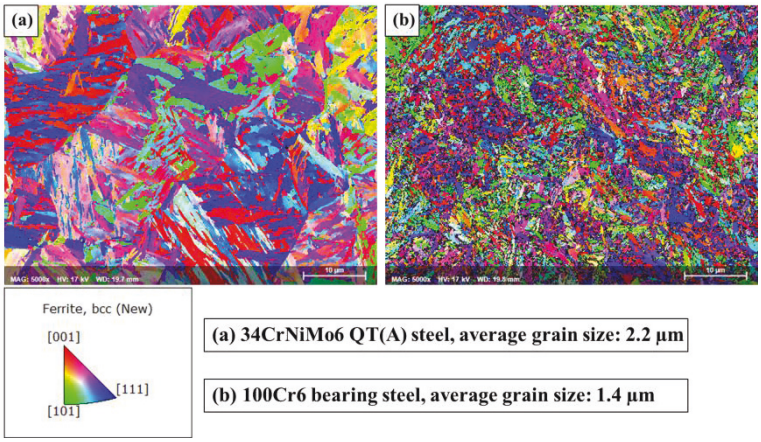

Figure 3. (a) Microstructure of 34CrNiMo6 QT(A) steel, and (b) microstructure of the 100Cr6 bearing steel. Both EBSD images are taken perpendicular to the loading direction of the test specimen.

Table 2. The chemical composition (wt %) of the 34CrNiMo6 QT and 100Cr6 steel.

Steel type	*C*	*Si*	*Mn*	*P*	*Cr*	*Ni*	*S*	*Mo*	*Cu*	*Al*
100Cr6	0.95	0.25	0.39	0.02	1.43	0.137	0.005	0.022	0.15	0.01
34CrNiMo6 QT(A&B)	0.34	0.28	0.65	0.008	1.67	1.63	0.01	0.24	0.19	0.02

3.2 Fatigue testing

3.2.1 Rotating bending fatigue testing

The fatigue properties of the steel studied in publication (I) were tested with the rotating bending fatigue test method. A Schenk rotating bending fatigue test machine was used to apply a four-point bending loading to the test bar that ensured a constant loading moment along the gauge length of the specimen. Rotation of the fatigue test bar under four-point bending results in the varying of the applied stress at a stress ratio of R = -1, at a frequency of 35 to 40 Hz. An illustration of the size and shape of the test bars is shown in Figure 4.

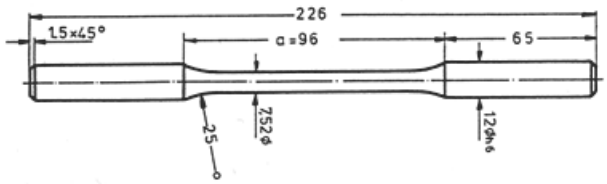

Figure 4. The geometry of the rotating bending fatigue test bar. All dimensions are in millimetres.

The fatigue test bars were removed from a forged steel roll at locations that were below the induction hardened surface. The bars that were taken tangential to the axis of the forged steel roll are called tangential test bars and correspond to the X-plane of the polished specimens used in the inclusion analysis. The test bars that were taken parallel to the axis are called axial test bars and correspond to the Y-plane of the polished specimens used in the inclusion analysis. An illustration of the direction of the test bars with respect to the steel roll is shown in Figure 5.

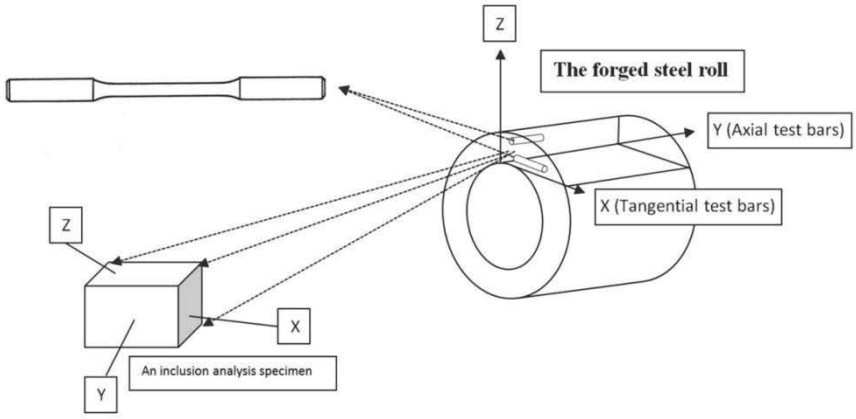

Figure 5. A schematic illustration of the location of the test bars as well as the specimens used for inclusion analysis.

After removal from the forged roll the test bars were machined and their surfaces were ground and polished. The transverse scratches were ground away and polished so that the effect of the surface features of the test bars on the fatigue limit was minimized. Testing was done using the staircase method with a step size of 5 MPa for tangential test bars and 10 MPa for axial test bars. The tests were performed at room temperature and the runout limit was set at 10^7 cycles. If a test bar reached the runout limit then the test was aborted and classified as a runout. All of the runouts were retested at a stress level that was 100 MPa higher than the runout

stress level. This was done to cause failure so that the largest inclusion causing failure could be studied.

3.2.2 Axial fatigue testing

The 100Cr6 bearing steel specimens (Figure 6) were taken from ¼ depth (17.5 mm from the surface) of a ϕ70 mm wrought bar. The 34CrNiMo6 QT(A&B) specimens according to Figure 7, were machined from the centreline of ϕ35 mm wrought bars.

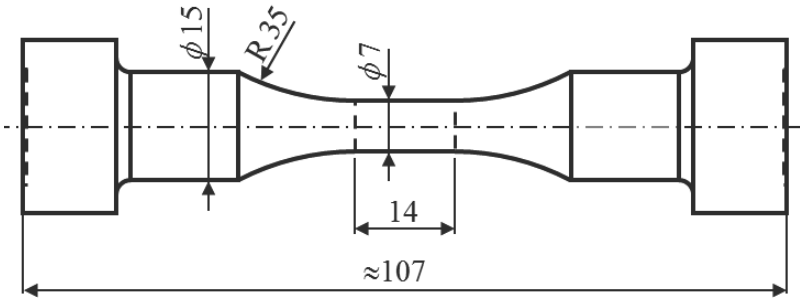

Figure 6. The dimensions of the axial fatigue test bar used for the bearing steel 100Cr6.

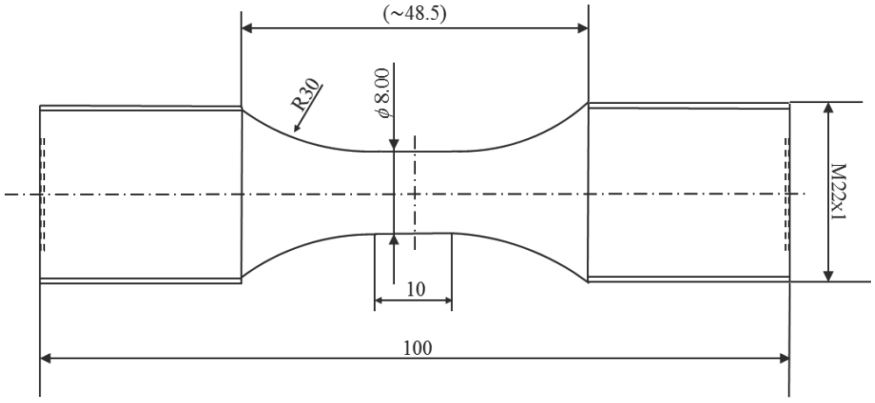

Figure 7. The dimensions of the test bar for the quenched and tempered 34CrNiMo6 (A&B) steel used for axial fatigue testing.

The test bar shown in Figure 7 was used in publications (III)-(VI), and the test bar shown in Figure 6 was used in publication (IV).

3.3 Inclusion analysis and distribution

In publication (I) the inclusions found on the polished specimens as well as the fracture surfaces were all photographed, measured and their chemical compositions were analyzed. The elemental analysis was done using an INCA Energy 300 Microanalysis System (EDS).

The specimens used for inclusion analysis were taken from three different locations in the steel roll. The three positions were: one from close to the outer surface, one from in-between the center and the outer surface and one closer to the center of the steel roll. Once cut from the steel roll the specimens were polished. After the polishing the specimens were analyzed using an automatic INCA Feature analysis program. The program distinguishes inclusions on the polished surface by using the electron backscatter detector to differentiate between the matrix and the inclusions. The automated inspection was set at a magnification of 300X, and the inspection area that was automatically scanned and analyzed was 25 mm^2. For each plane this inspection was performed six times to achieve a total inspection area of 150 mm^2 for the plane. Once the analysis was complete the process was repeated with the same specimen on a new plane until all planes X, Y, and Z had been analyzed. This process was repeated for all three inclusion analysis specimens taken from the steel roll. A standard inspection area (S_o) of 25 mm^2 was defined for an extreme value analysis of the inclusions. The largest inclusion in each standard inspection is used for the extreme value analysis.

3.4 Small crack growth and fatigue testing

In publications (III)-(V) we apply small notches or holes to smooth specimens and investigate the relevance of using them as small crack initiators. They were used to measure small crack growth rates and thresholds. This testing method is compared to small defects such as non-metallic inclusions in the steel.

Axial fatigue testing is performed at resonant frequencies around 100 Hz and the specimens were fatigued either close to the range of smooth specimen fatigue limit or at different R-ratios that are in the high-cycle fatigue regime. The small notches were optically monitored and video recorded for crack initiation, growth and arrest in real time. An example of this is shown in Figure 8. The high-speed video microscope is a Keyence VW-9000E system that uses a high-speed monochrome camera unit, VW-600M and a zoom lens (100X to 1000X), VH-Z100R.

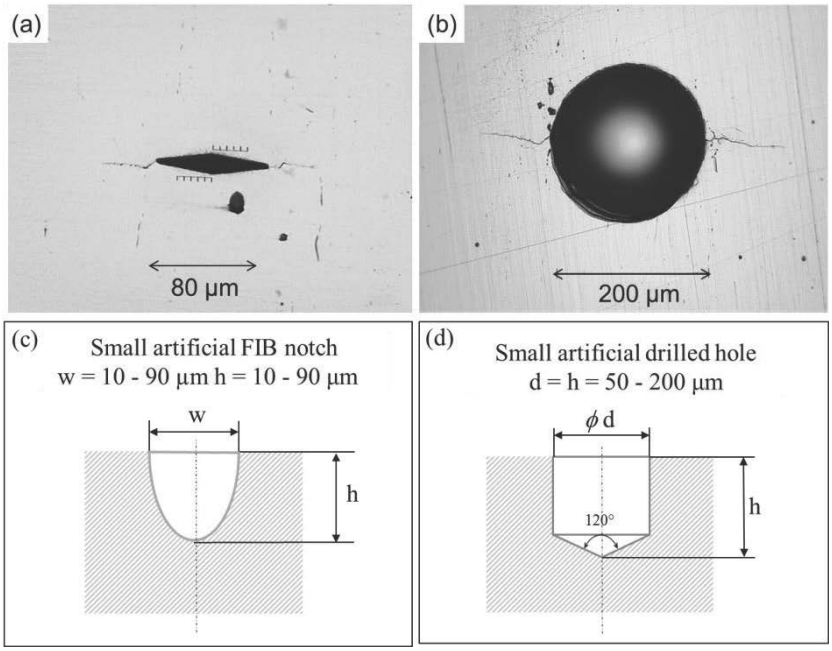

Figure 8. Examples of a) a FIB notch and b) a drilled hole being observed in-situ with a high-speed video microscope during testing, c) shows the cross-section dimensions of the FIB notch and d) the cross-section dimensions of the drilled hole. The measurements for both are given in µm.

The notches or holes were manufactured by drilling (ϕ 50 - 200 µm) and FIB milling (w = 10 – 90 µm) into the type of test bars shown in Figure 7. The FIB milling was done with a FEI Helios Nanolab dual focused beam system. The FIB was set to a voltage of 30 kV and a milling current of 21 nA was used. The pattern was defined with a diamond shape seen in Figure 8 and Figure 9 with a notch height typically of 5-10 µm.

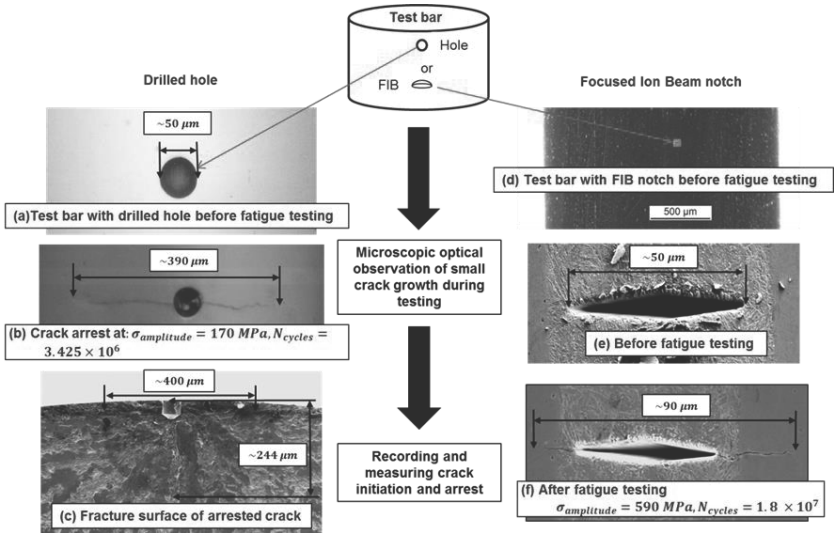

Figure 9. The test setup and method for measuring small crack growth from notches and holes. The parts (a) through (c) show the procedure used for drilled holes and (d) through (f) show the procedure used for FIB notches. A higher stress amplitude of 200 to 230 MPa was used to cause failure of the test bar and the fracture surface of the specimens shown in (c).

The small holes and notches were monitored optically during the testing to detect small crack initiation and growth. Once the test bar failed or the test was complete it was examined with SEM, laser and optical microscopes. Sometimes the test bars failed from some other location such as an inclusion. Then the initiation site was studied with a SEM and the type, size, and shape of the initiation site was recorded.

Two types of small crack growth fatigue tests were performed. One was constant amplitude loading and monitoring of the fatigue crack growth from a notch. This means that the crack initiation and growth from the notch or hole are constantly monitored and measured in-situ, while the loading of the test specimen is constant. These types of tests were done in publications (III)-(V)

The other type of test that is reported in publication (V) is where:

1. The loading was slowly decreased as the crack grows to measure the arrest threshold of the small crack. Once this is done and after the crack has arrested,
2. The compressive portion of the loading is increased, while the maximum tensile stress was held constant. In other words, the arrested crack experiences a decreasing mean stress along with the increasing stress amplitude, but a constant maximum stress. The test was continued in this way with steps of 20-50 MPa in mean stress and each step was applied for about 1 million cycles or until crack growth is detected.

3. After crack growth is detected the stress amplitude is kept constant and the mean stress was decreased with constant monitoring of crack growth until the crack arrest was again confirmed.

After the crack arrest, step 2 is repeated again until the crack growth is detected. This type of testing was done with a starting stress ratio of R = -1, and with a stress amplitude of 450 MPa. The same testing procedure was also performed with a starting stress ratio of R = -2, where the maximum stress was 350 MPa and the minimum stress was -700 MPa.

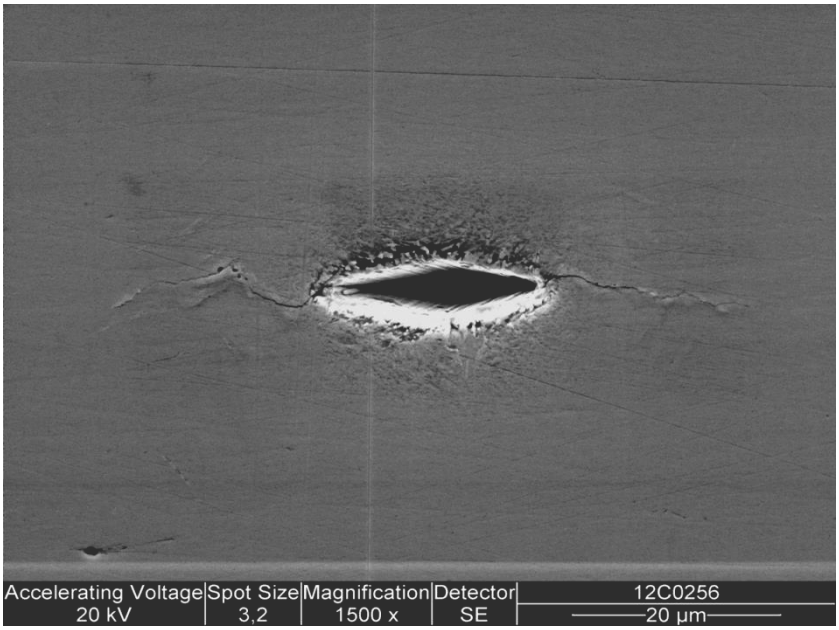

Figure 10. A SEM image of a 20 µm FIB notch milled into the side of a test bar after 50000 cycles of fatigue testing. Publication (III)

Calculation of stress intensity factors

The results are analysed and presented using the $\sqrt{\text{area}}$ for inclusions, and the surface crack length for small cracks as seen in Figure 10. The threshold for crack growth or initiation for the different sizes of inclusions was calculated by using equation (18) [28].

$$\Delta K_{th} = 0.65 \cdot \Delta\sigma \cdot \sqrt{\pi\sqrt{\text{area}}} \quad (18)$$

The other type of measurement was observed during testing, either in-situ or during interrupted loading. These results are reported as crack lengths on the specimen surface. The length of the surface crack was used to calculate the stress intensity factor range for the FIB notch test bar by using equation (19).

$$\Delta K = 0.65 \cdot \Delta\sigma \cdot \sqrt{\pi \mathrm{a}} \quad (19)$$

In equation (19) the variable '*a*' is from the observed crack length of '*2a*'. Any crack solution becomes arbitrary, because continuum fracture mechanics are no longer valid in the studied dimensions. The same shape factor (0.65) was applied in both equations. This shape factor value is arbitrarily selected within a wide range of values generally used in literature [80,81]. In geometrical terms this equals an aspect ratio of $\frac{\mathrm{a}}{\mathrm{c}} = \pi/2$, where c is crack depth of a semi-elliptical crack.
Using the crack length measured from the surface the positive portion of the stress intensity factor range was calculated with the following equation:

$$\Delta K_{+} = Y \cdot \Delta\sigma_{+} \cdot \sqrt{\pi a}, \quad (20)$$

which for the exception of one loading case reported is equal to:

$$K_{max} = Y \cdot \sigma_{max} \cdot \sqrt{\pi a}, \quad (21)$$

Where 'a' is half of the total crack length and Y is the geometry correction factor. The $\Delta\sigma_{+}$ is the positive portion of the stress range applied to the crack and σ_{max} is the maximum stress applied to the crack. In this study for all loading ratios, where R is negative K_{max} is equal to ΔK_{+}. In this study all the data except for one set of data (where R = 0.26), K_{max} and ΔK_{+} are the same value, although they are of course different in the fact that one is the stress intensity range (ΔK_{+}) and the other is the maximum stress intensity (K_{max}). The goal here is not to specify which works better, but rather to study the effect of compressive stress and therefore both work for the purpose required here.

There are two main differences between the two types of notches used. The FIB notches are smaller and more crack like with a high stress concentration ($K_t > 7$) and abrupt stress gradient. The drilled holes are larger and more like the non-metallic inclusions located in the steel with a lower but wider stress gradient ($K_t \approx 2$), which affects a larger volume of the steel around the hole than the FIB notch, also relative to their size.

3.5 Microstructure and small crack growth

In publication (IV) Focused Ion Beam (FIB) milling was used to create cross-sections, after which FIB imaging is used to make ion channeling contrast pictures of the microstructure [67-70,72]. This imaging technique has been applied to small cracks in steels to study the profile in depth [68, 82]. Researchers have recently used the FIB tools to show how the size and crystal orientation of the grains affect the growth and direction of small cracks in the steel or other metalic materials [67,68,83]. In publication (IV) these tools and techniques are used to study the role that martensite sub-grain microstructure has on the initiation and growth of small fatigue cracks in high-strength steels from inclusions and notches.

The interaction of non-metallic inclusions with the microstrucure in a hard bearing steel (100Cr6) and a quenched and tempered steel (34CrNiMo6) is examined in publication (IV). The non-metallic inclusions found in the steel promote subsurface crack initiation. A new technique used in publication (IV) is Focused Ion Beam (FIB) milling to study the microstructure around an inclusion that has caused fatigue failure in the ultra-long fatigue life regieme. These FIB millied and imaged cross-sections of the inclusion and microstrucure are then compared with similar cross-sections of small cracks which have grown from FIB-milled semi-elliptical notches tested near the endurance limit of the steel. The crack path of the small cracks from the FIB notches are then be compared with the crack paths of small cracks from non-metallic inclusions that failed at or near the endurance limit.

4. Results

4.1 Fatigue testing

4.1.1 Rotating bending fatigue testing

A total of 61 rotating bending fatigue test bars were tested from the large forged steel roll (see publication (I)). There were 42 test bars that were tangential to the axis of the steel roll and 19 that were parallel to it. The reason a greater number of test bars was sampled from the tangential direction is because of the larger inclusions that were found there and the greater scatter in the fatigue test results. The results of the fatigue tests are shown in Figure 11.

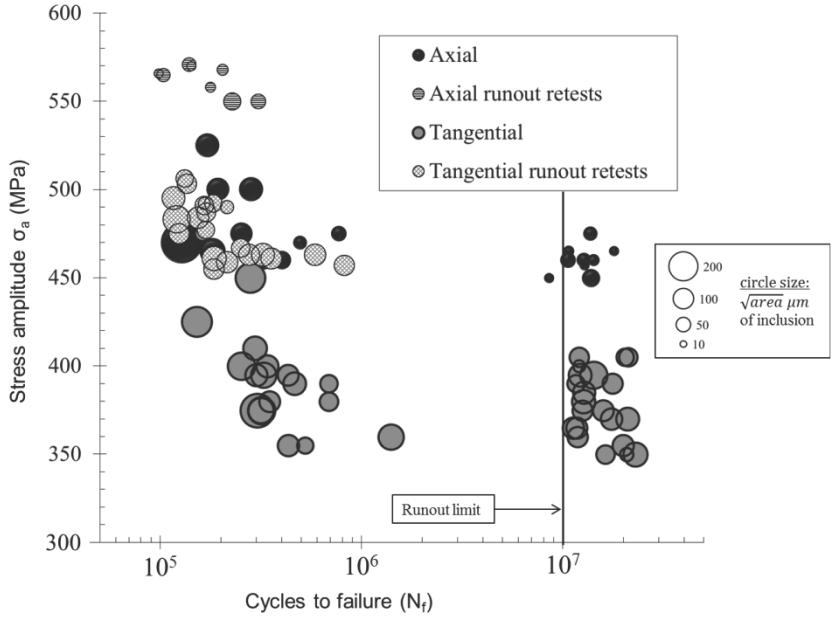

Figure 11. The results of the fatigue tests with cycles on the x-axis and the stress amplitude (MPa) on the y-axis. The circle sizes represent the size of the inclusion located at the site of fatigue crack initiation.

There was a significant difference between the two different directions from which the fatigue test bars were taken from the steel roll. The axial fatigue test bars displayed a significantly higher level of fatigue limit when compared to the tangential fatigue test bars.

4.2 Maximum likelihood analysis

The MML method of analyzing staircase fatigue test results is outlined in Ref. [38]. Using this method the fatigue limit of the tangential test bars was calculated to be 369.7 MPa, with a standard deviation of ± 35.6 MPa and the fatigue limit of the axial test bars was calculated to be 463.1 MPa, with a standard deviation of ± 11.2 MPa.

4.3 Binomial probability analysis

The binomial probability analysis method was applied to the fatigue test data. Using this method the average fatigue limit as well as the standard deviation of the strength was calculated for the tangential and axial test bars. The organization of the data along with the application of the binomial analysis method is shown in Table 3 for axial test bars and Table 4 for tangential test bars. The assumption that is made in the calculation of the amount of failed and runout test bars is that if the fatigue test at a certain stress level was a runout then the result would have been the same for all lower levels of stress. The opposite also applies when a failure occurs at a certain stress level and the test bar would have failed at all higher stress levels as well. The probabilities listed in these tables were calculated using equation (16). [39,40]

Table 3. Binomial probability analysis of axial test bars.

Stress (MPa)	*Runout*	*Failed*	*ΣFailed/ΣRunout*	*$\Sigma F/\Sigma N_{total}$*	*P(5%)*	*P(50%)*	*P(95%)*
450	1	1	1/8	1/9	3.70	16.20	39.40
457	1	0	1/7	1/8	4.10	18.00	42.90
460	3	2	3/6	3/9	15.00	35.50	60.70
465	2	1	4/3	4/7	28.90	56.00	80.70
470	0	2	6/1	6/7	52.90	79.90	95.40
475	1	2	8/1	8/9	60.60	83.80	96.30
500	0	2	10/0	10/10	76.10	93.80	99.50
525	0	1	11/0	11/11	77.90	94.30	99.50

Table 4. Binomial probability analysis of tangential test bars.

Stress (MPa)	*Runout*	*Failed*	*ΣFailed/ ΣRunout*	*ΣF/ΣN$_{tot-tal}$*	*P(5%)*	*P(50%)*	*P(95%)*
350	3	0	0/22	0/22	0.30	3.00	12.30
355	1	2	2/19	2/21	3.80	12.00	25.90
360	1	1	3/18	3/21	6.50	16.40	31.60
365	2	1	4/17	4/21	9.40	20.90	36.90
370	2	0	4/15	4/19	10.40	23.00	40.10
375	2	3	7/13	7/20	20.60	35.90	53.60
380	1	2	9/11	9/20	28.60	45.30	62.80
385	2	0	9/10	9/19	30.20	47.50	65.30
390	2	2	11/8	11/19	39.40	57.40	74.10
395	2	3	14/6	14/20	51.30	68.70	83.20
400	1	2	16/4	16/20	61.60	78.10	90.10
405	3	0	16/3	16/19	65.60	81.90	92.90
410	0	1	17/0	17/17	84.60	96.20	99.70
425	0	1	18/0	18/18	85.40	96.40	99.70
450	0	1	19/0	19/19	86.00	96.50	99.70
475	0	1	20/0	20/20	86.70	96.70	99.70

The fatigue limit of the tangential test bars calculated according to the binomial analysis is 386 MPa, with a standard deviation of ± 20 MPa, and for the axial test bars the fatigue limit is 463 MPa, with a standard deviation of ± 12 MPa.

In Figure 12 and Figure 13 the level of the estimated average fatigue limit (P(50%)) at 10^7 cycles is indicated by the intersection of the 50% failure probability red line and the 50% confidence blue line. The binomial analysis also gives the 95% and 5% confidence levels that are associated with each failure probability level.

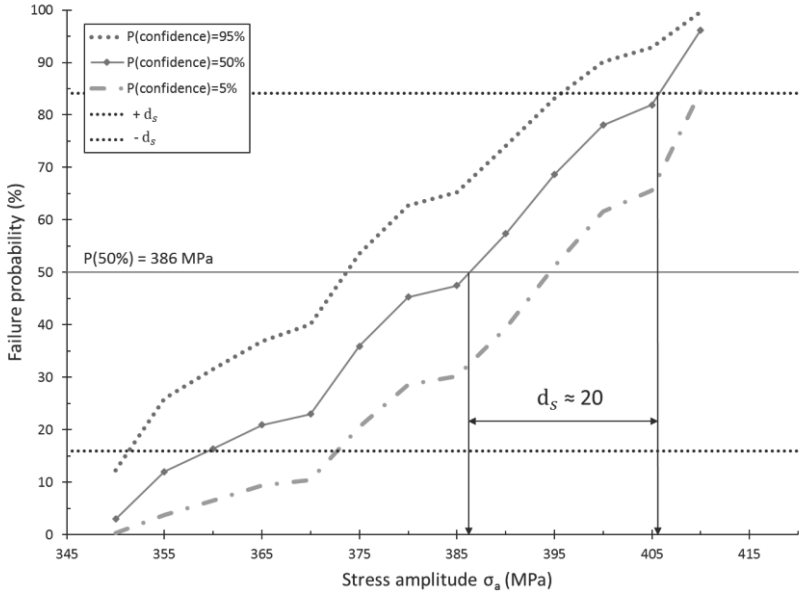

Figure 12. The results of the fatigue tests performed on the tangential test bars. The fatigue limit and standard deviation are calculated according to the binomial method. The black dotted lines indicate one standard deviation.

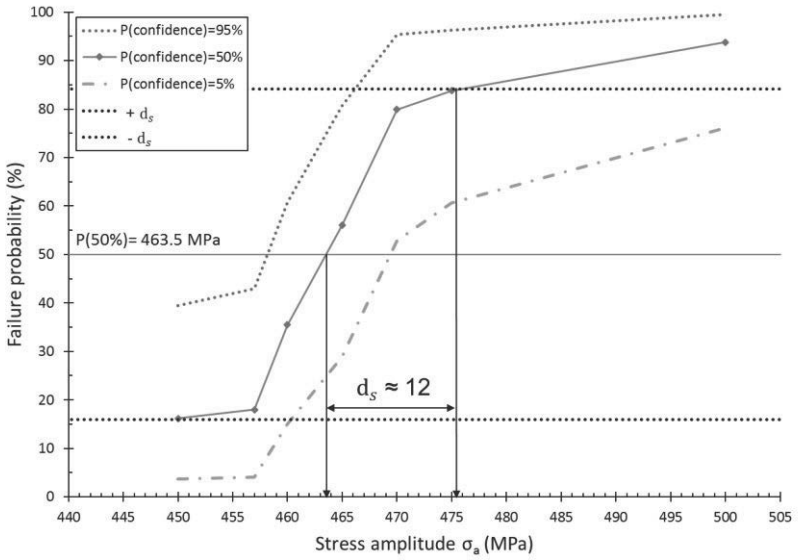

Figure 13. The results of the fatigue tests performed on the axial test bars. The fatigue limit and standard deviation are calculated according to the binomial method. The black dotted lines indicate one standard deviation.

The results of the two different analysis for the axial and tangential fatigue test bars are given in Table 5.

Table 5. The comparison of the two different methods used to calculate the fatigue limit and standard deviation from fatigue test results.

	Fatigue limit Axial (MPa)	*Deviation Axial* $\pm d_s$ *(MPa)*	*Fatigue limit Tangential (MPa)*	*Deviation Tangential* $\pm d_s$ *(MPa)*
MML Analysis	463.1	11.2	369.7	35.6
Binomial Analysis	463	12	386	20

4.3.1 Rotating bending fatigue and Murakami-Endo model

The use of equation (5) gives the lower bound fatigue limit considering that the maximum inclusion square root area is the largest in the specimen and that it is the cause of failure. The application of the Murakami-Endo model to the fatigue data is shown in Figure 14.

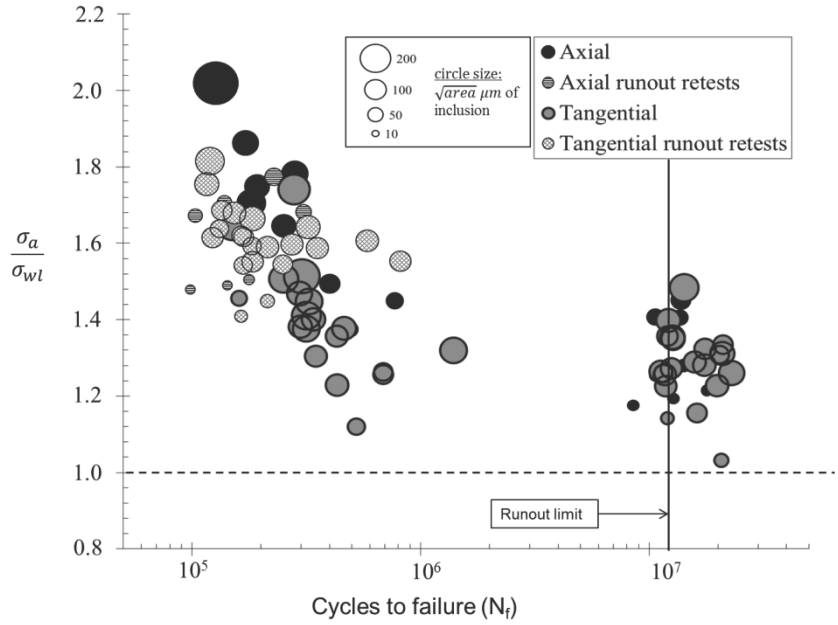

Figure 14. The application of the Murakami-Endo model to the fatigue test data.

4.3.1 Axial fatigue testing

The endurance limit at 10^7 cycles of the smooth un-notched test bars was determined at R = -1. The results of the fatigue testing are shown in Figure 15 (see publication (V)). The endurance limit was calculated to be 475 MPa ± 11 MPa by using the MML method described in Ref. [38].

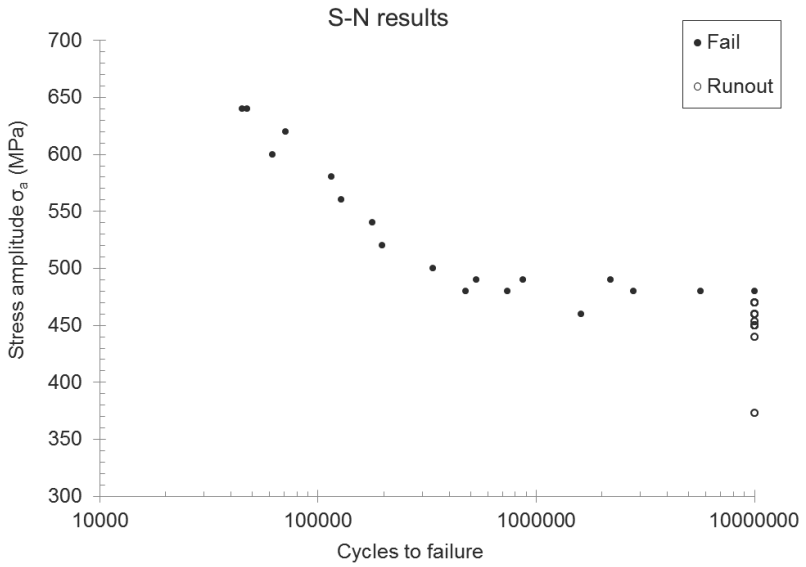

Figure 15. Fatigue stress - life curve and endurance limit determined for smooth bar specimens of the test material – quenched and tempered 34CrNiMo6(B) steel.

4.4 Inclusion analysis

4.4.1 Rotating bending fatigue and inclusion analysis

The results of the automated inspection of the polished specimens yielded a total of 11300 inclusions. A summary of the findings is presented in Table 6.

Table 6. The results of the INCA Feature inclusion analysis.

	Total number of inclusions	*Average size (μm²)*	*Average aspect ratio*
X-plane	3136	30.39	1.71
Y-plane	4812	21.5	1.63
Z-plane	3352	25.3	1.67
Total	11300	24.98	1.65

The calculation of the maximum inclusions found on the polished specimen was done by measuring the maximum length and width of the inclusion and then using the equation for the area of an ellipse, which is given as:

$$A = \pi \cdot \frac{(a \cdot b)}{4} \quad (22)$$

where a is the length and b is the width of an ellipse that best describes the shape of the largest inclusion found on the control surface of the polished specimen. The same method was used for fracture surface inclusions using an ellipse that best describes the shape of the inclusion or cluster on the fracture surface. An example of a maximum inclusion on a polished specimen is shown in Figure 16 and the measurement of the size of the inclusion on a fracture surface is shown in Figure 18. The $\sqrt{area}$ of an inclusion for both polished specimen as well as fracture surface inclusions is calculated as the square root of A in equation (22).

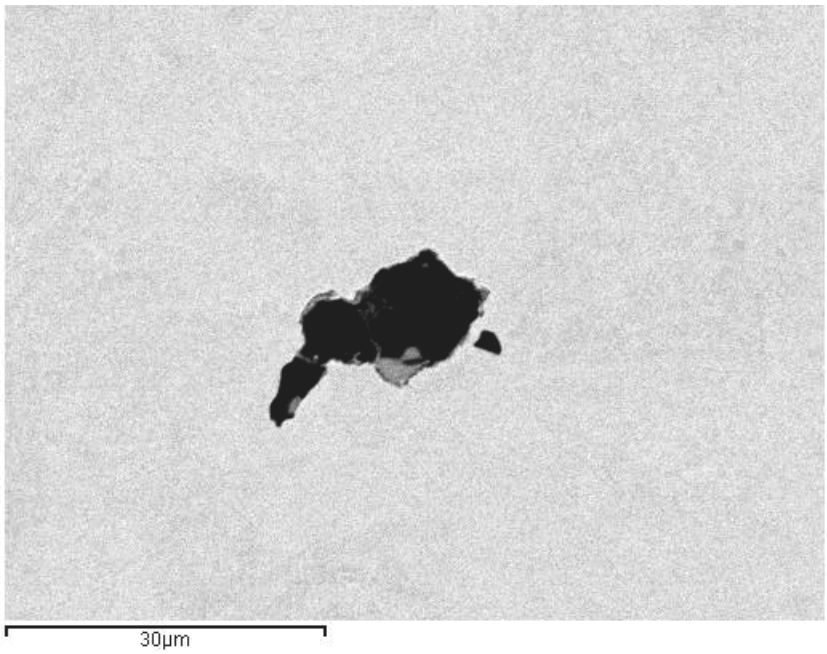

Figure 16. An example of a maximum inclusion found on a polished specimen.

The site of fatigue crack initiation on all except for three of the 61 fatigue test bars was an inclusion that was on or near the surface of the test bar. These three test bars that did not show evidence of inclusions at crack initiation sites were all from the axial test bar group and two of the three were runouts, with the third bar failing at 8 million cycles. The type of inclusions found at the site of crack initiation were mostly different types of aluminium oxides with the exception of 8 test bars, all of which were from the tangential group. In these test bars the fatigue cracks initiated from large inclusions composed of manganese sulfide. In Figure 17 is shown one of the MnS inclusions.

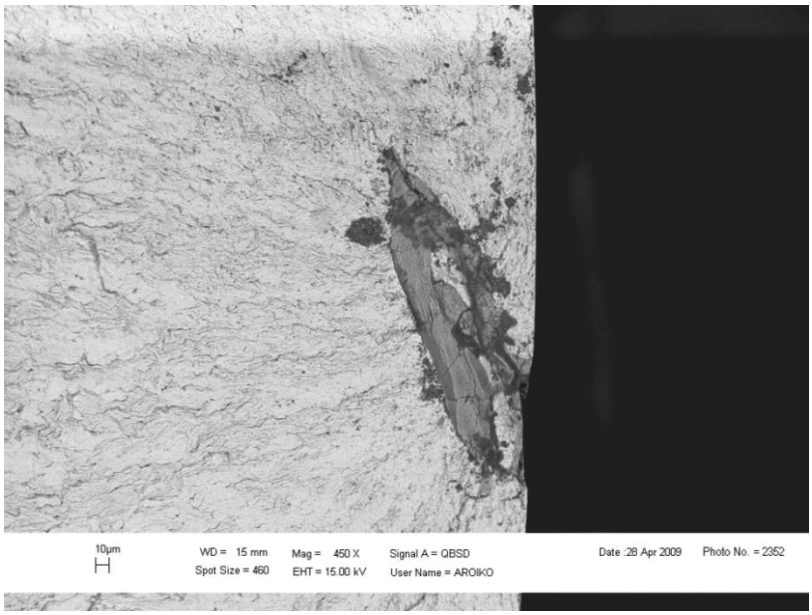

Figure 17. A manganese sulfide inclusion at the site of crack initiation on a test bar as an electron backscatter image.

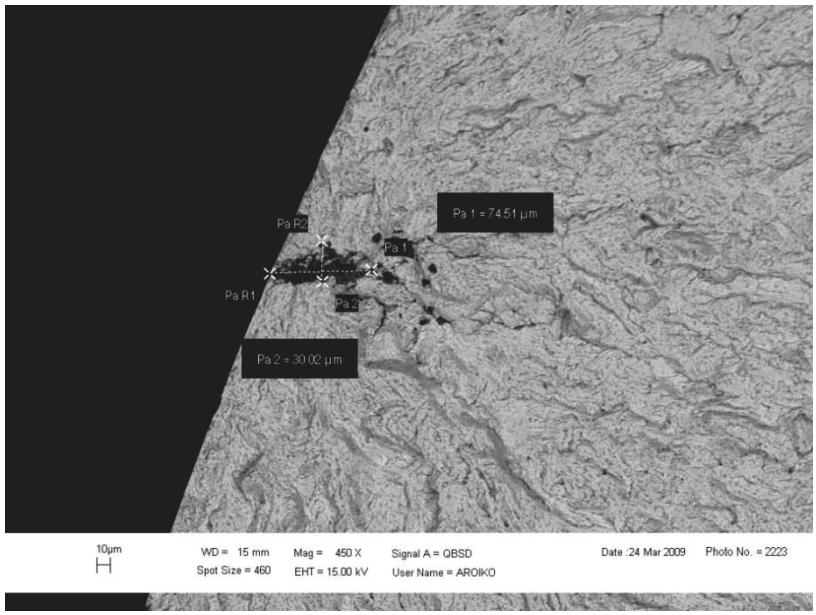

Figure 18. An example of the measurement that was done to determine the size of the projected area for the inclusions that are found on the site of fatigue crack initiation.

Using the MML method to estimate the parameters of the Gumbel distribution from the inclusion data obtained from the fracture surface and polished specimen it is possible to calculate the estimated largest extreme value distribution (LEVD), as well as the upper and lower confidence levels. These extreme value probability plots for the fracture surface inclusions as well as polished specimen inclusions are shown in Figure 19 and 20.

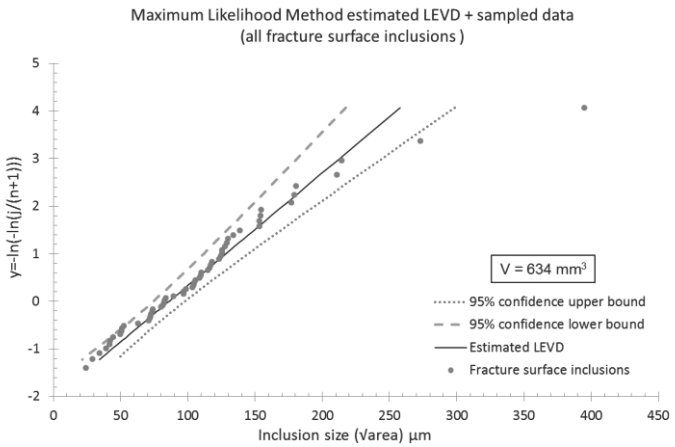

Figure 19. The extreme value probability graph of the largest inclusions from the fracture surface inclusions.

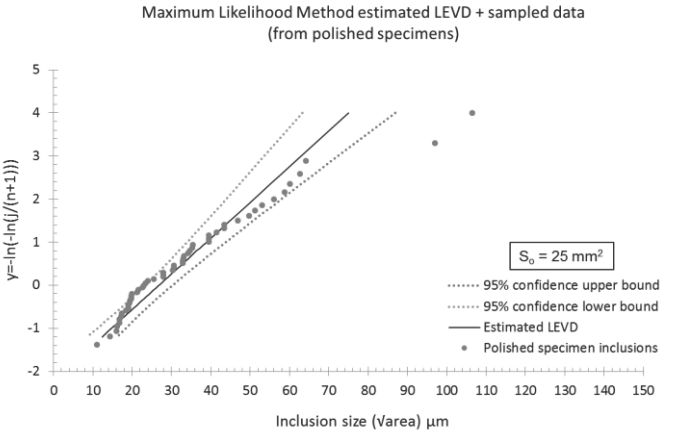

Figure 20. The extreme value probability graph of the largest inclusions from all the polished specimen maximum inclusions.

The comparison of the inclusion distribution within the various planes of the steel roll was done as well. The parameters and the average maximum inclusion size along with the standard deviation of these distributions are shown in Table 7. The differences in the extreme value distributions of the inclusions from the fracture surfaces compared to the polished specimens indicate that a larger inspection area is required.

Table 7. The average size of the inclusions in different positions of the test bars and polished specimens as well as their extreme value distribution parameters for the Gumbel distribution.

	Average ***Inclusion size (√area) µm*** $\bar{\lambda} = \lambda + \delta \cdot \gamma$	*Standard Deviation* ***Inclusion size (√area) µm*** $D_G = (\delta \cdot \pi)/\sqrt{6}$	*Lambda (λ) Location Parameter* ***Gumbel***	*Delta (δ) Scale Parameter* ***Gumbel***	*Number of Inclusions Studied*
All FS	110.42	54.25	86.0	42.3	58
All PS	33.78	15.52	26.8	12.1	54
Axial (Y)-FS	90.69	57.97	64.6	45.2	16
Axial (Y)-FS[1]	75.25	39.89	57.3	31.1	15
Tangential (X)-FS	115.42	49.38	93.2	38.5	42
Axial (Y)-PS	26.17	9.49	21.9	7.4	18
Tangential (X)-PS	45.43	22.96	35.1	17.9	18
Z-Plane (Z)-PS	29.45	11.67	24.2	9.1	18
Axial (Y)-FS (Ro)	43.72	16.03	36.5	12.5	6
Axial (Y)-FS (F)	121.62	68.49	90.8	53.4	10
Tangential (X)-FS (Ro)	101.32	38.48	84.0	30.0	16
Tangential (X)-FS (F)	137.15	58.10	111.0	45.3	19

[1] The calculation of parameters excluding the largest inclusion found on an axial test bar fracture surface that was exogenous in nature. FS = Fracture Surface, PS = Polished Specimen, Ro = Runout, F = Fail.

4.5 Small crack growth optical observation

4.5.1 Different types of notches compared to non-metallic inclusions

Data on crack initiation threshold was accumulated also through fractography of many specimens tested near the fatigue limit of the steel. A large set of test data for a different batch of the same steel type was available from a previous project

[84]. Results of five specimens in that set are used here for comparison. They exhibited crack initiation at an inclusion just breaking the specimen surface after more than 10 million fatigue cycles. This data is plotted in Figure 21, where a comparison can be made between different defects initiating a fatigue crack near the fatigue threshold.

The data used to calculate the stress intensity factor for the inclusion data points is the inclusion size and the stress level at which the test bar failed. The FIB data points are at the stress level at which the crack initiated and then arrested. Two of the drilled hole points represent crack initiation at the hole. Pre-cracking with compressive mean stress was introduced to one of them.

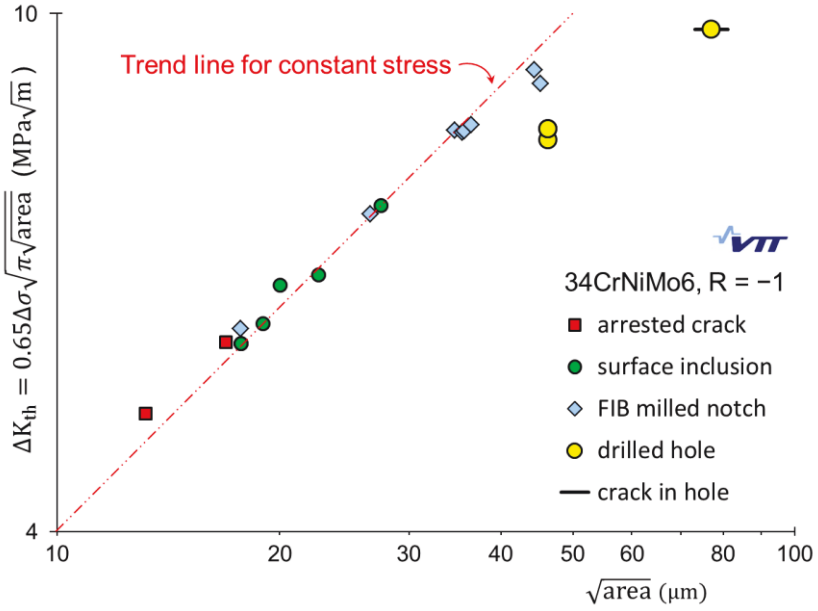

Figure 21. The stress intensity range vs. the square root area of the initiator at the growth threshold condition (≈ fatigue limit) for different types of notches.

The same data shown in Figure 21 is also plotted with respect to the stress amplitude of the fatigue test compared to the initiating defect size. This is shown in Figure 22, along with a trend line for constant stress amplitude.

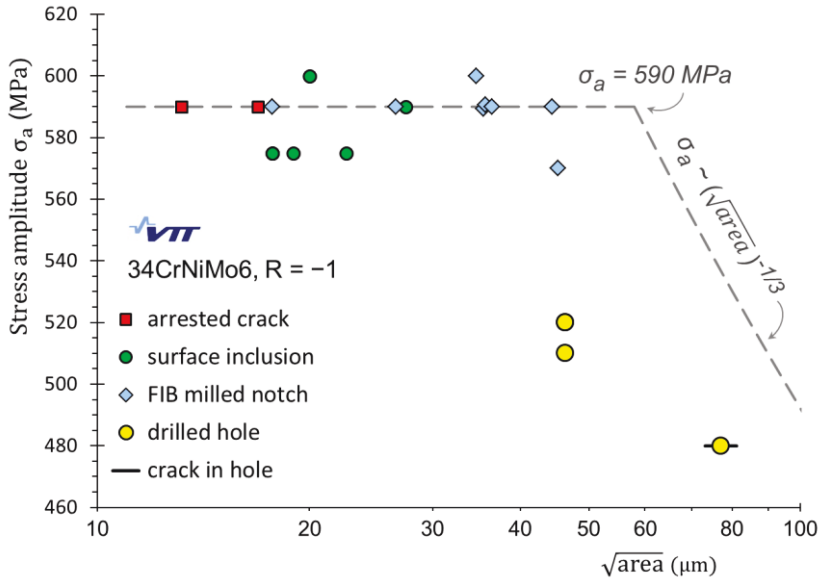

Figure 22. The same data as in Figure 21: fatigue limit as function of initiator size.

4.5.2 FIB notches for small crack growth

A test bar with 20 small FIB notches gave a large and interesting set of results, because crack growth was observed in almost all notches irrespective of their different sizes. The observed crack growth in 34CrNiMo6 QT(A) steel studied in publication (III) is shown in Figure 23.

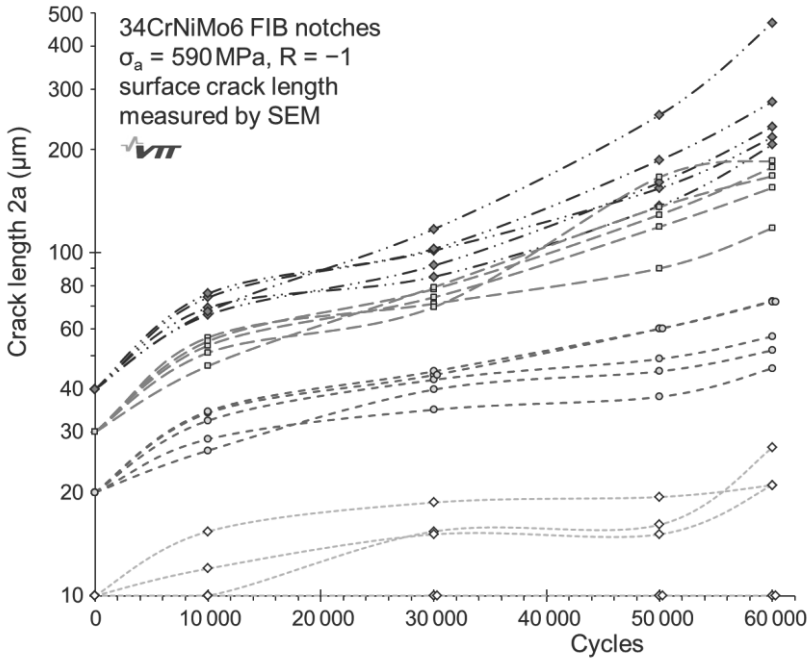

Figure 23. Growth of small cracks from 10, 20, 30 and 40 µm sized FIB-milled notches (5 of each) in a test bar of 34CrNiMo6 QT(A) steel.

The data in Figure 23 can be used to calculate the crack growth rate versus the stress intensity factor range. This was done by averaging the crack growth rate as well as the stress intensity factor range over each observation interval. These results are illustrated in Figure 24 where they are separated into original notch sizes. To illustrate the variation of growth rate along the cycle count, another grouping of the same data is also shown.

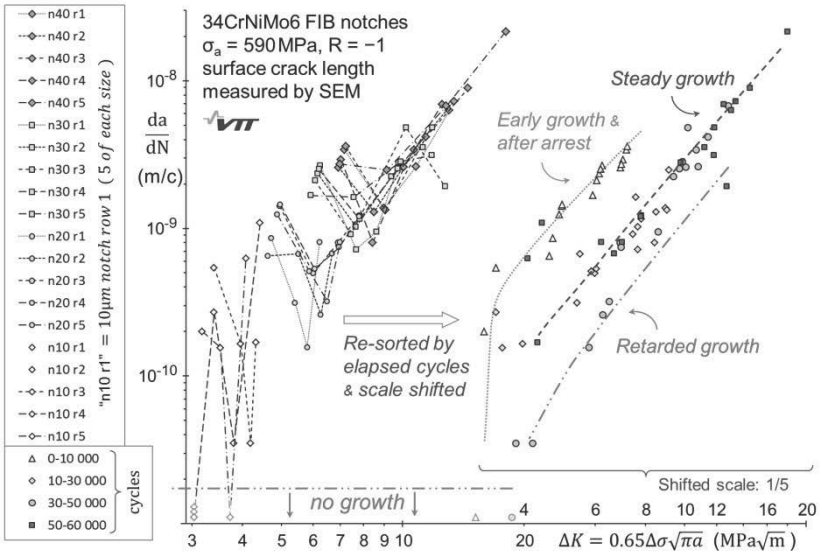

Figure 24. Crack growth rate curves based on data in Figure 23. On right the same data is sorted according to phase of test.

Crack growth from FIB notches was first studied with constant loading near the fatigue limit. This means that once the crack has initiated the test can be characterized as a rising ΔK test. Results from one such test from publication (VI) are shown in Figure 25.

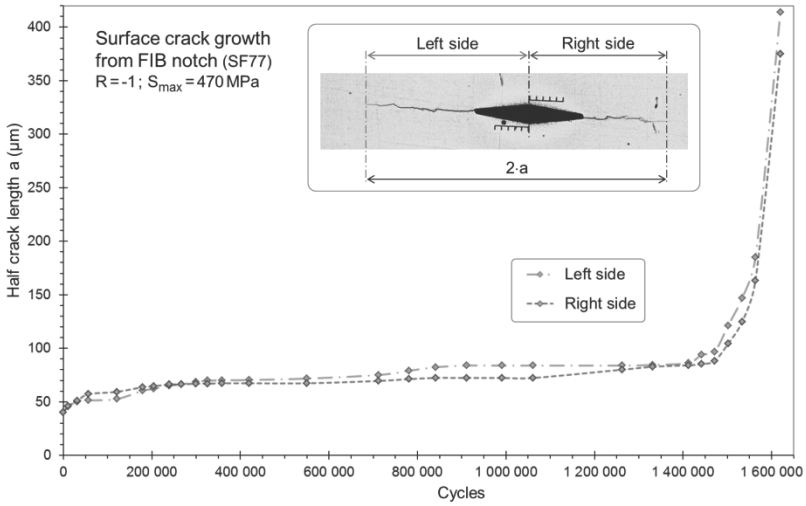

Figure 25. The results of in-situ optical measurements of crack growth from a FIB notch under constant amplitude loading. The x-axis is the number of fatigue cycles and the y-axis is the crack length on the left (red) and right (blue) side of the notch. These tests and the following test were done on 34CrNiMo6 QT(B) steel. S_{max} is the maximum value of the stress amplitude at which the fatigue test bar was loaded.

From Figure 25 it can be observed that the cracks initiate almost immediately and grow fast in the beginning of the test. Once the crack grows out of the area directly ahead of the notch where there is a stress gradient, the driving force decreases and the crack growth rate slows down. From around 50 000 cycles to around 1.4 million cycles there is a phase of slow, but constant and symmetric growth of the crack. This phase of slow growth leads the small crack out of the growth threshold region into the normal crack growth rate region for large cracks.

Using the data from Figure 25 and Equations (20) and (21) we can calculate the da/dN vs ΔK_+ or K_{max} correlation which is shown in Figure 26.

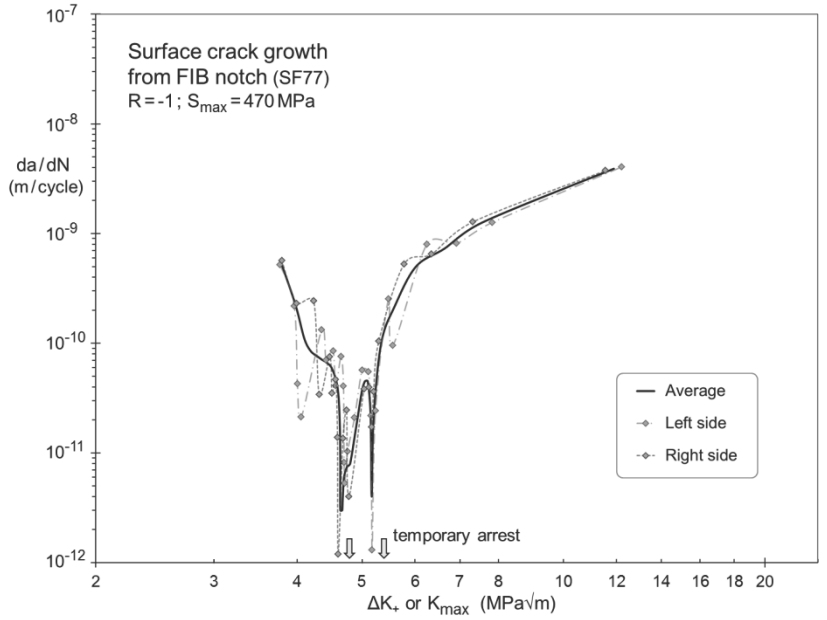

Figure 26. The crack growth data from Figure 25 is used to calculate the da/dN vs. ΔK_+ or K_{max} graph showing the crack growth rate from the FIB notch. S_{max} is the maximum value of the stress amplitude at which the fatigue test bar was loaded.

Figure 26 illustrates that in the slow growth region the crack is growing slower than the rate for determining the growth threshold (da/dN < 10^{-10} m/cycle) and the data shows a decreasing crack growth rate. This is because of the large increase in the fatigue cycles compared to the actual crack growth. What is also important to observe is that the crack is actually growing for most of the time, at least on the surface. This data shows that the small crack growth rate behaviour is a slow process that gradually approaches the threshold of crack growth for large cracks.

4.5.3 Small crack growth and loading

The averaged curve in Figure 26 is repeated together with the other test results obtained using FIB notches at different R-ratios. This compilation is shown in Figure 27.

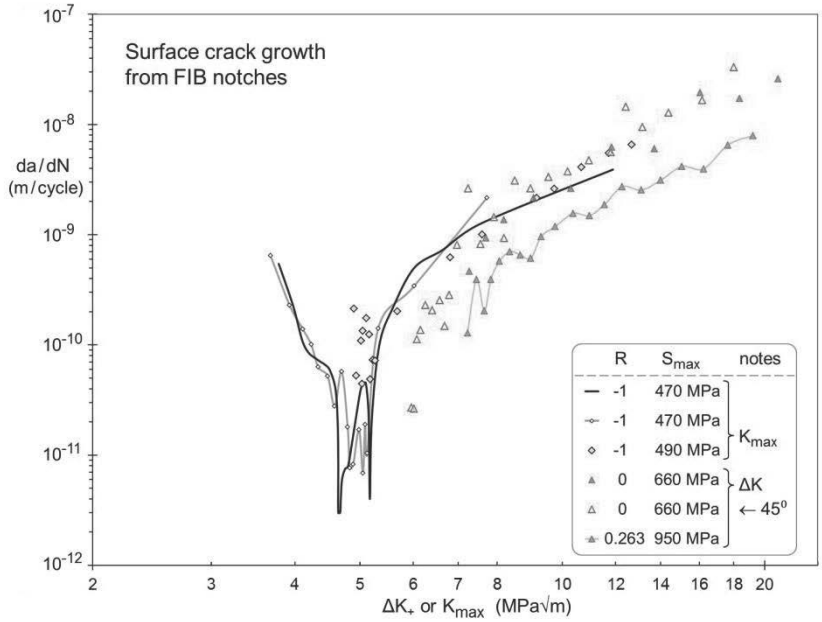

Figure 27. The initiation and growth of small cracks from FIB notches at different R-ratios. All results shown here are from test bars made with 34CrNiMo6 QT(B) steel. S_{max} is the maximum value of the stress amplitude at which the fatigue test bar was loaded. One data set marked 45° is a FIB notch that was milled at 45 degrees to the loading direction.

Once the positive portion of the stress intensity factor range (ΔK_+) is greater than 5 MPa$\sqrt{m}$, the crack grows out of the threshold zone into the conventional crack growth rate stage II of the Paris law curve.

4.5.4 Small drilled holes for small crack growth

The other type of small notch used was drilled holes. The crack growth rate from drilled holes during constant amplitude loading is shown in Figure 28.

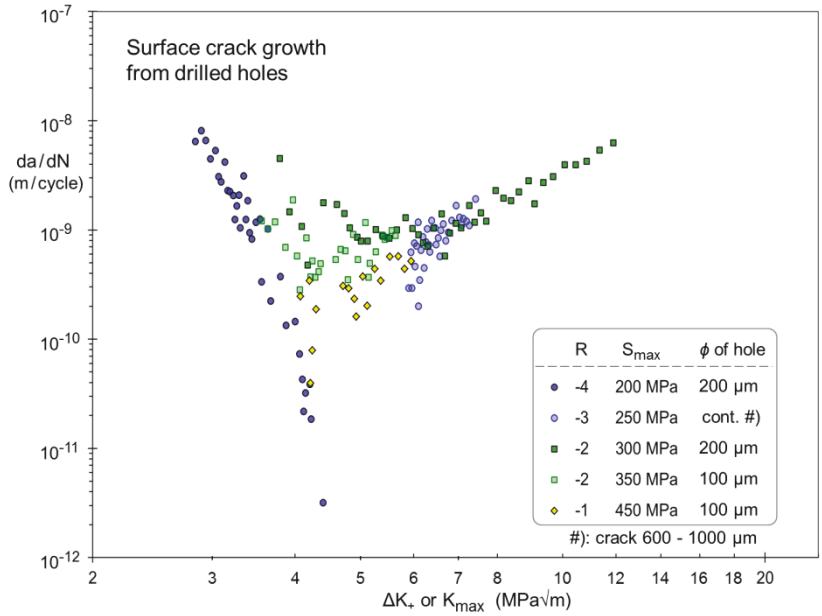

Figure 28. Growth rates of small cracks initiated from drilled holes at different R-ratios. All results shown here are from test bars made with 34CrNiMo6 QT(B) steel. S_{max} is the maximum value of the stress amplitude at which the fatigue test bar was loaded.

The constant amplitude crack growth rate data from the drilled holes and FIB notches are combined in Figure 29.

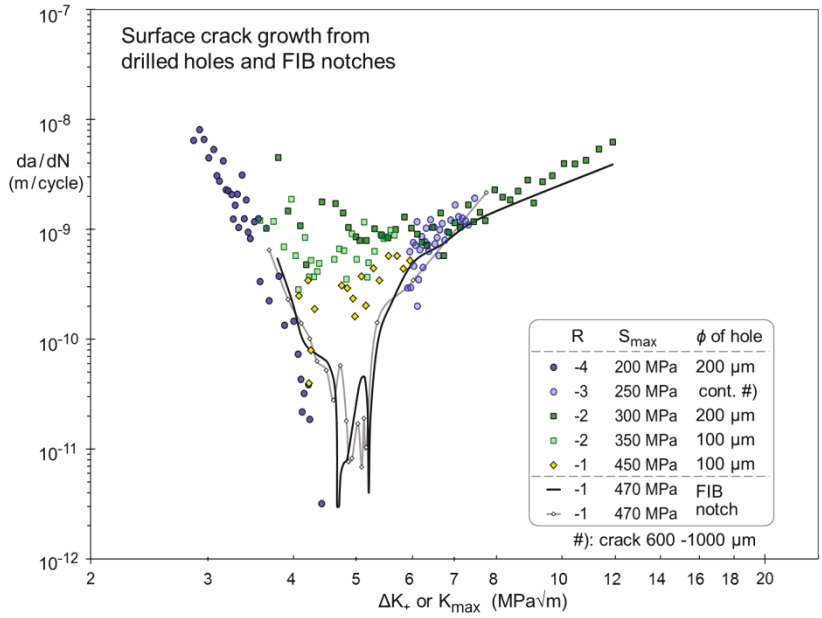

Figure 29. Growth rates of small cracks from drilled holes and FIB notches at different R-ratios. All results shown here are from test bars made with 34CrNiMo6 QT(B) steel. S_{max} is the maximum value of the stress amplitude at which the fatigue test bar was loaded.

The main difference with the crack growth rate from the drilled holes is that the crack growth rate is generally more stable and there is not as much crack growth rate deceleration as with the crack growth rate from FIB notches. This is due to the fact that the drilled holes have a stress gradient that decays gradually, whereas the FIB notches have stress gradients that are more crack like, so they are more severe, but affect a shorter distance.

When we combine the two data sets it can be seen that the drilled holes show a consistently higher crack growth rate and do not exhibit the same form of crack arrest with one exception of the crack that arrested under a R = -4 loading ratio. Total length of this crack was over 500 µm, when the growth rate became less than 10^{-10} m/cycle and over 600 µm at arrest. In other words, it was growing out of the stress gradient of the 200 µm hole during the decreasing rate phase. This means that the crack growth was greatly assisted by the compression portion of the loading as long as the crack tip was within the stress gradient of the hole. As the crack grew out of the stress gradient it gradually arrested.

The data in Figure 29 shows that using the positive portion of ΔK collapses the crack growth rate curves into the same curve for higher ΔK_+ regions. There is more scatter in the lower ΔK_+ regime due to the different nature of the notches, if they are drilled holes or FIB notches, and there is a larger influence of the microstructure that should be taken into consideration as well. However, once the cracks have grown out of the stress gradient they follow the same curve for the positive portion of the ΔK loading of the test material.

4.5.5 Effect of compressive loading on the threshold for crack growth

The other type of testing where the loading was controlled according to the growth of the crack from the drilled holes sheds light on the interaction between the compressive loading and small crack growth rate behaviour for different loading ratios. In this case the crack arrest was measured at a constant R-ratio of R = -1 and R = -2 and the results are shown in Figure 30.

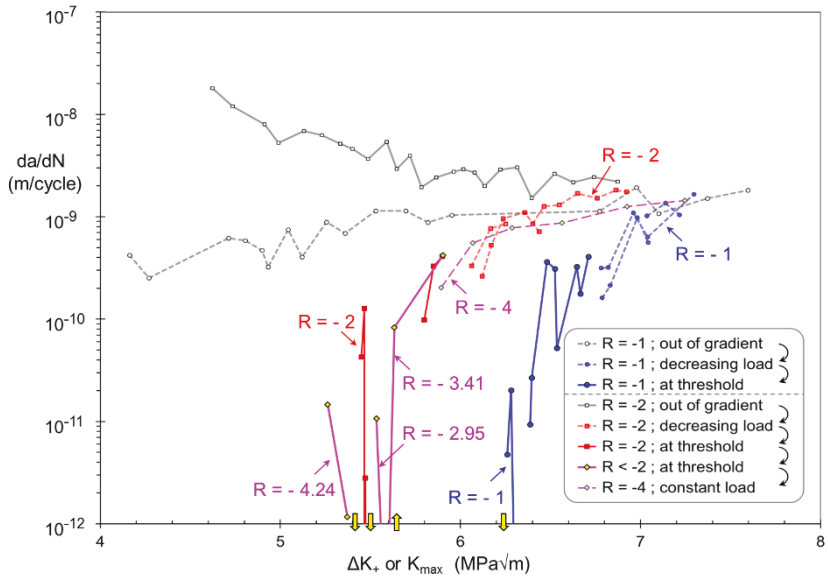

Figure 30. The initiation and growth as well as arrest threshold with decreasing ΔK (MPa√m). The grey lines are the original crack growth rate from the holes out of the stress gradient. After this the coloured data shows the arrest of the small cracks growing from small drilled holes as the stress amplitude is gradually decreased until the cracks have arrested. The blue data points and the blue lines are for the R = -1 loading and the red data points and the red lines for the R = -2 loading. The purple lines have the loading ratio assigned with an arrow showing the increased compressive portion of the loading. All results shown here are from test bars made with 34CrNiMo6 QT(B) steel.

It is clear from Figure 30 that under R = -2 loading the crack is growing at a faster rate than the crack under R = -1 loading, for comparable ΔK_+ or K_{max} values. When the two arrest thresholds are compared we see that the R = -2 threshold is about 12 % lower than the R = -1 threshold on the ΔK_+ or K_{max} scale.

The previous studies [53-55] about the effects of compressive loading on fatigue crack growth can be seen to apply also for small cracks in the steel that was studied here. It was measured that increasing the compressive loading for a crack can reinitiate its growth. This is due to the fact that increasing the compressive portion of the loading in constant amplitude testing decreases the ΔK_+ or K_{max} threshold for crack growth. The experimental work reported here is unique due to the new tools and methods that were employed to monitor and measure small fatigue crack growth under these unique conditions. For this reason there are almost no comparable data that could be used for comparison of the results reported in this study.

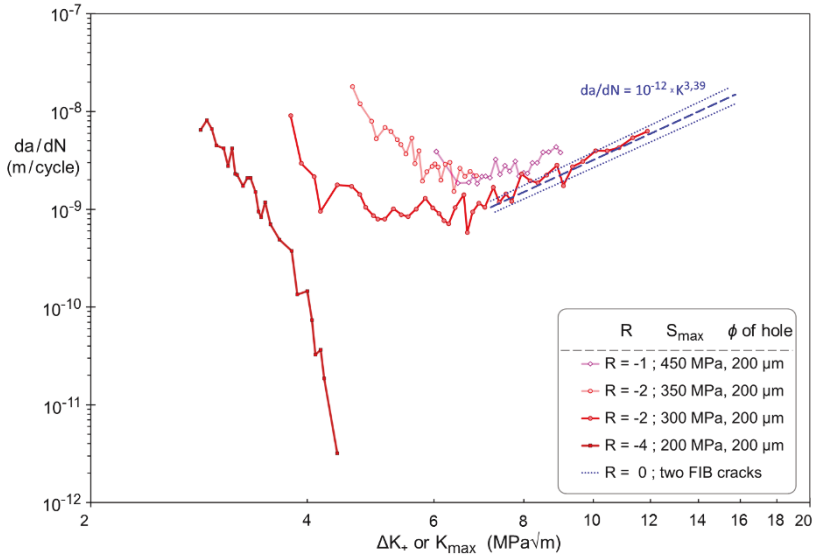

Figure 31. The comparison of the crack growth rates with the growth rate of small cracks loaded at R = 0. The average crack growth rate of small cracks loaded at R = 0 is shown with the dotted blue lines. All results shown here are from test bars made with 34CrNiMo6 QT(B) steel. S_{max} is the maximum value of the stress amplitude.

Figure 31 shows the difference between small crack growth rate at different R-ratios. The data shows that the average crack growth rate at R = 0 is in line with the crack growth rate at negative R-ratios and that there is a good correlation when using the positive portion of the stress intensity range once the crack has grown out

of the stress gradient of the hole. The interaction of the stress gradient from the hole and the crack growth rate is shown in Figure 32.

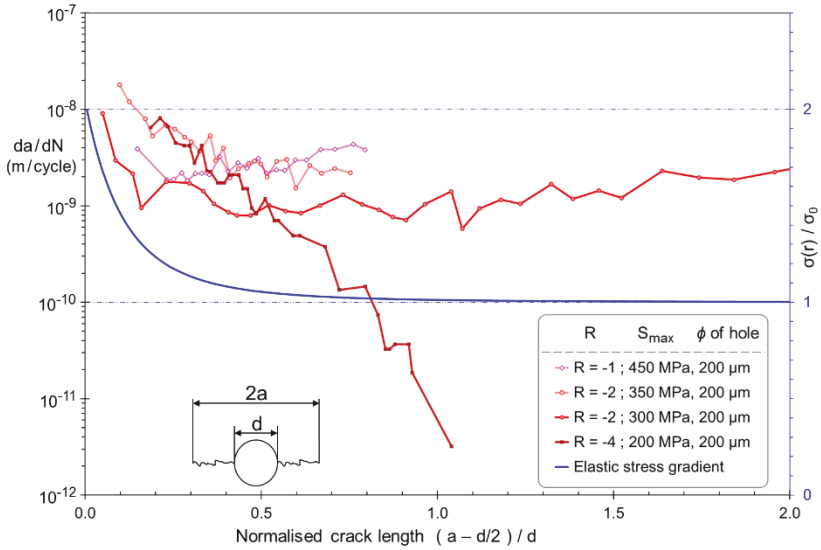

Figure 32. The change in the rate of crack growth from the hole with the crack length normalized to the diameter of the drilled hole. The legend gives the loading ratio R, after which is S_{max} which is the maximum value of the stress amplitude, and then the diameter of the drilled hole. The stress gradient for the drilled hole is given with the blue line which corresponds to the blue axis on the right side of the figure. All results shown here are from test bars made with 34CrNiMo6 QT(B) steel.

To obtain a better understanding of the behaviour of small crack growth rate under different negative R-ratios, the average crack growth rates were calculated for different portions of the crack growth test. This was done for crack growth measured at R = -2 to R = -3.73. This crack growth data is shown in Figure 33.

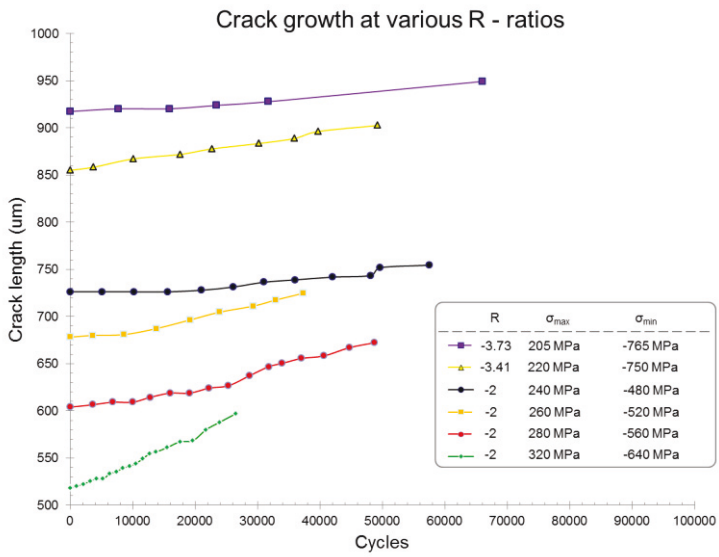

Figure 33. The crack growth measured during testing at different R-ratios. The maximum and minimum stress of the stress amplitude is given for the crack growth measured during 25000 to 70000 cycles of fatigue loading. All results shown here are from test bars made with 34CrNiMo6 QT(B) steel.

In Figure 33 the crack growth is shown for R-ratios -2 to -3.73. This data shows that generally the crack growth rate is linear for conditions where there is a large negative loading ratio. This data can be used to average the crack growth rate over a longer cycle count. Doing this a better overall picture is obtained of how the crack growth rate is behaving and eliminates some of the scatter caused by e.g. microstructural heterogeneity. The average crack growth rate data is shown in Figure 34.

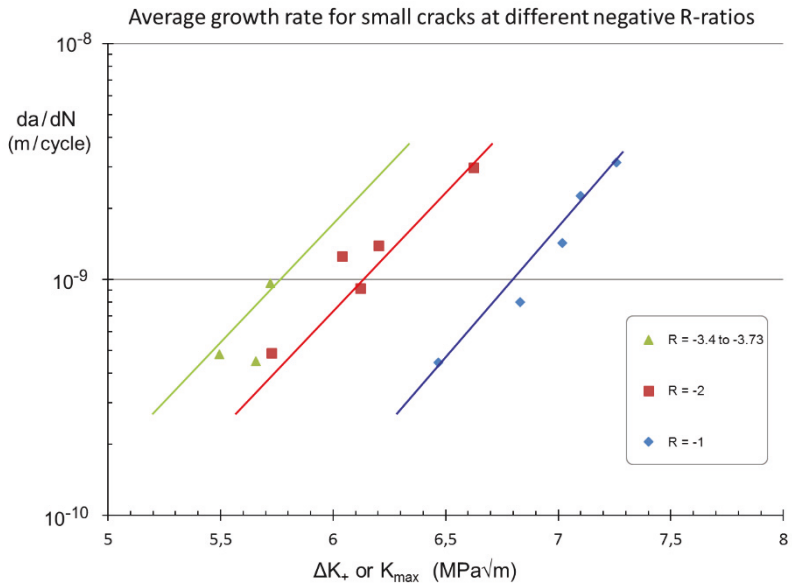

Figure 34. The effect of different loading ratios on crack growth rate with respect to ΔK_+ or K_{max}. All results shown here are from test bars made with 34CrNiMo6 QT(B) steel.

Figure 34 shows that as the compressive loading portion of the fatigue cycle increases, the ΔK_+ or K_{max} at which a selected crack growth rate occurs decreases. When comparing the K_{max} for R = -1 and R = -2, the decrease of similar effective ΔK_+ or K_{max} is around 12%, and there is around 7% decrease from R = -2 to R = -3.4 and -3.73. So it appears that there is a gradual saturation for the effect of the amount of compressive loading on the correlation between the crack growth rate and ΔK_+ or K_{max}.

4.6 Fractography and FIB cross-sections

4.6.1 Crack paths in quenched and tempered 34CrNiMo6 QT steel – notches on the surface

Using FIB notches as initiation points for small cracks, it is possible to mill the small cracks with the FIB as well as take ion images that reveal the local direction and flow of the microstructure. The crack shown in Figure 35 has been milled and imaged with a FIB and shows a small fatigue crack growing from a FIB notch along with the grain structure of the steel underneath the surface of the test specimen. In Figure 35 both (b) and (c) show how the location of the change in crack direction

corresponds to a change in the general martensite lath or packet direction. The paths of the small cracks that grew from the FIB notches show a clear preference in growth direction along the martensite packets or laths in the prior austenite grains. Once the crack grew through one prior austenite grain it changed direction and grew along the orientation of the martensite laths in the next prior austenite grain or martensite packet.

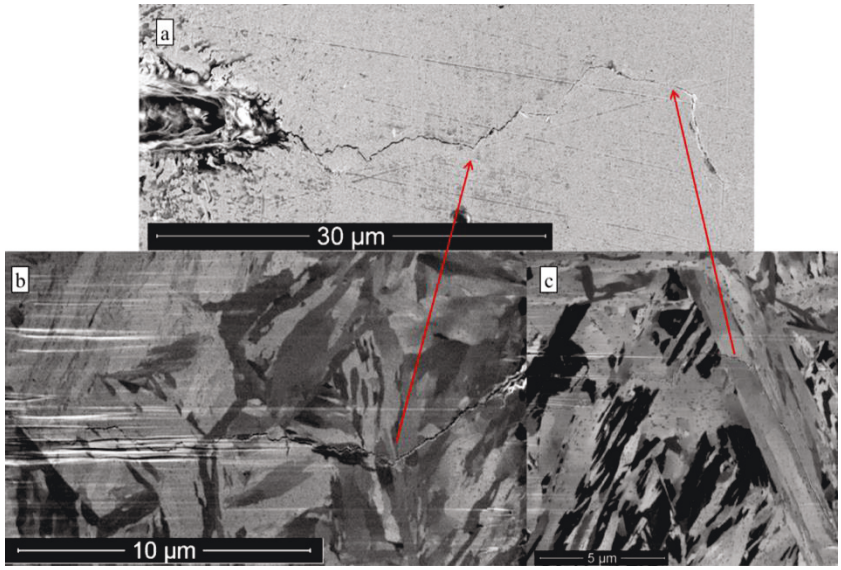

Figure 35. A small crack growing from a FIB notch (a) with two turning points correlated with the sub-grain microstructure (b, c). The stress ratio was R = -1 and the stress amplitude was 590 MPa. The test bar has been tested for 60000 cycles and was made of 34CrNiMo6 QT(A) steel. The remote stress is acting from top to bottom of the image.

The crack is propagating in a three-dimensional microstructure and the milling and imaging only shows a two dimensional structure, so it does not always follow exactly the specific martensite features. There is a noticeable change in direction at clear points where the martensite microstructure also changes. This is shown in Figure 35(c) where the crack turns abruptly away from the path that it was traveling and follows a large martensite packet or lath that is orientated in the same direction. This demonstrates that the local orientation of the microstructure has a definite influence on the growth direction of the small fatigue crack tested near the fatigue endurance limit.

Figure 35 and other similar images from publication (IV) show how the growth of small cracks from notches is greatly affected by the local sub-grain microstructure,

namely the orientation and size of the martensite microstructure along the path of the crack.

4.6.2 Crack paths in 34CrNiMo6 QT steel – subsurface inclusions and ODA

To study the microstructure and its eventual effects on crack growth from a non-metallic inclusion a long-life specimen was studied by cross-sectioning the initiation site. First we introduce some reference observations, and in particular, the fractographic feature “Optically Dark Area” (ODA) as defined by Murakami [6]. A comparison of observations on the same fracture surface by using different imaging techniques can be found in Ref. [20]. The images show an area of the fracture surface directly next to the inclusion that has an observably different topography than the rest of the surrounding fracture surface.

A smooth 34CrNiMo6 QT steel test bar was tested for $100 \cdot 10^6$ cycles at a stress amplitude of 550 MPa with an R-ratio of -1. The stress amplitude was then raised to 575 MPa and after $1.7 \cdot 10^6$ cycles at this stress amplitude the specimen failed. SEM images of the inclusion that caused the failure are shown in Figure 36 - 40. The area corresponding to the definition of “ODA” is marked besides the inclusion.

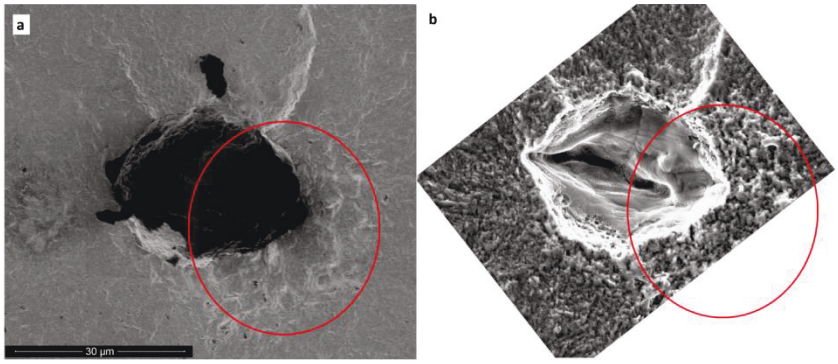

Figure 36. The non-metallic inclusion that caused failure in a smooth test bar. Picture (a) is an ion image taken with a FIB, and picture (b) is taken of the opposite fracture surface with a SEM microscope. Picture (b) has been flipped for easier comparison to picture (a). Both pictures have the same ODA area circled. The stress ratio was R = -1 and the stress amplitude was 550 MPa. The test bar has been tested for $100 \cdot 10^6$ cycles after which the stress level was raised to 575 MPa and the specimen failed after $1.7 \cdot 10^6$ cycles. This specimen was made of 34CrNiMo6 QT(A) steel.

The two images in Figure 36 show the opposing sides of the fracture surface obtained by different types of microscopy. Figure 36(a) shows the fracture surface with

the inclusion in an ion image, and the conventional SEM image in Figure 36(b) shows the respective site on the opposite surface. Figure 36(b) has been flipped and rotated so that it is easier to compare with the fracture surface in Figure 36(a). The length scale is the same for both images.

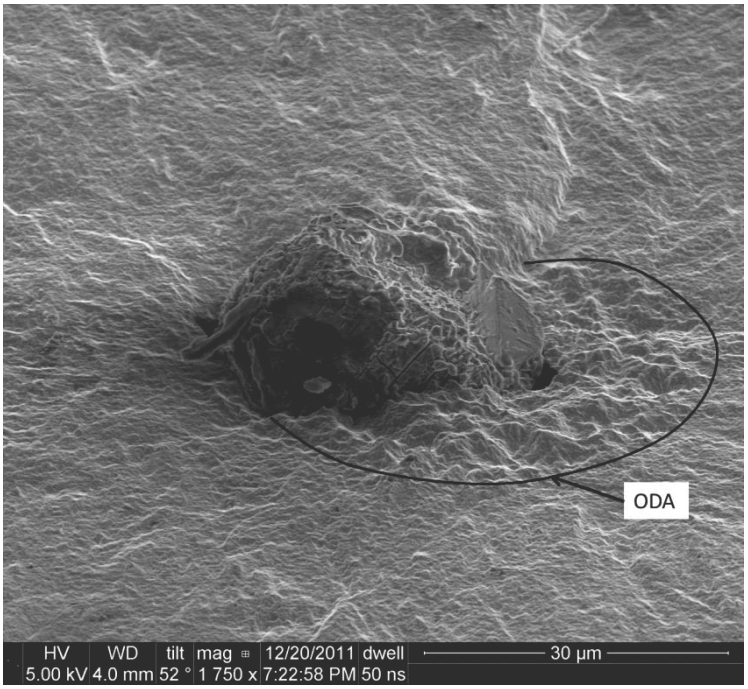

Figure 37. The non-metallic inclusion that caused failure in a smooth test bar. The part of the fracture surface circled by a black line is the ODA. This SEM picture was taken at an angle for a better topographic feature contrast. This specimen was made of 34CrNiMo6 QT(A) steel.

The inclusion and crack paths besides it were cut by FIB to see the microstructure below the fracture surface. The resulting cross-section is shown in Figure 38 and the images of the metal matrix on different sides of the inclusion are compared in Figure 39.

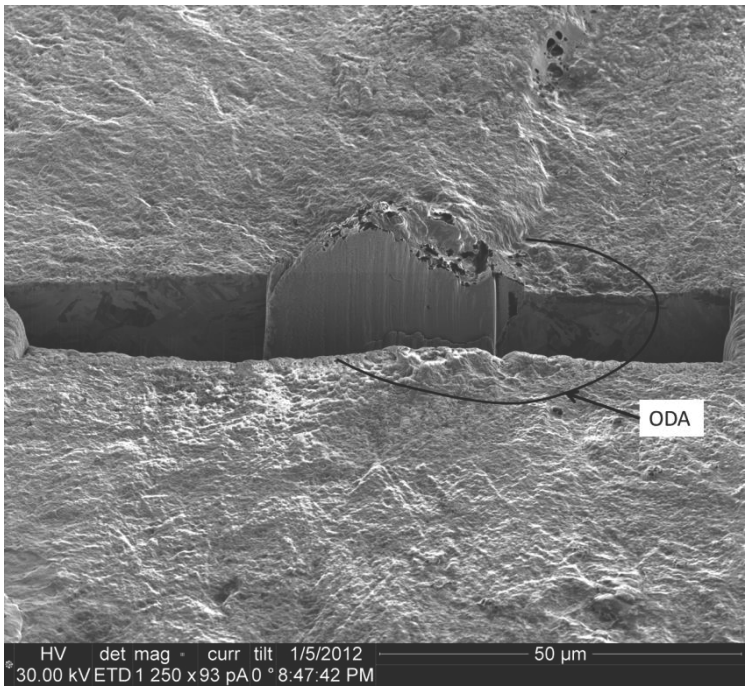

Figure 38. The cross-section FIB image of the ODA side and no ODA side of the non-metallic inclusion. This specimen was made of 34CrNiMo6 QT(A) steel.

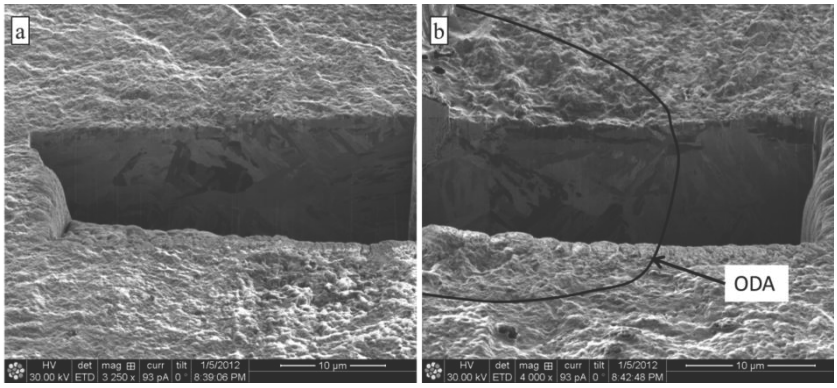

Figure 39. A comparison of the two cross-sections around the inclusion where (a) is from the side where there is no ODA and (b) is from the side where there is an ODA. This specimen was made of 34CrNiMo6 QT(A) steel.

In Figure 39(b) we can observe local martensite structure near and adjacent to the surface located inside the ODA area. This local microstructure is orientated in the same direction as the crack growth. By comparison in Figure 39(a), which is outside

of the ODA area on the other side of the non-metallic inclusion, it can be seen that the microstructural features are smaller and not orientated as preferentially to the direction of crack growth as the microstructure in Figure 39(b). This supports the connection between small crack growth and the size, shape and orientation of the microstructure and provides more information about the ODA area. It indicates that the formation of the ODA is connected to the initiation and growth of the small crack into the most preferential local microstructure surrounding the non-metallic inclusion.

4.6.3 Crack paths in 100Cr6 bearing steel – subsurface inclusions and ODA

A unique set of eleven 100Cr6 bearing steel test bars was tested at a common stress amplitude of 735 MPa at stress ratio R = -1 [19]. All specimens failed after high numbers of cycles ($N_f > 10^7$) from subsurface spherical oxides as shown in Figure 40.

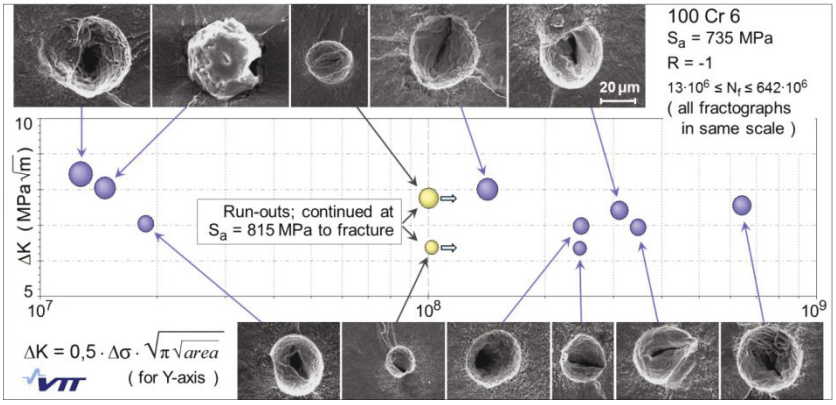

Figure 40. Fatigue initiators in 100Cr6 bearing steel. Sizes of balls indicate √area of inclusion. [19]

In Figure 40 can be seen a slight downward trend in the size of the crack initiating inclusion that correlates with an increase in fatigue life, but this correlation is not perfect. Some degree of scatter is inevitably expected in the UHCF regime, but we wished to take a closer look on crack initiation and growth paths over $10 \cdot 10^6$ cycles. In the following we focus on the test bar that gave the longest fatigue life of $642 \cdot 10^6$ cycles. Figure 41 shows the fracture surface around the inclusion, which was not the smallest in this set of specimens. Furthermore, the inclusion was located relatively close to the specimen surface, which is seen on top of Figure 41.

As shown in Figure 41, there are at least three crack initiation sites around the inclusion. Crack 1 occupies more than half of the inclusion circumference and has advanced the longest until the fish eye pattern is created by propagation of the crack to the specimen surface. Crack 3 lies on clearly different plane and has grown below cracks 1 and 2, thus causing retardation and unsymmetrical crack growth. It is worth of noting how long the ridges between the cracks reach. This demonstrates that the retardation effect has continued even beyond the crack sizes marked by the fish eye until the adjacent cracks have coalesced. We consider the rough surface besides the inclusion and in direction of crack 1 – opposite to crack 3 – as ODA. There seems to be a small area of ODA also within the crack 2.

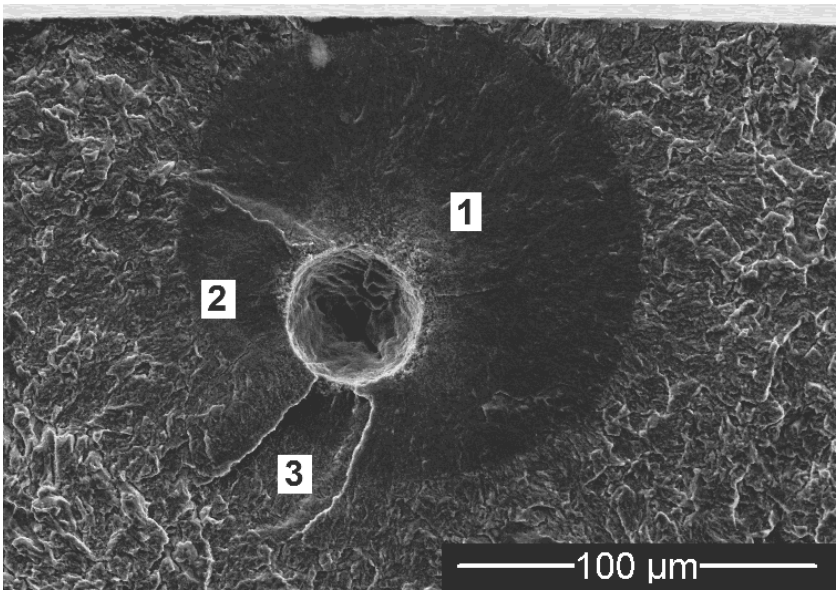

Figure 41. Crack paths around the inclusion associated with the longest endurance of 100Cr6 bearing steel. The stress ratio was R = -1 and the stress amplitude was 735 MPa. The test bar had been tested for $642 \cdot 10^6$ cycles.

The microstructure immediately below the fracture surface around the inclusion was studied. Two milled cross-sections were done (see Figure 42). The angled view clearly shows the long and about constant height of the step between the cracks 1 and 3. Once the first milled section was complete the surface of the cross-section was polished and then imaged with ions at a low current. The overview of the first cross-section with a comparison to the fracture surface is shown in Figure 42.

The left side of the first milled section shows the cross-section of the main ODA area next to the inclusion as well as the microstructure underneath the step between

the crack levels labelled ‘1’ and ‘2’ in Figure 41. The orientation difference revealed by the clear contrast in the underlying microstructure gives us a good reason to locate the two areas ‘1’ and ‘2’ in different prior austenite grains.

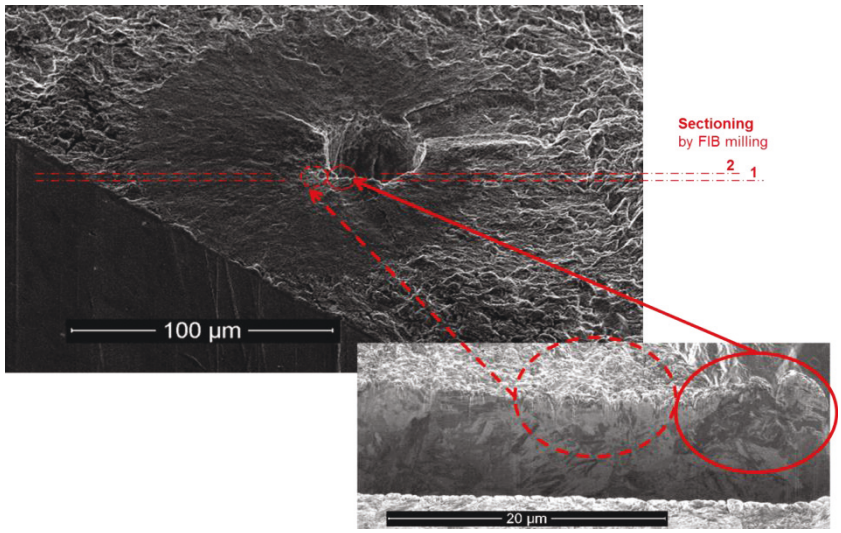

Figure 42. Comparing the microstructure of the step or ridge portion between crack levels ‘1’ and ‘2’ (see Figure 41) circled with a solid line and the microstructure of the ODA area circled with a dotted line.

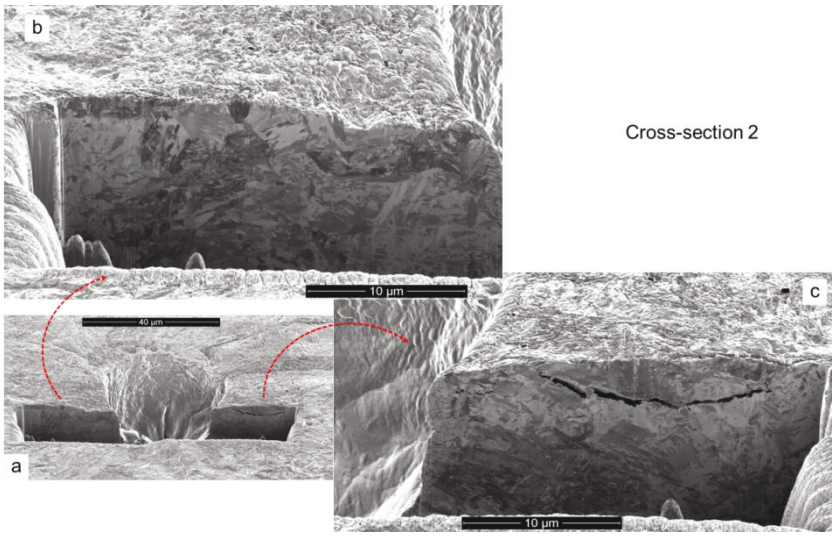

Figure 43. The second milled section, where (a) is the overview, and (b) is the left side and (c) is the right side. All images are taken with ion imaging.

In the right side of the cross-section 2 (

Figure 43(c)) there is a secondary crack which provides an opportunity to investigate both microstructure sides of a very small crack that initiated and grew close to the subsurface inclusion. The left side of the inclusion hole (
Figure 43(b)), where the milled cross-section shows a step in the fracture surface where the small crack was growing away from the inclusion.

5. Discussion

5.1 Anisotropy, inclusions and fatigue endurance limit

The fatigue limit of the axial test bars of the forged steel roll was higher when compared to the tangential test bars. The tangential test bars were taken normal to the forging direction which means that they would have elongated grains as well as inclusions; this would explain why the fatigue limit is lower in that direction as well. There is also a significant difference in the scatter of the fatigue test results. A larger amount of scatter in the tangential fatigue test bars is calculated according to two types of analysis. However, the binomial analysis gave an average fatigue limit that is larger, as well as a smaller amount of scatter for the tangential test bars than the MML method. One reason for this is that the tangential test bars have a calculated standard deviation that is more than twice as large as the calculated standard deviation of the axial test bars, and the use of a staircase step size of 5 MPa is not large enough to accurately measure the standard deviation of the fatigue limit. The step size for a staircase test should be close to the true standard deviation of the fatigue limit to properly calculate it according to the MML method. The step size used for the tests was half of the calculated standard deviation for the axial test bars and around 1/7 of the calculated standard deviation for the tangential test bars.

Another reason for the difference in the results between the different methods is that the binomial analysis takes into consideration all of the fatigue tests bars used in testing whereas the MML method uses only the smaller group to calculate the fatigue limit as well as the scatter. This gives an incomplete picture of the true values and can give different results depending on the situation.

The effect of inclusions on the fatigue limit of steels has been shown to be detrimental. The larger amount of scatter in the distribution of the inclusion $\sqrt{area}$ in the axial test bars compared to the tangential test bars is mainly due to the occurrence of a single large inclusion that was the largest of all inclusions that were found in the steel. This inclusion is likely exogenous in nature, meaning that its occurrence is not due to the cleanliness of the steel, but rather was in the steel due to the casting process of the forged steel roll.

Figure 44 illustrates the effect that the inclusions have on the fatigue limit of the steel. The circles illustrate the size of the inclusions located at the site of fatigue crack initiation. The relationship in-between the size of the inclusion and the fatigue life is shown in Figure 44. This figure illustrates a relationship between lower fatigue limit as well as a larger amount of scatter with a population of larger inclusions.

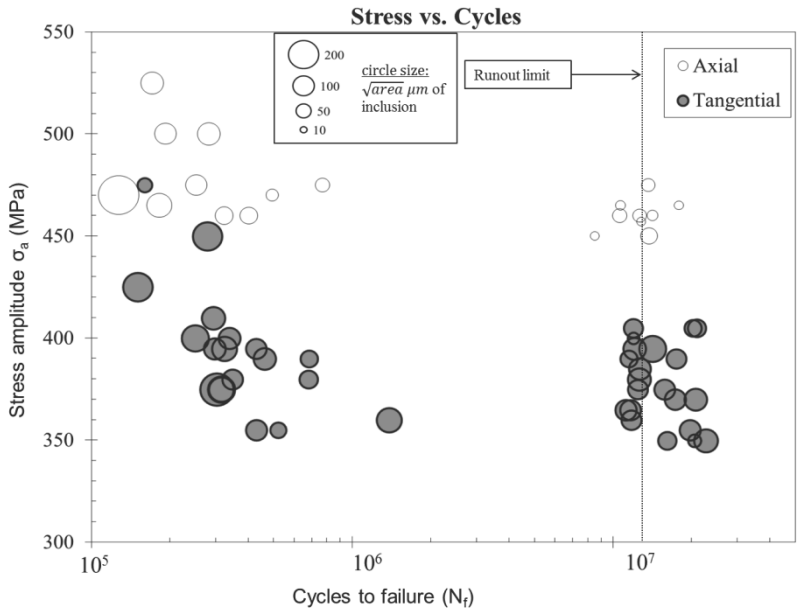

Figure 44. A stress vs. cycle graph where the area of the inclusion found at the site of fracture initiation is shown as the spot size. The results are from the steel studied in publication (I) taken from an industrial forged steel roll.

Using the microhardness of the matrix of the steel along with the maximum inclusion predicted by the extreme value distribution of the inclusions we can use the Murakami-Endo model to predict the lower fatigue limit of the steel. The upper limit of fatigue limit can be calculated from the microhardness of the steel. The relationship is given as:

$$\sigma_{wu} = 1.6 \cdot HV \pm 0.1HV \tag{23}$$

Using equation (23) the result of 514.3 ± 32.1 MPa is obtained for an upper limit of fatigue limit for the forged steel roll. The lower fatigue limit was calculated by using equation (17).

Comparing the upper fatigue limit to the actual calculated fatigue limits of both methods shows the amount of the decrease in the fatigue limit. The axial test bars are 51 MPa below the upper limit, and the tangential test bars are 144 – 128 MPa below the upper fatigue limit. The difference in the fatigue limit between the axial and tangential test bars is in agreement with other studies that have tested the anisotropic fatigue properties of steel [85,86].

The extreme value analysis of the inclusions from all the polished specimens provided an estimate that is within 4 μm of the average inclusion located on the fracture

surface. This indicates that the extrapolation of the extreme value distribution calculated for the inclusions located on the polished specimen is accurate in predicting the average inclusion size causing fatigue failure. The estimated inclusion for the axial polished surface is accurate as well when the exogenous inclusion is not considered. The tangential polished specimen results are more conservative and estimate larger inclusions than what were actually found on the fracture surface.

In publication (I) The analysis of the average size and average aspect ratio of all of the inclusions that were studied on the polished specimens indicate a clear anisotropic nature of the steel studied. The average size of the inclusions found on the X-plane (corresponding to tangential test bars) is 30.4 μm^2 and average aspect ratio is 1.71 (with a value of one representing a perfect circle). The average size of the inclusions found on the Y-plane (corresponding to axial test bars) is 21.5 μm^2 and the average aspect ratio is 1.63. This difference in the average size and aspect ratio is in agreement with the difference in size of the inclusions found on the fracture surfaces as well as the anisotropic nature of the fatigue limit for the different test bars.
A difference in the PDF of the maximum inclusions on the fracture surfaces is observed when dividing the inclusions into two separate groups. One group comprised of inclusions that caused fatigue crack growth and failure before the runout limit of 10^7 cycles, and the other group being the inclusions that were found on the fracture surface of the runout test bars. The comparison of these two groups can be seen in Figure 45. This figure shows the estimated probability density that was estimated from the histogram plots of the inclusions using the ks-density smoothing kernel in MATLAB.

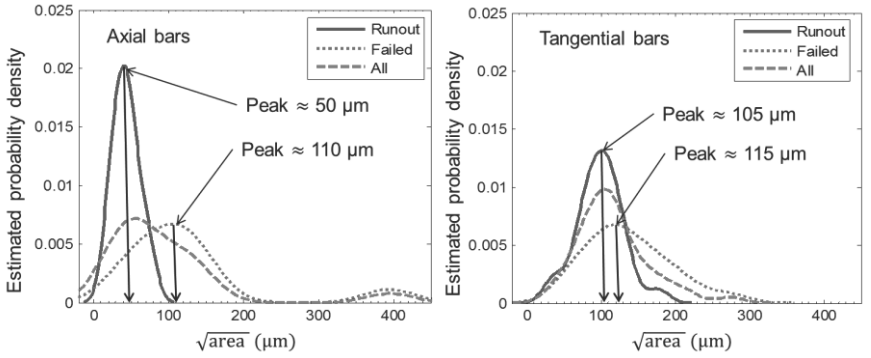

Figure 45. The estimated probability density of the inclusion square root area in µm located on the fracture surfaces of the fatigue test bars. The results are from the steel studied in publication (I) taken from an industrial forged steel roll.

Figure 45 shows that the location of the 'All' inclusion peak for tangential test bars is around 110 µm, and for both axial and tangential test bars the Failed peak is

located around 110-115 µm. The fact that the 'All' inclusion distribution peak location in the tangential test bars is almost the same as the failure peak location indicates that the maximum inclusions in the tangential fatigue test bars caused a greater decrease in the fatigue limit and an increase in the amount of scatter.

5.2 Small crack growth

The experimental results of publications (III) and (V) are in agreement with the general results that have been published in earlier studies [80,84,87-89]. The variability along with the faster growth rate of small cracks is evident in Figure 24. This variability is interesting due to the fact that it is the result of reliable measurements obtained with a SEM and that all the data in this figure comes from one fatigue test bar. Therefore the results provide a good picture of the inherent scatter of small crack growth rate that occurs in the microstructure since other variables such as different specimen variability along with possible changes in testing conditions do not contribute to the results.

The organization of the data in Figure 24 according to cycles count shows the variation between slow and fast crack growth rates. The data shows that the cracks grow at faster rates either as they initiate or after they start to grow again after an arrest. It also shows that the growth rate turns into a steady state of growth once the crack grows large enough.

The good correlation between the inclusions and FIB notch thresholds shown in Figure 21 shows that the use of FIB notches as initial defects is a good and relevant way to test the initiation and growth of small cracks in high-strength steels. This is seen as well in Figure 22 where the correlation between defect or crack size versus the stress amplitude shows that there is no decreasing trend for the inclusions or the FIB-milled notches. Rather all these data points are close to the fatigue limit, which means that the studied defect sizes are below the limit for decreasing fatigue limit as function of defect size. The thresholds obtained for the drilled holes indicate that such holes act well as conservative simulations of inclusions. One difference besides the shape in between the FIB-milled notches and the drilled holes is the residual stresses that are introduced by the mechanical removal of material. The ability to quantify or measure this difference is difficult. The other important contributing factor of drilled holes is the difference in shape from the FIB-milled notches. The holes used in this study are equal in depth as in width whereas the FIB notches have a smaller depth when compared to width. The drilled hole will also concentrate the stress into a larger area when compared to the notch due to geometrical factors which means that crack growth will more likely occur when considering a weakest link approach. This means that the size of the volume of material affected by the stress concentration of the hole is larger than that of the notch. Other shape differences include the sharp corners in the drilled hole which may play a crucial role in

early crack initiation and growth. Such mechanically made sharp corners are not present in FIB-milled notches.

5.3 Small cracks, ODA, and microstructure

5.3.1 Fractography

The type of fracture surface referred to as the ODA has been studied in detail. The ODA circled in Figure 36 shows similar fracture surface features as the ones shown in Ref. [20], and when comparing images in Figure 36 and Figure 37 we clearly see similar features that are common among ODA fracture surfaces.

The fracture surface images taken from 100Cr6 bearing steel test bars shown in Figure 40 and Figure 41 do not show as clear an ODA area for which there are several reasons. The 100Cr6 bearing steel is high-strength steel with a much finer grain structure. This can also be seen in the ion images of the milled cross-sections shown in Figure 38 for the 34CrNiMo6 QT(A) steel and in Figure 42 for the 100Cr6 bearing steel. The comparison of these figures shows that the sub-grain structure is noticeably finer in the 100Cr6 bearing steel than in the 34CrNiMo6 QT(A) steel. Since the microstructure is finer, the fracture surface created by a crack following the microstructure will also be finer and will not show as clear lath like structures shown in Figures 37, 38, and 39.

In Figure 40 a weak correlation can be seen between the size of inclusion (also ΔK on y-axis) and endurance. In addition to inclusion size, properties of the metal matrix around the inclusion and configuration of multiple cracks can affect early growth of the crack [84,90]. An influence of adjacent grain orientations has been demonstrated by numerical mesoscale models [91,92]. The correlation between microstructure and crack path are in line with such models. In addition, microstructure may affect through initiation, simultaneous growth and interaction of multiple cracks.

Our fractographic observations reveal the role of multiple crack initiation on slightly different planes. The asymmetrical crack growth that is observed around the inclusion (Figure 41) shows effects of the microstructure and/or multiple crack initiation on the crack path and direction. The fish eye around the inclusion also tells us that the fatigue crack did not propagate directly toward the surface rather obliquely towards it while growing slower on the opposite side of the inclusion, where overlapping of multiple cracks is shown. It is possible that the original initiation of the crack growth into the ODA toward the surface caused a growing stress concentration on the opposite side of the inclusion and initiated cracks on different planes on the other side before the first crack had grown round the circumference.

It is worth of noting that the longest life in Figure 40 is associated with a medium size inclusion less than 100 µm below the specimen surface. The fracture of the fatigue test bar shown in Figure 41 shows how three cracks have grown on adjacent planes before coalescence. This has led to a non-symmetrical crack (marked by the fish eye pattern) and retarded growth, in particular on the side where crack “3” has grown on a separate plane still when crack “1” reached the open surface. Similar “butterfly” looking marks around inclusions on UHCF fracture surfaces are commonly seen in literature and also in other inclusions shown in Figure 40.

In summary fatigue cracks do not always initiate exactly at the equator of a spheroid inclusion and several of them initiate to be later coalesced. Depending on the configuration, notable retardation of growth may result and affect the obtained fatigue life. It is possible that in some cases crack arrest occurs at the most critical inclusion and thus fatigue limit will be affected. However, unless such crack arrest can be confirmed, any proof on a correlation with the fatigue limit cannot be presented – just an effect on endurance.

5.3.2 FIB milling

In the quenched and tempered 34CrNiMo6 steel the crack shows a clear preferential growth direction along the martensite laths in the sub-grain microstructure. The pictures in Figure 37 – 40 show that the ODA was formed on the right hand side of the inclusion where horizontal martensite laths can be seen below the ODA region parallel to the direction of crack growth. The lengths of these martensite laths are close to the average prior austenite grain size. They are probably among the first ones to form across the whole prior austenite grain in question. We assume that the crack has first grown and that ODA was formed on this side, where the microstructure provides the most preferential direction for crack growth. Thus, our observations on the preferential crack paths from surface notches (Figure 35) and subsurface inclusions (Figure 38,
Figure 42, and 43) are in agreement. Furthermore, an additional explanation to the formation and origin of the ODA is proposed based on the connection to microstructure.

The FIB milling performed on the test bar of 100Cr6 bearing steel showed a finer microstructure than that of the 34CrNiMo6 QT(A) steel. There was evidence of the crack growth direction being influenced by the martensite lath sub-grain microstructure as well as the grain structure. This is shown in
Figure 42 where the step in fracture surface is due to either a large martensite lath or a difference in grain structure. In
Figure 43(c) secondary crack is observed near the inclusion underneath the actual fracture surface. The crack follows the martensite lath structure until a turning point where the surrounding microstructure changes and the crack changes the direction of growth.

5.3.3 Hydrogen, microstructure and ODA

Earlier work by Murakami et al. has shown that there is a link between the formation of the ODA and hydrogen trapped by the inclusion [22,28,56-62]. A lowering of the threshold stress intensity range by hydrogen for cracks initiating from inclusions has been shown [93]. On the other hand, little hydrogen exists in the steel matrix at milled surface notches. This may explain, why no ODA areas were observed around the FIB notches. However, the hydrogen content of our specimens is not studied. Neither did we search for ODA from the surface notched specimens because we were focusing on the interaction of the small cracks with the microstructure. Nagao et al. and others have studied the interaction of hydrogen and martensite laths [94]. They showed that the presence of hydrogen during monotonic loading caused cracks to preferentially grow along the prior austenite grain or martensite lath boundaries. One other important matter to understand when comparing a non-metallic inclusion with a FIB notch is that the notch is randomly placed into the surface of the test bar, whereas the inclusion is solid in the steel during the steel production process when the steel itself is still molten. This means that there are interactions that take place when the steel solidifies around the inclusion and may be a key reason why there are ODA formations around the inclusion.

Studies such as Ref. [95] show that there may be some kind of grain refinement that takes place around inclusions during the fatigue life. Whereas other studies have concentrated on the fact that the crack growth takes place usually in a vacuum inside the test bar and shown that crack growth in vacuum has a decreased rate when compared to the tests done in air [96]. While the effect of the crack growing in a vacuum certainly does impact the growth of the crack, the effect of the microstructure is critical. The former study used FIB milling to observe the microstructure and it is possible that the fine grains or grain refinement observed was from redeposition of the milled steel by the FIB. Some redeposition in the form of very fine grains is usually observed when milling larger cuts with the FIB.

In our study it was observed that crack growth begins within a region besides the inclusion, later seen as ODA on the fracture surface. It is also observed that the initiation and early growth of the crack are affected by the martensite lath and packet orientation.

The referenced earlier results and our observations are in agreement. Two main factors together affect the early growth of the cracks from the inclusion: the hydrogen trapped and the microstructure around the inclusion. These two factors work together to form the fractographic feature known as ODA on the fracture surface around the inclusions in high-strength steel specimens with ultra-long fatigue lives.

5.4 Small crack growth and compressive loading

The previous studies [53-55] about the effects of compressive loading on fatigue crack growth can be seen to apply also for small cracks in the steel that was studied here. It was measured that increasing the compressive loading for a crack can reinitiate its growth. This is due to the fact that increasing the compressive portion of the loading in constant amplitude testing decreases the ΔK_+ or K_{max} threshold for the crack growth. The experimental work reported here is unique due to the new tools and methods that were employed to monitor and measure small fatigue crack growth under these unique conditions. For this reason there are almost no comparable data that could be used for comparison of the results reported in this study.

The growth rates of small cracks under large compressive cyclic loads are slower when comparing their respective da/dN vs ΔK_+ or K_{max} values. A possible reason for this is that the compressive loading does not affect the crack growth the same way as the tensile portion of the loading does. Rather the compressive loading affects the crack growth through the bulk response of the material along with the full reversal or sharpening of the portion of the crack tip that is held open by the deformations of the plastic zone ahead and around the crack tip. The scale with which the compressive loading affects this could be material dependent. The effectiveness of compressive loading is reducing as the amount of compressive loading is increased.

The saturation of the effect of the compressive loading does not remove the challenges that the increase of the compressive loading has on the initiation and growth of cracks. It has been shown that initiation and crack growth can occur if the compressive portion of the loading is increased. The decrease in the ΔK_+ or K_{max} in the crack arrest is around 12% less for cracks at R = -2 when compared to cracks at R = -1. This is in agreement with the crack growth data at higher growth rates than at crack arrest where the influence of increasing the compressive loading from R = -1 to R = -2 will decrease the ΔK_+ or K_{max} required for crack growth by around 10 to 12%. If examined from the crack growth rate point of view the growth rate is increased by a factor of around 4 when doubling the compressive loading from R = -1 to R = -2. This indicates that the mechanism through which it affects the crack growth is possibly caused by the removal of crack closure or crack tip sharpening. Once the compression portion of the loading has enhanced the crack growth through these mechanisms, a further increase in compressive loading has less of an effect on the crack growth.

Conclusions

The distribution of non-metallic inclusions in steel is affected by the anisotropy caused by forging. This effect is then mirrored by a lower fatigue limit with a larger amount of scatter in the steel for test specimen taken normal to the forging direction. The estimation of the best distribution for the extreme value theory showed that the Gumbel distribution is best suited to predict the possible largest inclusion in a critical volume for the forged steel studied.

Crack paths around non-metallic inclusions and surface notches were studied in high-strength steels. Fatigue testing was done on specimens with small FIB notches. The cross-sections of the cracks showed that the small cracks tended to follow the martensite laths and packet boundaries.

The fractographic analysis of the non-metallic inclusions indicated that the ODA forms around the inclusion and that there can be several cracks that initiate around the inclusion on different planes. This multiple crack initiation can cause crack arrest due to cracks growing perpendicularly on different planes.

A connection between the microstructure and growth path of small cracks is demonstrated. The general preferential growth direction and formation of “optically dark area” (ODA) can be linked to adjacent grain orientations and sub-grain structures such as martensite lath and packet orientation. Local martensite lath packets in the microstructure surrounding a non-metallic inclusion together with the presence of hydrogen trapped around the inclusion provide an explanation to the formation and origin of the ODA.

The crack path observations show that the behaviour of small cracks is similar near the fatigue endurance limit for FIB notches and non-metallic inclusions. Using this information it is possible to use the measured crack growth data to model cracks growing from inclusions. This provides the ability to model the crack growth rate and fatigue life for a component where the non-metallic inclusion is the critical defect in the steel.

The use of FIB notches as small crack initiators in round test bars provides a reliable method of obtaining small crack growth data that correlates well with the results from test bars that failed from non-metallic inclusions. The microscopic observation of small crack growth from FIB notches during testing is a useful test method for small crack growth observation and can provide results for many loading ratios. The results are in line with previous studies of small crack growth showing a large variability in the crack growth rate as well a decrease in crack size that corresponds with a decrease in ΔK required for crack initiation.

Examining small crack growth using in-situ optical measurement of surface cracks in high-cycle fatigue using multiple test bars with small notches gives unique insights into the initiation and growth of small cracks in HCF. The results show that small crack growth occurs near the fatigue endurance limit of the studied quenched and tempered steel through a process of an accelerated crack growth immediately after initiation. After this brief initiation and accelerated growth of the small crack there follows a period of very slow growth until the large crack growth threshold is reached.

The comparison of small crack behavior at different R-ratios indicates that a good correlation can be obtained by only using the positive portion of the stress amplitude for small cracks. Compressive loading decreases the ΔK_+ or K_{max} threshold for small crack growth and increases the crack growth rate of small cracks. This effect is more pronounced when increasing from R = -1 to R = -2, than when increasing from R = -2 to R = -3.73.

The main conclusions are as follows:

- Anisotropy affects inclusion size and distribution and therefore the fatigue endurance limit and scatter.
- Small cracks initiating from FIB notches and non-metallic inclusions follow the local microstructure.
- Small cracks, at first, initiate quickly and then grow very slowly below and close to the threshold of large crack growth.
- The parameter ΔK_+ works well to compare the crack growth rate of small cracks in the studied quenched and tempered steel.
- Crack arrest ΔK_+ or K_{max} thresholds are lower for cracks with higher compressive loading.
- Increasing only the compressive portion of loading can reinitiate arrested small cracks.
- The ΔK_+ or K_{max} values for small cracks are lower for similar crack growth rates under larger compressive loads.

Acknowledgements

The research was part of three consecutive research projects: FATE-DEFEX, MACY, and SCarFace funded by the Finnish Funding Agency for Innovation (TEKES), VTT and industry.

References

[1] H. Kitagawa and S. Takahashi, “Applicability of fracture mechanics to very small cracks or crack in the early stage,” in *Proceedings of the Second International Conference on Mechanical Behaviour of Material*, 1976.

[2] R. Smith, “On the short crack limitations of fracture mechanics,” *International Journal of Fracture,* vol. 13, pp. 717-720, 1977.

[3] D. Taylor, “Fatigue of short cracks: the limitations of fracture mechancis,” in *The Behaviour of Short Fatigue Cracks, EGF Pub. 1*, K. J. Miller and E. R. de los Rios, Eds., London, Mechancial Engineering Publications, pp. 479-490, 1986.

[4] K. Tanaka, Y. Nakai and M. Yamashita, “Fatigue growth threshold of small cracks,” *International Journal of Fracture,* vol. 17, pp. 519-533, 1981.

[5] Y. Murakami and M. Endo, “Effect of hardness and crack geometry on delta K threshold of small cracks,” *Journal of the Society of Materials Science, Japan,* vol. 35, pp. 911-917, 1985.

[6] S. Suresh and R. Ritchie, "Propagation of short fatigue cracks," *International Metal Reviews,* pp. 445-476, 1984.

[7] A. McEvily, D. Eifler and E. Macherauch, “An analysis of the growth of short fatigue cracks,” *Engineering Fracture Mechanics,* vol. 40, pp. 571-584, 1991.

[8] A. J. McEvily, M. Endo and Y. Murakami, “On the square root area relationship and the short fatigue crack threshold,” *Fatigue and Fracture of Engineering Materials and Structures,* no. 26, pp. 269-278, 2003.

[9] P. Lukas and L. Kunz, “Small cracks—nucleation, growth and implication to fatigue life,” *International Journal of Fatigue,* vol. 25, pp. 855-862, 2003.

[10] W. Duckworth and E. Ineson, “The effects of externally introduced alumina particles on the fatigue life of En24 steel,” *Clean Steel 77 (Iron Steel Inst.),* pp. 87-103, 1963.

[11] R. Kiessling, “Non-metallic inclusions in steel, Parts I-IV,” *The Metals Society,* 450 p., 1978.

[12] R. Kiessling, “Clean steel: a debatable concept,” *Metal Science,* vol. 14, pp. 161-172, 1980.

[13] R. Kiessling, “Non-metallic inclusions in steel, Part V,” *The Institute of Metals,* 194 p., 1989.

[14] Y. Murakami and M. Endo, “Quantitative evaluation of fatigue strength of metals containing various small defects or cracks,” *Engineering Fracture Mechanics,* vol. 17, pp. 1-15, 1983.

[15] J. Cogne, B. Heritier and J. Monnot, "Cleanness and fatigue life of bearing steels In: Clean Steel 3," Balatonfured, Hungary, The Institute of Metals, pp. 26-31, 1987.

[16] Y. Murakami, S. Kodama and S. Konuma, “Quantitative evaluation of effects of non-metallic inclusions on fatigue strength of high strength steels. I: Basic fatigue mechanism and evaluation of correlation between the fatigue fracture stress and the size and location of non-metallic inclusions,” *International Journal of Fatigue,* vol. 11, pp. 291-298, 1989.

[17] Y. Murakami and H. Usuki, “Quantitative evaluation of effects of non-metallic inclusions on fatigue strength of high strength steels. II: Fatigue limit evaluation based on statistics for extreme values of inclusion size,” *International Journal of Fatigue,* vol. 11, pp. 299-307, 1989.

[18] Y. Murakami, K. Kawakami and W. Duckworth, Quantitative evaluation of effects of shape and size of artificially introduced alumina particles on the fatigue strength of 1.5Ni-Cr-Mo (En24) steel, *International Journal of Fatigue*, pp. 489-499, 1991.

[19] Y. Murakami and M. Endo, "Effects of defects, inclusions and inhomogeneities on fatigue strength," *International Journal of Fatigue,* vol. 16, no. 3, pp. 163-182, 1994.

[20] S. Beretta, A. Blarasin, M. Endo, T. Giunti and Y. Murakami, “Defect tolerant design of automotive components.,” *International Journal of Fatigue,* vol. 19, pp. 319-333, 1997.

[21] S. Beretta and Y. Murakami, “Statistical analysis of defects for fatigue strength prediction and quality control of materials,” *Fatigue & Fracture of Engineering Materials & Structures,* vol. 21, pp. 1049-1065, 1998.

[22] Y. Murakami, T. Nomoto and T. Ueda, “Factors influencing the mechanism of superlong fatigue failure in steels,” *Fatigue & Fracture of Engineering Materials & Structures ,* vol. 22, pp. 581-590, 1999.

[23] Y. Murakami and S. Beretta, "Small defects and inhomogeneities in fatigue strength: experiments, models and statistical implications," *Extremes,* pp. 123-147, 1999.

[24] S. Beretta and Y. Murakami, “Largest-extreme-value distribution analysis of multiple inclusion types in determining steel cleanliness,” *Metallurgical and Materials Transactions B,* vol. 32B, pp. 517-523, 2001.

[25] M. Todinov, “Probability distribution of fatigue life controlled by defects,” *Computers and Structures,* vol. 79, pp. 313-318, 2001.

[26] F. Meurling, A. Melander, M. Tidesten and L. Westin, “Influence of carbide and inclusion contents on the fatigue properties of high speed steels and tool steels,” *International Journal of Fatigue,* vol. 23, pp. 215-224, 2001.

[27] S. Beretta, G. Chai and E. Soffiati, "A weakest–link analysis for fatigue strength of components containing defects," in *Proceedings of the 11th Int Conf Fract*, Turin, 2005.

[28] Y. Murakami, Metal Fatigue: Effects of Small Defects and Nonmetallic Inclusion, Kyushu University: Elsevier, 2002.

[29] M. Tiryakioglu, "On the size distribution of fracture-initiating defects in Al- and Mg-alloy castings," vol. 476, pp. 174-177, 2008.

[30] N. Cyril and A. Fatemi, “Experimental evaluation and modeling of sulfur content and anisotropy of sulfide inclusions on fatigue behavior of steels,” *International Journal of Fatigue,* vol. 31, pp. 526-537, 2009.

[31] K. Wallin, “Statistical aspects of fatigue life and endurance limit,” *Fatigue and Fracture of Engineering Materials and Structures,* vol. 33, pp. 333-344, 2010.

[32] M. Tiryakioglu, "Statistical distributions for the size of fatigue-initiating defects in Al–7%Si–0.3%Mg alloy castings: A comparative study," *Materials Science and Engineering A,* pp. 119-125, 2008.

[33] M. Tiryakioglu, "On the size distribution of fracture-initiating defects in Al- and Mg-alloy castings," *Materials Science and Engineering A,* vol. 476, pp. 174-177, 2008.

[34] R. Kiessling and N. Lange, Non-metalic Inclusions in Steel, London: The Institute of Materials, 1978.

[35] A. M. Freudenthal and E. J. Gumbel, “Minimum life in fatigue,” *Journal of the American Statistical Association,* vol. 49, no. 267, pp. 575-597, 1954.

[36] S. Beretta and Y. Murakami, "Statistical analysis of defects for fatigue strength prediction and quality control of materials," *Fatigue & Fracture of Engineering Materials & Structures,* vol. 21, pp. 1049-1065, 1998.

[37] S. Beretta and Y. Murakami, "Largest-extreme-value distribution analysis of multiple inclusion types in determining steel cleanliness," *Metallurgical and Materials Transactions B,* vol. 32, pp. 517-523, 2001.

[38] J. W. Dixon and A. M. Mood, “A method for obtaining and analyzing sensitivity data,” *Journal of the American Statistical Association,* vol. 43, pp. 109-126, 1948.

[39] K. R. Wallin, “Statistical uncertainty in the fatigue threshold staircase method,” *International Journal of Fatigue,* vol. 33, pp. 354-362, 2011.

[40] K. Wallin, R. Voskamp, J. Schmidbauer, H. Ostermeyer and G. Nagel, "Statistical assessment method for the optimization of the inspection need for nuclear steam generators based on existing inspection data," in *20th International Conference on Structural Mechanics in Reactor Technology (SMiRT 20)*, 2009.

[41] M. El Haddad, T. Topper and K. Smith, “Prediction of non propagating cracks,” *Engineering Fracture Mechanics,* vol. 11, pp. 573-584, 1979.

[42] M. James and G. Smith, “Crack closure and surface microcrack thresholds some experimental observations,” *International Journal of Fatigue,* vol. 5, pp. 75-78, 1983.

[43] M. Chapetti, “Fatigue propagation threshold of short cracks under constant amplitude loading,” *International Journal of Fatigue,* vol. 25, pp. 1319-1326, 2003 .

[44] N. Fleck, C. Shin and R. Smith, “Fatigue crack growth under compressive loading,” *Engineering Fracture Mechanics,* vol. 21, pp. 173-185, 1985.

[45] S. Suresh, “Crack initiation in cyclic compression and its applications,” *Engineering Fracture Mechanics,* vol. 21, pp. 453-463, 1985.

[46] R. Pippan, “The growth of short cracks under cyclic compression,” *Fatigue & Fracture of Engineering Materials & Structures,* vol. 9, pp. 319–328, 1987.

[47] R. Hermann, “Fatigue crack growth in ductile materials under cyclic compressive loading,” *Fatigue & Fracture of Engineering Materials & Structures,* vol. 17, pp. 93-103, 1994.

[48] K. Kasaba, T. Sano, S. Kudo, T. Shoji, K. Katagiri and T. Sato, “Fatigue crack growth under compressive loading,” *Journal of Nuclear Materials,* vols. 258-263, pp. 2059-2063, 1998.

[49] M. Aratani and J. Knott, “The growth of short fatigue cracks ahead of a notch in high strength steel,” *Engineering Failure Analysis,* vol. 17, pp. 200-207, 2010.

[50] T. Hsua and Z. Wanga, “Fatigue crack initiation at notch root under compressive cyclic loading,” *Procedia Engineering,* vol. 2, pp. 91-100, 2010.

[51] W. Elber, “Fatigue crack closure under cyclic tension,” *Engineering Fracture Mechanics,* vol. 2, pp. 37-45, 1970.

[52] W. Elber, “The significance of fatigue crack closure,” *Damage Tolerance in Aircraft Strucures,* vol. ASTM STP 486, pp. 230-242, 1971.

[53] F. Silva, “Crack closure inadequacy at negative stress ratios,” *International Journal of Fatigue,* vol. 26, pp. 241-252, 2004.

[54] F. Silva, “The importance of compressive stresses on fatigue crack propagation rate,” *International Journal of Fatigue,* vol. 27, pp. 1441–1452, 2005.

[55] C. Benz and M. Sander, “Reconsiderations of fatigue crack growth at negative stress ratios: Finite element analyses,” *Engineering Fracture Mechanics,* vol. 145, pp. 98-114, 2015.

[56] Y. Murakami, T. Nomoto, T. Ueda and Y. Murakami, "On the mechanism of fatigue failure in the superlong life regime ($N>10^7$ cycles). Part 1: influence of hydrogen trapped by inclusions," *Fatigue & Fracture of Engineering Materials & Structures,* vol. 23, pp. 893-902, 2000.

[57] Y. Murakami, T. Nomoto, T. Ueda and Y. Murakami, "On the mechanism of fatigue failure in the superlong life regime ($N>10^7$ cycles). Part II: influence of

hydrogen trapped by inclusions," *Fatigue & Fracture of Engineering Materials & Structures,* vol. 23, pp. 903-910, 2000.

[58] Y. Murakami, H. Konishi, K. Takai and Y. Murakami, “Acceleration of superlong fatigue failure by hydrogen trapped by inclusions and elimination of conventional fatigue limit,” *Tetsu-to-Hagane,* vol. 86, pp. 777-783, 2000.

[59] Y. Murakami, N. Yokoyama and J. Nagata, "Mechanism of fatigue failure in ultralong life regime," *Fatigue & Fracture of Engineering Materials & Structures,* vol. 25, pp. 735-746, 2002.

[60] T. Ueda and Y. Murakami, “Effect of hydrogen on ultralong life fatigue failure of a high strength steel and fracture morphology of ODA,” *Transactions of the Japan Society of Mechanical Engineers, Series A,* vol. 69, pp. 908-915, 2003.

[61] Y. Murakami and J. Nagata, “Effect of hydrogen on high cycle fatigue failure of high strength steel, SCM435,” *Journal of the Society of Materials Science Japan,* vol. 54, pp. 420-427, 2005.

[62] Y. Murakami and J. Nagata, “Influence factors of fatigue design in ultralong life regime and effect of hydrogen on fatigue strength of high strength steel,” *Transactions of the Japan Society of Mechanical Engineers, Series A,* vol. 70, pp. 1093-1101, 2005.

[63] H. Uyama, M. Nakashima, K. Morishige, Y. Mine and Y. Murakami, “Effects of hydrogen charge on microscopic fatigue behaviour of annealed carbon steels,” *Fatigue & Fracture of Engineering Materials & Structures,* vol. 29, pp. 1066-1074, 2006.

[64] Y. Hong, Z. Lei, C. Sun and A. Zhao, “Propensities of crack interior initiation and early growth for very-high-cycle fatigue of high strength steels,” *International Journal of Fatigue,* vol. 58, pp. 144-151, 2014.

[65] T. Sakai, N. Oguma and A. Morikawa, “Microscopic and nanoscopic observations of metallurgical structures around inclusions at interior crack initiation site for a bearing steel in very high-cycle fatigue,” *Fatigue & Fracture of Engineering Materials & Structures,* vol. 38, pp. 1305-1314, 2015.

[66] A. Grabulov, R. Petrov and H. Zandbergen, “EBSD investigation of the crack initiation and TEM/FIB analyses of the microstructural changes around the cracks formed under Rolling Contact Fatigue (RCF),” *International Journal of Fatigue,* vol. 32, pp. 576-583, 2010.

[67] T. Olson, R. Lee and J. Morgan, “Contrast mechanisms in focused ion beam imaging.,” in *Proceedings of ISTFA '92, 18th International Symposium for Testing and Failure Analysis*, Los Angeles, 1992.

[68] Y.-Z. Wang, R. Revie, M. W. Phaneuf and J. Li, “Application of focused ion beam (FIB) microscopy to the study of crack profiles,” *Fatigue and Fracture of Engineering Materials and Strucures,* vol. 22, pp. 251-256, 1999.

[69] Y. Motoyashiki, A. Brückner-Foit and A. Sugeta, “Investigation of small crack behaviour under cyclic loading in a dual phase steel with an FIB tomography

technique," *Fatigue & Fracture of Engineering Materials & Structures,* vol. 30, pp. 556-564, 2007.

[70] Y. Motoyashiki, A. Brückner-Foit and A. Sugeta, "Microstructural influence on small fatigue cracks in a ferritic–martensitic steel," *Engineering Fracture Mechanics,* vol. 75, pp. 768-778, 2008.

[71] E. Keehan, L. Karlsson, H. Bhadeshia and M. Thuvander, "Three-dimensional analysis of coalesced bainite using focused ion beam tomography," *Materials Characterization,* vol. 59, pp. 877-882, 2008.

[72] C. Volkert and A. Minor, "Focused ion beam microscopy and micromachining," *MRS Bulletin,* vol. 32, pp. 389-395, 2007.

[73] Y. Sakai, T. Yamada, T. Suzuki, T. Sato, H. Itoh and T. Ichinokawa, "Contrast mechanisms in scanning ion microscope imaging for metals," *Applied Physics Letters,* vol. 73, pp. 611-613, 1998.

[74] M. Marx, W. Schäf, H. Vehoff and C. Holzapfel, "Interaction of microcracks with selected interfaces: Focused ion beam for a systematic crack initiation," *Materials Science and Engineering A,* pp. 595-601, 2006.

[75] C. Holzapfel, W. Schäf, M. Marx, V. H. and F. Mucklicha, "Interaction of cracks with precipitates and grain boundaries: Understanding crack growth mechanisms through focused ion beam tomography," *Scripta Materialia,* vol. 56, pp. 697-700, 2007.

[76] W. Schaef, M. Marx, H. Vehoff, A. Heckl and P. A. Randelzhofer, "3-D view on the mechanisms of short fatigue cracks interacting with grain boundaries.," *Acta Materialia,* vol. 59, pp. 1849-61, 2011.

[77] J. Nagata and Y. Murakami, "Factors influencing the formation of ODA in ultralong fatigue regime," *Journal of the Society of Materials Science Japan,* vol. 52, pp. 966-973, 2003.

[78] Y. Murakami, T. Nomoto and T. Ueda, "Factors influencing the mechanism of superlong fatigue failure in steels," *Fatigue & Fracture of Engineering Materials & Structures,* vol. 22, pp. 581-590, 1999.

[79] Y. Murakami, T. Nomoto, T. Ueda, Y. Murakami and M. Ohori, "Analysis of the mechanism of superlong fatigue failure by optical microscope and SEM/AFM observations," *Journal of the Society of Materials Science Japan,* vol. 48, pp. 1112-1117, 1999.

[80] N. Couroneau and J. Royer, "Simplified model for the fatigue growth analysis of surface cracks in round bars under mode I," *International Journal of Fatigue,* vol. 20, pp. 711-718, 1998.

[81] Y. Murakami, Ed., Stress Intensity Factors Handbook, Pergamon, 1987.

[82] M. Marx, W. Schäf, H. Vehoff and C. Holzapfel, "Interaction of microcracks with selected interfaces: Focused ion beam for a systematic crack initiation," *Materials Science and Engineering A,* Vols. 435-436, pp. 595-601, 2006.

[83] A. Tesch, R. Pippan, K.-H. Trautmann and H. Döker, “Short cracks initiated in Al 6013-T6 with the focused ion beam (FIB)-technology,” *International Journal of Fatigue,* vol. 29, pp. 1803-1811, 2007.

[84] J. Solin, J. Alhainen and P. Varis, “Ultra high cycle fatigue and inclusions in wrought steels,” in *Int Symposium on Fatigue Design and Material Defects*, Trondheim, 2011.

[85] E. Pessard, F. Morel, A. Morel and D. Bellett, “Modelling the role of non-metallic inclusions on the anisotropic fatigue behaviour of forged steel,” *International Journal of Fatigue,* vol. 33, pp. 568-577, 2011.

[86] J. Ma, B. Zhang, D. Xu, E. Han and W. Ke, “Effects of inclusion and loading direction on the fatigue behavior of hot rolled low carbon steel,” *International Journal of Fatigue,* vol. 32, pp. 1116-1125, 2010.

[87] B. Menzel and R. Dauskardt, “Fatigue damage initiation and growth from artificial defects in Zr-based metallic glass.,” *Acta Materialia,* vol. 56, pp. 2955-2965, 2008.

[88] M. Roy, Y. Nadot, C. Nadot-Martin, P.-G. Bardin and D. Maijer, “Multiaxial Kitagawa analysis of A356-T6.,” *International Journal of Fatigue,* vol. 33, pp. 823-832, 2011.

[89] Y. Yang, H. Ruan, J. Lu, N. Yao, W. Shan and W. Soboyejo, “Development of a microbeam method to investigate the fatigue crack growth mechanisms of submicron-scale cracks,” *Experimental Mechanics,* vol. 49, pp. 731-742, 2009.

[90] U. Krupp, H. Knobbe, H.-J. Christ, P. Köster and C.-P. Fritzen, “The significance of microstructural barriers during fatigue of a duplex steel in the high- and very-high-cycle-fatigue (HCF/VHCF) regime,” *International Journal of Fatigue,* vol. 32, pp. 914-920, 2010.

[91] E. Mikkola, G. Marquis and J. Solin, “Mesoscale modelling of crack nucleation from defects in steel,” *International Journal of Fatigue,* vol. 41, pp. 64-71, 2012.

[92] D. McDowell and F. Dunne, “Microstructure-sensitive computational modeling of fatigue crack formation,” *International Journal of Fatigue,* vol. 32, pp. 1521-1542, 2010.

[93] Y. Murakami, T. Kanezaki and P. Sofronis, “Hydrogen embrittlement of high strength steels: Determination of the threshold stress intensity for small cracks nucleating at nonmetallic inclusions,” *Engineering Fracture Mechanics,* vol. 97, pp. 227-243, 2013.

[94] K. Nagao, C. D. Smith, M. Dadfarnia, P. Sofronis and I. M. Robertson, “The role of hydrogen in hydrogen embrittlement fracture of lath martensitic steel,” *Acta Materialia,* vol. 60, pp. 5182-5189, 2012.

[95] P. Grad, B. Reuscher, A. Brodyanski, M. Kopnarski and E. Kerscher, “Mechanism of fatigue crack initiation and propagation in the very high cycle

fatigue regime of high-strength steels," *Scripta Materialia,* vol. 67, pp. 838-841, 2012.

[96] S. Stanzl-Tschegg and B. Schonbauer, "Near-threshold fatigue crack propagation and internal cracks in steel," *Procedia Engineering,* vol. 2, pp. 1547-1555, 2010.

Publication I

A. Roiko, H. Hänninen, H. Vuorikari, Anisotropic distribution of non-metallic inclusions in a forged steel roll and its influence on fatigue limit, International Journal of Fatigue, Volume 41, August 2012, Pages 158-167, ISSN 0142-1123

International Journal of Fatigue 41 (2012) 158–167

Contents lists available at SciVerse ScienceDirect

International Journal of Fatigue

journal homepage: www.elsevier.com/locate/ijfatigue

Anisotropic distribution of non-metallic inclusions in a forged steel roll and its influence on fatigue limit

Andrew Roiko [a,*], Hannu Hänninen [a], Hannu Vuorikari [b]

[a] Aalto University, P.O. Box 14200, 00076 Aalto, Finland
[b] Metso Paper, Inc., Wärtsilänkatu 100, FI-04400 Järvenpää, Finland

ARTICLE INFO

Article history:
Received 30 April 2011
Received in revised form 29 December 2011
Accepted 30 December 2011
Available online 18 January 2012

Keywords:
Fatigue limit
Non-metallic inclusions
Extreme value analysis
Binomial analysis
Staircase test

ABSTRACT

The objective of this work is to determine the fatigue limit of a forged heavy-weight steel roll, and to compare the estimated fatigue limit and its standard deviation with the theoretically predicted lower fatigue limit. The examination of the extreme value distribution of the inclusions located at the site of fatigue crack nucleation on the fracture surface of the fatigue test bars is compared with the extreme value distribution of the inclusions found on polished specimen. The extreme value distribution of the non-metallic inclusions is used to predict the theoretical lower fatigue limit of the steel. The experimental part of the paper consists of the fatigue testing of 61 test bars that were taken from a process industry forged steel roll. The estimation and comparison of the fatigue limit and its deviation was done using the least squares and binomial analysis methods. The results from this analysis are compared with the theoretically predicted upper and lower fatigue limit. The fatigue tests show that the fatigue test bars orientated tangentially to the axis of the forged steel roll have significantly lower fatigue lives when compared to the fatigue lives of the test specimens orientated along the axial direction of the forged steel roll.

1. Introduction

The fatigue limit of steels can be calculated using different assumptions for the mechanism causing fatigue crack nucleation. The steel can be defect free which would mean that a fatigue limit of this type of steel would be the upper limit, or as is generally the case a steel can have defects of varying sizes in its matrix which would result in a lower fatigue limit. The fatigue life or fatigue limit for steels is often studied with respect to the distribution of non-metallic inclusions in the steel. The connection between the distribution of defects in metallic materials and their fatigue properties has been discussed in many papers (see Refs. [1–19]). The general approach that has evolved to deal with this problem is based on the probabilistic modelling of the distribution of the inclusions. The occurrence of the largest inclusions in the steel is predicted by studying different cross-sections of steel and recording the sizes of the maximum inclusions found. Then by applying the theory of extreme values it is possible to predict the occurrence of the largest inclusion that will cause fatigue failure. The inclusion distribution model is then applied in a crack growth model which is used to calculate a distribution of cycles to failure or the decrease in the fatigue limit of the material. This kind of a predictive model outlined in Refs. [9,16], is applied to the steel in this paper.

The fatigue limit of steel is empirically estimated with fatigue tests. The staircase test method is used in this study to estimate the fatigue limit of the steel. Two different methods are used for the analysis of the test data. The first is the Maximum Likelihood (MML) method that has been developed by Dixon and Mood for the staircase test [20], which uses the method of least squares to estimate the fatigue limit and its standard deviation from the data. The second method analyses the data with the binomial probability theory to estimate the fatigue limit of the steel. This method has been developed by Wallin [21].

2. Materials and methods

2.1. Fatigue testing

The test bars studied in the fatigue tests were taken from an industrial forged steel roll. The approximate dimensions of the roll are around 1 m in diameter and 6 m long. The chemical composition of the steel is given in Table 1.

The manufacturing process of the steel roll starts with the casting of a steel ingot, after which it is forged to a degree of deformation that ranges from 4 to 7. The forged steel is pre-machined after which it is quenched and tempered, and the surface is then

* Corresponding author. Current address: VTT Technical Research Centre of Finland, Kemistintie 3, Espoo, P.O. Box 1000, FI-02044 VTT, Finland.
E-mail address: andrew.roiko@vtt.fi (A. Roiko).

0142-1123/$ - see front matter © 2012 Elsevier Ltd. All rights reserved.
doi:10.1016/j.ijfatigue.2011.12.023

Nomenclature

$\sqrt{area}$	the square root projected area of the inclusion on the plane normal to the stress	PDF	probability density function
σ_w	the predicted fatigue limit	PS	polished specimen
σ_{wu}	the predicted upper fatigue limit	R	the stress ratio, $\sigma_{min}/\sigma_{max}$
σ_{wl}	the predicted lower fatigue limit	Ro	runout
EDS	energy dispersive X-ray spectroscopy	SEM	scanning electron microscope
FS	fracture surface	α	$0.226 + HV \times 10^{-4}$
GEV	generalized extreme value	δ	scale parameter used in extreme value theory
HV	the Vickers hardness of the matrix around the inclusion (kg f/mm^2)	λ	location parameter used in extreme value theory
LEVD	largest extreme value distribution	σ	the stress acting on a specimen
MML	Maximum likelihood	S_0	standard inspection area (mm^2)
N	the number of stress cycles	T	return period
		V	volume of test bar (mm^3)
		V_o	standard control volume (mm^3)

induction hardened and machine finished. The microhardness of the steel test bars is 320 HV.

The fatigue properties of the steel were tested with rotating bending fatigue test method. A Schenk rotating bending fatigue test machine was used to apply a four-point bending loading to the test bar that ensured a constant loading moment along the gauge length of the specimen. Rotation of the fatigue test bar under four-point bending resulted in the varying of the applied stress at a stress ratio of $R = -1$, at a frequency of 35–40 Hz. An illustration of the size and shape of the test bars is shown in Fig. 1.

The fatigue test bars were removed from a forged steel roll at locations that were below the induction hardened surface. The bars that were taken tangential to the axis of the forged steel roll are called tangential test bars and correspond to the X-plane of the polished specimens used in the inclusion analysis. The test bars that were taken parallel to the axis are called axial test bars and correspond to the Y-plane of the polished specimens used in the inclusion analysis. An illustration of the direction of the test bars with respect to the steel roll is shown in Fig. 2.

After removal from the forged roll the test bars were machined and their surfaces were ground and polished. The transversal scratches were ground away and polished so that the effect of the surface features of the test bars on the fatigue limit was minimized. Testing was done using the staircase method with a step size of 5 MPa for tangential test bars and 10 MPa for axial test bars. The tests were performed at room temperature and the runout limit was set at 10^7 cycles. If a test bar reached the runout limit then the test was aborted and classified as a runout. All of the runouts were retested at a stress level that was 100 MPa higher than the runout stress level. This was done to cause failure so that the largest inclusion causing failure could be studied.

2.1.1. Maximum likelihood analysis

The calculation of the fatigue limit is done using a special case of the Maximum likelihood method, which is commonly called the method of least squares. This method is the minimization of the following equation which is called the sum of the squares:

$$S = \sum_{i=1}^{n} \left(\frac{X_i - \overline{X}}{\sigma} \right)^2 \tag{1}$$

Table 1
The chemical composition (wt.%) of the forged steel.

	C	Mn	P	S	Cr	V	Mo	Si
Weight%	0.61	0.50	0.005	0.005	1.34	0.08	0.26	0.23

The average $\overline{X}$ and the standard deviation σ are assumed to be from the normal distribution and are fitted to the data so that Eq. (1) is minimized. This method has been developed by Dixon and Mood and is used for the analysis of the staircase test results [20].

2.1.2. Binomial probability analysis

The results of the staircase test resemble a binomial distribution because the test specimen either fails at the stress level or it survives. The probability of having a certain number of failures at a certain stress level can be calculated according to the binomial theory as:

$$P(X = r) = \binom{n}{r} \cdot p^r \cdot (1-p)^{n-r} \tag{2}$$

where

$$\binom{n}{r} = \frac{n!}{r!(n-r)!} \tag{3}$$

Eq. (2) gives the discrete probability that there are (r) failures in (n) trials. In a staircase test the probability of the event p is not known. This probability can be calculated with a certain confidence (P_{conf}) with the following equation:

$$P_{conf}(p \le x) = \frac{\int_{p=0}^{x} \binom{n}{r} \cdot p^r \cdot (1-p)^{n-r} \cdot dp}{\int_{p=0}^{x} \binom{n}{r} \cdot p^r \cdot (1-p)^{n-r} \cdot dp} \tag{4}$$

The results can then be ranked according to binomial probability which starts at zero. The ranking can give the P_{conf} level of 5%, 50%, and 95% for each stress level [21,22].

2.2. The Murakami–Endo model

The Murakami–Endo Model predicts that when the location of the fracture origin is a small defect or non-metallic inclusion then the fatigue limit of the material can be determined by the Vickers

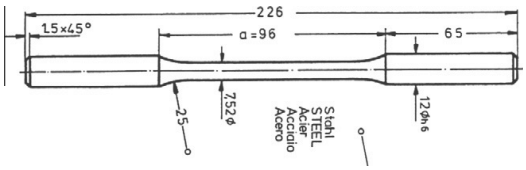

Fig. 1. The geometry of the fatigue test bar. All dimensions are in millimeters.

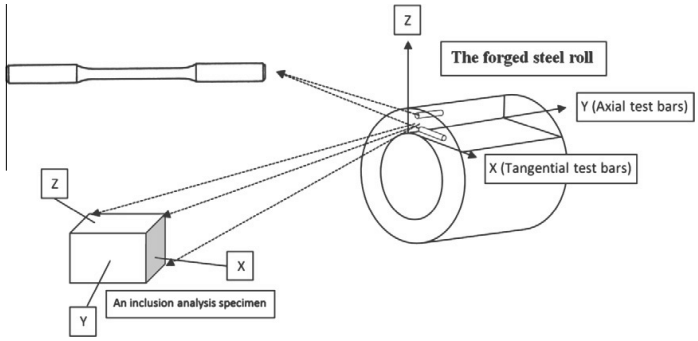

Fig. 2. A schematic illustration of the location of the test bars as well as the specimens used for inclusion analysis.

hardness of the microstructure surrounding the non-metallic inclusion and the square root of the projected area ($\sqrt{area}$) of the defect normal to the stress [16].

The model treats the inclusions or defects that are smaller than $\sqrt{area} \leq 1000$ μm as small cracks and it has been tested to be valid for high strength steels ($HV \geqslant 400$). The general equation is given as:

$$\sigma_{wl} = C \cdot (HV + 120)/(\sqrt{area})^{1/6} \tag{5}$$

where C is 1.43 for inclusions on the surface of a test specimen, 1.41 for inclusions in touch with the surface and 1.56 for inclusions underneath the surface. The σ_{wl} is the predicted fatigue limit (MPa), HV is the Vickers hardness of the matrix around the inclusion (kg f/mm^2), $\sqrt{area}$ is the square root projected area of the inclusion on the plane normal to the stress (μm) [16].

2.3. Inclusion analysis

2.3.1. Polished specimen inclusion analysis

The inclusions found on the polished specimens were all photographed, measured and their chemical compositions were analyzed. The elemental analysis was done using an INCA Energy 300 Microanalysis System (EDS).

The specimens used for inclusion analysis were taken from three different locations in the steel roll. The three positions were: one from close to the outer surface, one from in-between the center and the outer surface and one closer to the center of the steel roll. Once cut from the steel roll the specimens were polished. After the polishing the specimens were analyzed using an automatic INCA Feature analysis program. The program distinguishes inclusions on the polished surface by using the electron backscatter detector to differentiate between the matrix and the inclusions. The automated inspection was set at a magnification of 300×, and the inspection area that was automatically scanned and analyzed was 25 mm^2. For each plane this inspection was performed six times to achieve a total inspection area of 150 mm^2 for the plane. Once the analysis was complete the process was repeated with the same specimen on a new plane until all planes *X*, *Y*, and *Z* had been analyzed. This process was repeated for all three inclusion analysis specimens taken from the steel roll. A standard inspection area (S_o) of 25 mm^2 was defined for an extreme value analysis of the inclusions. The largest inclusion in each standard inspection is used for the extreme value analysis.

2.3.2. Fracture surface inclusion analysis

The inclusions found at the site of fatigue crack nucleation on the test bars were all photographed, measured and their chemical compositions were analyzed. The elemental analysis was done using an INCA Energy 300 Microanalysis System (EDS).

2.3.3. Extreme value analysis

The inclusion data from the fatigue tests and inclusion analysis can be described using different types of distributions. The largest inclusions found in steels can be considered to be the extreme maximum of the general population of inclusions. To choose which type of extreme distribution model to use the GEV, Fréchet, and Gumbel extreme value distributions were tested with a Kolmogorov–Smirnov test using the inclusion data. The best fit of these three was the Gumbel distribution. This distribution is given as follows:

$$P(X \leq x) = \exp\left\{-\exp\left(-\frac{x-\lambda}{\delta}\right)\right\} \tag{6}$$

where the values λ and δ are the location and scale parameters [23,24]. For the Gumbel distribution the mean ($\bar{\lambda}$) is calculated as follows:

$$\bar{\lambda} = \lambda + \delta \cdot \gamma \tag{7}$$

where γ is calculated as:

$$\gamma = -\int_0^1 \left(\ln\left(\ln\left(\frac{1}{x}\right)\right)\right)dx \approx 0.57721 \tag{8}$$

The standard deviation (σ) for the Gumbel distribution is:

$$\sigma = \frac{\delta \cdot \pi}{\sqrt{6}} \tag{9}$$

The distribution parameters of a Gumbel distribution for the inclusion populations studied were estimated by using the Maximum likelihood method. This method uses the probability density function to directly calculate the parameters of a distribution by calculating whether a certain probability distribution function can describe a set of data. The parameters of the probability distribution are fitted to maximize the likelihood which is calculated as follows:

$$L = \prod_{i=1}^{n} f(x_i) \tag{10}$$

In Eq. (10) the function $f(x_i)$ is the probability density function. The Gumbel probability density function is given as:

$$f(x, \lambda, \delta) = \frac{1}{\delta} \cdot \exp\left\{-\frac{(x-\lambda)}{\delta}\right\} \cdot \exp\left\{-\exp\left\{-\frac{(x-\lambda)}{\delta}\right\}\right\} \tag{11}$$

To estimate the parameters λ and δ of the distribution by MML method the logarithm of the MML is usually used for simplicity. This equation is called the log likelihood and is given as:

$$\ln(L) = \sum_{i=1}^{n} \ln\{f(x_i)\} \quad (12)$$

The maximization of Eq. (12) is done with an iterative process. The two parameters λ and δ are manipulated to maximize $\ln(L)$ in Eq. (12). Once the maximum log likelihood $\ln(L)$ is known then the parameters λ and δ that produced the MML are the parameters that best fit the distribution according to MML method.

When the λ and δ Maximum likelihood estimates for the Gumbel distribution are known these values are used to estimate for the maximum size of the inclusion $\sqrt{area}_{max}$ with a return period T and it is given as:

$$x(T) = \lambda + \delta \cdot y \quad (13)$$

where $y = -\ln(-\ln[(T-1)/T])$ with the return period T being defined as V/V_o, where V_o is the inspection volume and V being the volume of the part for which the maximum inclusion is being predicted. In this case V_o is calculated as follows: $S_0 \cdot h_0$, where h_o is the average $\sqrt{area}$ of the maximum inclusion distribution obtained from the inspection. The calculation of V for a test bar that is placed under rotating bending loading is considered to be the volume where the local stress is greater than 90% of the nominal stress. Murakami proposes in Ref. [16] the following volume: $V = 0.05\pi d^2 l$, where d is the diameter of the gauge length and l is its length. In this case V is calculated to be 634.5 mm^3.

3. Results

3.1. Fatigue test results

A total of 61 rotating bending fatigue test bars were tested. There were 42 test bars that were tangential to the axis of the steel roll and 19 that were parallel to it. A greater number of test bars were sampled in the tangential direction, since this exhibited a larger scatter in the fatigue properties and a larger projected area of the inclusions than the axial direction. The results of the fatigue tests are shown in Fig. 3.

There was a significant difference between the two different directions from which the fatigue bars were taken from the steel roll. The axial fatigue test bars displayed a significantly higher level of fatigue limit when compared to the tangential fatigue test bars.

3.1.1. Maximum likelihood analysis results

The MML method of analyzing staircase fatigue test results is outlined in Ref. [20]. Using this method the fatigue limit of the tangential test bars was calculated to be 369.7 MPa, with a standard deviation of ±35.6 MPa and the fatigue limit of the axial test bars was calculated to be 463.1 MPa, with a standard deviation of ±11.2 MPa.

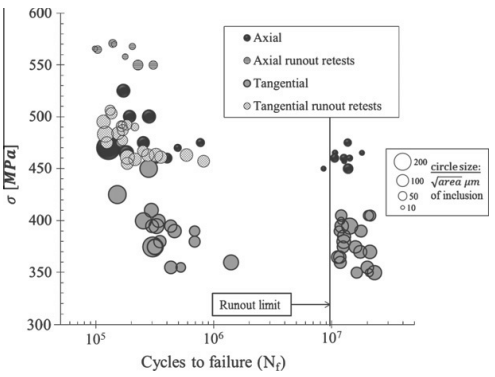

Fig. 3. The results of the fatigue tests with cycles on the x-axis and the stress amplitude (MPa) on the y-axis. The circle sizes represent the size of the inclusion located at the site of fatigue crack initiation.

3.1.2. Binomial probability analysis results

The binomial probability analysis method was applied to the fatigue test data. Using this method the average fatigue limit as well as the standard deviation of the strength was calculated for the tangential and axial test bars. The organization of the data along with the application of the binomial analysis method is shown in Table 2 for axial test bars and Table 3 for tangential test bars. The assumption that is made in the calculation of the amount of failed and runout test bars is that if the fatigue test at a certain stress level was a runout then the result would have been the same for all lower levels of stress. The opposite also applies when a failure occurs at a certain stress level and the test bar would have failed at all higher stress levels as well. The probabilities listed in these tables were calculated using Eq. (4) [21,22].

The fatigue limit of the tangential test bars calculated according to the binomial analysis is 386 MPa, with a standard deviation of ±20 MPa, and for the axial test bars the fatigue limit is 463 MPa, with a standard deviation of ±12 MPa.

In Fig. 4 the level of the estimated average fatigue limit ($P(50\%)$) at 10^7 cycles for tangential test bars is indicated by the intersection of the 50% failure probability red line and the 50% confidence blue line. The binomial analysis also gives the 95% and 5% confidence levels that are associated with each failure probability level. The same analysis was applied to the axial bars and is illustrated in Fig. 5. The comparisons of the binomial results with the Maximum likelihood results are presented in Table 4.

3.2. Murakami–Endo model results

The use of Eq. (5) gives the lower bound fatigue limit considering that the maximum inclusion square root area is the largest in the specimen and that it is the cause of failure. The application of the Murakami–Endo model to the fatigue data is shown in Fig. 6.

3.3. Inclusion analysis results

3.3.1. Polished specimen inclusion analysis results

The results of the automated inspection of the polished specimens yielded a total of 11300 inclusions. A summary of the findings is presented in Table 5.

The calculation of the maximum inclusions found on the polished specimen was done by measuring the maximum length and breadth of the inclusion and then using the equation for the area of an ellipse which is given as:

$$A = \pi \cdot \frac{(a \cdot b)}{4} \quad (14)$$

where (a) is the length and (b) is the width of an ellipse that best describes the shape of the largest inclusion found on the control surface of the polished specimen. The same method was used for fracture surface inclusions using an ellipse that best describes the shape of the inclusion or cluster on the fracture surface. An example of a maximum inclusion on a polished specimen is shown in Fig. 7 and the measurement of the size of the inclusion on a fracture surface is shown in Fig. 9. The $\sqrt{area}$ of an inclusion for both polished specimen as well as fracture surface inclusions is calculated as the square root of A in Eq. (14).

3.3.2. Fracture surface inclusion analysis results

The site of fatigue crack nucleation on all except for three of the 61 fatigue test bars was an inclusion that was on or near the surface of the test bar. These three test bars that did not show

Table 2
Binomial probability analysis of axial test bars.

Stress (MPa)	Runout	Failed	ΣFailed/ΣRunout	$\Sigma F/\Sigma N_{total}$	*P*(5%)	*P*(50%)	*P*(95%)
450	1	1	1/8	1/9	3.70	16.20	39.40
457	1	0	1/7	1/8	4.10	18.00	42.90
460	3	2	3/6	3/9	15.00	35.50	60.70
465	2	1	4/3	4/7	28.90	56.00	80.70
470	0	2	6/1	6/7	52.90	79.90	95.40
475	1	2	8/1	8/9	60.60	83.80	96.30
500	0	2	10/0	10/10	76.10	93.80	99.50
525	0	1	11/0	11/11	77.90	94.30	99.50

Table 3
Binomial probability analysis of tangential test bars.

Stress (MPa)	Runout	Failed	ΣFailed/ΣRunout	$\Sigma F/\Sigma N_{total}$	*P*(5%)	*P*(50%)	*P*(95%)
350	3	0	0/22	0/22	0.30	3.00	12.30
355	1	2	2/19	2/21	3.80	12.00	25.90
360	1	1	3/18	3/21	6.50	16.40	31.60
365	2	1	4/17	4/21	9.40	20.90	36.90
370	2	0	4/15	4/19	10.40	23.00	40.10
375	2	3	7/13	7/20	20.60	35.90	53.60
380	1	2	9/11	9/20	28.60	45.30	62.80
385	2	0	9/10	9/19	30.20	47.50	65.30
390	2	2	11/8	11/19	39.40	57.40	74.10
395	2	3	14/6	14/20	51.30	68.70	83.20
400	1	2	16/4	16/20	61.60	78.10	90.10
405	3	0	16/3	16/19	65.60	81.90	92.90
410	0	1	17/0	17/17	84.60	96.20	99.70
425	0	1	18/0	18/18	85.40	96.40	99.70
450	0	1	19/0	19/19	86.00	96.50	99.70
475	0	1	20/0	20/20	86.70	96.70	99.70

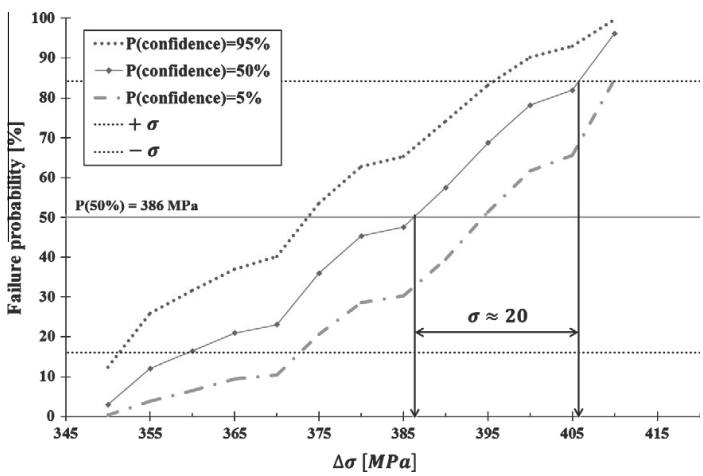

Fig. 4. The results of the fatigue tests performed on the tangential test bars. The fatigue limit and standard deviation are calculated according to the binomial method. The black dotted lines indicate one standard deviation.

evidence of inclusions at crack nucleation sites were all from the axial test bar group and two of the three were runouts, with the third bar failing at 8 million cycles. The type of inclusions found at the site of crack nucleation were mostly different types of aluminum oxides with the exception of 8 test bars, all of which were from the tangential group. In these test bars the fatigue cracks initiated from large inclusions composed of manganese sulfide. In Fig. 8 is shown one of the MnS inclusions.

3.3.3. Extreme value analysis results

Using the MML method to estimate the parameters of the Gumbel distribution from the inclusion data obtained from the fracture surface and polished specimen it is possible to calculate the estimated largest extreme value distribution (LEVD), as well as the upper and lower confidence levels. These extreme value probability plots for the fracture surface inclusions as well as polished specimen inclusions are shown in Figs. 10–12.

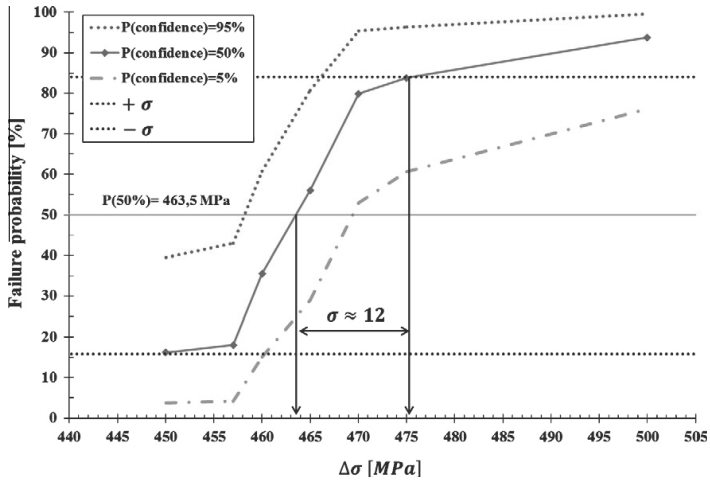

Fig. 5. The results of the fatigue tests performed on the axial test bars. The fatigue limit and standard deviation are calculated according to the binomial method. The black dotted lines indicate one standard deviation.

Table 4
The comparison of the two different methods used to calculate the fatigue limit and standard deviation from fatigue test results.

	Fatigue limit axial (MPa)	Deviation axial ± σ (MPa)	Fatigue limit tangential (MPa)	Deviation tangential ± σ (MPa)
MML analysis	463.1	11.2	369.7	35.6
Binomial analysis	463	12	386	20

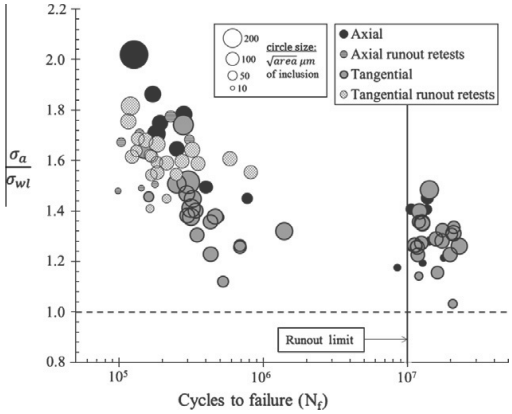

Fig. 6. The application of the Murakami–Endo model to the fatigue test data.

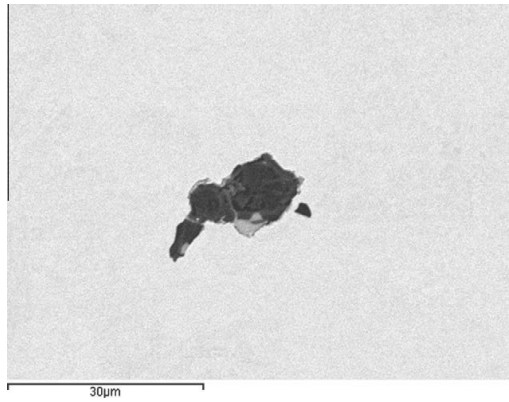

Fig. 7. An example of a maximum inclusion found on a polished specimen.

Table 5
The results of the INCA feature inclusion analysis.

	Total number of inclusions found	Average size (μm²)	Average aspect ratio
X-plane	3136	30.39	1.71
Y-plane	4812	21.5	1.63
Z-plane	3352	25.3	1.67
Total	11,300	24.98	1.65

The comparison of the inclusion distribution within the various planes of the steel roll was done as well. The parameters and the average maximum inclusion size along with the standard deviation of these distributions are shown in Table 6. The differences in the extreme value distributions of the inclusions from the fracture surfaces compared to the polished specimens indicate that a larger inspection area is required.

4. Discussion

4.1. Fatigue limit analysis

The fatigue limit of the axial test bars was higher when compared to the tangential test bars. The tangential test bars were

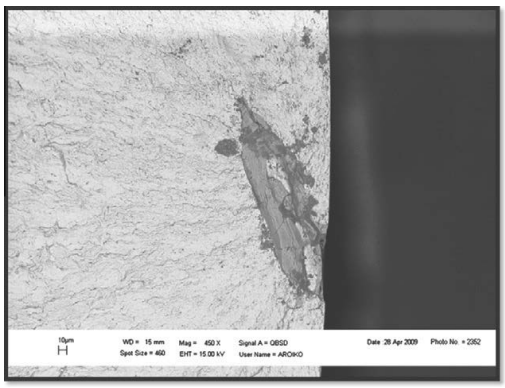

Fig. 8. A manganese sulfide inclusion at the site of crack nucleation on a test bar as an electron backscatter image.

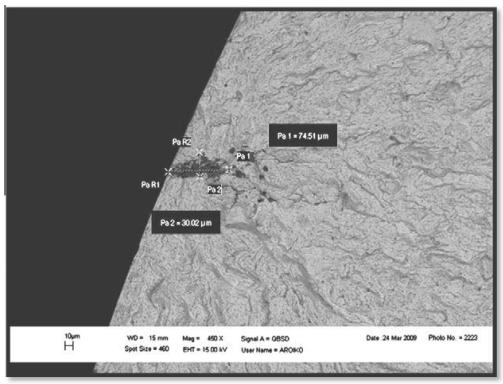

Fig. 9. An example of the measurement that was done to determine the size of the projected area for the inclusions that are found on the site of fatigue crack nucleation.

taken normal to the forging direction which means that they would have longer grains as well as inclusions; this would explain why the fatigue limit is lower in that direction as well. There is also a significant difference in the scatter of the fatigue test results. A larger amount of scatter in the tangential fatigue test bars is calculated according to both types of analysis. However, the binomial analysis gave an average fatigue limit that is larger, as well as a smaller amount of scatter for the tangential test bars than the MML method. One reason for this is that the tangential test bars have a calculated standard deviation that is more than twice as large as the calculated standard deviation of the axial test bars, and the use of a staircase step size of 5 MPa is not large enough to accurately measure the standard deviation of the fatigue limit. The step size for a staircase test should be close to the true standard deviation of the fatigue limit to properly calculate it according to the MML method. The step size used for the tests was half of the calculated standard deviation for the axial test bars and around 1/7 of the calculated standard deviation for the tangential test bars.

Another reason for the difference in the results between the different methods is that the binomial analysis takes into consideration all of the fatigue tests bars used in testing whereas the MML method uses only the smaller group to calculate the fatigue limit as well as the scatter. This gives an incomplete picture of the true values and can give different results depending on the situation.

The effect of inclusions on the fatigue limit of steels has been shown to be detrimental. The larger amount of scatter in the distribution of the inclusions $\sqrt{area}$ in the axial test bars compared to the tangential test bars is mainly due to the occurrence of a single large inclusion that was the largest of all inclusions that were found in the steel. This inclusion is likely exogenous in nature, meaning that its occurrence is not due to the cleanliness of the steel, but rather was in the steel due to the casting process of the forged steel roll.

Fig. 12 illustrates the effect that the inclusions have on the fatigue limit of the steel. The circles illustrate the size of the inclusions located at the site of fatigue crack nucleation. The relationship in-between the size of the inclusion and the fatigue life is shown in Fig. 12. This figure illustrates a relationship between lower fatigue limit as well as a larger amount of scatter with a population of larger inclusions.

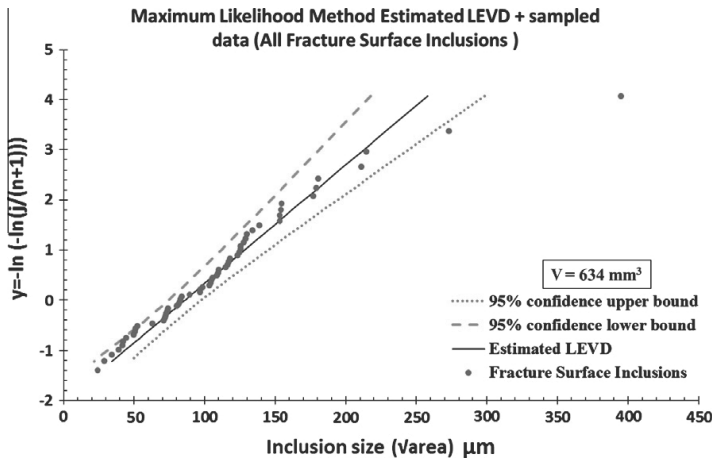

Fig. 10. The extreme value probability graph of the largest inclusions from the fracture surface inclusions.

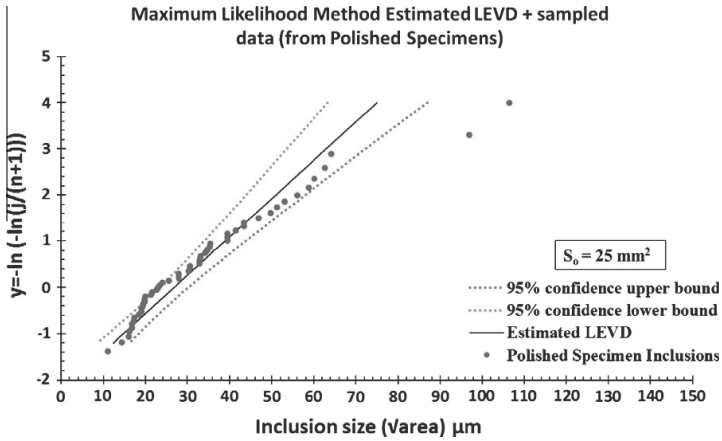

Fig. 11. The extreme value probability graph of the largest inclusions from all the polished specimen maximum inclusions.

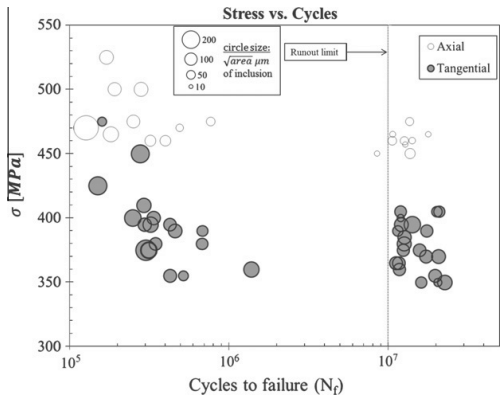

Fig. 12. A stress vs. cycle graph where the area of the inclusion found at the site of fracture nucleation is shown as the spot size.

Using the microhardness of the matrix of the steel along with the maximum inclusion predicted by the extreme value distribution of the inclusions we can use the Murakami–Endo model to predict the lower fatigue limit of the steel. The upper limit of fatigue limit can be calculated from the microhardness of the steel. The relationship is given as:

$$\sigma_{wu} = 1.6 \cdot HV \pm 0.1HV \tag{15}$$

Using Eq. (15) the result of 514.3 ± 32.1 MPa is obtained for an upper limit of fatigue limit for the forged steel roll. The lower fatigue limit was calculated by using Eq. (5) for each group shown in Table 7. The lower fatigue limit for the polished specimen inclusion groups used the maximum inclusion predicted by extreme value statistics for the volume (V) that was tested in the test bars. The result of these calculations can be seen in Table 7.

Comparing the upper fatigue limit to the actual calculated fatigue limits of both methods shows the amount of the decrease in the fatigue limit. The axial test bars are 51 MPa below the upper limit, and the tangential test bars are 144–128 MPa below the upper fatigue limit. The difference in the fatigue limit between the axial and tangential test bars is in agreement with other studies that have tested the anisotropic fatigue properties of steel [25,26].

Table 6
The average size of the inclusions in different positions of the test bars and polished specimens as well as their extreme value distribution parameters for the Gumbel distribution.

	Average Inclusion size ($\sqrt{}$area) µm $\bar{\lambda} = \lambda + \delta \cdot \gamma$	Standard deviation Inclusion size ($\sqrt{}$area) µm $\sigma = (\delta \cdot \pi)/\sqrt{6}$	Lambda (λ) Location parameter Gumbel	Delta (δ) Scale parameter Gumbel	Number of inclusions studied
All FS	110.42	54.25	86.0	42.3	58
All PS	33.78	15.52	26.8	12.1	54
Axial (*Y*)-FS	90.69	57.97	64.6	45.2	16
Axial (*Y*)-FS[a]	75.25	39.89	57.3	31.1	15
Tangential (*X*)-FS	115.42	49.38	93.2	38.5	42
Axial (*Y*)-PS	26.17	9.49	21.9	7.4	18
Tangential (*X*)-PS	45.43	22.96	35.1	17.9	18
Z-Plane (*Z*)-PS	29.45	11.67	24.2	9.1	18
Axial (*Y*)-FS (Ro)	43.72	16.03	36.5	12.5	6
Axial (*Y*)-FS (F)	121.62	68.49	90.8	53.4	10
Tangential (*X*)-FS (Ro)	101.32	38.48	84.0	30.0	16
Tangential (*X*)-FS (F)	137.15	58.10	111.0	45.3	19

[a] The calculation of parameters excluding the largest inclusion found on an axial test bar fracture surface that was exogenous in nature. FS = Fracture Surface, PS = Polished Specimen, Ro = Runout, F = Fail.

Table 7
The comparison of the different estimated fatigue limits of the axial and tangential fatigue test bars, as well as the lower fatigue limit calculated by using Eq. (5).

	Fatigue limit σ_w (MPa) (Staircase method)	Fatigue limit σ_w (MPa) (Binomial method)	Average maximum inclusion size ($\sqrt{}$area) μm	Lower Fatigue limit predicted by the Murakami–Endo model σ_{wl} (MPa)
All FS	–	–	110.42	287.9
All PS (V_o = 0.84 mm^3)	–	–	106.90*	289.1
Axial (*Y*)-FS	463.1 ± 11.2	463 ± 12	90.69	297.5
Axial (*Y*)-FS[a]			75.25	306.9
Tangential (*X*)-FS	369.7 ± 35.6	386 ± 20	115.42	285.8
Axial (*Y*)-PS (V_o = 0.65 mm^3)	–	–	70.89*	309.7
Tangential (*X*)-PS (V_o = 1.14 mm^3)	–	–	148.13*	274.2
Z-Plane (*Z*)-PS (V_o = 0.88 mm^3)	–	–	152.93*	272.7
Axial (*Y*)-FS (Ro)	–	–	43.72	335.9
Axial (*Y*)-FS (F)	–	–	121.62	283.3
Tangential (*X*)-FS (Ro)	–	–	101.32	292.1
Tangential (*X*)-FS (F)	–	–	137.15	277.7

[a] The calculation of parameters excluding the largest inclusion found on an axial test bar fracture surface that was exogenous in nature. FS = Fracture surface, PS = Polished specimen, Ro = Runout, F = Fail.
* Predicted with EVT for test bar volume, V_o = Standard control volume calculated for the polished specimen (mm^3).

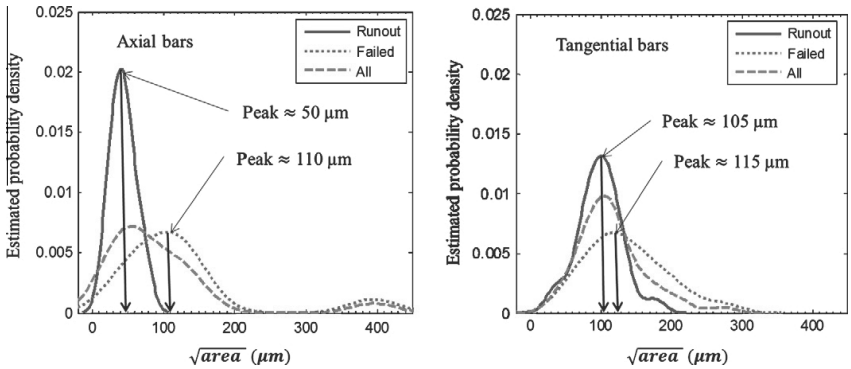

Fig. 13. The estimated probability density of the inclusion square root area in microns located on the fracture surfaces of the fatigue test bars.

4.2. Inclusion analysis

The analysis of the average size and average aspect ratio of all of the inclusions that were studied on the polished specimens indicate a clear anisotropic nature of the steel studied. The average size of the inclusions found on the *X*-plane (corresponding to tangential test bars) is 30.4 μm^2 and average aspect ratio is 1.71 (with a value of one representing a perfect circle). The average size of the inclusions found on the *Y*-plane (corresponding to axial test bars) is 21.5 μm^2 and the average aspect ratio is 1.63. This difference in the average size and aspect ratio is in agreement with the difference in size of the inclusions found on the fracture surfaces as well as the anisotropic nature of the fatigue limit for the different test bars.

The extreme value analysis of the inclusions from all the polished specimens provided an estimate that is within 4 μm of the average inclusion located on the fracture surface. This indicates that the extrapolation of the extreme value distribution calculated for the inclusions located on the polished specimen is accurate in predicting the average inclusion size causing fatigue failure. The estimated inclusion for the axial polished surface is accurate as well when the exogenous inclusion is not considered. The tangential polished specimen results estimate larger inclusions than what were actually found on the fracture surface.

A difference in the PDF of the maximum inclusions on the fracture surfaces is observed when dividing the inclusions into two separate groups. One group comprised of inclusions that caused fatigue crack growth and failure before the runout limit of 10^7 cycles, and the other group being the inclusions that were found on the fracture surface of the runout test bars. The comparison of these two groups can be seen in Fig. 13. This figure shows the estimated probability density that was estimated from the histogram plots of the inclusions using the ks-density smoothing kernel in MATLAB.

Fig. 13 shows that the location of the All inclusion peak for tangential test bars is around 110 μm, and for both axial and tangential test bars the Failed peak is located around 110–115 μm. The fact that the 'All' inclusion distribution peak location in the tangential test bars is almost the same as the failure peak location indicates that the maximum inclusions in the tangential fatigue test bars caused a greater decrease in the fatigue limit and an increase in the amount of scatter.

5. Conclusions

A total of 61 fatigue test bars were studied. Of these, 29 bars failed before the runout limit that was set at 10^7 cycles. The test bars that were runouts were retested at a higher stress level. The estimated fatigue limit as well as the standard deviation was calculated according to the MML method and the binomial method. These two different ways of estimating the fatigue limit and

standard deviation were compared. The use of the binomial method gave results that were similar to the MML method for the axial test bars. However, the size of the standard deviation was smaller and the mean fatigue limit was higher in the tangential test bars when using the binomial method compared to the staircase method.

The nucleation sites of the cracks that lead to failure were identified as inclusions on or near the surface of the test samples for 58 out of 61 test bars. The inclusions consisted mainly of a mixture of aluminum oxides with small traces of MnS. Of all of the inclusions causing fatigue failure only 8 out of the total 58 are not aluminum oxide inclusions. Of these 8 inclusions all are MnS. All of the MnS inclusions were found at the fatigue crack initiation sites of tangential test bars.

The prediction of the lower bound fatigue limit according to the Murakami–Endo model provided a conservative estimate for the lower bound fatigue limit. All the fatigue tests failed above the lower bound limit predicted by the Murakami–Endo model. Applying the statistics of extremes to inclusions on polished specimen to predict the inclusion causing fatigue failure provided accurate results for the average inclusion in the 'All' inclusion group and the axial group. The extreme value prediction for the tangential group of inclusions was much larger than what was discovered.

The results of the comparison of the estimated PDF of the inclusions on the fracture surfaces show that the maximum inclusion distribution had a larger effect on the tangential test bars than the axial test bars due to its peak location which is close to the failure peak location. It also shows that the average size along with the standard deviation of the extreme value population has a large impact on the fatigue limit and deviation of the steel.

Acknowledgement

The authors wish to thank the Research Project FATE-DEFEX for support in the research.

References

[1] Duckworth WE, Ineson E. The effects of externally introduced alumina particles on the fatigue life of En24 steel. Clean Steel Iron Steel Inst Spec Rep 1963;77:87–103.
[2] Kiessling R, Lange N. Non-metallic inclusions in steel. Parts I–IV. London: The Institute of Materials; 1978.
[3] Kiessling R. Clean steel: a debatable concept, clean steels. In: Proceeding of the second int conf on clean steels, Balatonfured, Hungary, 1981 June 1–3. London: Institute of Metals; 1983. p. 1–9.
[4] Kiessling R. Non-metallic inclusions in steel. Part V. London: The Institute of Metals; 1989.
[5] Murakami Y, Endo M. Quantitative evaluation of fatigue strength of metals containing various small defects or cracks. Eng Fract Mech 1983;17:1–15.
[6] Cogne JY, Heritier B, Monnot J. Cleanness and fatigue life of bearing steels, clean steels. In: Proceeding of the second int conf on clean steels, Balatonfured, Hungary, 1986 June. London: Institute of Metals; 1983. p. 29–31.
[7] Murakami Y, Kodama S, Konuma S. Quantitative evaluation of effects of non-metallic inclusions on fatigue strength of high strength steels. I: basic fatigue mechanism and evaluation of correlation between the fatigue fracture stress and the size and location of non-metallic inclusions. Int J Fatigue 1989;11:291–8.
[8] Murakami Y, Usuki H. Quantitative evaluation of effects of non-metallic inclusions on fatigue strength of high strength steels. II: fatigue limit evaluation based on statistics for extreme values of inclusion size. Int J Fatigue 1989;11:299–307.
[9] Murakami Y, Endo M. Effects of defects, inclusions and inhomogeneities on fatigue strength. Int J Fatigue 1994;16:163–82.
[10] Beretta S, Blarasin A, Endo M, Giunti T, Murakami Y. Defect tolerant design of automotive components. Int J Fatigue 1997;19:319–33.
[11] Beretta S, Murakami Y. Statistical analysis of defects for fatigue strength prediction and quality control of materials. Fatigue Fract Eng Mater Struct 1998;21:1049–65.
[12] Beretta S, Murakami Y. Largest-extreme-value distribution analysis of multiple inclusion types in determining steel cleanliness. Metall Mater Trans B 2001;32:517–23.
[13] Todinov MT. Probability distribution of fatigue life controlled by defects. Comput Struct 2001;79:313–8.
[14] Meurling F, Melander A, Tidesten M, Westin L. Influence of carbide and inclusion contents on the fatigue properties of high speed steels and tool steels. Int J Fatigue 2001;23:215–24.
[15] Beretta S, Chai G, Soffiati E. A weakest-link analysis for fatigue strength of components containing defects. In: Proceedings of the 11th int conf fract, Turin; 2005.
[16] Murakami Y. Metal fatigue: effects of small defects and nonmetallic inclusion. Kyushu University: Elsevier; 2002.
[17] Tiryakioglu M. On the size distribution of fracture-initiating defects in Al- and Mg-alloy castings. Mater Sci Eng A 2008;476:174–7.
[18] Cyril N, Fatemi A. Experimental evaluation and modeling of sulfur content and anisotropy of sulfide inclusions on fatigue behavior of steels. Int J Fatigue 2009;31:526–37.
[19] Wallin K. Statistical aspects of fatigue life and endurance limit. Fatigue Fract Eng Mater Struct 2010;33:333–44.
[20] Dixon JW, Mood AM. A method for obtaining and analyzing sensitivity data. J Am Stat Assoc 1948;43:109–26.
[21] Wallin K. Statistical uncertainty in the fatigue threshold staircase method. Int J Fatigue 2011;33:354–62.
[22] Wallin K, Voskamp R, Schmidbauer J, Ostermeyer H, Nagel G. Statistical assessment method for the optimization of the inspection need for nuclear steam generators based on existing inspection data. In: 20th International conference on structural mechanics in reactor technology (SMiRT 20), vol. VIII; 2009. p. 1731.
[23] Freudenthal AM, Gumbel EJ. Minimum life in fatigue. J Am Stat Assoc 1954;49:575–97.
[24] Tiryakioglu M. Statistical distributions for the size of fatigue-initiating defects in Al–7%Si–0.3%Mg alloy castings: a comparative study. Mater Sci Eng A 2008;497:119–25.
[25] Pessard E, Morel F, Morel A, Bellett D. Modelling the role of non-metallic inclusions on the anisotropic fatigue behaviour of forged steel. Int J Fatigue 2011;33:568–77.
[26] Ma J, Zhang B, Xu D, Han E, Ke W. Effects of inclusion and loading direction on the fatigue behavior of hot rolled low carbon steel. Int J Fatigue 2010;32:1116–25.

Publication II

A. Roiko, Y. Murakami, A design approach for components in ultralong fatigue life with step loading, International Journal of Fatigue, Volume 41, August 2012, Pages 140-149, ISSN 0142-1123

International Journal of Fatigue 41 (2012) 140–149

Contents lists available at SciVerse ScienceDirect

International Journal of Fatigue

journal homepage: www.elsevier.com/locate/ijfatigue

A design approach for components in ultralong fatigue life with step loading

A. Roiko [a,b,*], Y. Murakami [c,d]

[a] Aalto University, Espoo, Finland
[b] VTT Technical Research Centre of Finland, Kemistintie 3, Espoo P.O. Box 1000-FI-02044 VTT, Finland
[c] International Institute for Carbon-Neutral Energy Research (I2CNER), Kyushu University, Japan
[d] Research Center for Hydrogen Industrial Use and Storage (HYDROGENIUS), National Institute of Advanced Industrial Science and Technology (AIST), 744 Moto-oka, Nishi-ku, Fukuoka 819-0395, Japan

ARTICLE INFO

Article history:
Received 29 April 2011
Received in revised form 23 December 2011
Accepted 28 December 2011
Available online 5 January 2012

Keywords:
Ultralong fatigue life
Fatigue design
High strength steel
Non-metallic inclusion
The $\sqrt{area}$ parameter model

ABSTRACT

An overview of critical variables that affect fatigue failure with respect to steel components in ultralong life regimes is presented. The key role of hydrogen trapped by non-metallic inclusions in the ultralong life fatigue failure process is documented. The role of non-metallic inclusions on ultralong fatigue life is shown in the master curve of ODA (Optically Dark Area surrounding a non-metallic inclusion at fracture origin) growth. The master curve of ODA growth shows the correlation of the size of the ODA with the size of the non-metallic inclusion as it corresponds to fatigue life. The ability to predict the presence of non-metallic inclusions in steels with extreme value methods is incorporated with the master curve of ODA growth to determine the maximum threshold stress for ultralong fatigue life using the $\sqrt{area}$ parameter model. Most machine components experience variable loads in service. A design approach is introduced for calculating the effects of different loading levels for ultralong fatigue life.

1. Introduction

The study of ultralong life fatigue was begun due to the fatigue failure of steel parts and test specimen with fatigue lives that are beyond the conventional fatigue limit, which is defined by a fatigue life cycle amount that is $N_f \geqslant 10^7$ cycles. Research into the cause of ultralong life fatigue failure in high strength steels has revealed that fatigue crack nucleation occurs at subsurface non-metallic inclusions. Next to these subsurface inclusions a dark area is observed that is called Optically Dark Area (ODA). The presence of an ODA is not observed on fracture surfaces of specimens with short fatigue lives. The appearance of the ODA next to subsurface inclusions has been researched and documented in the following Refs. [1–6].

The disappearance of the conventional fatigue limit in the fatigue life of high strength steels can be seen in Fig. 1. The failure of test specimen at ultralong fatigue lives ($N_f > 10^7$) and the effect caused by the size of the test specimen can be united by understanding the role that non-metallic inclusions play in causing fatigue failure in ultralong fatigue.

To predict fatigue failure due to the presence and role of the ODA and its growth from non-metallic inclusions this paper reviews the research that has been performed by Murakami and his co-workers in Refs. [7–10]. The results of these studies reveal that there are several factors that should be considered. These factors are:

(1) The growth of the ODA with respect to the fatigue life of the specimen and internal hydrogen in the specimen.
(2) The statistical aspect of fatigue due to the difference in volumes tested and the distribution of the maximum inclusions in the steel.
(3) The dependency of the threshold stress intensity factor range ΔK_{th} on crack size.

This paper will review these three main factors involved in ultralong life fatigue failure in high strength steels from internal inclusions and will propose a fatigue design approach for ultralong fatigue lives of high strength steel components. This design approach incorporates the effect of the volume as well as the distribution of the inclusions in the steel, along with the growth of the ODA from the inclusions in ultralong fatigue life regimes. This design approach is only meant to be used for ultralong life fatigue failure in high strength steels caused by subsurface non-metallic inclusions. This design approach does not take into consideration other factors in fatigue such as mean stress, environmental effects, surface effects or notch effects.

2. Materials and methods

The high strength steels that are studied in this paper are a Cr–Mo steel (JIS SCM435) [1–3,7] and a bearing steel (SAE52100)

* Corresponding author at: VTT Technical Research Centre of Finland, Finland.
E-mail address: andrew.roiko@vtt.fi (A. Roiko).

0142-1123/$ - see front matter © 2012 Elsevier Ltd. All rights reserved.
doi:10.1016/j.ijfatigue.2011.12.021

Nomenclature

σ'_w	the modified $\sqrt{area}$ model for ODA predicted lower bound fatigue limit	S	area of prediction (mm^2)
$\sqrt{area}$	the square root projected area of the inclusion on the plane normal to the stress	S_0	standard inspection area (mm^2)
σ_w	the $\sqrt{area}$ model predicted lower bound fatigue limit	SEM	Scanning Electron Microscope
ΔK_{ODA}	threshold Stress Intensity Factor Range for ODA	SIMS	secondary ion mass spectrometry
ΔK_{th}	threshold Stress Intensity Factor Range	T	return period
AFM	Atomic Force Microscopy	V	volume of prediction (mm^3)
HV	the Vickers Hardness of the matrix around the inclusion (kgf/mm^2)	V_0	standard control volume (mm^3)
N_f	the number of stress cycles to failure	V_s	control volume for prospective fatigue failure (mm^3)
ODA	Optically Dark Area	α	$0.226 + HV \times 10^{-4}$
R	the stress ratio, $\sigma_{min}/\sigma_{max}$	γ	$\sqrt{area}_{ODA}/\sqrt{area}_{inclusion}$
		δ	scale parameter used in Extreme Value Theory
		λ	location parameter used in Extreme Value Theory
		σ	the stress acting on a specimen

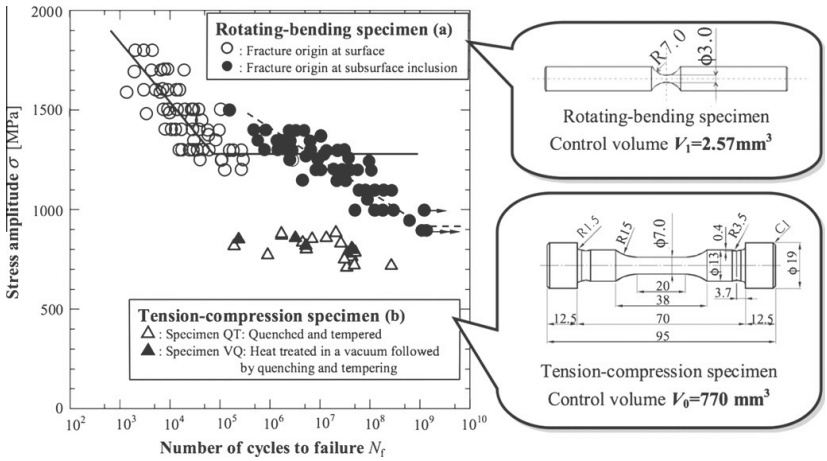

Fig. 1. The effect of different critical volumes tested on fatigue life properties. The figure compares the rotating bending (a), with tension–compression (b), *S–N* data of SAE52100 [8,11].

[8]. The type of heat treatment hardness and hydrogen content is shown in Table 1. To study the effect of the amount of hydrogen contained in the steel the difference between two series of specimen made from JIS SCM435 that have different amounts of hydrogen is discussed. The fatigue tests were performed with a stress ratio $R = -1$ and the test frequency $f = 1$–300 Hz. The tension–compression specimen shown in Fig. 1 is the test specimen used in the tests. The original reports for the material data and experimental procedures used as well as the results are written in the Refs. [1–3,7–10,2].

3. Theory

3.1. Factors affecting ultralong fatigue life

Fatigue fracture that occurs at ultralong fatigue lives in high strength steel has certain typical characteristics. These characteristics can be listed as follows:

(1) The nucleation of the fatigue crack originates at subsurface non-metallic inclusions. The inclusions have been shown to be Al_2O_3, $Al_2O_3{\cdot}(CaO)_x$, TiN, MnS [1,3,7,8]. An example of this kind of inclusion that has caused fatigue failure is shown in Figs. 2 and 3.

(2) The presence of an Optically Dark Area (ODA) next to the inclusion and the increase in the size of the ODA with longer fatigue lives. The correlation between the fatigue life and ODA size is shown in Fig. 2a–d. It is notable that the ODA is not present at short fatigue lives which can be seen from Fig. 2a [7].

(3) Experiments performed on test specimens with ultralow levels of hydrogen (~0.01 ppm hydrogen content) reveal smaller ODAs when compared with specimens with higher hydrogen content (0.7–0.8 ppm hydrogen content) with identical fatigue lives (N_f). Fig. 3 shows the fatigue fracture origin of test specimens that have been vacuum quenched to a low level of hydrogen content. The fracture surfaces of these specimens reveal that the relative size of the ODA to the inclusion is smaller than what is found on specimens with normal levels of hydrogen and having comparable fatigue lives such those shown in Fig. 2. The conclusion from this can be made that hydrogen content is directly connected to the formation of the ODA.

Table 1
Steel types and types of heat treatment as well as Vickers Hardness and Hydrogen content of the three series of specimen [1,8].

Materials	Series of specimens	Heat treatment	Vickers Hardness HV	Hydrogen content (ppm)
Cr–Mo steel (JIS SCM435)	QT	Quenched at 850 °C Tempered at 170 °C Carbonitrided	~561	0.7–0.9
	VQ	Heat treated in a vacuum at 850 °C followed by quenching Tempered at 170 °C Carbonitrided	~586	~0.01
Bearing steel, SAE52100 (JIS SUJ2)	QT	Quenched at 840 °C Tempered at 180 °C	~700	0.8

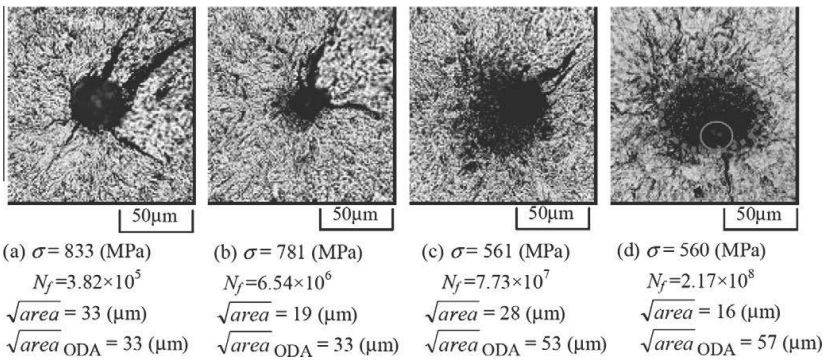

Fig. 2. The presence and size of the ODA is shown in the optical micrographs (a–d) of four different fracture surfaces of fatigue test specimen made form QT JIS SCM435, with a hydrogen content of 0.7–0.9 ppm. In picture (d) the ODA is circled with a blue dotted line and the inclusion with a red solid line [2]. (For interpretation of the references to colour in this figure legend, the reader is referred to the web version of this article.)

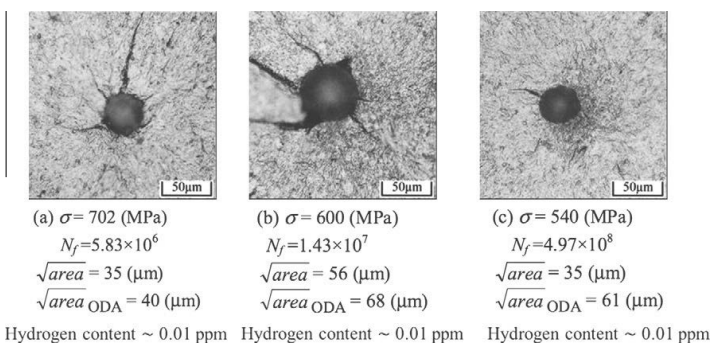

Fig. 3. The three pictures (a–c) are optical micrographs of fatigue fracture origins of fatigue test bars made from JIS SCM435 which has been vacuum quenched (VQ) to a low hydrogen content of 0.01 ppm [7].

(4) Examinations of the fracture surface of the ODA with Scanning Electron Microscopy (SEM), as well as with Atomic Force Microscopy (AFM) and laser microscopy show that the morphology of the fracture surface is rougher as well as being significantly different when compared with normal fracture surface morphology. This kind of examination is shown in Fig. 4 [5].
(5) Studies of the interaction of inclusions in steels with hydrogen in Ref. [12] have shown that non-metallic inclusions strongly trap hydrogen. The difference in the amount of hydrogen trapped by the inclusion on the fracture surface between QT and VQ specimens was studied in Ref. [4]. The results of these fracture surface studies with secondary ion imaging show trapped hydrogen around the inclusion for higher hydrogen levels (QT hydrogen content 0.7–0.9 ppm), and almost no trapped hydrogen for low hydrogen levels (VQ hydrogen content 0.01 ppm). These images are shown in Fig. 5.

This is a list of the main factors that are critical factors affecting fatigue failure of high strength steels in the ultralong fatigue life regime. Using these findings Murakami et al. proposed a model for ultralong life fatigue failure of high strength steels [2]. The schematic representation of this model is shown in Fig. 6. The

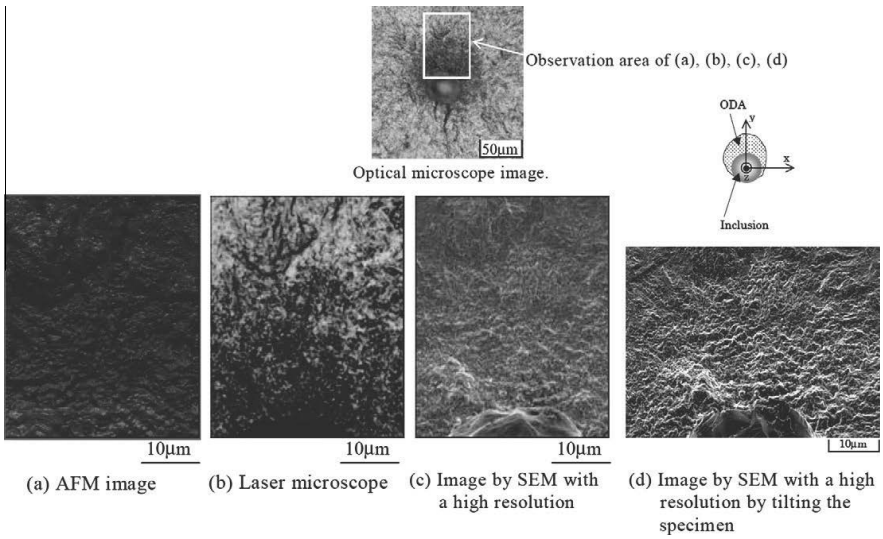

Fig. 4. Different imaging methods taken of an ODA surrounding an inclusion that was the site of fatigue fracture. Stress: 560 MPa, $N_f = 1.11 \times 10^8$, $\sqrt{area} = 29$ (μm), $\sqrt{area_{ODA}} = 55$ (μm) [5].

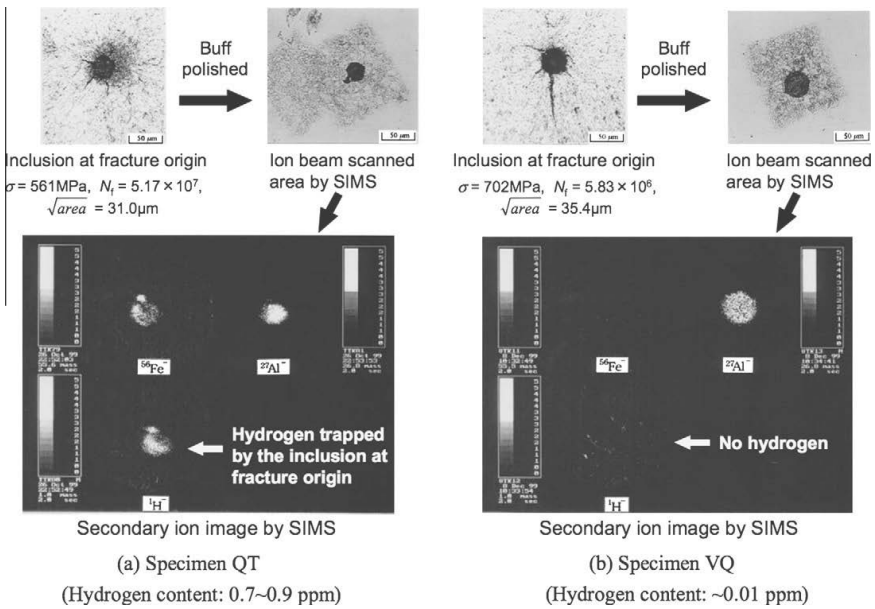

Fig. 5. The comparison of the amount of hydrogen trapped by the inclusion $(Al_2O_3(CaO)_x)$ located at the fracture surface. The images shown are secondary ion images as well as optical microscopy images of QT and VQ specimens [4].

model proposes that the growth of the ODA does not occur cycle by cycle as conventional fatigue crack growth; rather it is caused by the combined effects of hydrogen that is trapped by the inclusion along with the cyclical application of stress. The result of this is the subsequent formation of a crack that grows until it reaches the critical threshold for conventional fatigue crack growth that then causes fatigue failure.

To summarize: The process of ultralong fatigue failure in high strength steels is caused by non-metallic inclusions in the steel which are strong traps for hydrogen that is present in the steel. The inclusion and the trapped hydrogen cause ODA growth around the inclusion which causes crack growth to occur below the normal fatigue crack growth threshold of the steel. Once this hydrogen enhanced crack growth reaches the threshold for conventional

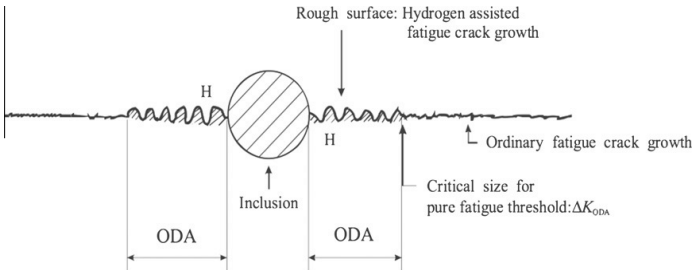

Fig. 6. A cross-section view of an inclusion and the ODA surrounding the inclusion.

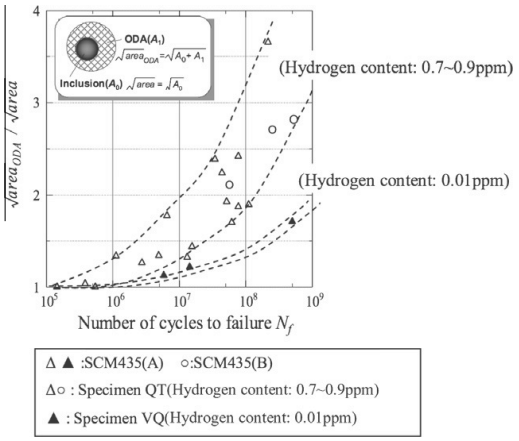

Fig. 7. The relationship of ODA growth normalized with respect to the inclusion size verses the number of fatigue cycles to failure for QT and VQ SCM435 [1].

fatigue crack growth, the specimen fails due to normal fatigue crack propagation.

3.2. Master curve for ODA

The presence of an ODA on a fracture surface around the subsurface inclusion that initiated fatigue crack growth has been studied for over a decade [10]. At present the formation and growth of ODA cannot be directly observed directly. Due to this, the subsequent method that has been used to determine the growth of the ODA experimentally is to perform ultralong fatigue tests and to study the fracture surface of failed specimens and record the size of the inclusion that caused fatigue failure along with the size of the ODA accompanying it. The results of these tests done on JIS SCM435 and SAE52100 are shown in Figs. 7 and 9 [1,13]. These figures show the ratio of $\sqrt{area_{ODA}}/\sqrt{area}$ with respect to an increasing fatigue life N_f. The difference between the QT JIS SCM435 specimens and the VQ JIS SCM435 specimens in Fig. 7 clearly shows the effect lower hydrogen content has on the resulting size of the ODA that is formed. The graph that shows the correlation between the ratio of the size of the ODA to the inclusion and the total fatigue life is called the master curve of ODA growth [1,12].

Using the relationship between the normalized ODA size and number of cycles to failure that is shown in Figs. 7 and 9, it is possible to estimate the growth of the ODA in a specimen from an inclusion using the estimated cycles to failure. For example using the ODA growth curve in Fig. 1. it is possible to estimate the relative ODA growth size for a specimen that fails at 10^7 cycles. The ODA growth would be: $\sqrt{area_{ODA}}/\sqrt{area} \approx 2$.

The conclusion that can be made based on the findings presented in Figs. 7 and 9 is that the ODA grows with increasing fatigue life as well as minimizing the amount of hydrogen in the steel decreases the rate of ODA growth. A schematic illustration of the growth of the ODA from the inclusions is presented in Fig. 8.

The effect of step loading has been tested by Murakami et al. [8]. The step loading tests were done using QT SAE52100 specimens that started testing at a certain stress level that was raised by 40 MPa after the fatigue test had run for 10^7 cycles. This was repeated until the specimen failed. The results of step loading tests for two specimens are given in Table 2. The process of the ODA growth is predictable from step to step by using the master curve for ODA growth shown in Figs. 7 and 9. The results for the step tests also show that step loading does not accelerate the growth of ODA, as can be seen in Fig. 9.

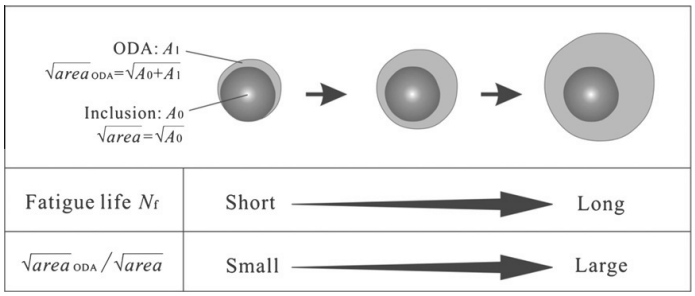

Fig. 8. The growth of ODA from inclusions with respect to fatigue life.

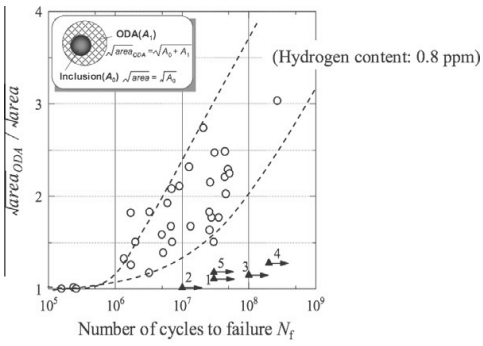

○▲: SAE52100
▲1 : Growth of ODA up to the third step (σ=760 MPa)
(σ= 680, 720, 760 MPa, $N = 1\times10^7 \rightarrow \sigma$=800 MPa)
▲2 : σ=720 MPa, $N = 1\times10^7 \rightarrow \sigma$=760 MPa, $N = 3.96\times10^6$
▲3 : σ=668 MPa, $N = 1\times10^8 \rightarrow \sigma$=982 MPa, $N = 1.48\times10^6$
▲4 : σ=667 MPa, $N = 2\times10^8 \rightarrow \sigma$=981 MPa, $N = 6.07\times10^6$
▲5 : σ=704 MPa, $N = 3\times10^7 \rightarrow \sigma$=978 MPa, $N = 2.00\times10^6$

Fig. 9. The relationship of ODA growth normalized with respect to inclusion size verses the number of fatigue cycles to failure for QT SAE52100 (JIS SUJ2) [13].

Table 2
Results of step loading fatigue tests [8].

Specimen NT1				
Growth of ODA (↓)				
Stress amplitude (MPa)	680	720	760	800
Number of cycles	1×10^7	1×10^7	1×10^7	3.06×10^6
$\sqrt{area}_{(\mu m)}$	29.9	$\sqrt{area}_{680}$	$\sqrt{area}_{720}$	$\sqrt{area}_{760}$
	↓	↓	↓	↓
$\sqrt{area}_{(\mu m)}$	$\sqrt{area}_{680}$	$\sqrt{area}_{720}$	$\sqrt{area}_{760}$	47.9
Specimen NT2				
Growth of ODA (↓)				
Stress amplitude (MPa)	720	760		
Number of cycles	1×10^7	3.96×10^6		
$\sqrt{area}_{(\mu m)}$	48.4	$\sqrt{area}_{720}$		
	↓	↓		
$\sqrt{area}_{(\mu m)}$	$\sqrt{area}_{720}$	71.7		

Using the data in Table 2 as well as other tests it is possible to compare ODA growth in step loading with ODA growth in constant amplitude loading. This can be done by using the Master Curve for the ODA shown in Fig. 10. For example for specimen NT1 the test began with a stress amplitude of 680 MPa, which is raised by 40 MPa after 10^7 cycles. This process is repeated until failure, that occurred at a cycle count of $N_f = 3.06\times10^6$, and a stress level of 800 MPa. The fracture origin is located at an inclusion that was surrounded by an ODA with a size of $\sqrt{area}_{ODA}$ = 47.9 μm, and the inclusion size is $\sqrt{area}_{inclusion}$ = 29.9 μm. Using these two values the ratio of ODA growth to the inclusion is calculated to be: $\sqrt{area}_{ODA}/\sqrt{area}_{inclusion} = 1.6$. Counting all of the cycles for all step loading levels for this test bar (NT1) gives a total fatigue life of 3.306×10^7. This fatigue life along with an ODA to inclusion ratio of 1.6 is similar to other test results from constant loading shown in Figs. 9 and 10. Furthermore the results of all the step loading tests that were performed show that the Master Curve

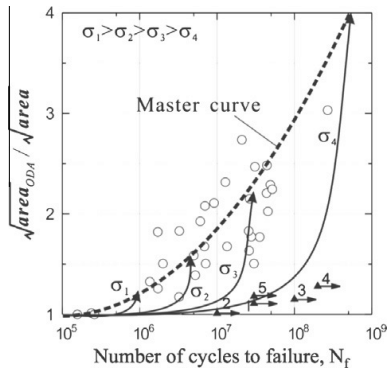

Fig. 10. The Master Curve of ODA growth calculated as the best fit curve for the data [12].

for ODA growth can be used to predict ODA growth for increasing step loading [13].

3.3. The statistical aspects of fatigue for high strength steels

The scatter in the fatigue strength of high strength steels is mostly caused by the scatter of the size of the inclusions that are in the specimen [14]. The scatter in the size of the inclusions present in the steel is caused by two main factors. The first factor is the volume of steel that is in question, and the second is the distribution of the inclusion sizes in the steel. The effect the volume has on lowering the fatigue limit can be seen in Fig. 1.

The distribution of inclusion sizes has been researched and a method for inclusion rating based on extreme value statistics has been developed [14–16]. This method can also be found in the ASTM standard E 2283-03 and can be implemented as follows:

(1) The maximum size $\sqrt{area_{max,j}}$ of the largest inclusion is determined for a standard inspection area S_o or volume V_o. This process is repeated n times and the resulting maximum inclusions are ranked as follows: $\sqrt{area_{max,1}} \leq \sqrt{area_{max,2}} \leq \cdots \leq \sqrt{area_{max,j}}$. The cumulative distribution function F_j(%) as well as the reduced variates y_j for the inclusion distribution are then calculated according to the following equations:

$$F_j = j \times 100/(n+1) \tag{1}$$

$$Y_j = -ln\{-ln[j/(n+1)]\} \tag{2}$$

(2) The maximum size $\sqrt{area_{max,j}}$ are then ploted according to the ranking that was done on a probability plot with the abscissa coordinates as $\sqrt{area_{max,j}}$ and the ordinate axis being either F_j or y_j. An example of this kind of a plot is shown in Fig. 11.

(3) As can be seen in Fig. 11 the reduced variate plotted against the $\sqrt{area_{max,j}}$ has a linear relationship. This relationship can be used to predict for a larger volume of steel. The linear relationship can be written as follows:

$$\sqrt{area_{max}} = a \cdot y + b \tag{3}$$

where $y = -ln\{-ln[j/(n+1)]\}$. To predict the maximum inclusion in an area S or volume V we get: $T = S/S_o$ or V/V_o and since we know that $T = 1/(1-F)$, so by using the previous equations we can write Eq. (3) as:

$$x(T) = b - a \cdot ln\{-ln[1 - 1/T]\} \tag{4}$$

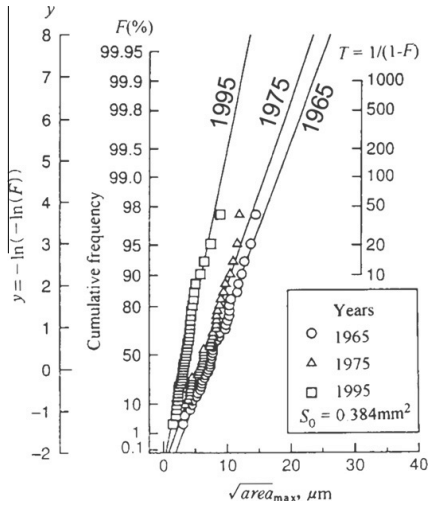

Fig. 11. The results show the improvement in production quality for SAE52100 steel for different years with respect to the distribution of the maximum inclusions in the steel [14].

This equation can be used to predict the largest inclusion in a given volume of steel. The parameters a and b are determined experimentally [14].

3.4. The threshold stress intensity factor range ΔK_{th} for ODA

The study of the threshold stress intensity factor range for small cracks has shown that the ΔK_{th} is not constant and is smaller when compared with the ΔK_{th} for large cracks [17–19]. The initiation of fatigue cracks from non-metallic inclusions in steels needs to be approached using ΔK_{th} theory and values for small cracks. The basic model for ultralong fatigue failure from non-metallic inclusions that has been reviewed here states that the ODA boarder is where conventional fatigue fracture begins after being initiated and propagated through the ODA by a synergistic effect between cyclic loading and hydrogen trapped by the inclusion.

In Ref. [14] Murakami proposes the following equation that uses the ODA size ($\sqrt{area}_{ODA}$) to calculate the stress intensity factor range for internal cracks.

$$\Delta K_{ODA} = 0.5 \cdot \Delta\sigma \cdot \sqrt{\pi\sqrt{area}_{ODA}} \tag{5}$$

where ΔK_{ODA} is MPa $\sqrt{m}$, $\Delta\sigma$ is in MPa, and $\sqrt{area}_{ODA}$ is in meters. Using this equation to calculate the ΔK_{ODA} gives results that fit well with the predictions made by the $\sqrt{area}$ parameter model when the $\sqrt{area}_{ODA}$ = 40–100 μm [14,17]. The results obtained with Eq. (5) are shown in Fig. 12. The solid line in Fig. 12 is the prediction of the ΔK_{th} that is calculated with the following equation:

$$\Delta K_{th} = 2.77 \times 10^{-3} \cdot (\mathrm{HV} + 120) \cdot (\sqrt{area}_{ODA})^{1/3} \tag{6}$$

where ΔK_{th} is MPa $\sqrt{m}$, HV is in kgf/mm^2, and $\sqrt{area}_{ODA}$ is in microns. This model has been verified in other high strength steels such as SAE52100 as well as a martensitic stainless steel [18].

The $\sqrt{area}$ parameter model can then be modified by using the $\sqrt{area}_{ODA}$ to calculate the fatigue limit. Eq. (7) gives a modified fatigue limit σ'_w for a stress ratio of $R = -1$ [14,17].

$$\sigma'_w = 1.56 \cdot (\mathrm{HV} + 120)/(\sqrt{area}_{ODA})^{1/6} \tag{7}$$

This equation can be used to normalize the S–N data of SCM435 as shown in Fig. 13. What is evident from Fig. 13 is that value σ/σ'_w is equal to, or greater than 1 for all results with the special exception of one test. Fig. 13 along with Fig. 12 support the model of ultralong fatigue life that has been reviewed in this paper by illustrating the link between the ODA size and ΔK_{th} for small cracks, along with the relationship between ODA size and fatigue limit.

4. Results

4.1. Design approach for ultralong life fatigue

To solve the problem of ultralong life fatigue from subsurface inclusions it is necessary to use new design approaches that take into consideration the growth of the ODA around the inclusion assisted by the presence of hydrogen. The ODA growth has a correlation with the total number of fatigue cycles to failure. This means that the design approach should incorporate the number of fatigue cycles to determine the survival of the component.

The design approach requires the following data:

(1) The maximum inclusion predicted for the volume of steel by statistics of extremes (see Fig. 11).
(2) The Master Curve of ODA, used to determine the growth of the ODA as a function of the fatigue life, N_f (see Fig. 10).
(3) The calculation of the threshold stress for the ODA size by using the $\sqrt{area}$ parameter model (see Fig. 12).

The design approach for ultralong fatigue life is outlined as follows:

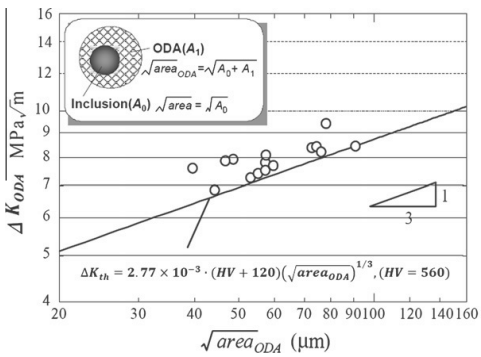

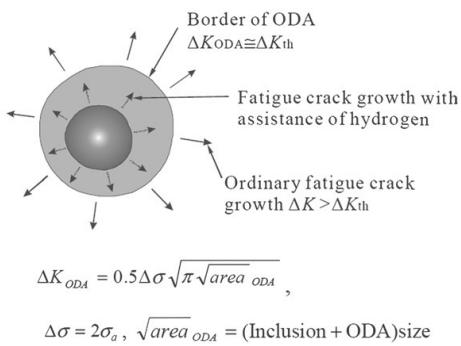

Fig. 12. The relationship between $\sqrt{area}_{ODA}$ and ΔK_{ODA} (Test specimen QT JIS SCM435) [18].

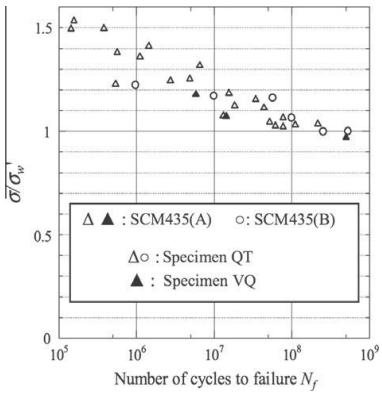

Fig. 13. *S–N* data of SCM435 normalized by using Eq. (7) [1].

(1) Start with the design life N_f that will be used for the component.
(2) Use the Master Curve of ODA growth along with the design life (N_f) to predict the relative growth of the ODA with respect to the maximum inclusion ($\sqrt{area_{ODA}}/\sqrt{area_{max}} = \gamma$).
(3) Calculate the maximum inclusion that is expected for the volume of steel equal to the component using the statistics of extremes method (determine $\sqrt{area_{max}}$).
(4) Use the relationship of ODA growth from step 2 ($\sqrt{area_{ODA}}/\sqrt{area_{max}} = \gamma$) along with the maximum inclusion calculated to occur in step 3 to calculate the size of the ODA ($\sqrt{area_{ODA}} = \gamma \cdot \sqrt{area_{max}}$).
(5) Use the $\sqrt{area_{ODA}}$ in the $\sqrt{area}$ parameter model to determine the allowable stress in the component: $\sigma_{allowable} = 1.56 \cdot (HV) + 120)/(\sqrt{area_{ODA}})^{1/6}$.

The allowable stress level that is calculated as a result of step 5 is the maximum stress allowed for the component in question. An illustration of this design approach is shown in Fig. 14 as a flow chart.

4.2. Design approach for ultralong life fatigue with step loading

Most components are subject to different types of loadings in service. Due to this it is important to create a design approach for ultralong fatigue lives that takes into consideration the use of multiple stress levels. This can be done by using the Master Curve of ODA growth along with the $\sqrt{area_{max}}$ of the inclusion predicted as well as the stress levels ($\sigma_1, \sigma_2, \ldots, \sigma_n$) and their respective number of cycles ($n_1, n_2, \ldots, n_n$).

Once the stress levels along with the respective number of cycles are determined for the component in question, it is necessary to combine these with the data of the ODA growth from the master curve and with the maximum inclusion predicted for the volume of the component. This information is then compared with the prediction of the critical crack size that will cause normal fatigue crack growth. This is done by using the following equation:

$$\sqrt{area_c} = \left(\frac{1.56 \cdot (HV + 120)}{\sigma}\right)^6 \tag{8}$$

Eq. (8) is derived from Eq. (7) and uses the applied stress amplitude, σ in MPa, as well as the micro hardness HV in kgf/mm^2 of the steel to calculate the critical size of an inclusion or defect $\sqrt{area_c}$ in μm that will initiate conventional fatigue crack growth. Using this critical inclusion size it is possible to calculate the amount of ODA growth needed to initiate normal fatigue crack growth. This calculation is done by calculating the ratio $\gamma(\sigma)$ of the critical size needed for fatigue crack growth ($\sqrt{area_c}$) with the maximum size of the inclusion for the volume of steel that is being used as shown in the following equation:

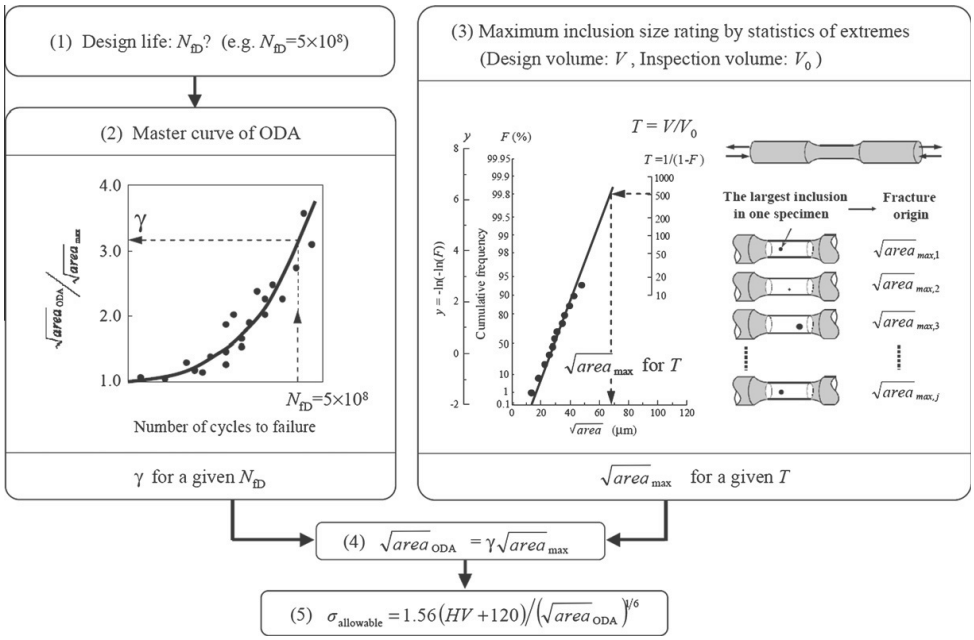

Fig. 14. The design approach illustrated as a flow chart for ultralong life fatigue.

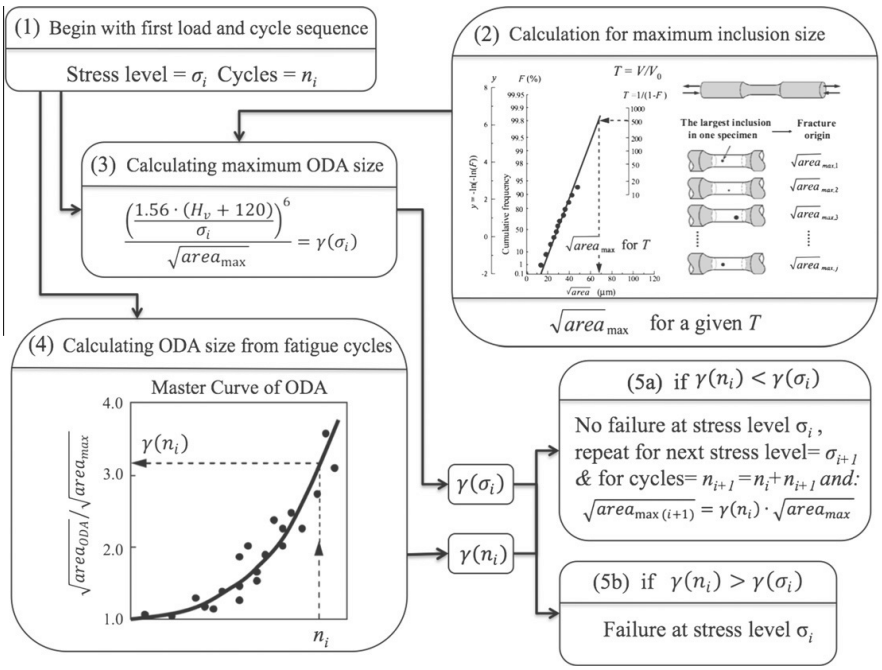

Fig. 15. The design approach for ultralong fatigue life in high strength steels.

$$\gamma(\sigma) = \sqrt{area_c}/\sqrt{area_{max}} \tag{9}$$

Using Eq. (9) it is possible to estimate the number of cycles to failure due to ODA growth by using the Master Curve of ODA growth.

The master curve that is shown in Fig. 10 represents the relative growth of the ODA corresponding to different fatigue lives. Using the curve shown in Fig. 10 along with the multiple step loading results that are presented in Fig. 9 as well as in Table 2 it is possible to propose the use of the Master Curve of ODA growth for use in the design of multiple step loading for increasing stress levels. The reason this can be done is due to the fact that the results of ODA growth in these step loading tests fit the expected trend of ODA growth for specimens that were not subjected to step loading. Therefore the following design approach for step loading for ultralong fatigue life of high strength steels is proposed:

(1) Begin with the first stress level σ_1 and number of cycles n_1.
(2) Calculate the maximum inclusion size for the steel volume in question
(3) Calculate the maximum allowable growth of ODA using Eq. (9) for the first stress level.
(4) Use the Master Curve of ODA to predict the growth of ODA due to the amount of cycles.
(5) Compare the ODA growth from cycles to the maximum allowable from step 3.
If ODA growth is greater than step 3 the result is failure.
If ODA growth is less than step 3 then repeat the process starting from step 1, with cycles $n_2 = n_1 + n_2$ and the stress level = σ_2.
This design approach is illustrated in Fig. 15.

5. Conclusions

A design approach for ultralong fatigue life with step loading is introduced in this paper. The design approach is constructed on the following elements:

1. The Master Curve of ODA growth with respect to the number of fatigue cycles.
2. The estimation of the largest inclusion present in the volume of steel under fatigue loading.
3. The calculation of the critical crack size that will initiate conventional fatigue crack growth according to the $\sqrt{area}$ parameter model.

This design approach can be used to determine the maximum allowable stress for a given design life without step loading as shown in Fig. 14, or as according to Fig. 15 these elements can be used to calculate the number of steps and cycles that will cause failure. The proposed design approach shown in Fig. 14 has been used successfully in the design of a half toroidal type transmission, CVT, for automobiles [19].

Acknowledgments

The research has been supported by the research Project FATEDEFEX in Finland and by the NEDO Fundamental Research Project on Advanced Hydrogen Science (2006–2012) in Japan.

References

[1] Murakami Y, Nomoto T, Ueda T, Murakami Y. On the mechanism of fatigue failure in the superlong life regime ($N > 10^7$ cycles). Part 1: influence of

hydrogen trapped by inclusions. Fatigue Fract Eng Mater Struct 2000;23:893–902.
[2] Murakami Y, Nomoto T, Ueda T. Factors influencing the mechanism of superlong fatigue failure in steels. Fatigue Fract Eng Mater Struct 1999;22:581–90.
[3] Murakami Y, Nomoto T, Ueda T, Murakami Y. On the mechanism of fatigue failure in the superlong life regime ($N > 107$ cycles). Part II: influence of hydrogen trapped by inclusions. Fatigue Fract Eng Mater Struct 2000;23:903–10.
[4] Murakami Y, Nomoto T, Ueda T, Murakami Y. Acceleration of superlong fatigue failure by hydrogen trapped by inclusions and elimination of conventional fatigue limit. Tetsu-to-Hagane 2000;86:777–83.
[5] Ueda T, Murakami Y. Effect of hydrogen on ultralong life fatigue failure of a high strength steel and fracture morphology of ODA. Trans Jpn Soc Mech Eng, Series A 2003;69:908–15.
[6] Murakami Y, Nomoto T, Ueda T, Murakami Y, Ohori M. Analysis of the mechanism of superlong fatigue failure by optical microscope and SEM/AFM observations. J Soc Mater Sci Jpn 1999;48:1112–7.
[7] Murakami Y, Konishi H, Takai K, Murakami Y. Acceleration of superlong fatigue failure by hydrogen trapped by inclusions and elimination of conventional fatigue limit. Tetsu-to-Hagane 2000;86:777–83.
[8] Murakami Y, Yokoyama NN, Nagata J. Mechanism of fatigue failure in ultralong life regime. Fatigue Fract Eng Mater Struct 2002;25(8–9):735–46.
[9] Murakami Y, Nagata J. Influence factors of fatigue design in ultralong life regime and effect of hydrogen on fatigue strength of high strength steel. Trans Jpn Soc Mech Eng, Series A 2005;70:1093–101.
[10] Murakami Y, Nagata J. Effect of hydrogen on high cycle fatigue failure of high strength steel, SCM435. J Soc Mater Sci Jpn 2005;54:420–7.
[11] Sakai T, Takeda M, Shiozawa K, Ochi Y, Nakajima M, Nakamura T, et al. Experimental reconfirmation of characteristic *S–N* property for high carbon chromium bearing steel in wide life region in rotating bending. J Soc Mater Sci Jpn 2000;49:779–85.
[12] Takai K, Homma Y, Izutsu K, Nagumo M. Identification of trapping sites in high-strength steels by secondary ion mass spectrometry for thermally desorbed hydrogen. J Jpn Inst Metals 1996;60:1155–62.
[13] Nagata J, Murakami Y. Factors influencing the formation of ODA in ultralong fatigue regime. J Soc Mater Sci Jpn 2003;52:966–73.
[14] Murakami Yukitaka. Metal fatigue: effects of small defects and nonmetallic inclusions. Oxford: Elsevier Ltd.; 2002.
[15] Beretta S, Murakami Y. Statistical analysis of defects for fatigue strength prediction and quality control of materials. Fatigue Fract Eng Mater Struct 1998;21:1049–65.
[16] Beretta S, Murakami Y. Largest-extreme-value distribution analysis of multiple inclusion types in determining steel cleanliness. Metall Mater Trans B 2001;32:517–23.
[17] Murakami Y, Endo M. Effect of hardness and crack geometry on delta K threshold of small cracks. J Soc Mater Sci Jpn 1985;35:911–7.
[18] Nagata J, Guy N, Murakami Y. Effect of hydrogen charge of fatigue strength of martensitic stainless steel. J Soc Mater Sci Jpn 2005;54:1217–24.
[19] Machida H, Murakami Y. Development of the Half Toroidal CVT POWERTOROS UNIT. NSK Tech J 2000;669:9–20.

Publication III

A. Roiko, J. Solin, Measurement of small cracks initiating from inclusions, Focused Ion Beam notches and drilled holes, International Journal of Fatigue, Volume 62, May 2014, Pages 154-158, ISSN 0142-1123

International Journal of Fatigue 62 (2014) 154–158

Contents lists available at SciVerse ScienceDirect

International Journal of Fatigue

journal homepage: www.elsevier.com/locate/ijfatigue

Measurement of small cracks initiating from inclusions, Focused Ion Beam notches and drilled holes

A. Roiko *, J. Solin

VTT Technical Research Centre of Finland, P.O. Box 1000, FI-20044 VTT, Espoo, Finland

ARTICLE INFO

Article history:
Received 16 November 2012
Received in revised form 23 January 2013
Accepted 17 March 2013
Available online 27 March 2013

Keywords:
Small crack
Initiation
Focused Ion Beam
Defect
Threshold

ABSTRACT

The focus of this study is small crack initiation, growth and arrest from small defects in quenched and tempered steels. To study the initiation and growth threshold of microcracks from small defects a specialised test method was developed. Round bars were axially loaded at $R = -1$ and fatigue initiators were manufactured by drilling ($\varnothing$ 50 μm) and Focused Ion Beam (FIB) milling (a = 10–50 μm). The specimens were fatigued at the range of the smooth specimen fatigue limit. The initiated microcracks were monitored to observe crack initiation; growth and arrest. The high correlation of the FIB small crack growth results with inclusion test results indicates that using a FIB notch to initiate small cracks is a good way to test small crack growth in high strength steels.

1. Introduction

In fatigue of high strength steels the early growth mechanisms, paths and rates of the microstructurally small cracks are not well known. Small cracks tend to initiate from stress concentrations or the largest non-metallic inclusions within the stressed volume of modern high strength steels. Fatigue crack nucleation and growth from surface or subsurface non-metallic inclusions in steels is of importance in many industries. It has been the focus of many studies [1–6] and a book by Murakami [7] However, many questions still remain relating to the initiation and growth of microstructurally small cracks in high strength steels. Recent studies have used FIB milling to create small notches into different materials to study the growth of small cracks emanating from notches[8–18]. In this study we apply this method to smooth specimens and investigate the relevance of using FIB notches as small crack initiators. They are applied to measure small crack growth thresholds and are compared to small defects such as non-metallic inclusions in the steel.

2. Experimental method

In this study axial fatigue tests were performed for quenched and tempered wrought steel 34CrNiMo6 with 1065 MPa and 1180 MPa yield and tensile strengths respectively. The martensitic microstructure of the steel normal to the forging direction is shown in Fig. 1. The test bars were machined from the centreline of Ø35 mm wrought bars. The test bar dimensions are shown in Fig. 2.

Fatigue tests for all specimens were performed using a Rumul pulsator in laboratory conditions at room temperature with resonant frequencies that varied from 100 to 200 Hz. For the ultra long fatigue tests resonant frequencies close to 200 Hz were used. The lower frequency ($\geqslant$104 Hz) were applied for the testing of notched specimen. Small fatigue initiators were manufactured by drilling ($\varnothing$50 μm) and FIB milling (a = 10–50 μm) into the test bars as shown in Fig. 2. The size of the FIB notches and drilled holes were chosen so that they could be compared to the natural occurring defects in the steel typically ranging from 10 to 40 μm. The maximum notch size of 50 μm was chosen to exceed the largest natural defect that we observed in over 50 test specimen. The FIB milling was done with a FEI Helios Nanolab dual focused beam system. The FIB was set to a voltage of 30 kV and a milling current of 21 nA was used. The pattern was defined in a diamond shape seen in Fig. 3e and f and Fig. 4 with a notch height typically of 5–10 μm.

The growth of small cracks was also studied using one special multi-notch test bar into which was milled altogether 20 small FIB notches in five rows and each row having four notches of 40, 30, 20, and 10 μm in length. An overview of the layout of the notches is given in Fig. 2 and a SEM picture of one of these notches is shown in Fig. 4. The distance between notches was greater than 390 μm and the test was stopped before the cracks grew to a size larger enough to interact in any major way. A mixed distribution round the specimen was applied to avoid systematic errors e.g. due to bending. Afterwards, the results proved that no bending

* Corresponding author. Tel.: +358 401451737.
E-mail addresses: andrew.roiko@vtt.fi (A. Roiko), jussi.solin@vtt.fi (J. Solin).

0142-1123/$ - see front matter © 2013 Elsevier Ltd. All rights reserved.
http://dx.doi.org/10.1016/j.ijfatigue.2013.03.010

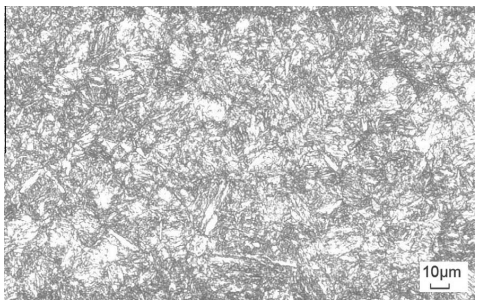

Fig. 1. Microstructure of the steel studied taken normal to the forging direction.

occurs or interaction occurs. The notched specimen was fatigued for 10,000 or 20,000 cycles at a time and then carefully studied by SEM to observe crack initiation and growth. The test was conducted at $R = -1$ and at a constant amplitude of 590 MPa. The stress range applied in the tests was close to the fatigue limit of the steel which was determined from SN test data of 30 specimen to be around 570 MPa. Therefore the crack growth behaviour which was observed corresponds to crack growth rates near the threshold for crack growth initiation and arrest.

The small holes and notches were monitored optically during the tests to detect small crack initiation and growth. Once the test bar failed or the test was complete it was examined with SEM, laser and optical microscopes. Sometimes the test bars failed from some other location such as an inclusion. Then the nucleation site was studied with a SEM and the type, size, and shape of the nucleation site was recorded. An overview of the test method is shown in Fig. 3.

3. Calculation of stress intensity factors

Two different types of measurements are reported in this paper. One type of measurements was done from the fracture surfaces (Figs. 7 and 8). These results are analysed and presented using the $\sqrt{\text{area}}$ of the small crack and/or initiating defect on the cross-section normal to the stress. The threshold for crack growth or initiation for the different sizes of notches, holes and inclusions were calculated by using the following equation [7]:

$$\Delta K_{th} = 0.65 \cdot \Delta\sigma \cdot \sqrt{\pi\sqrt{\text{area}}} \quad (1)$$

The other type of measurement was observed during testing, either in situ or during interrupted loading (Figs. 5 and 6). These results are reported as crack lengths on the specimen surface. The length of the surface crack was used to calculate the stress intensity factor range for the FIB notch test bar by using the following equation:

$$\Delta K_{th} = 0.65 \cdot \Delta\sigma \cdot \sqrt{\pi a} \quad (2)$$

In Eq. (2) the variable 'a' is from the observed crack length of '$2a$'. Any crack solution becomes arbitrary, because continuum fracture mechanics are no longer valid in the studied dimensions. The same shape factor (0.65) was applied in both equations. This shape factor value is arbitrarily selected within a wide range of values generally used in literature [19]. Its value just affects the horizontal axis scale position in Fig. 6. In geometrical terms this would equal to an aspect ratio of $\frac{a}{c} = \pi/2$, where c is crack depth of a semi-elliptical crack.

4. Results

4.1. Multi-notch specimen (FIB)

The test bar with 20 small FIB notches gave a large and interesting set of results, because crack growth was observed in almost all notches irrespective of their different sizes. The observed crack growth is shown in Fig. 5.

The data in Fig. 5 can be used to calculate the crack growth rate versus the stress intensity factor range. This was done by averaging the crack growth rate as well as the stress intensity factor range over each observation interval. These results are illustrated in Fig. 2 where they are separated into original notch sizes. To illustrate the variation of growth rate along the cycle count, another grouping of the same data is also shown in Fig. 6.

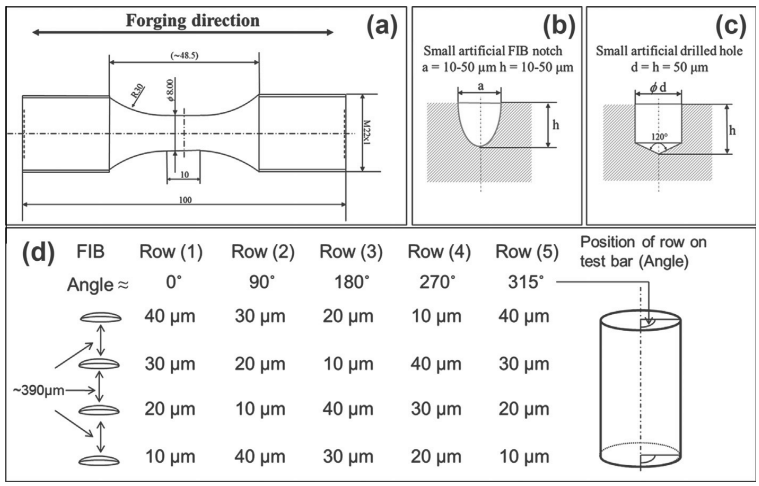

Fig. 2. The dimensions of the test bar are shown in (a) with the shape, size, and types of holes made in the side of the test bars shown in (b and c). The postions and placement of the FIB notches with respect to the test bar are shown in part (d) for the multi-notch test bar that was tested with 20 FIB notches.

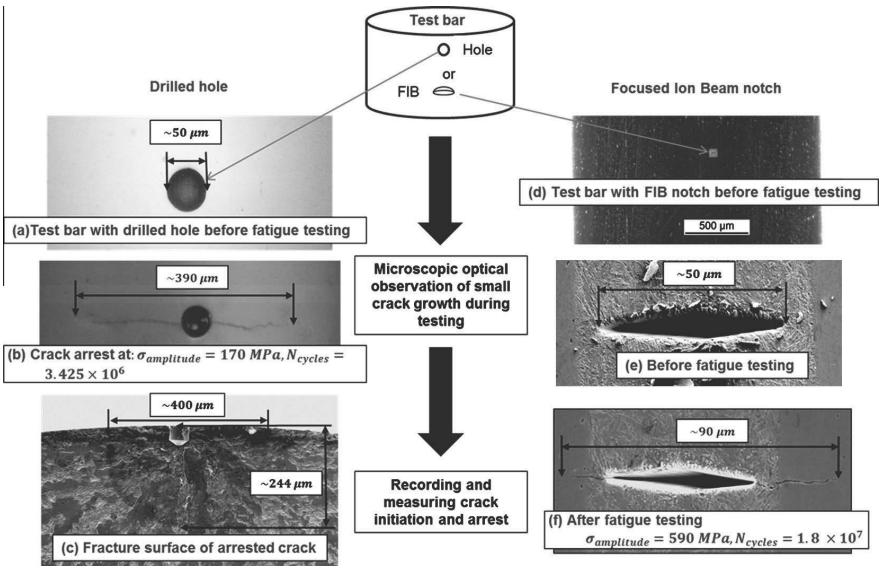

Fig. 3. The test setup and method for measuring small crack growth from notches and holes. The parts (a) through (c) show the procedure used for drilled holes and (d) through (f) show the procedure used for FIB notches. A higher stress amplitude of 200–230 MPa was used to cause failure of the test bar and there by the fracture surface of the specimen shown in part (c).

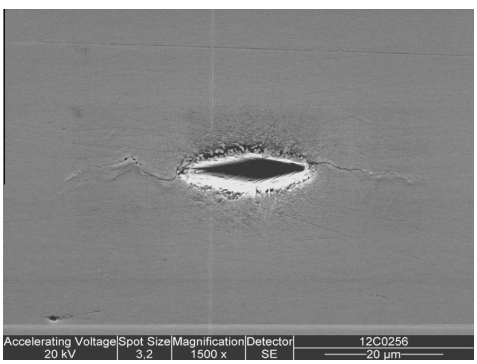

Fig. 4. A 20 μm FIB notch in row 3 milled into the side of a test bar after 50,000 cycles of fatigue testing.

4.2. Different types of notches or defects

Data on crack initiation threshold was accumulated also through fractography of many specimens tested near the fatigue limit of the steel. A large set of test data for a different batch of the same steel type was available from a previous project [20]. Results of five specimens in that set are used here for comparison. They exhibited crack initiation at an inclusion just breaking the specimen surface after more than 10 million fatigue cycles. This data is plotted in Fig. 7, where a comparison can be made between different defects initiating a fatigue crack near the fatigue threshold.

The data used to calculate the stress intensity factor for the inclusion data points is the inclusion size and the stress level at which the test bar failed. The FIB data points are at the stress level at which the crack initiated and then arrested. Two of the drilled hole points represent crack initiation at the hole. Precracking with compressive mean stress was introduced to one of them.

The same data shown in Fig. 7 is also plotted with respect to the stress amplitude of the fatigue test compared to the initiating defect size. This is shown in Fig. 8. Trend lines for constant stress amplitude and constant ΔK are also shown.

5. Discussion

The experimental results of this study are in agreement with the general results that have been published in earlier studies [15–17,11,18,19]. The variability along with the faster growth rate of small cracks is evident in Fig. 6. This variability shown in Fig. 6 is

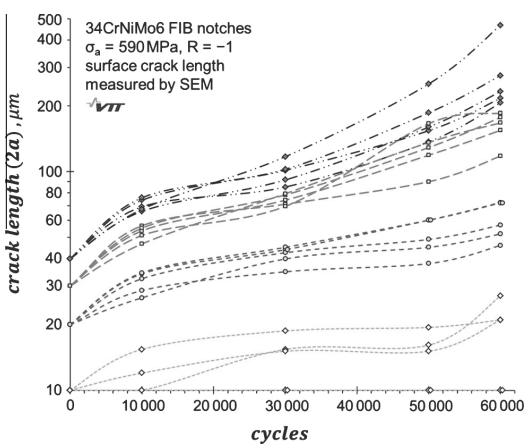

Fig. 5. Growth of small cracks from 10, 20, 30 to 40 μm sized FIB milled notches (5 of each).

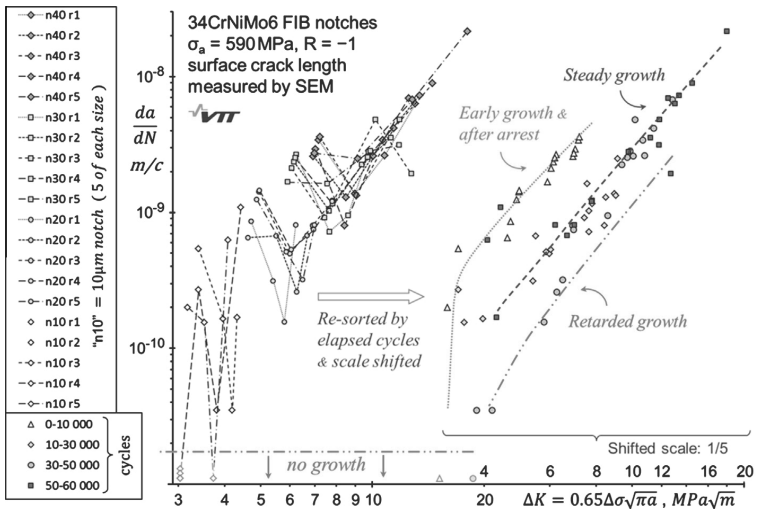

Fig. 6. Crack growth rate curves based on data in Fig. 5. On right the same data sorted according to phase of test.

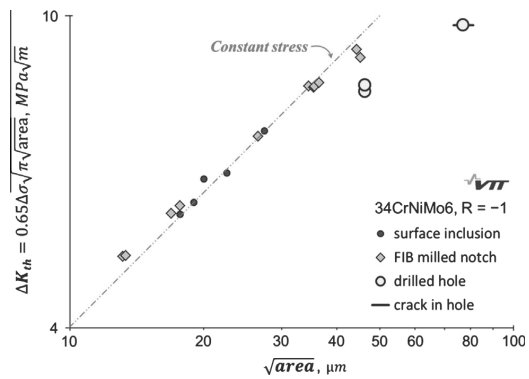

Fig. 7. The stress intensity range vs. the square root area of the initiator at the growth threshold condition (≈fatigue limit) for different types of notches.

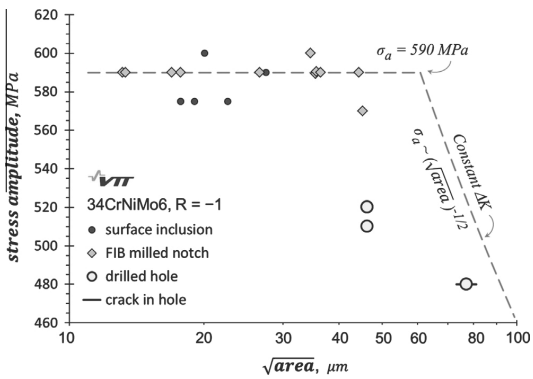

Fig. 8. The same data as in Fig. 7: fatigue limit as function of initiator size.

interesting due to the fact that it is the results of reliable measurements obtained with a SEM and that all the data in this figure comes from one fatigue test bar. Therefore the results provide a good picture of the inherent scatter of small crack growth that occurs in the microstructure since other variables such as different specimen variability along with possible changes in testing conditions could not contribute to the results.

The organisation of the data in Fig. 6 according to cycles count shows the variation between slow and fast crack growth. The data shows that the cracks grow at faster rates either as they initiate or after they start to grow again after an arrest. It also shows that the growth rate turns into a steady state of growth once the crack grows large enough.

The good correlation between the inclusions and FIB notch thresholds shown in Fig. 7 is a good indication that the use of FIB notches as initial defects is a good and relevant way to test the initiation and growth of small cracks in high strength steels. This is seen as well in Fig. 8 where the correlation between defect or crack size versus the stress amplitude shows that there is no decreasing trend for the inclusions or the FIB milled notches. Rather all these data points are close to the fatigue limit, which means that the studied defect sizes are below the limit for decreasing fatigue limit as function of defect size. The thresholds obtained for the drilled holes indicate that such holes act well as conservative simulations of inclusions. One difference besides the shape in between the FIB milled notches and the drilled holes are the residual stresses that are introduced by the mechanical removal of material. The ability to quantify or measure this difference is difficult. The other important contributing factor of drilled holes is the difference in shape from the FIB milled notches. The holes used in this study are equal in depth as in width whereas the FIB notches have a smaller depth when compared to width. The drilled hole will also concentrate the stress into a larger area when compared to the notch due to geometrical factors which means that crack growth will more likely occur when considering a weakest link approach. This means that the size of the volume of material affected by the stress concentration of the hole is larger than that of the notch. Other shape differences include the sharp corners in the drilled hole which may play a crucial role in early crack initiation and growth. Such mechanically made sharp corners are not present in FIB milled notches.

6. Conclusions

The use of FIB notches as small crack initiators in round test bars provides a reliable method of obtaining small crack growth data that correlates well with results from test bars that failed from non-metallic inclusions. The microscopic observation of small crack growth from FIB notches during testing is a useful test method for small crack growth observation and can provide results for many loading ratios. The results are in line with previous studies of small crack growth showing a large variability in the growth rate as well a decrease in crack size that corresponds with a decrease in ΔK required for initiation.

Acknowledgements

This research was part of three consecutive research projects: FATE-DEFEX, MACY, and SCAR-FACE funded by the Finnish Funding Agency for Technology and Innovation TEKES, VTT and industry.

References

[1] Duckworth WE, Ineson E. The effects of externally introduced alumina particles on the fatigue life of En24 steel. Clean Steel 77 (Iron Steel Inst.) 1963:87–103.
[2] Murakami Y, Endo M. Quantitative evaluation of fatigue strength of metals containing various small defects or cracks. Eng Fract Mech 1983;17:1–15.
[3] Murakami Y, Kodama S, Konuma S. Quantitative evaluation of effects of non-metallic inclusions on fatigue strength of high strength steels. I: Basic fatigue mechanism and evaluation of correlation between the fatigue fracture stress and the size and location of non-metallic inclusions. Int J Fatigue 1989;11:291–8.
[4] Murakami Y, Usuki H. Quantitative evaluation of effects of non-metallic inclusions on fatigue strength of high strength steels. II: Fatigue limit evaluation based on statistics for extreme values of inclusion size. Int J Fatigue 1989;11:299–307.
[5] Murakami Y, Endo M. Effects of defects, inclusions and inhomogeneities on fatigue strength. Int J Fatigue 1994;16(3):163–82.
[6] Murakami Y, Beretta S. Small defects and inhomogeneities in fatigue strength: experiments, models and statistical implications. Extremes 1999:123–47.
[7] Murakami Y. Metal Fatigue: Effects of Small Defects and Nonmetallic Inclusion. Kyushu University: Elsevier; 2002.
[8] Marx M, Schäf W, Vehoff H, Holzapfel C. Interaction of microcracks with selected interfaces: Focused ion beam for a systematic crack initiation. Mater Sci Eng A 2006:595–601.
[9] Motoyashiki Y, Brückner-Foit A, Sugeta A. Microstructural influence on small fatigue cracks in a ferritic–martensitic steel. Eng Fract Mech 2008;75:768–78.
[10] Holzapfel C, Schäf W, Marx M, Vehoff H, Mucklicha F. Interaction of cracks with precipitates and grain boundaries: Understanding crack growth mechanisms through focused ion beam tomography. Scripta Mater 2007;56:697–700.
[11] Tesch A, Pippan R, Trautmann K-H, Döker H. Short cracks initiated in Al 6013-T6 with the focused ion beam (FIB)-technology. Int J Fatigue 2007;29:1803–11.
[12] Motoyashiki Y, Brückner-Foit A, Sugeta A. Investigation of small crack behaviour under cyclic loading in a dual phase steel with an FIB tomography technique. Fatigue Fract Eng Mater Struct 2007;30:556–64.
[13] Schaef W, Marx M, Vehoff H, Heckl A, Randelzhofer P. A 3-D view on the mechanisms of short fatigue cracks interacting with grain boundaries. Acta Mater 2011;59:1849–61.
[14] Man J, Vystavel T, Weidner A, Kubena I, Petrenec M, Kruml T, et al. Study of cyclic strain localization and fatigue crack initiation using FIB technique. Int J Fatigue 2012;39:44–53.
[15] Menzel BC, Dauskardt RH. Fatigue damage initiation and growth from artificial defects in Zr-based metallic glass. Acta Mater 2008;56:2955–65.
[16] Roy MJ, Nadot Y, Nadot-Martin C, Bardin P-G, Maijer DM. Multiaxial Kitagawa analysis of A356-T6. Int J Fatigue 2011;33:823–32.
[17] Yang Y, Ruan HH, Lu J, Yao N, Shan WL, Soboyejo WO. Development of a micro-beam method to investigate the fatigue crack growth mechanisms of submicron-scale cracks. Exp Mech 2009;49:731–42.
[18] Tesch A, Pippan R, Trautmann K-H, Döker H. Short cracks initiated in Al 6013-T6 with the focused ion beam (FIB)-technology. Int J Fatigue 2007;29:1803–11.
[19] Couroneau N, Royer J. Simplified model for the fatigue growth analysis of surface cracks in round bars under mode I. Int J Fatigue 1998;20:711–8.
[20] Solin J, Alhainen J, Varis P. Ultra high cycle fatigue and inclusions in wrought steels. In: International symposium on fatigue design and material defects. Trondheim; 2011.

Publication IV

A. Roiko, J. Solin, T. Sarikka, H. Hänninen, The paths of small fatigue cracks in high-strength steels initiated from inclusions and small defects, Accepted at: Materials Performance and Characterization on 21.4.2017

ASTM INTERNATIONAL

Materials Performance and Characterization

A. Roiko,[1] J. Solin,[2] T. Sarikka,[3] and H. Hänninen[3]

DOI: 10.1520/MPC20160115

The Paths of Small Fatigue Cracks in High-Strength Steels Initiated from Inclusions and Small Defects

VOL. 6 / NO. 1 / 2017

Materials Performance and Characterization

doi:10.1520/MPC20160115 / Vol. 6 / No. 1 / 2017 / available online at www.astm.org

A. Roiko,[1] J. Solin,[2] T. Sarikka,[3] and H. Hänninen[3]

The Paths of Small Fatigue Cracks in High-Strength Steels Initiated from Inclusions and Small Defects

Reference

Roiko, A., Solin, J., Sarikka, T., and Hänninen, H., "The Paths of Small Fatigue Cracks in High-Strength Steels Initiated from Inclusions and Small Defects," *Materials Performance and Characterization*, Vol. 6, No. 1, 2017, pp. 1–16, https://doi.org/10.1520/MPC20160115.
ISSN 2379-1365

ABSTRACT

In fatigue, the early growth mechanisms, paths, and rates of the microstructurally small cracks are not well known. Growth of subsurface—undetected—cracks cannot be monitored in real time, and postfracture fractography is complicated because of the statistical nature of local microstructure. Furthermore, hammering or sliding often damages the fracture surface before the test is stopped. We addressed this challenge with two approaches. This paper deals with fractographic details connected to local microstructure obtained by milling and imaging with a focused ion beam in a scanning electron microscope (SEM). The results provided input such as crack growth on adjacent planes and their coalescence, as well as formation of the "optically dark areas" that play a key role in the early growth and initiation of small cracks in fatigue. A subset of data consisting of eleven 100Cr6 bearing steel specimens loaded at the same stress amplitude to lives in the range of $10{\cdot}10^6 < N_f < 650{\cdot}10^6$ are studied and discussed. The second test series revealed that very early initiation and crack arrest are typical for small notches in the 34CrNiMo6 QT steel. The relation of crack path and microstructure, along with their connection to the optically dark area, is discussed.

AQ1

Keywords

fatigue, small crack, non-metallic inclusion, optically dark area

Manuscript received May 31, 2016; accepted for publication April 21, 2017; published online xxxx xx, xxxx.

[1] VTT Technical Research Centre of Finland, Espoo 20044, Finland (corresponding author), e-mail: andrew.roiko@vtt.fi

[2] VTT Technical Research Centre of Finland, Espoo 20044, Finland

[3] Department of Engineering Materials, Aalto University School of Engineering, Espoo 20044, Finland

Nomenclature

ODA = Optically Dark Area
FIB = Focused Ion Beam
QT = Quenched and Tempered
GBF = Granular Bright Facet

Introduction

Fatigue crack initiation and growth from surface or subsurface non-metallic inclusions in high-strength steels is of importance in many industries. This has been the focus of many studies and, in particular, a book by Murakami [1]. One open question is a fracture surface feature commonly refered to as an optically dark area (ODA) or granular bright facet (GBF). This feature is found adjacent to the inclusion on the fracture surfaces of test specimen that failed in high and ultra high cycle fatiuge. The formation and cause of the ODA has been studied and researched in several papers. Some studies have found that hydrogen trapped around the nonmetallic inclusion provides an explanation for a cause of failure in ultra-long fatigue life of high-strength steel and the formation of the ODA [2–11]. However, there are yet questions about the characterization and prediction of initiation and growth of microstructurally small cracks in high-strength steels. Recently, some researchers have shown other factors such as the fact that the crack grows in a vacuum inside the test specimen or changes in the microstrucure around the inclusion [12–14]. Other studies have used focused ion beam (FIB) milling to create cross sections, after which FIB imaging is used to make ion channeling contrast pictures of the microstructure [14–17]. This imaging technique has been applied to small cracks in steels to study the profile in depth [15,18]. Researchers have recently used the FIB tools to show how the size and crystal orientation of the grains affect the growth and direction of small cracks from notches and inclusions in the steel [14,15]. In this paper, these tools and techniques are used to study the role the martensite subgrain microstructure has on the initiation and growth of small fatigue cracks in high-strength steels from inclusions and notches.

In this study, the role of nonmetallic inclusions in a hard-bearing steel (100Cr6) and a quenched and tempered (QT) steel (34CrNiMo6) are examined. The inclusions promote subsurface crack initiation, which makes direct observation of initiation and early growth of cracks extremely challenging. A new technique used in this study is FIB milling, which is utilized to study the microstructure around an inclusion that has caused fatigue failure in the ultra-long fatigue life regime. This technique gives futher insight into the causes of these failures.

Introducing FIB-milled semielliptical notches simulates the situation, where fatigue relevant inclusions are on the specimen surface, and in this case the paths and growth of microcracks can be monitored. The fatigue testing that was done on the QT steel (34CrNiMo6) was near the endurance limit of the steel. The test specimens with FIB notches were also tested at or near the fatigue endurance limit of the steel. The growth and behavior of the small cracks from the FIB notches can then be compared with the crack paths of small cracks from nonmetallic inclusions that failed at or near the endurance limit. In the past, there have been various definitions used to define small cracks; however, for the purposes of this paper, we consider small cracks to be those that are less than 1 mm in length.

Experimental

Different batches of two steel types were studied. In this paper, we report results for a bearing steel of type 100Cr6 QT at 180°C to hardness 720 HV (tensile strength 1,630 MPa) and a QT 34CrNiMo6 steel with a hardness of 380 HV, and with 1,065 MPa and 1,180 MPa yield and tensile strength, respectively. The 100Cr6 bearing steel specimens (Fig. 1a) were taken from 1/4 depth of a ϕ70 mm wrought bar. The 34CrNiMo6 QT specimens according to Fig. 1b were machined from the centerline of ϕ35 mm wrought bars. Fig. 1c shows the orientation and location of the FIB notches. The left image in Fig. 1c shows the cross section of the FIB notch, which is perpendicular to the stress axis.

Axial fatigue tests for smooth and polished specimens were performed at resonant frequencies below 200 Hz. The fatigue life target area was in the UHCF (Ultra High Cycle Fatigue) region ($10^6 < N_f < 10^9$). Run-out specimens were broken at increased stress amplitudes and every fracture surface was studied. The statistics of fatigue-relevant inclusions in the 100Cr6 steel could be accurately studied because 94 % (80/83) of failures initiated from subsurface inclusions. However, in the 34CrNiMo6 QT steel, only 40 % of failures initiated within the volume of subsurface material. Smaller inclusions or unidentified origins may have played a role in 40 % of the failures initiated at the surface and 20 % immediately below the surface.

Artificial initiation sites were introduced to the 34CrNiMo6 QT steel specimens. Fatigue initiators were manufactured by FIB milling (a = 10 … 50 μm) and the specimens were fatigued at the range of the smooth specimen fatigue limit. These small notches were optically monitored and video recorded for crack initiation, growth, and arrest in real time. The small crack growth results are reported in Ref. [19]. The notches were later carefully examined with SEM and optical microscopes. Furthermore, cross sections of the cracks were milled with FIB and the crack paths within the microstructure were imaged and studied using incident ions, which is similar to SEM imaging, but only using ions instead

FIG. 1 Dimensions of the test bars: (a) for smooth bars only; (b) also for notches. (c) The shape, size, and type of notches made in the side of the test bars.

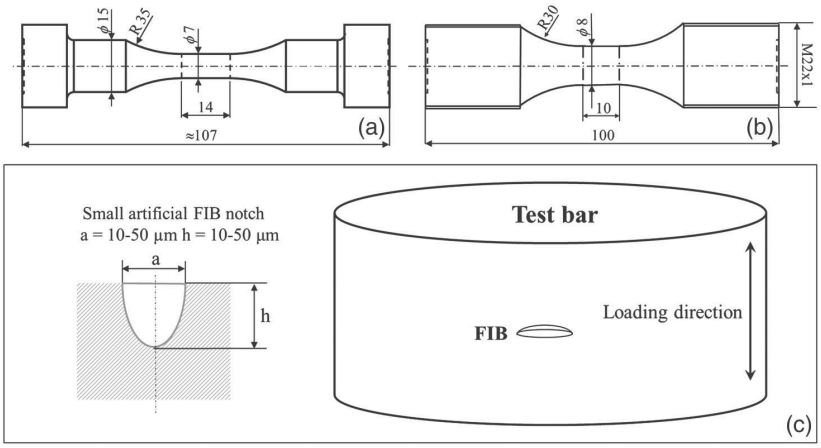

FIG. 2 (a) Microstructure of 34CrNiMo6 QT steel, and (b) microstructure of the 100Cr6 bearing steel. Both EBSD images are taken perpendicular to the loading direction of the test specimen.

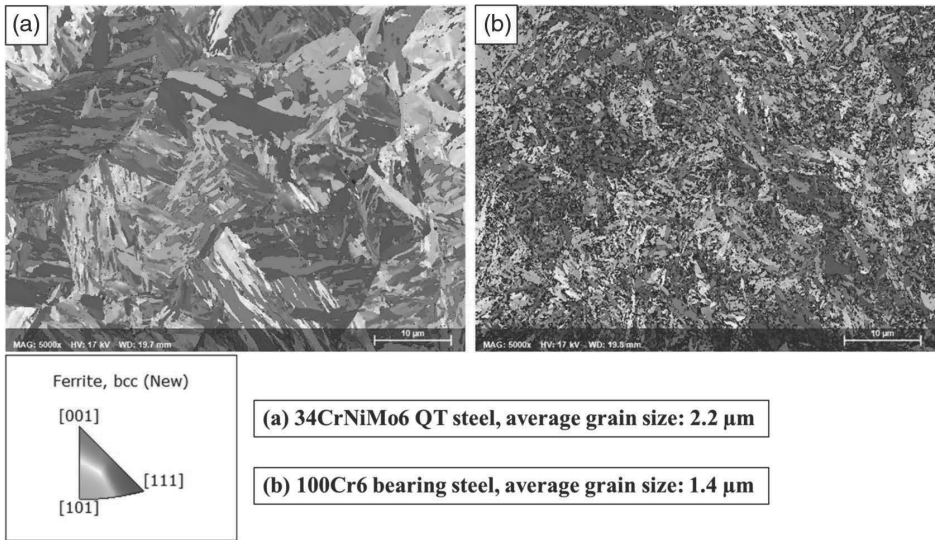

of electrons. Ion channeling obtains contrast images of the microstructure because the different orientation of the crystal lattice reflects the ions in different ways. If the crystal lattice spacing is larger or the orientation is preferential to ion absorption, it will appear darker, and conversely, brighter if the crystal lattice spacing is smaller or the orientation is more preferential to ion reflection. [20]

Electron BackScatter Diffraction (EBSD) images of the microstructure of the two steels studied are shown in Fig. 2. The average grain size is 2.2 µm for the 34CrNiMo6 QT steel, and around 1.4 µm for the 100Cr6 bearing steel. This average grain size of the ferrite grains is obtained based on the EBSD analysis. It should be noted that this is not the average grain size of the prior austenite grains (which is around 20 µm for the QT steel and around 7 µm for the bearing steel).

Results

CRACK PATHS IN QUENCHED AND TEMPERED 34CRNIMO6 QT STEEL—NOTCHES ON THE SURFACE

The crack shown in Fig. 3 shows a small fatigue crack growing from a FIB notch along the grain structure of the steel underneath the surface of the test specimen. In the figure, both (b) and (c) show how the location of the change in crack direction corresponds to a change in the general martensite lath or packet direction. The paths of the small cracks that grew from the FIB notches show a clear preference in growth direction along the martensite packets or laths in the prior austenite grains. Once the crack grew through one prior austenite grain, it changed direction and grew along the orientation of the martensite laths in the next prior austenite grain or martensite packet.

FIG. 3

A small crack growing from a FIB notch (a) with two turning points correlated with the subgrain microstructure (b, c). The stress ratio was R = –1 and the stress amplitude was 590 MPa. The test bar has been tested for 60,000 cycles and was made of 34CrNiMo6 QT steel. The loading direction is from the top to the bottom of the images.

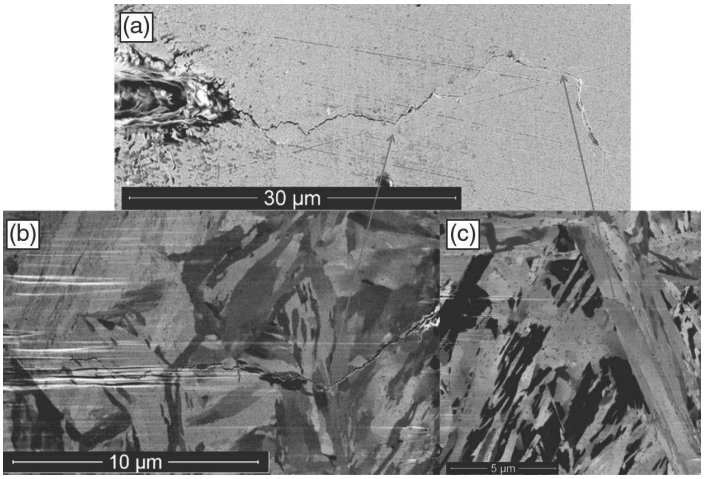

The general direction and rate of crack growth is affected by the microstructure besides the notch. Fig. 4 shows how a crack initiated from a FIB notch tends to grow along the direction of the martensite laths. In Fig. 4 the stress direction is from top to bottom of the figure. It is self-evident that the crack is propagating in a three-dimensional microstructure so it does not always follow exactly the specific martensite features. It does, however, change direction at clear points where the martensite microstructure also changes. This is seen most clearly in Fig. 3c where the crack turns almost 90° from the path that it

FIG. 4

The effect of martensite laths on the direction of small crack growth from a FIB notch. An overall surface view of the FIB notch with cracks (a). A subsurface cross section and FIB image of the subgrain structure affecting the crack growth (b). The stress ratio was R = –1 and the stress amplitude was 590 MPa. The test bar has been tested for 60,000 cycles, and made of 34CrNiMo6 QT steel. The loading direction is from the top to the bottom of the images.

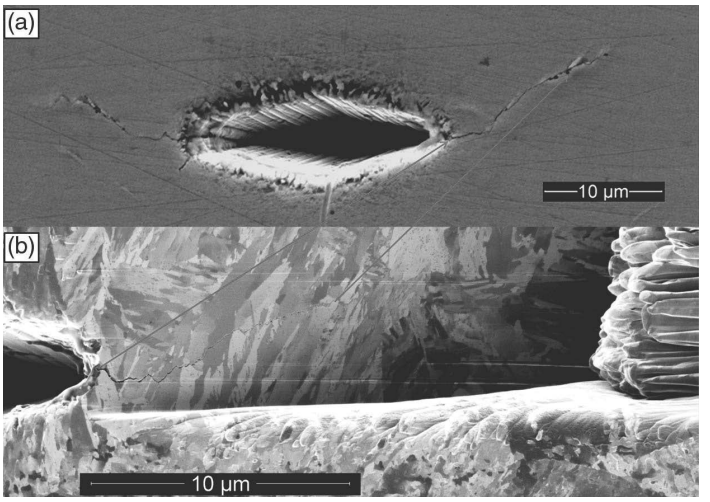

was traveling and follows a large martensite packet or lath that is orientated in the same direction. This shows that the local martensite structure has a definite influence on the growth direction and path of the small fatigue crack tested near the fatigue endurance limit.

Figs. 3 and 4 show how the growth of small cracks from notches is greatly affected by the local subgrain microstructure, namely, the orientation and size of the martensite laths along the path of the crack. The direction of the crack is angled up and does not grow perpendicular to the remote stress, which is acting from top to bottom of Fig. 4. When the microstructure is shown underneath the surface, it can be observed that the martensite laths are also angled up in the same general direction as the crack growth shown between the two arrows in Figs. 4a and 4b.

CRACK PATHS IN 34CRNIMO6 QT STEEL—SUBSURFACE INCLUSIONS

To study the microstructure and its eventual effects on crack growth from a nonmetallic inclusion, a long-life specimen was studied by cross sectioning the initiation site. First we introduce some reference observations, in particular, the fractographic feature ODA as defined by Murakami [1]. A comparison of observations on the same fracture surface by using different imaging techniques can be found in Ref. [7]. The images show an area of the fracture surface directly next to the inclusion that has an observably different topography than the rest of the surrounding fracture surface.

A smooth 34CrNiMo6 QT steel test bar was tested for $100{\cdot}10^6$ cycles at a stress amplitude of 550 MPa with an R-ratio of −1. The stress amplitude was then raised to 575 MPa and after $1.7{\cdot}10^6$ cycles at this stress amplitude the specimen failed. SEM and FIB images of the inclusion that caused the failure are shown in Figs. 5–7. The area corresponding to the definition of ODA is marked besides the inclusion.

FIG. 5 The nonmetallic inclusion that caused failure in a smooth test bar. Picture (a) is an ion image taken with a FIB, and picture (b) is taken of the opposite fracture surface with a SEM microscope. Picture (b) has been flipped for easier comparison to picture (a). Both pictures have the same ODA area circled. The stress ratio was R = −1 and the stress amplitude was 550 MPa. The test bar was tested for $100{\cdot}10^6$ cycles after which the stress level was raised to 575 MPa and the specimen failed after $1.7{\cdot}10^6$ cycles. This test bar was made of 34CrNiMo6 QT steel.

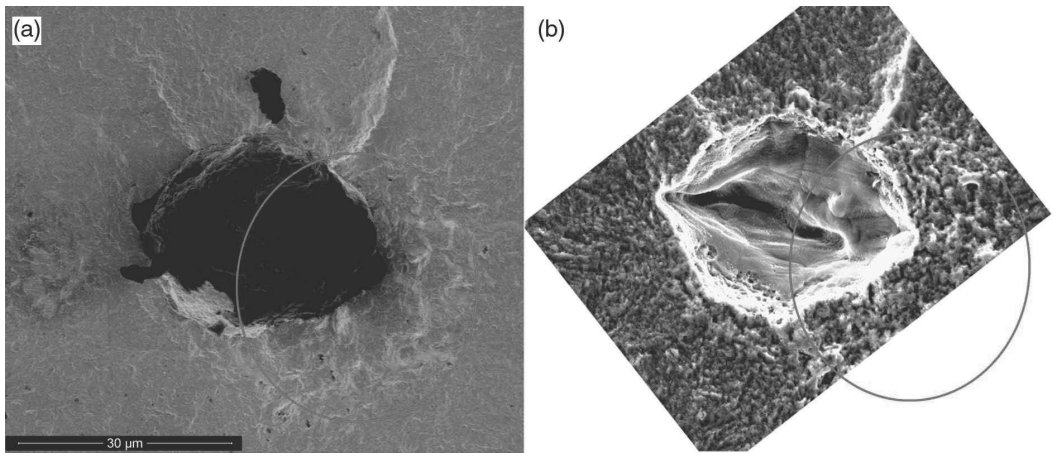

FIG. 6

The nonmetallic inclusion that caused failure in a smooth test bar. The part of the fracture surface circled by a black line is the ODA. This SEM picture was taken at an angle for a better topographic feature contrast.

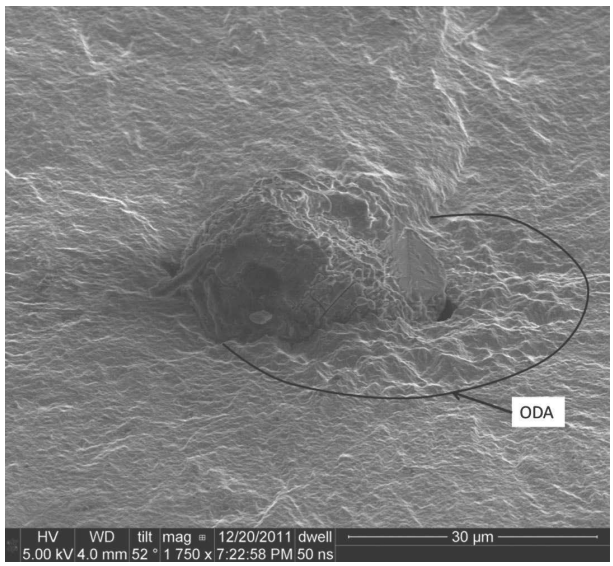

The two images in Fig. 5 show the opposing sides of the fracture surface obtained by different types of microscopy. Fig. 5a shows the fracture surface with the inclusion in an ion image, and the conventional SEM image in Fig. 5b shows the same location on the opposite fracture surface. Fig. 5b has been flipped and rotated so that it is easier to compare with the fracture surface in Fig. 5a. The length scale is the same for both images.

The inclusion and crack paths beside it were cut by FIB to see the microstructure below the fracture surface. The resulting cross section is shown in Fig. 7 and the images of the metal matrix on different sides of the inclusion are compared in Fig. 8.

In Fig. 8b we can observe local martensite structure near and adjacent to the surface located inside the ODA area. This local microstructure is orientated in the same direction as the crack growth. By comparison of Fig. 8a, which is outside of the ODA area on the other side of the nonmetallic inclusion, it can be seen that the microstructural features are smaller and not orientated as preferentially to the direction of crack growth as the microstructure in Fig. 8b. This supports the connection between small crack growth and the size, shape, and orientation of the microstructure and provides more information about the ODA area. It indicates that the formation of the ODA is connected to the initiation and growth of the small crack into the most preferential local microstructure surrounding the nonmetallic inclusion.

CRACK PATHS IN 100CR6 BEARING STEEL—SUBSURFACE INCLUSIONS

A unique set of eleven 100Cr6 bearing steel test bars was tested at a common stress amplitude of 735 MPa at stress ratio $R = -1$ [10]. All specimens failed after a high number of cycles ($N_f > 10^7$) from subsurface spherical oxides as shown in Fig. 9.

In Fig. 9, a slight downward trend in the size of the inclusion that correlates with an increase in fatigue life can be seen, but this correlation is not perfect. Some degree of scatter

FIG. 7

The cross section FIB image of the ODA side and no ODA side of the nonmetallic inclusion.

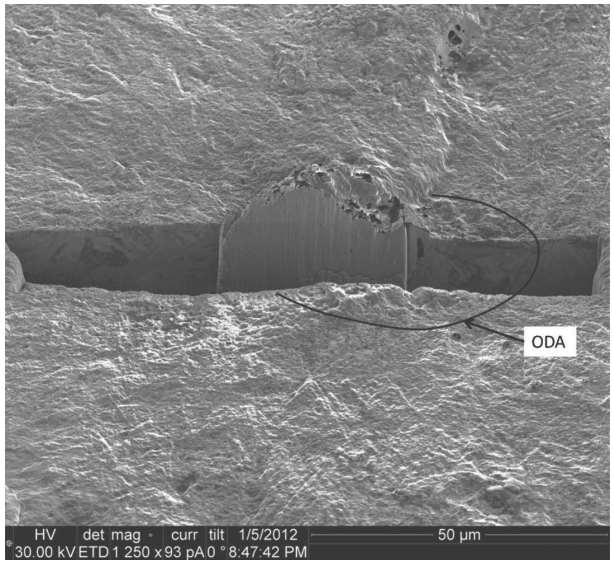

FIG. 8 A comparison of the two cross sections around the inclusion where (a) is from the side where there is no ODA and (b) is from the side where there is an ODA.

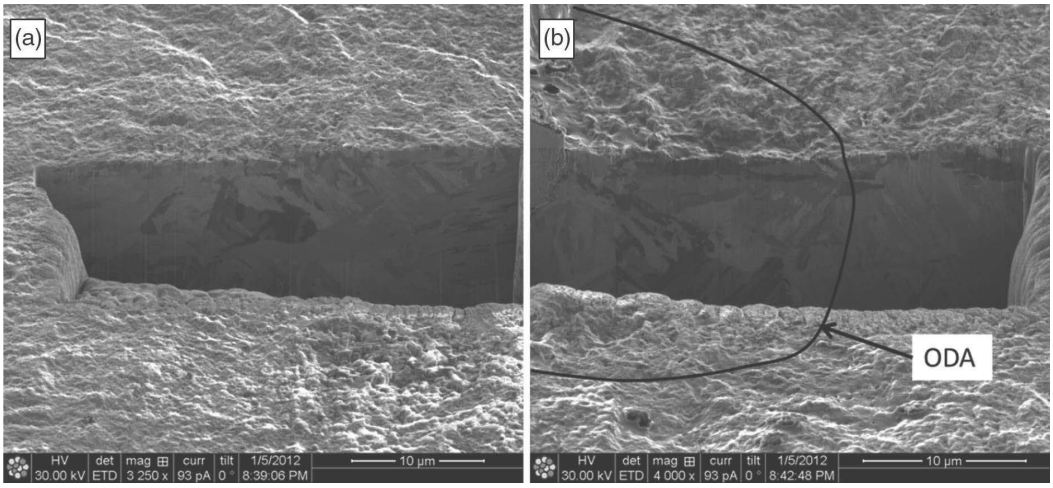

is inevitably expected in the UHCF regime, but we wished to take a closer look at crack initiation and growth paths over $10{\cdot}10^6$ cycles. In the following, we focus on the test bar that gave the longest fatigue life of $642{\cdot}10^6$ cycles. Fig. 10 shows the fracture surface around the inclusion, which was not the smallest in this set of specimens.

FIG. 9 Fatigue initiators in 100Cr6 bearing steel. Sizes of balls indicate $\sqrt{area}$ of inclusion. [21]

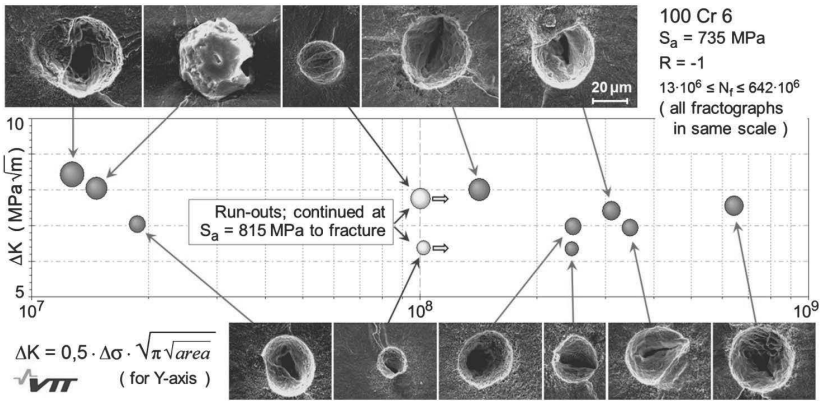

FIG. 10

Crack paths around the inclusion associated with the longest endurance of 100Cr6 bearing steel. The stress ratio was R = –1 and the stress amplitude was 735 MPa. The test bar had been tested for $642 \cdot 10^6$ cycles.

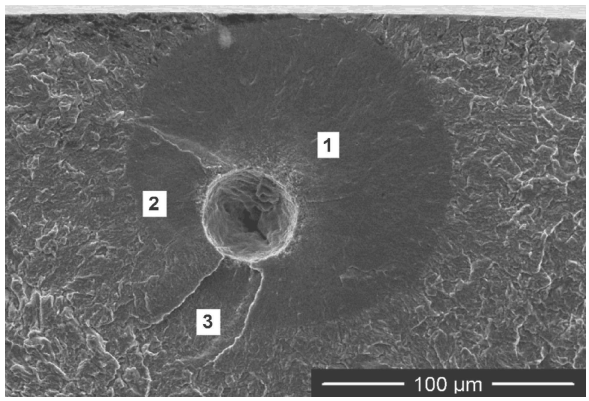

Furthermore, the inclusion was located relatively close to the specimen surface, which is seen at the top of Fig. 10.

As shown in Fig. 10, there are at least three crack initiation sites around the inclusion. Crack 1 occupies more than half of the inclusion circumference and advances the longest until the fish eye pattern was created by propagation of the crack to the specimen surface. Crack 3 lies clearly on a different plane and grows below cracks 1 and 2, thus causing retardation and unsymmetrical crack growth. It is worth noting how long the ridges between the cracks are. This demonstrates that the retardation effect of overlapping cracks has continued even beyond the crack sizes marked by the fish eye until the adjacent cracks have coalesced. We consider the rough surface beside the inclusion and in the direction of crack 1—opposite to crack 3—as ODA. There also seems to be a small area of ODA within crack 2.

FIG. 11 Comparing the microstructure of the step or ridge portion between crack levels "1" and "2" (see Fig. 10) circled with a solid line and the microstructure of the ODA area circled with a dotted line.

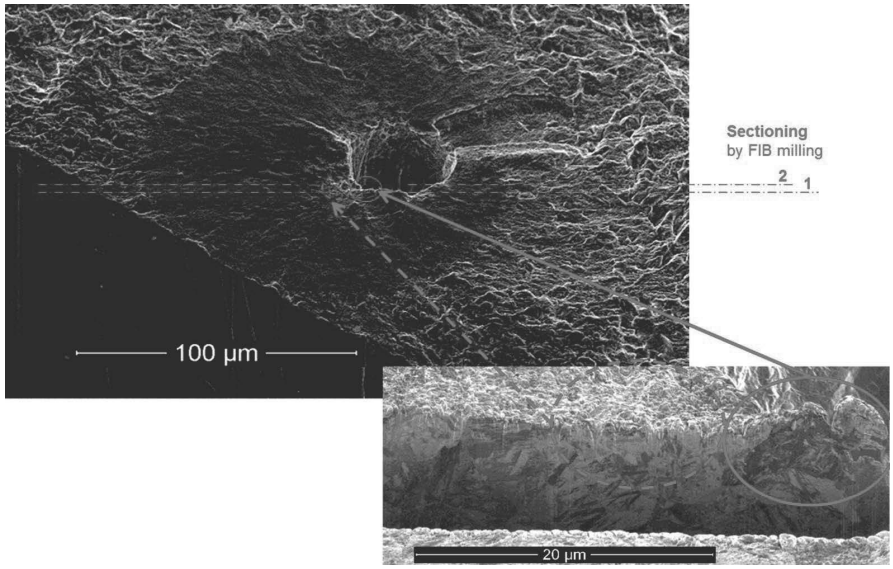

The microstructure immediately below the fracture surface around the inclusion was studied. Two milled cross sections were done (see **Fig. 11**). The angled view clearly shows the long and nearly constant height of the step between cracks 1 and 3. Once the first milled section was complete, the surface of the cross section was polished and then imaged with ions at a low current. The overview of the first cross section with a comparison to the fracture surface is shown in **Fig. 11**.

The left side of the first milled section shows the cross-section of the main ODA area next to the inclusion as well as the microstructure underneath the step between the crack levels labelled "1" and "2" in **Fig. 10**. The orientation difference revealed by the clear contrast in the underlying microstructure gives us a good reason to locate both areas "1" and "2" in different prior austenite grains.

In the right side of the cross section 2 (**Fig. 12c**), there is a secondary crack that provides an opportunity to investigate the microstructure on both sides of a very small crack that initiated and grew close to the subsurface inclusion. On the left side of the inclusion hole (**Fig. 12b**), the milled cross section shows a step in the fracture surface where the small crack was growing away from the inclusion. The right cross section is enlarged and explained in **Fig. 13**.

The change in the direction of a secondary crack is shown in **Fig. 13**. It is clear that the growth of the crack follows the orientation of the martensite lath structure until the microstructure around the crack changes and then the crack changes its direction. Another secondary crack is shown circled with a similar growth direction as the left side of the larger secondary crack. The smaller secondary crack has formed between microstructures with different lattice orientations. The crack growth direction along the martensite laths is seen on the left of the cross section.

FIG. 12 The second milled section, where (a) is the overview, (b) is the left side, and (c) is the right side. All images are taken with ion imaging.

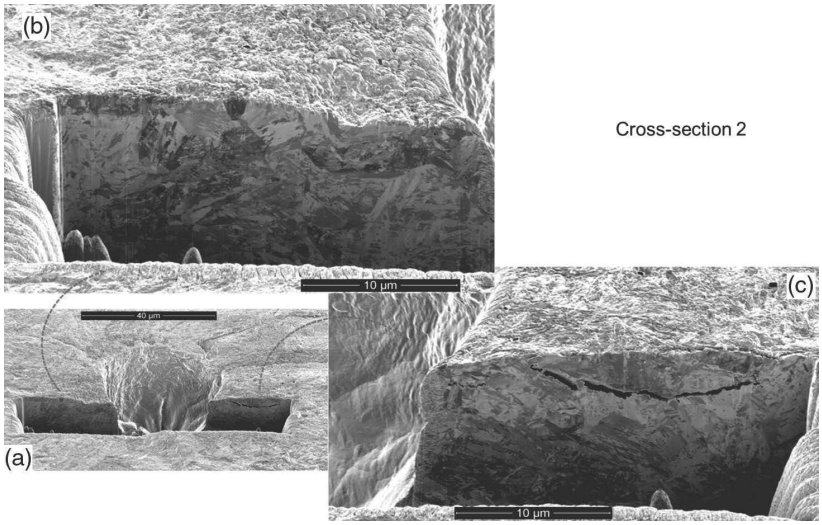

The left side of cross section 2 is shown in **Fig. 14**, where a change in the crack direction can be seen as a step on the fracture surface. Underneath, in the microstructure, there is a change in the martensite lath orientation as well. It should be noted that a very fine-grained area seen on the right side of **Fig. 14** on the inside wall of the inclusion hole is redeposition of the steel, which always occurs during FIB milling. This kind of a fine-grained area can also be seen in **Fig. 12c** on the inside wall of the inclusion hole.

Discussion

FRACTURE SURFACE OBSERVATIONS

The type of fracture surface referred to as the ODA has been studied in detail in Ref. [7]. The ODA circled in **Fig. 5** shows similar fracture surface features as the ones shown in Ref. [7], and when comparing images in **Figs. 5** and **6**, we clearly see similar features that are common among ODA fracture surfaces.

The fracture surface images taken from the 100Cr6 bearing steel test bar (**Figs. 10** and **11**) are not as clear, for which there are several reasons. The 100Cr6 bearing steel is high-strength steel with a much finer grain structure. This can also be seen in the ion images of the milled cross-sections shown in **Fig. 7** for the 34CrNiMo6 QT steel and in **Fig. 11** for the 100Cr6 bearing steel. These figures show that the subgrain structure is noticeably finer in the 100Cr6 bearing steel than in the 34CrNiMo6 QT steel. Because the microstructure is finer, the fracture surface created by a crack following the microstructure will also be finer and does not show as clear lath-like structures as in the other steel shown in **Figs. 5** and **6**.

In **Fig. 9**, a weak correlation can be seen between the size of inclusion (also ΔK on y-axis) and endurance. In addition to inclusion size, properties of the metal matrix around the inclusion and configuration of multiple cracks can affect early growth of the crack [21].

FIG. 13

A higher magnification of Fig. 12c.

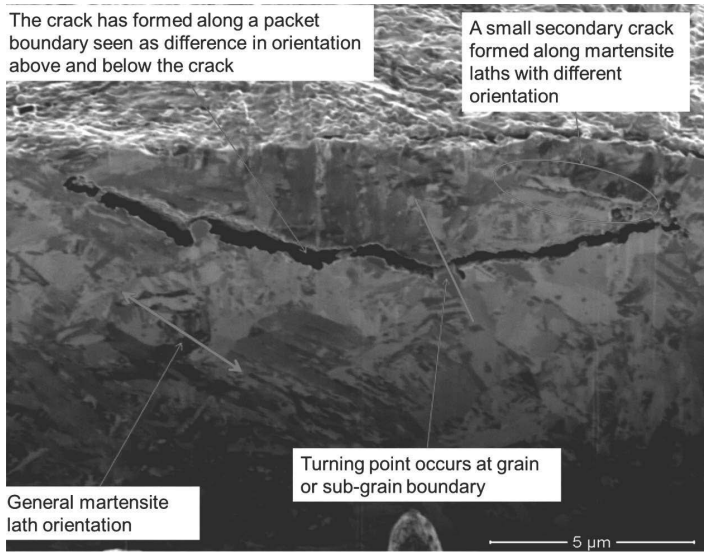

FIG. 14

A higher magnification of Fig. 12b.

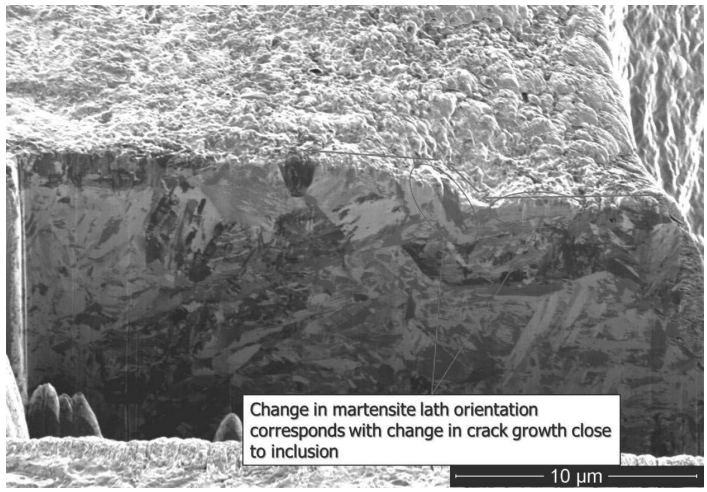

An influence of adjacent grain orientations has been demonstrated by numerical mesoscale models [22,23]. Our findings on the correlation between microstructure and crack path are in line with such models. In addition, microstructure may affect through initiation, simultaneous growth, and interaction of multiple cracks.

Our fractographic observations reveal the role of multiple crack initiations on slightly different planes. The asymmetrical crack growth that is observed around the inclusion (Fig. 10) shows effects of the microstructure and/or multiple crack initiation on the crack path and direction. The fish eye around the inclusion also tells us that the fatigue crack did not propagate directly toward the surface but rather went obliquely toward it while growing slower on the opposite side of the inclusion where the overlapping of multiple cracks is shown. It is possible that the original initiation of the crack growth into the ODA toward the surface caused a growing stress concentration on the opposite side of the inclusion and initiated cracks on different planes on the other side before the first crack had grown around the circumference.

It is worth noting that the longest life in Fig. 9 is associated with a medium-sized inclusion less than 100 μm below the specimen surface. Figs. 10–14 reveal how three cracks grew on adjacent planes before coalescence. This led to a nonsymmetrical crack (marked by the fish eye pattern) and retarded growth, particularly on the side where crack 3 grew on a separate plane when crack 1 reached the open surface. Similar butterfly-looking marks around inclusions on UHCF fracture surfaces are commonly seen in literature and in other inclusions, as shown in Fig. 10.

In summary, we assume that fatigue cracks do not always initiate exactly at the equator of a spheroid inclusion and several of them initiate to be later coalesced. Depending on the configuration, notable growth retardation may result and affect the obtained fatigue life. It is possible that in some cases crack arrest occurs at the most critical inclusion and thus fatigue limit will be affected. However, unless such a crack arrest can be confirmed, any proof of a correlation with the fatigue limit cannot be presented—just an effect in endurance.

FIB MILLING SUBSURFACE OBSERVATIONS

In the QT 34CrNiMo6 steel, the crack shows a clear preferential growth direction along the martensite laths in the subgrain microstructure. The pictures in Figs. 5–8 show that the ODA was formed on the right-hand side of the inclusion where horizontal martensite laths can be seen below the ODA region parallel to the direction of crack growth. The lengths of these martensite laths are close to the average grain size, which means that they are probably among the first martensite laths to form across the whole prior austenite grain. We assume that the crack has first grown and then the ODA formed on the side where the microstructure provides the most preferential direction for crack growth. Thus, our observations on the preferential crack paths from surface notches (Figs. 3 and 4) and subsurface inclusions (Figs. 6–8) are in agreement. Furthermore, an additional explanation to the formation and origin of the ODA is proposed based on the connection to the microstructure.

The FIB milling performed on the test bar of 100Cr6 bearing steel showed a finer microstructure than that of the 34CrNiMo6 QT steel. There was evidence of the crack growth direction being influenced by the martensite lath subgrain microstructure, as well as the grain structure. This is shown in Fig. 11, where the step in fracture surface is due to either a large martensite lath or a difference in grain structure. In Fig. 13a, a secondary crack is observed near the inclusion underneath the actual fracture surface. The crack follows the martensite lath structure until a turning point where the surrounding microstructure changes and the crack changes its growth direction. Fig. 14 shows how even very near the inclusion the small crack that has initiated and grown changes direction as the underlying martensite structure changes its orientation.

HYDROGEN, MICROSTRUCTURE AND ODA

Earlier work by Murakami et al. has shown that there is a link between the formation of the ODA and hydrogen trapped by the inclusion [1–9]. A lowering of the threshold stress intensity range by hydrogen for cracks initiating from inclusions has been shown [24]. On the other hand, little hydrogen exists in the steel matrix at milled surface notches. This may explain why no ODA areas were observed around the FIB notches. However, we have not measured the hydrogen content in our specimens. Neither did we intensively search for ODA from the surface notched specimens. Nagao et al. have studied the interaction of hydrogen and martensite laths [25] and have shown that the presence of hydrogen during monotonic loading causes cracks to preferentially grow along the prior austenite grain or martensite lath boundaries. One other important matter to understand when comparing a nonmetallic inclusion with an FIB notch is that the notch is randomly placed into the surface of the test bar, whereas the inclusion is solid in the steel during the steel production process when the steel itself is still molten. This means that there are interactions that take place when the steel solidifies around the inclusion and could be a key reason why there are ODA formations around the inclusions.

Studies such as Ref. [26] show that there can be grain refinement that takes place around inclusions during the fatigue life, whereas other studies have concentrated on the fact that this crack growth takes place usually in a vacuum inside the test bar, and that crack growth in vacuum has a decreased rate when compared to tests done in air [27]. While the effect of the crack growth in vacuum certainly does impact the growth of the crack, the effect of the microstructure is critical. The former study using FIB milling to observe the microstructure showed that the fine grains or grain refinement observed was from redeposition of the milled steel by the FIB. Some redeposition in the form of very fine grains is usually observed when milling larger cuts with the FIB. This can be observed on the right edge of **Fig. 14** as well.

In our study, it was observed that crack growth begins within a region beside the inclusion, later seen as ODA on the fracture surface. It is also observed that the initiation and early growth of the crack are affected by the martensite lath and packet orientation.

The referenced earlier results and our observations agree. Two main factors together affect the early growth of the cracks from the inclusion: the hydrogen trapping and the microstructure around the inclusion. These two factors work together to form the fractographic feature known as ODA on the fracture surface around the inclusions in high-strength steel specimens with ultra-long fatigue lives.

Conclusions

Crack paths around nonmetallic inclusions and surface notches were studied in high-strength steels. Fatigue testing was done on specimens with small FIB notches. The cross sections of the cracks showed that the small cracks tended to follow the martensite laths and packet boundaries.

The fractographic analysis of the nonmetallic inclusions indicated that the ODA forms around the inclusion and that there can be several cracks that initiate around the inclusion on different planes. This multiple-crack initiation can cause crack arrest when cracks grow perpendicularly on different planes.

A connection between the microstructure and growth path of small cracks is demonstrated. The general preferential growth direction and formation of the ODA can be

linked to adjacent grain orientations and subgrain structures such as martensite lath and packet orientation. Local martensite lath packets in the microstructure surrounding a nonmetallic inclusion, together with the presence of hydrogen trapped around the inclusion, provide an explanation to the formation and origin of the ODA. The interaction between the stress concentration, microstructure, hydrogen concentration, the preferential crack paths together with multiple small cracks initiating from the nonmetallic inclusions can explain long initiation and crack growth periods in specimens and components failing in the high and ultra-long fatigue regimes.

ACKNOWLEDGEMENTS

This research was part of three consecutive research projects: FATE-DEFEX, MACY, and SCAR-FACE funded by the Finnish Funding Agency for Technology and Innovation TEKES, VTT and industry.

References

[1] Murakami, Y., *Metal Fatigue: Effects of Small Defects and Nonmetallic Inclusions*, Elsevier Science, Amsterdam, 2002, p. 384.

[2] Murakami, Y., Nomoto, T., and Ueda, T., "Factors Influencing the Mechanism of Superlong Fatigue Failure in Steels," *Fatigue Fract. Eng. Mater. Struct.*, Vol. 22, No. 7, 1999, pp. 581–590.

[3] Murakami, Y., Nomoto, T., Ueda, T., and Murakami, Y. "On the Mechanism of Fatigue Failure in the Superlong Life Regime (N>107 cycles). Part 1: Influence of Hydrogen Trapped by Inclusions," *Fatigue Fract. Eng. Mater. Struct.*, Vol. 23, No. 11, 2000, pp. 893–902.

[4] Murakami, Y., Nomoto, T., Ueda, T., and Murakami, Y., "On the Mechanism of Fatigue Failure in the Superlong Life Regime (N>107 cycles). Part II: Influence of Hydrogen Trapped by Inclusions," *Fatigue Fract. Eng. Mater. Struct.*, Vol. 23, No. 11, 2000, pp. 903–910.

[5] Murakami, Y., Konishi, H., Takai, K., and Murakami, Y., "Acceleration of Superlong Fatigue Failure by Hydrogen Trapped by Inclusions and Elimination of Conventional Fatigue Limit," *Tetsu-to-Hagane*, Vol. 86, 2000, pp. 777–783.

[6] Murakami, Y., Yokoyama, N., and Nagata, J., "Mechanism of Fatigue Failure in Ultralong Life Regime," *Fatigue Fract. Eng. Mater. Struct.*, Vol. 25, Nos. 8–9, 2002, pp. 735–746.

[7] Ueda, T. and Murakami, Y., "Effect of Hydrogen on Ultralong Life Fatigue Failure of a High Strength Steel and Fracture Morphology of ODA," *Trans. Jpn. Soc. Mech. Eng., Series A*, Vol. 69, No. 681, 2003, pp. 908–915, https://doi.org/10.1299/kikaia.69.908

[8] Murakami, Y. and Nagata, J., "Effect of Hydrogen on High Cycle Fatigue Failure of High Strength Steel, SCM435," *J. Soc. Mater. Sci. Jpn.*, Vol. 54, No. 4, 2005, pp. 420–427.

[9] Murakami, Y. and Nagata, J., "Influence Factors of Fatigue Design in Ultralong Life Regime and Effect of Hydrogen on Fatigue Strength of High Strength Steel," *Trans. Jpn. Soc. Mech. Eng., Series A*, Vol. 70, No. 696, 2004, pp. 1093–1101.

[10] Uyama, H., Nakashima, M., Morishige, K., Mine, Y., and Murakami, Y., "Effects of Hydrogen Charge on Microscopic Fatigue Behaviour of Annealed Carbon Steels," *Fatigue Fract. Eng. Mater. Struct.*, Vol. 29, No. 12, 2006, pp. 1066–1074.

[11] Yamashita, Y. and Murakami, Y., "Small Crack Gr, owth Model from Low to Very High Cycle Fatigue Regime for Internal Fatigue Failure of High Strength Steel," *Int. J. Fatigue*, Vol. 93, Part 2, 2016, pp. 406–414.

[12] Hong, Y., Lei, Z., Sun, C., and Zhao, A., "Propensities of Crack Interior Initiation and Early Growth for Very-High-Cycle Fatigue of High Strength Steels," *Int. J. Fatigue*, Vol. 58, 2014, pp. 144–151.

[13] Sakai, T., Oguma, N., and Morikawa, A., "Microscopic and Nanoscopic Observations of Metallurgical Structures Around Inclusions at Interior Crack Initiation Site for a Bearing Steel in Very High-Cycle Fatigue," *Fatigue Fract. Eng. Mater. Struct.*, Vol. 38, No. 11, 2015, pp. 1305–1314.

[14] Olson, T., Lee, R., and Morgan, J., "Contrast Mechanisms in Focused Ion Beam Imaging," presented at the *18th International Symposium for Testing and Failure Analysis*, Los Angeles, CA, October 19–23, 1992, ASM International, Materials Park, OH, pp. 373–382.

[15] Wang, Y.-Z., Revie, R., Phaneuf, M. W., and Li, J. "Application of Focused Ion Beam (FIB) Microscopy to the Study of Crack Profiles," *Fatigue Fract. Eng. Mater. Struct.*, Vol. 22, No. 3, 1999, pp. 251–256.

[16] Motoyashiki, Y., Brückner-Foit, A., and Sugeta, A., "Investigation of Small Crack Behaviour Under Cyclic Loading in a Dual Phase Steel with an FIB Tomography Technique," *Fatigue Fract. Eng. Mater. Struct.*, Vol. 30, No. 6, 2007, pp. 556–564.

[17] Motoyashiki, Y., Brückner-Foit, A., and Sugeta, A., "Microstructural Influence on Small Fatigue Cracks in a Ferritic–Martensitic Steel," *Eng. Fract. Mech.*, Vol. 75, Nos. 3–4, 2008, pp. 768–778.

[18] Marx, M., Schäf, W., Vehoff, H., and Holzapfel, C., "Interaction of Microcracks with Selected Interfaces: Focused Ion Beam for a Systematic Crack Initiation," *Mater. Sci. and Eng., A*, Vols. 435–436, 2006, pp. 595–601.

[19] Roiko, A. and Solin, J., "Measurement of Small Cracks Initiating from Inclusions, Focused Ion Beam Notches and Drilled Holes," *Int. J. Fatigue*, Vol. 62, 2014, pp. 154–158.

[20] Volkert, C. and Minor, A., "Focused Ion Beam Microscopy and Micromachining," *MRS Bulletin*, Vol. 32, 2007, pp. 389–395.

[21] Solin, J., Alhainen, J., and Varis, P., "Ultra High Cycle Fatigue and Inclusions in Wrought Steels," *presented at the International Symposium on Fatigue Design and Material Defects*, Trondheim, Norway, May 23–25, 2011, Elsevier, Amsterdam, Netherlands.

[22] Mikkola, E., Marquis, G., and Solin, J., "Mesoscale Modelling of Crack Nucleation from Defects in Steel," *Int. J. Fatigue*, Vol. 41, 2012, pp. 64–71.

[23] McDowell, D. and Dunne, F., "Microstructure-Sensitive Computational Modeling of Fatigue Crack Formation," *Int. J. Fatigue*, Vol. 32, No. 9, 2010, pp. 1521–1542.

[24] Murakami, Y., Kanezaki, T., and Sofronis, P., "Hydrogen Embrittlement of High Strength Steels: Determination of the Threshold Stress Intensity for Small Cracks Nucleating at Nonmetallic Inclusions," *Eng. Fract. Mech.*, Vol. 97, 2013, pp. 227–243.

[25] Nagao, K., Smith, C. D., Dadfarnia, M., Sofronis, P., and Robertson, I. M., "The Role of Hydrogen in Hydrogen Embrittlement Fracture of Lath Martensitic Steel," *Acta Mater.*, Vol. 60, 2012, pp. 5182–5189.

[26] Grad, P., Reuscher, B., Brodyanski, A., Kopnarski, M., and Kerscher, E., "Mechanism of Fatigue Crack Initiation and Propagation in the Very High Cycle Fatigue Regime of High-Strength Steels," *Scr. Mater.*, Vol. 67, No. 10, 2012, pp. 838–841.

[27] Stanzl-Tschegg, S. and Schonbauer, B., "Near-Threshold Fatigue Crack Propagation and Internal Cracks in Steel," *Procedia Eng.*, Vol. 2, No. 1, 2010, pp. 1547–1555.

Publication V

A. Roiko, J. Solin, H. Hänninen, Behaviour of small cracks under negative stress ratio fatigue loading, submitted to: International Journal of Fatigue on 17.2.2017 under review.

International Journal of Fatigue 104 (2017) 379–388

Contents lists available at ScienceDirect

International Journal of Fatigue

journal homepage: www.elsevier.com/locate/ijfatigue

Behavior of small cracks under negative stress ratio fatigue loading

A. Roiko [a,*], J. Solin [a], H. Hänninen [b]

[a] VTT Technical Research Centre of Finland Ltd., P.O. Box 1000, FI-20044 VTT (Espoo), Finland
[b] Aalto University School of Engineering, Finland

ARTICLE INFO

Article history:
Received 17 February 2017
Received in revised form 7 July 2017
Accepted 9 July 2017
Available online 11 July 2017

ABSTRACT

In this paper we analyze growth of small cracks initiated from microscopic notches and loaded near the growth threshold under different stress ratios. The results of in-situ optical measurements during high cycle fatigue testing show that small cracks initiate and grow quickly after which there is a long period of slow growth until the large crack growth threshold is reached. The crack growth rate data from different loading ratios indicates that the positive portion of the stress amplitude or the maximum stress intensity factor can be used to compare crack growth rates. The test data also shows that increasing only the compressive stress portion of the loading will cause an arrested small crack to grow again.

1. Introduction

The designer of machines or mechanical components that experience numerous loading cycles needs to understand the material response to the loads and possible defects or cracks that can grow or initiate fatigue cracks. This has given rise to many studies about small fatigue cracks and unique phenomena that occur in their initiation and growth. The effect of the compressive portion of the fatigue cycle on the behavior of small cracks is important for many industrial components that, for example, use various surface hardening treatments to improve their fatigue strength or endurance. Many of these fatigue improving treatments cause high compressive stresses on the component surface. This can prevent fatigue, but if not used properly, cause failure for example in axels and gears where incorrect surface hardening can warp the component or cause cracks to initiate and grow.

The general focus of most small crack growth research has been in the range of tension - tension loading ($R > 0$) or symmetric loading at $R = -1$. Several researchers have studied also the initiation and arrest of small cracks from notches under fully compressive loading [1–5]. An interesting question is the amount of crack closure in small cracks because the original studies done on crack closure by Elber were performed on large cracks in soft metals [6,7]. More recently Silva studied the effect of compressive loading on crack growth. One of the main focuses of his research was the inability to explain some of the effects of compression on the crack growth in fatigue by crack closure [8]. The research showed that there is a significant effect of compressive loading on the crack growth and this varies from material to material. It was concluded that some intrinsic material properties should be incorporated into models that were previously developed [9]. A recent study demonstrated using finite element analysis that the largest effect of underloads or compressive loading was the reduction of retardation effects and acceleration of crack growth [10]. Other researchers have shown that an increase in the compressive portion of the fatigue loading lowers the threshold of fatigue crack growth, and that this effect slowly becomes saturated as the compressive loading increases [11].

The focus of this paper is to study the effect of compressive fatigue loading on the growth of small fatigue cracks in the quenched and tempered steel. More specifically, the effect of the compressive portion of fatigue loading on small cracks and their growth rates near and at the threshold for crack growth. The measurements are performed at the High-Cycle Fatigue (HCF) regime by introducing very small surface notches, which initiate cracks close or even below the fatigue endurance limit ($N_f > 10^7$) of the specimen. For the purposes of this study, small cracks are generally defined as less than 1 mm in length.

A fundamental reason why small crack growth in high-cycle fatigue has been difficult to study is due to the lack of proper tools to undertake the measurement and documentation of very small cracks that are tested for very long fatigue lives. The in-situ high-speed optical microscope combined with Focused Ion Beam (FIB) notches and small drilled holes used in this study provides a novel combination of tools for reliable and consistent in-situ method of measuring the growth of the small cracks during long periods of fatigue testing. Furthermore the experimental set-up used here provides a tool to investigate the behavior of small cracks under large compressive fatigue loads in the high-cycle fatigue regime.

* Corresponding author.
E-mail addresses: andrew.roiko@vtt.fi (A. Roiko), hannu.e.hanninen@aalto.fi (H. Hänninen).

http://dx.doi.org/10.1016/j.ijfatigue.2017.07.006
0142-1123/

2. Experimental

The steel studied in this paper is a quenched and tempered 34CrNiMo6 steel with 1065 MPa and 1180 MPa yield and tensile strength, respectively. The micro-hardness is 373 HV0.1. The quenched and tempered microstructure of the studied steel is shown in Fig. 1. The microstructure has a large impact on the behaviour of small cracks. Although this is not the focus of this study, the microstructure of the steel is important background information to help understand the steel that is studied.

The test specimens were machined from the centreline of ϕ 25 mm wrought bars according to the dimensions shown in Fig. 3a.

The endurance limit at 10^7 cycles of the smooth un-notched test bars was determined at R = −1. The results of the fatigue testing is shown in Fig. 2. The endurance limit is calculated to be 475 ± 11 MPa.

Two types of small notches aimed to serve as artificial initiation sites were manufactured on smooth and polished specimens by FIB milling or drilling. FIB milling was used to make small almost planar defects resembling semi-elliptical cracks (h = w = 50 … 90 μm). Also, the drilled notches were small and shallow (d = 100 μm or 200 μm), but for clarity and contrast, we call them as "holes". See Fig. 3(b, c) for more details where the cross-section of the notches and holes normal to the fatigue loading direction are shown (with one exception where the FIB notch was at 45° marked in Fig. 7).

Axial fatigue tests were performed at resonant frequencies around 100 Hz and the specimens were fatigued either close to the range of smooth specimen fatigue limit or at different R-ratios that are in the high-cycle fatigue regime. The small notches were optically monitored and video recorded for crack initiation, growth and arrest in real time. The frequency that was used is relatively near to what most engine components such as axels and gears experience. At this loading rate there is no major frequency dependence with respect to fatigue life, as long as the fatigue test bars do not produce excessive amounts of heat during testing. This does not happen with quenched and tempered steels near the fatigue limit at this frequency range.

The fatigue testing machine was a Rumul pulsator with a threaded attachment. The pulsator uses a resonator with a spring to load the specimen. As shown in Fig. 3, the test specimen is round and short to help ensure that in-plane bending under compression does not occur. The test machines are also calibrated to ensure proper measurement and testing.

Two types of small crack growth fatigue tests were performed. One is where the crack initiation and growth from the notch or hole are constantly monitored and measured in-situ, while the loading of the test specimen is constant.

The other type of test is where:

1. The loading was slowly decreased as the crack grows to measure the arrest threshold of the small crack. Once this is done and after the crack has arrested.
2. The compressive portion of the loading was increased, while the maximum tensile stress was held constant. In other words, the arrested crack experiences a decreasing mean stress along with the increasing stress amplitude, but a constant maximum stress. The test was continued in this way with steps of 20–50 MPa in mean stress and each step was applied for about 1 million cycles or until crack growth is detected.
3. After crack growth is detected the stress amplitude is kept constant and the mean stress was decreased with constant monitoring of crack growth until the crack arrest was again confirmed.

After the arrest, phase 2 is repeated again until the crack growth is detected. This type of testing was done with a starting stress ratio of R = −1, and with a stress amplitude of 450 MPa. The same testing procedure was also performed with a starting stress ratio of R = −2, where the maximum stress was 350 MPa and the minimum stress was −700 MPa.

Using the crack length (as seen in Fig. 4) measured from the surface the positive portion of the stress intensity factor range was calculated using the following equation:

$$\Delta K_+ = Y \cdot \Delta\sigma_+ \cdot \sqrt{\pi a}, \quad (1)$$

which for the exception of one loading case reported is equal to:

$$K_{max} = Y \cdot \sigma_{max} \cdot \sqrt{\pi a}, \quad (2)$$

where 'a' is half of the total crack length and Y is the geometry correction factor and $\Delta\sigma_+$ is the positive portion of the stress range applied to the crack. In this study for all loading ratios where R is negative K_{max} is equal to ΔK_+. In this paper all the data except for one set of data where R = 0.26, K_{max} and ΔK_+ are the same value, although they are of course different in the fact that one is the stress intensity factor range ΔK_+ and the other is the maximum stress intensity factor (K_{max}). The goal here is not to specify which works better rather to study the effect of compressive stress and therefore both work for the purpose required here. These equations have been used in previous studies (see Refs.: [12–16] and have been shown to work for small cracks growing from various small notches as well as holes.

There are two main differences between the two types of notches used. The FIB notches are smaller and more crack like with a high stress concentration ($K_t > 7$) and abrupt stress gradient. The drilled holes are larger and more like the non-metallic inclusions located in the steel with a lower but wider stress gradient ($K_t \approx 2$), which affects a larger volume of the steel around the hole than the FIB notch, also relative to their size. The reason two different notches are used is to study the difference between more crack-like defects such as the FIB notches with small drilled holes which are more similar to non-metallic inclusions.

All of the tests reported here are meant to study the growth of small cracks under mechanical loading, in a laboratory environment.

3. Results and discussion

Crack growth from FIB notches and drilled holes was first studied with constant amplitude loading. This means that once the crack has initiated the test can be characterized as a rising ΔK test. Results from one test is shown in Fig. 5.

From Fig. 5 it can be observed that the cracks initiate almost immediately and grow faster in the beginning of the test. Once they have grown out of the area directly ahead of the notch where there is a large stress gradient, the driving force decreases and the crack growth rate decreases. From around 50 000 cycles to around 1.4 million cycles there is a phase of slower, but constant and symmetric growth of the crack. This phase of slower growth leads the small crack out of the growth threshold region into the normal crack growth rate regime for large cracks. The crack growth data in Fig. 5 also shows that there is no in-plane bending; both sides of the crack are growing symmetrically.

Using the data from Fig. 5 and Eq. (1) or (2) we can calculate the da/dN vs ΔK_+ or K_{max} correlation which is shown in Fig. 6. To calculate the da/dN it is necessary to calculate the difference between the crack growth from one measurement to another in (da), and then to divide it by the amount of cycles between the two measurements (dN). The ΔK_+ is then calculated by using equation (1)

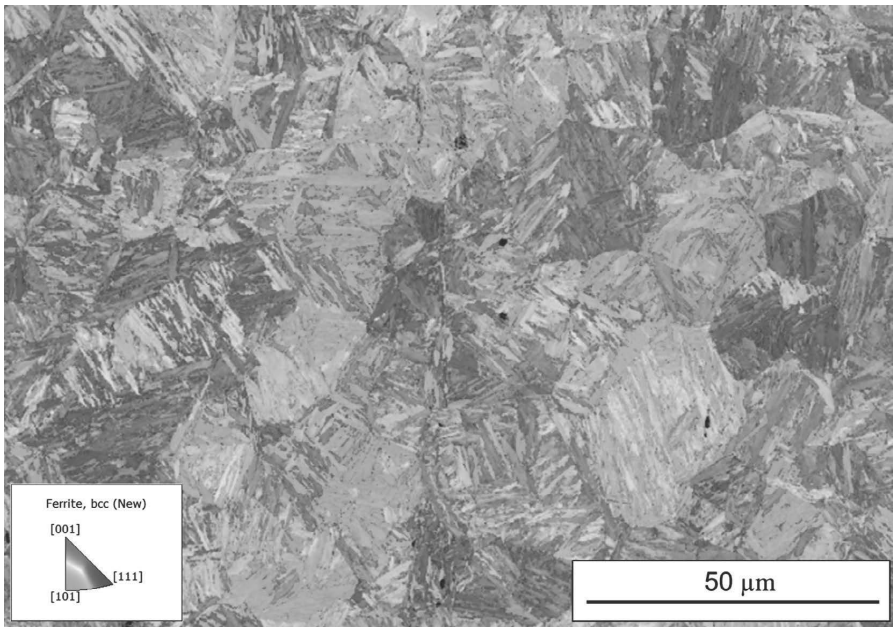

Fig. 1. The microstructure of the studied quenched and tempered 34CrNiMo6 steel.

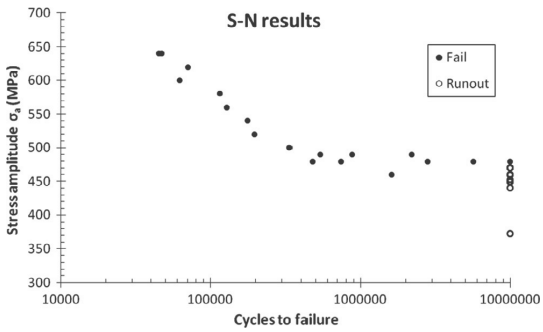

Fig. 2. Fatigue stress-life curve and endurance limit determined for smooth bar specimens of the test material – quenched and tempered 34CrNiMo6 steel.

or (2) where 'a' is the average crack length between the two crack lengths used to calculate 'da'.

Fig. 6 illustrates that in the slow growth region the crack is growing slower than the rate for determining the growth threshold ($da/dN < 10^{-10}$ m/cycle) and the data shows a decreasing crack growth rate. This is because of the large increase in fatigue cycles compared to the actual crack growth. What is important to observe is that the crack is actually growing for most of the test, at least on the surface. This data shows that the small crack growth behaviour is a variable and slow process that gradually approaches the threshold of crack growth for large cracks. The measured temporary arrest is caused by the very slow growth rate of the crack. This is when the fatigue cycles approach large numbers so that the calculation of the crack growth rate shows very small or no growth. In reality the small crack is constantly growing but at a rate that is so small it is difficult to measure or calculate. There are common situations where the small crack stops growing for millions of fatigue cycles; the difference why some cracks grow at a very slow rate while others appear to arrest for millions of cycles is not clear.

The averaged curve in Fig. 6 is repeated together with the other test results obtained using FIB notches at different R-ratios. This compilation is shown in Fig. 7.

Once the maximum stress intensity factor range is greater than 5 MPa $\sqrt{m}$, the crack grows out of the threshold zone into the conventional crack growth Stage II of the Paris law curve.

The other type of small notch used was drilled holes. The crack initiation and growth from drilled holes during constant amplitude loading is shown in Fig. 8.

The main difference with the crack growth from the drilled holes is that the crack growth is generally more stable and there is not as much crack growth deceleration as with the crack growth from FIB notches. This is due to the fact that the drilled holes have a stress gradient that decays gradually, whereas the FIB notches have stress gradients that are more crack like, so they are more severe, but affect a shorter distance. The constant amplitude crack growth rate data from the drilled holes and FIB notches are combined in Fig. 9.

When we combine the two data sets it can be seen that the drilled holes show a consistently higher crack growth rate and do not exhibit the same form of crack arrest with one exception of the crack that arrested under a $R = -4$ loading ratio. Total length of this crack was over 500 μm, when the growth rate became less than 10^{-10} m/cycle and over 600 μm at arrest. In other words, it was growing out of the stress gradient of the 200 μm hole during the decreasing crack growth rate phase. This means that the crack growth was greatly assisted by the compression portion of the loading as long as the crack tip was within the stress gradient of the hole. As the crack grew out of the stress gradient it gradually arrested. This crack data corresponded well with the data from cracks growing from FIB notches, which are arresting at the same rate as the larger crack growing from a small drilled hole.

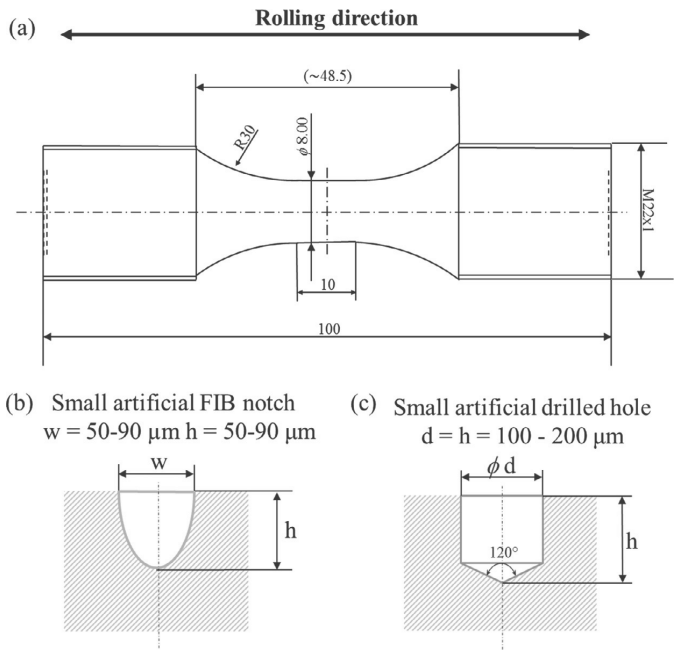

Fig. 3. (a) Dimensions of the test bar in mm, (b) FIB notch dimensions in µm, and (c) dimensions of the drilled hole in µm.

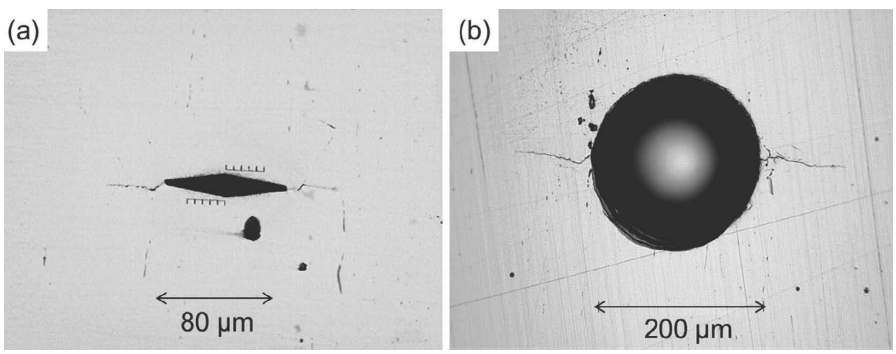

Fig. 4. Examples of (a) a FIB notch and (b) a drilled hole being observed in-situ with a high-speed video microscope during testing.

The data in Fig. 9 shows that using the positive portion of the loading to calculate ΔK, collapses the crack growth rate curves into the same curve for higher ΔK_+ regions. There is more scatter in the lower ΔK_+ regime due to the different nature of the notches, if they are drilled holes or FIB notches, and there is a larger influence of the microstructure that should be taken into consideration as well. However, once the cracks have grown out of the stress gradient they follow the same curve for the positive portion of the ΔK loading of the test material, and approach the Stage II of the Paris long crack growth rate regime where most of the scatter of the small crack growth rate starts to disappear.

The other type of testing where the loading was controlled according to the growth of the crack from the drilled holes sheds light on the interaction of the compressive load effect on the crack growth rate behaviour under different loading ratios. In this case the crack arrest occurring at a constant R-ratio of R = −1 and R = −2 is shown in Fig. 10.

In Fig. 10 the [1]blue data points and the blue lines are for the R = −1 loading and the red data points and the red lines for the R = −2 loading. The purple lines have the loading ratio assigned with an arrow showing the increased compressive portion of the loading. The data shown with the purple lines is the crack growth rate from cracks that were reinitiated by increasing the compressive load portion of the loading. In the legend the order in which the test was conducted is marked with black arrows noting the next step for each crack growth rate curve. One test loading series was done at R = −1 and the other started at R = −2. The two series are separated in the legend with a dotted line. The only crack growth rate curves

[1] For interpretation of color in Fig. 10, the reader is referred to the web version of this article.

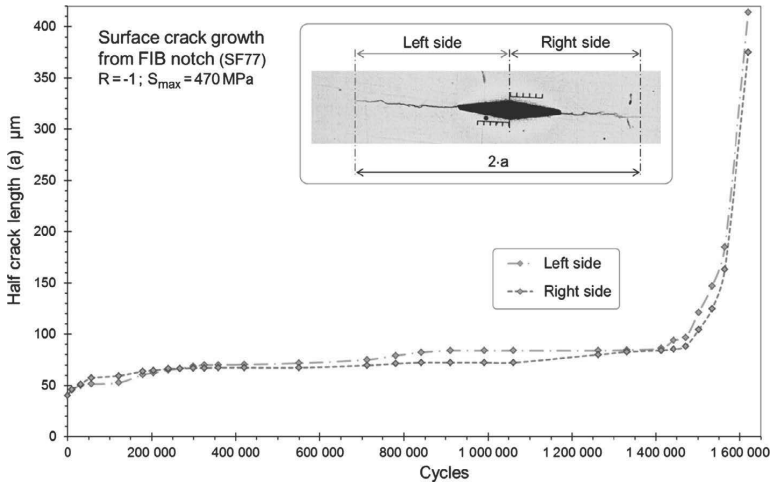

Fig. 5. The results of in-situ optical measurements of crack growth from a FIB notch under constant amplitude loading. The x-axis is the number of fatigue cycles and the y-axis is the crack length on the left (red) and right (blue) side of the notch. (For interpretation of the references to colour in this figure legend, the reader is referred to the web version of this article.)

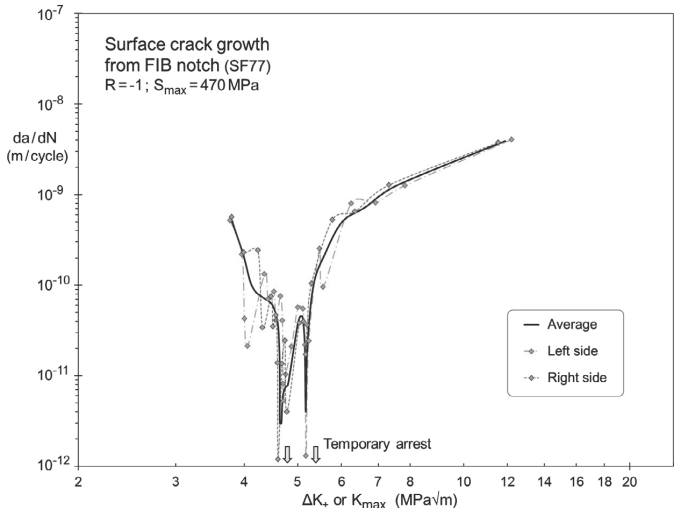

Fig. 6. The crack growth data from Fig. 5 is used to calculate the da/dN vs. ΔK_+ or K_{max} graph showing the crack growth rate from the FIB notch.

that were measured with variable loading are the constant blue and red curves (for R = −1 (blue) and −2 (red)) where the threshold is being measured by slowly decreasing the amplitude of the loading in small steps while measuring the crack growth.

It is clear from Fig. 10 that under R = −2 loading the crack is growing at a faster rate than the crack under R = −1 loading, for comparable ΔK_+ or K_{max} values. When the two arrest thresholds are compared we see that the R = −2 threshold is around 12% lower than the R = −1 threshold on the ΔK_+ or K_{max} scale.

Fig. 11 shows the difference between the small crack growth rate at different R-ratios. The data shows that the average crack growth rate at R = 0 is in line with the crack growth rate at negative R-ratios and that there is a good correlation when using the positive portion of the stress intensity factor range once the crack has grown out of the stress gradient of the hole. The interaction of the stress gradient of the hole and the crack growth rate is shown in Fig. 12.

To get a better understanding of the behaviour of small crack growth rate under different negative R-ratios, the average crack growth rates were calculated for different portions of the crack growth test. This was done for the crack growth rates at R = −1 to R = −3.73; the crack growth data from which this is calculated is shown in Fig. 13.

In Fig. 13 the crack growth data is shown for R-ratios −2 to −3.73 originally from a drilled hole. The crack growth shown in the figure is well past the effect of the stress gradient of the hole (as seen from the crack length shown in the y-axis of the figure) the data can be considered as crack data and is no longer linked to the small hole from which it originally initiated.

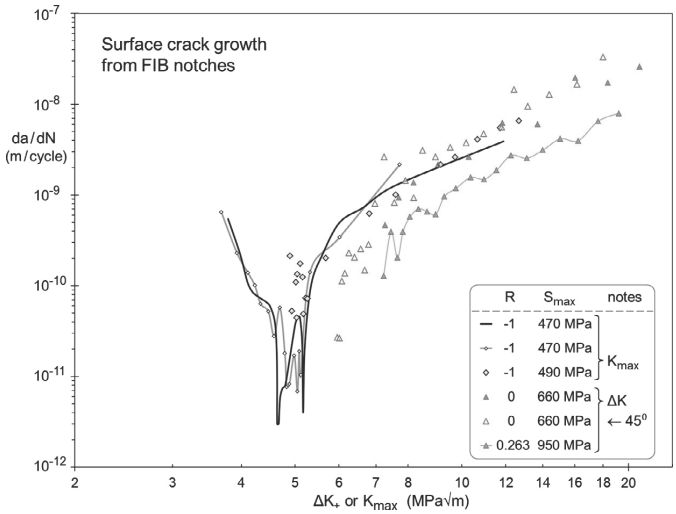

Fig. 7. The initiation and growth of small cracks from FIB notches at different R-ratios.

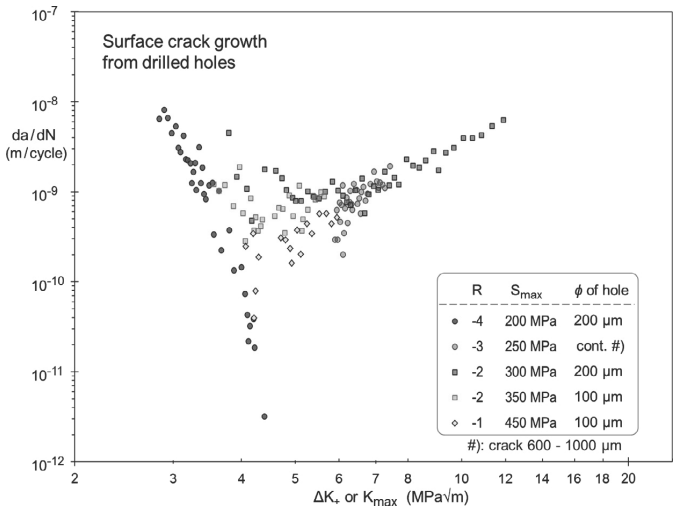

Fig. 8. Growth rates of small cracks initiated from drilled holes at different R-ratios. The symbol cont. #) is used and further explained under the legend as the continuation of crack growth. In other words, it is not a new crack initiating from a drilled hole, rather it is a test of a pre-existing crack already propagated to a total length of 600 μm, from which it is continued and tested at a R-ratio of R = −3 until it reaches a length of 1000 μm.

This data shows that generally the crack growth rate is linear for situations where there is a large negative loading ratio. This can be used to average the crack growth over a longer cycle count. Doing this, a better overall picture is obtained of how the crack growth rate is behaving and eliminates some of the scatter caused by e.g. microstructural heterogeneity. The average crack growth rate data is shown in Fig. 14.

Fig. 14 shows that as the compressive loading portion of the fatigue cycle increases, the ΔK_+ or K_{max} at which a selected crack growth rate occurs decreases. When comparing the K_{max} for R = −1 and R = −2, the decrease of similar effective ΔK_+ or K_{max} is around 12%, and there is around 7% decrease from R = −2 to R = −3.4 and −3.73. So it appears that there is a gradual saturation for the effect of the amount of compressive loading on the correlation between the crack growth rate and ΔK_+ or K_{max}.

4. Final discussion

The previous studies [5,8–11] about the effects of compressive loading on fatigue crack growth can be applied also for small cracks in the steel that were studied here. It was measured that increasing the compressive loading for a crack can reinitiate its growth. This is due to the fact that increasing the compressive portion of the loading in the constant amplitude testing decreases the ΔK_+ or K_{max} threshold for the crack growth. The experimental work reported here is unique due to the new combination of tools and methods

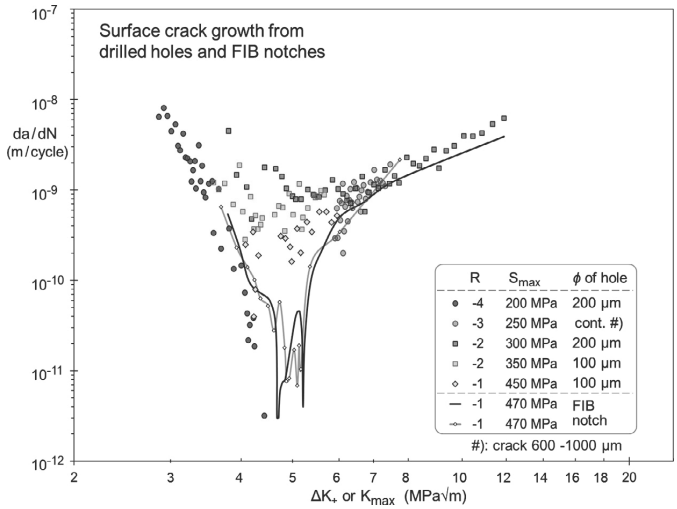

Fig. 9. Growth rates of small cracks from drilled holes and FIB notches at different R-ratios. The symbol cont. #) is used and further explained under the legend as the continuation of crack growth. In other words, it is not a new crack initiating from a drilled hole, rather it is a test of a pre-existing crack already propagated to a total length of 600 μm, from which it is continued and tested at a R-ratio of R = −3 until it reaches a length of 1000 μm.

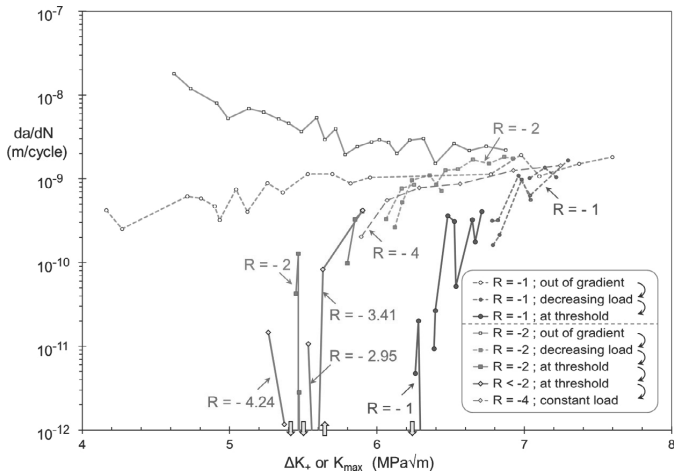

Fig. 10. The beginning crack growth rate, as well as arrest threshold with decreasing ΔK (MPa√m). This data shows the arrest of the small cracks growing from small drilled holes as the stress amplitude is gradually decreased until the cracks have arrested.

that were employed to monitor and measure the small fatigue crack growth under these unique conditions. For this reason there are almost no comparable data that can be used for comparison of the results reported in this study.

The growth rates of small cracks under large compressive cyclic loads are slower when comparing their respective da/dN vs ΔK_+ or K_{max} values. A possible reason for this is that the compressive loading does not affect the crack growth through the same way as the tensile portion of the loading does. Rather the compressive loading affects the crack growth through the bulk response of the material along with the full reversal or sharpening of the portion of the crack tip that is held open by the deformations of the plastic zone ahead and around the crack tip. The scale with which the compressive loading affects this can be material dependent. The effectiveness of compressive loading is reducing as the amount of compressive loading is increased. A doubling of the compressive load from R = −1 to −2 decreases the ΔK_+ or K_{max} of similar growth rate by around 12%, whereas another doubling to around R = −3.73 reduces the ΔK_+ or K_{max} only 5% more. This indicates that the mechanism through which it affects the crack growth is caused by the removal of crack closure or crack tip sharpening. Once the compression portion of the loading has enhanced the crack growth through these mechanisms, a further increase in the compressive loading has less of an effect on the crack growth.

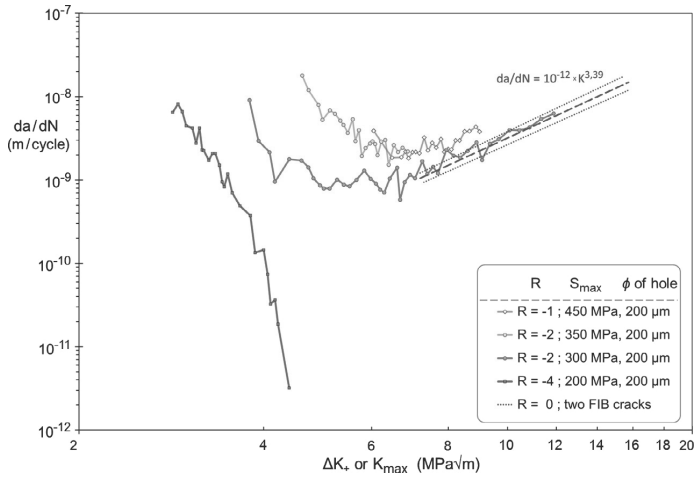

Fig. 11. The comparison of the crack growth rates with the growth rate of small cracks loaded at R = 0. The average crack growth rate of small cracks loaded at R = 0 is shown with the dotted blue lines. (For interpretation of the references to colour in this figure legend, the reader is referred to the web version of this article.)

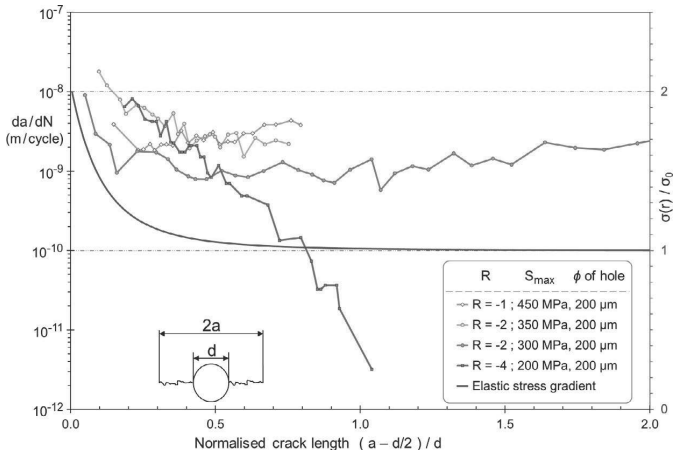

Fig. 12. The change in the rate of crack growth from the hole with the crack length normalized to the diameter of the drilled hole. The legend gives the loading ratio R, after which is the maximum stress of the cyclic loading and then the diameter of the drilled hole. The stress gradient for the drilled hole is given with the blue line which corresponds to the blue axis on the right side of the figure. (For interpretation of the references to colour in this figure legend, the reader is referred to the web version of this article.)

The saturation of the effect of the compressive loading does not remove the challenges that the increase of the compressive loading has on the initiation and growth of fatigue cracks. It has been shown that initiation and crack growth can occur if the compressive portion of the loading is increased. The decrease in the ΔK_+ or K_{max} in the crack arrest is around 12% less for cracks at $R = -2$ when compared to a crack at $R = -1$. This is in agreement with the crack growth data at higher growth rates than at crack arrest where the influence of increasing the compressive loading from $R = -1$ to $R = -2$ will decrease the ΔK_+ or K_{max} required for crack growth by around 10 to 12%. If examined from the crack growth rate point of view the growth rate is increased by a factor of around 4 when doubling the compressive loading from $R = -1$ to $R = -2$.

5. Conclusions

This study examined the small crack growth using in-situ optical measurement of surface cracks in high-cycle fatigue using multiple test bars with different shape and size small notches. The data shows that small crack growth occurs near the fatigue endurance limit of the studied quenched and tempered steel through the process of an accelerated growth immediately after initiation. After this brief initiation and accelerated growth of the small crack there follows a period where a very slow crack growth rate is observed until the large crack growth threshold is reached.

The comparison of crack behavior at different R-ratios indicates that for this material under these conditions a good correlation can be obtained by only using the positive portion of the stress range.

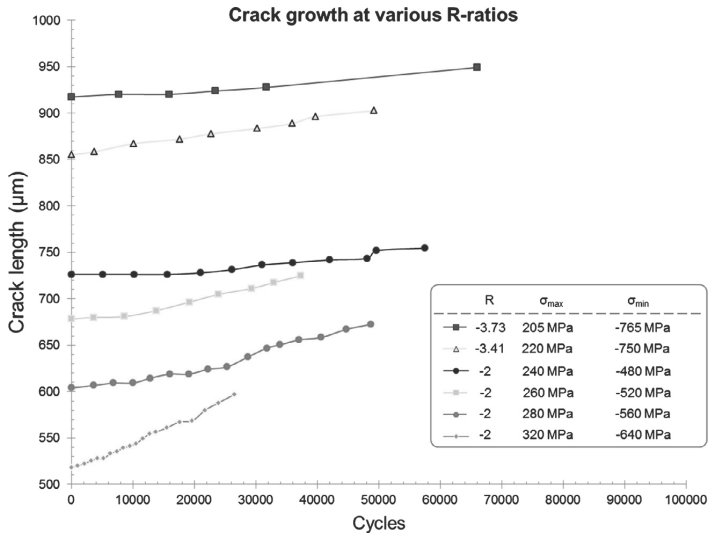

Fig. 13. The crack growth measured during testing at different R-ratios. The maximum and minimum stress of the stress amplitude is given for the crack growth measured during 25000–70000 cycles of fatigue loading.

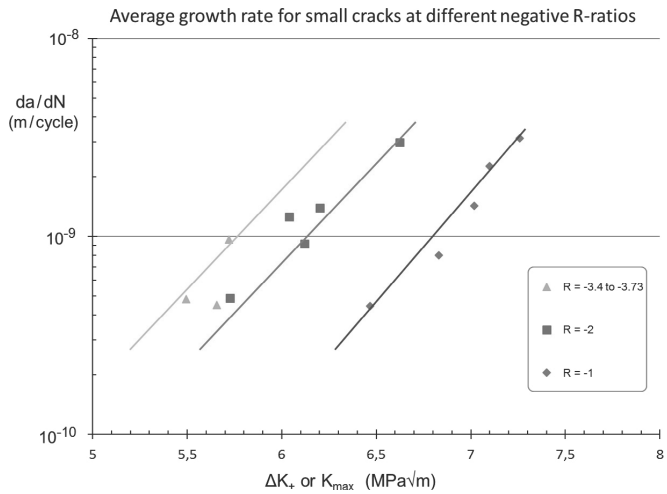

Fig. 14. The effect of different loading ratios on fatigue crack growth rate with respect to ΔK_+ or K_{max}.

Compressive loading decreases the ΔK_+ or K_{max} threshold for the small crack growth and increases the crack growth rate of small cracks. This effect is more pronounced when increasing from $R = -1$ to $R = -2$ than when increasing from $R = -2$ to $R = -3.73$.

The main conclusions of the study are as follows:

- Small fatigue cracks, at first, initiate quickly and then grow very slowly below and close to the threshold of large fatigue crack growth.
- The parameter ΔK_+ works well to compare the crack growth rate of small fatigue cracks in the studied quenched and tempered steel.
- Crack arrest ΔK_+ or K_{max} thresholds are lower with higher compressive loading.
- Increasing only the compressive portion of loading can reinitiate arrested small cracks.
- The crack growth rates for small fatigue cracks near the fatigue crack growth threshold level are increased by as much as a factor of 4 for larger compressive loads.

Acknowledgements

This research was part of three consecutive research projects: FATE-DEFEX, MACY, and SCAR-FACE funded by the Finnish Funding Agency for Technology and Innovation TEKES, VTT and industry.

References

[1] Fleck N, Shin C, Smith R. Fatigue crack growth under compressive loading. Eng Fract Mech 1985;21:173–85.
[2] Suresh S. Crack initiation in cyclic compression and its applications. Eng Fract Mech 1985;21:453–63.

[3] Pippan R. The growth of short cracks under cyclic compression. Fatigue Fract Eng Mater Struct 1987;9:319–28.
[4] Hermann R. Fatigue crack growth in ductile materials under cyclic compressive loading. Fatigue Fract Eng Mater Struct 1994;17:93–103.
[5] Kasaba K, Sano T, Kudo S, Shoji T, Katagiri K, Sato T. Fatigue crack growth under compressive loading. J Nucl Mater 1998;2258–263:2059–63.
[6] Elber W. Fatigue crack closure under cyclic tension. Eng Fract Mech 1970;2:37–45.
[7] Elber W. The significance of fatigue crack closure. Damage Tolerance Aircraft Struct, ASTM STP 1971;486:230–42.
[8] Silva F. Crack closure inadequacy at negative stress ratios. Int J Fatigue 2004;26:241–52.
[9] Silva F. The importance of compressive stresses on fatigue crack propagation rate. Int J Fatigue 2005;27:1441–52.
[10] Benz C, Sander M. Reconsiderations of fatigue crack growth at negative stress ratios: Finite element analyses. Eng Fract Mech 2015;145:98–114.
[11] Kardomatlas G, Carlso R. Predicting the effects of load ratio on the fatigue crack growth rate and fatigue threshold. Fatigue Fract Eng Mater Struct 1998;21:411–23.
[12] Murakami Y, Endo M. Effects of hardness and crack geometries on delta K_{th} of small cracks. J Soc Mater Sci, Japan 1986:911–7.
[13] Murakami Y, editor. Stress intensity factors handbook, Pergamon.
[14] Murakami Y, Beretta S. Small defects and inhomogeneities in fatigue strength: experiments, models and statistical implications. Extremes 1999:123–47.
[15] Roiko A, Solin J. Measurement of small cracks initiating from inclusions, Focused Ion Beam notches and drilled holes. Int J Fatigue 2014;62:154–8.
[16] Murakami Y. Theory of elasticity and stress concentration, Kyushu University: Wiley, 2017.

Publication VI

A. Cetin, A. Roiko, M. Lind, Towards proper sampling and statistical modelling of defects. Fatigue & Fracture of Engineering Materials & Structures, Volume 38, September 2015, Pages 1056-1065 ISSN 1460-2695

FFEMS Fatigue & Fracture of Engineering Materials & Structures
SPECIAL ISSUE CONTRIBUTION
doi: 10.1111/ffe.12317

Towards proper sampling and statistical modelling of defects

A. CETIN[1], A. ROIKO[2] and M. LIND[3]

[1]*4Subsea AS, Nesbru, Norway,* [2]*VTT Technical Research Centre of Finland, Espoo, Finland,* [3]*School of Science, Aalto University, Espoo, Finland*

Received Date: 16 October 2014; Accepted Date: 16 April 2015; Published Online: 2015

ABSTRACT Predicting the size of the largest defect expected to occur in components based on samples obtained from polished inspection areas is a common exercise, which is even addressed in standards. However, the standard practice may occasionally yield poor results. This paper presents a comprehensive method that aims to improve some of the shortcomings of the standard practice. The method is utilized on actual defect data, which showed that the proposed method is able to predict significant experimental observations that the standard practice missed.

Keywords statistical model; statistics of extremes; steel; steel cleanness.

NOMENCLATURE

A_0 = inspection area
a = distribution parameter
b = distribution parameter
F_X = Probability distribution of X (dummy variable)
k = number of inspection areas
S_A = observable defect size (small circle)
S_V = representative defect size (great circle)
V_0 = inspection volume
V = target volume
Z_A = largest observable defect size
Z_V = largest representative defect size
α = probability level
γ = distribution parameter
η = distribution parameter
μ = distribution parameter
ρ = distribution parameter (defect density)

INTRODUCTION

The fatigue strength of a component is related to the size of the material defects it contains. Thus, attempting to predict the size of the largest defects expected to occur in an arbitrary component based on samples obtained from appropriately prepared inspection areas is a common exercise in the field of material-oriented fatigue engineering and research. In fact, the issue is even addressed in a standard,[1] which is based on the popular work of Murakami and his collaborators, extensively summarized in Ref [2]. The approach promoted in the standard is simple and practical because of its heuristic nature. Unfortunately, it may occasionally not perform according to expectations. There are other methods[3–5] that ought to be more suitable in a wider range of scenarios but at the cost of practical applicability; the mathematical complexity involved is often considerable.

In the present work, the standard practice is considered as basis, and improvements are suggested while mostly maintaining the practical applicability. The improvements are both practical and mathematical in nature and cover the following:

- Statistical analysis and modelling of defects sampled from inspection areas.
- Consistently converting inspection areas into equivalent *inspection volumes*.
- Proper utilization of extreme value statistics for consistent predictions.

Correspondence: A. Cetin. E-mail: ali.cetin@4subsea.com

Furthermore, actual defect samples obtained from an ultra strong 100Cr6 bearing steel are utilized to demonstrate the improvements while comparing the results to the standard practice.

METHOD AND THEORY

First, the intention is not necessarily to introduce a completely new method. Instead, individual and partial improvements, some of which are already available in the literature, are compiled and presented as a consistent and comprehensive approach. The core of this approach may be summarized as (i) sampling strategy, (ii) describe the observed data (i.e. the samples), and (iii) predict unobserved events (i.e. the size of the largest defects). It is essential to realize that these are all interrelated issues and should be considered in a holistic framework. The focus should then be on selecting the optimal path with respect to the end goal: to make reasonable predictions about the size of the largest defects expected to occur in an arbitrary component.

Defect sampling

In the standard practice, block maximum sampling of defects is recommended. Accordingly, k inspection areas of equal size, A_0, are prepared. Only the defect with the largest observable size is sampled from each inspection area, such that k samples are obtained. This sampling strategy is both practical and cost efficient.

However, the type of the sampled defects is not always uniform. Even worse, samples obtained from inspection areas may not even correspond to the type of defects found on the fracture surface of failed components. It is conceivable that a particular type of defects obscures the presence of another type during sampling, which may emerge as the dominant type in larger volumes. This is in fact a practical shortcoming of block maximum sampling and may be addressed by pragmatically modifying the sampling strategy.

For instance, different defect types can be sampled simultaneously from the same inspection area, that is, the defect with the largest observable size for each type is sampled. Consequently, several samples are obtained from each inspection area rather than just one. The crucial point is to consider the different types as separate populations and, thus, keep the samples separate. Determining the type of defects during sampling will certainly introduce technical limitation and requirements that may exclude the simplest equipment. Nonetheless, a modified block maximum sampling appears to be practically feasible, as presented in Application Example section.

On the other hand, it is in theory possible to address the issue of mixed defect types through suitable statistical modelling without altering the sampling strategy, for example, Ref. [6]. This requires that (i) each defect type is sufficiently represented in the samples and (ii) the statistical distributions of the different defect populations present in the samples are practically distinguishable. These two conditions are seldom fulfilled, and therefore, the pragmatic approach with the modified sampling strategy appears more robust.

Descriptive statistical modelling

Once the samples are available, it is necessary to adequately describe them through proper statistical models. However, note that samples obtained from inspection areas are necessarily indirect and, in general, do not correspond of the actual size of the defects. The observable size of a particular defect on an inspection area is merely the size of a random cross section of that defect. The relationship between the observable and the representative sizes of spherical defects was first derived by Wicksell in 1925[7] and often referred to as *Wicksell transform*. Wicksell and others have followed up the initial work and showed that this unique relationship is in practice only applicable for spherical defects.[8]

An important consequence of Wicksell's findings is that sampling from inspection areas makes sense only if the defects can be assumed spherical. Thus, the assumption of spherical defects must also be adopted here. This limitation, which arises from the underlying mathematics of the physical problem, is often neglected (including the standard practice). Consequently, this limitation excludes pores and shrinkage cavities because of their often complex geometry.

A key claim of the proposed approach is proper statistical modelling of the samples. Accordingly, the *Wicksell transform* ought to be an integral part of the model. However, the mathematical complexity of a general model is considerable as discussed in, for example, Refs. [9–14]. In order to avoid most of these complexities, an approximate modelling approach that is consistent and sufficiently accurate for the observed data will be presented. However, this model is likely to yield poor results when extrapolated beyond the observed data, that is, utilized for predictions.

The size of a defect may be described by various parameters such as length, area or volume. Here, *size* will refer the area of cross sections; let S_A denote the observable size of a particular defect on an inspection area and S_V the corresponding representative size for the same defect. For spherical defects, S_V would be the area of the great circle while S_A the area of a random small circle. Note that $S_V \geq S_A$.

Furthermore, let $\{S_{V,i}, i = 1, \ldots, m\}$ be the sequence of representative sizes of defects (of a particular type) enclosed in a volume in a material body, and $\{S_{A,j}, j = 1,.., n\}$ be the sequence of observable defect sizes present on an inspection area obtained from the same body. In block maximum sampling, only the largest observable defect size is sampled:

$Z_A = \max\{S_{A,j}, j = 1,..,n\}$. Similarly, the largest representative defect size may be denoted $Z_V = \max\{S_{V,i}, i = 1,..,m\}$. Note that Z_A and Z_V do not necessarily originate from the same defect. This is the core issue at hand, properly describing Z_V while only observing Z_A.

Analogous to the standard practice, the distribution function describing the random variable Z_A may be expressed as[15]

$$F_{Z_A} = \text{Prob}(Z_A \le s) \simeq exp\left(-exp\left(-\left(\frac{s^\gamma - b^*}{a}\right)\right)\right) \quad (1)$$

This is the common Gumbel distribution function (where s^γ is considered as the random variable) and can be considered as a generalization of the standard practice because $\gamma = 1/2 \rightarrow s^{1/2}$ (which coincides with the $\sqrt{area}$ formulation). The parameter estimation process is rather straight forward; a, b^*, and γ may be estimated by means of any suitable method, for example, maximum likelihood. Common software intended for the Gumbel distribution may be utilized to estimate a and b^*, where s^γ is treated as the variable; different values of γ may be attempted to maximize the likelihood function.[16] Typically, γ is an element of (0.5, 2.0).

Next will be an attempt to estimate the 'actual' sample set $\{Z_{V,i}, i = 1, \ldots, k\}$ and the corresponding inspection volume, V_0, based on the observed sample set $\{Z_{A,i}, i = 1, \ldots, k\}$ and the known inspection area, A_0. The proposed solution to this problem differs from the standard practice, which bluntly assumes that

$$\{Z_{V,i}, i = 1, \ldots, k\} = \{Z_{A,i}, i = 1, \ldots, k\} \quad (2)$$

and

$$V_0 \approx \frac{A_0}{k} \sum_{i=1}^{k} Z_{A,i}^{\frac{1}{2}} \quad (3)$$

Essentially, Z_V is assigned the same distribution function as Z_A, that is, Eq. (1), and the inspection volume is estimated with an empirical formula. However, this is not consistent with *Wicksell transform*.

A consistent approximation of the distribution function describing the random variable Z_V may be expressed as[17]

$$F_{Z_V}(s) = \text{Prob}(Z_V \le s) \simeq \exp\left(-\frac{V_0}{\sqrt{\pi} A_0} g(s) \exp\left(-\left(\frac{s^\gamma - b^*}{a}\right)\right)\right) \quad (4)$$

where

$$g(s) = \frac{\int_s^\infty \frac{u^{\gamma-1} exp\left(-\frac{u^\gamma}{a}\right)}{\sqrt{u - s}} du}{\int_s^\infty u^{\gamma-1} \exp\left(-\frac{u^\gamma}{a}\right) du} \quad (5)$$

It is clear that *Wicksell transform* significantly complicates the model. Fortunately, Eq. (4) is not evaluated directly. Instead, the relationship between Eqs. (1) and (4) is exploited to obtain $\{Z_{V,i}, i = 1, \ldots, k\}$ by setting

$$F_{Z_V}(s) = F_{Z_A}(t) \quad (6)$$

That is, for a given Z_A, there is a corresponding Z_V with equal probability; rearranging Eq. (6) will give

$$Z_{A,i}^\gamma = Z_{V,i}^\gamma - a\left[ln\left(g\left(Z_{V,i}\right)\right) + ln\left(\frac{V_0}{\sqrt{\pi} A_0}\right)\right] \quad (7)$$

A suitable inspection volume may be estimated by matching the medians $\widetilde{Z}_V = \widetilde{Z}_A$:

$$V_0 = \frac{\sqrt{\pi} A_0}{g\left(\widetilde{Z}_A\right)} \quad (8)$$

Inserting Eq. (8) into Eq. (7):

$$Z_{A,i}^\gamma = Z_{V,i}^\gamma - aln\left(\frac{g\left(Z_{V,i}\right)}{g\left(\widetilde{Z}_A\right)}\right) \quad (9)$$

Note that Eqs. (8) and (9) must be evaluated numerically because Eq. (5) has no closed form solution. This may be considered as the cost of consistently incorporating *Wicksell transform* into the present model. On the other hand, the practical cost is marginal because it only involves numerically integrating well behaving smooth functions.

The effort so far has been to properly describe and interpret the observed sample data. The main result is the ability to estimate the 'actual' sample set and the corresponding inspection volume, summarized in Eqs. (8) and (9). In the following, a comprehensive predictive modelling approach that builds on top of the results obtained so far will be presented.

Predictive statistical modelling

The primary objective is to derive a statistical model for predicting the size of the largest defects expected to occur in an arbitrary component with volume V. This may be achieved by extrapolating a suitable statistical distribution with parameters based on sample data obtained from an inspection volume, V_0. Often, this extrapolation can be quite significant as the target volume tends to be much larger than the inspection volume, $V_0 \ll V$. To that end, the standard practice suggests to utilize the regular Gumbel distribution with the $\sqrt{area}$ as the random variable (cf. Eq. (1) where $\gamma = 12$). However, the classical

extreme value distributions such as Gumbel, Fréchet, and Weibull may not be optimal choices when the application involves significant extrapolation.[15]

The selection of a statistical model intended for predictions should be based on two considerations: consistency and accuracy. It is difficult to achieve the latter without the former. Given a consistent model, the accuracy is often related to the amount of data available for parameter estimation. Considering the typical sample sizes available for defect analysis, it would be unrealistic to expect high degree of accuracy and certainty in the predictions. Therefore, the focus should be on deriving consistent models that sufficiently capture the underlying physical processes and properties of the problem. In that manner, the predictions will at least be consistent and capture significant trends and qualities observed in experiments and 'real world' applications.

The exact statistical distribution of the largest representative defect sizes is well defined (under reasonably general assumptions):

$$F_{Z_V}(s) = \exp(-\rho V[1 - F_{S_V}(s)]) \tag{10}$$

where ρ is the number of defects per unit volume (i.e. defect density) and $F_{S_V}(s)$ is the cumulative distribution function of the entire defect population (of a certain type). The challenge is that the distribution function of the defect population is in general unknown. In that regard, the classical extreme value distribution functions have been a last resort as Eq. (10) will asymptotically ($\rho V \to \infty$) approach either Gumbel, or Fréchet, or Weibull distributions. (The underlying distribution function must satisfy certain mathematical conditions. The most common distribution functions will in fact approach the Gumbel distribution). The problem is that the asymptote condition is seldom satisfied for inspection volumes. Thus, indiscriminate utilization of these distribution functions for extrapolation purposes may lead to inconsistencies and inaccuracies.[15]

An alternative approach is to assume a parametrization of $F_{S_V}(s)$. The underlying physical processes and experimental observations should be considered when determining the appropriate parametrization; it would be unreasonable to assume that the problem has a single unique solution valid for all defect types. However, the log-normal distribution appears to be a strong candidate[18,19,4] and will be adopted here as well. Accordingly, Eq. (10) could be expressed as[20]

$$F_{Z_V}(s) = \exp\left(-\frac{\rho V}{2}\operatorname{erfc}\left(\frac{ln s - \mu}{\sqrt{2}\eta}\right)\right) \tag{11}$$

where μ and η are suitable parameters, and *erfc* is the complementary error function.

The parameters in Eq. (10) could be estimated by means of nonlinear regression:

$$\min \sum_{i=1}^{k} \left[y_i - C + \ln\left(\operatorname{erfc}\left(\frac{x_i - \mu}{\sqrt{2}\eta}\right)\right)\right]^2 \tag{12}$$

where

$$\begin{aligned} y_i &= ln\left(ln\left(\frac{1}{\hat{F}_{Z_V,i}}\right)\right) \\ x_i &= ln(Z_{V,i}) \\ C &= ln\left(\frac{\rho V_0}{2}\right) \end{aligned} \tag{13}$$

and $\hat{F}_{Z_V}$ is the empirical distribution function. Note that

$$\rho = \frac{2\exp(C)}{V_0} \tag{14}$$

and may vary noticeably with C. Also, it should be mentioned that different estimation methods may yield slightly different results for small sample sizes. Therefore, the physical feasibility of the parameter values should not be overemphasized, unless the sample size is considerable. Nonetheless, the parameters μ, η and ρ may be estimated by evaluating Eq. (12) for the sample set $\{Z_{V,i}, i = 1, \ldots, k\}$ originating from an inspection volume V_0.

The largest defect size expected to occur in component with volume V with probability α may be predicted by inverting Eq. (11):

$$Z_V, \alpha = F_{Z_V}^{-1}(\alpha|V) \tag{15}$$

Summary

A rather comprehensive approach is presented, and the step-by-step procedure may be summarized as follows:

- Prepare k equally sized inspection areas with size A_0.
- Sample the largest observable defect in each inspection area. If several defect types are present, sample the largest observable defect of each type.
  1 There will be k samples of each defect type.
  2 Treat the samples from different defect types separately.
- *Repeat the following for each defect type…*
- Fit the observed sample set $\{Z_{A,i}, i = 1, \ldots, k\}$ to Eq. (1) and estimate γ, a (and b^*).
- Estimate the corresponding inspection volume, V_0, utilizing Eq. (8).
- Estimate the 'actual' sample set $\{Z_{V,i}, i = 1, \ldots, k\}$ by adjusting the observed sample set $\{Z_{A,i}, i = 1, \ldots, k\}$ with Eq. (9).
- Estimate the parameters μ, η and ρ in Eq. (11) utilizing the 'actual'sample set $\{Z_{V,i}, i = 1, \ldots, k\}$ and the inspection volume V_0.

- Once the parameters are ready, predict the largest defect size expected to occur in component with volume V with probability α by evaluating Eq. (15).

The presented approach is obviously more complicated and involves more steps than the standard practice. However, it incorporates *Wicksell transform* and utilizes extreme value statistics properly while remaining transparent and practically applicable.

APPLICATION EXAMPLE

The method presented earlier is applied to actual experimental data obtained from ultra strong 100Cr6 bearing steel. An automated sampling from inspection areas was performed as well as fatigue tests to compare the inclusions found from the inspection areas and the fracture surfaces of the fatigue specimen.

Experimental data

A batch of 100Cr6 steel was studied. The steel is quenched and 180 °C tempered to hardness HRC 61 (1630 MPa tensile strength). Fatigue specimen were taken from 14 depth of a 70 mm wrought bar; see Fig. 1. The inspection areas were obtained from similar locations in the wrought bar.

Sampling from inspection areas

Thirty-one inspection areas (i.e. $k = 31$) were polished using increasingly finer grit of emery paper. Cooling water was used to eliminate the undue heating of the steel while polishing. After this preparation was complete, the specimens were then analysed in a scanning electron microscope (SEM) using an automatic INCA Feature analysis programme. The automatic programme distinguishes inclusions on the polished surface by using the electron back scatter detector to differentiate between the matrix and the inclusions. Once an inclusion is detected, the INCA Feature programme analyses the elements in the inclusions with an Energy-dispersive X-ray spectroscopy sensor in the SEM. It then classifies the inclusion according to its chemical composition and records its size and shape. The parameters for the automated inspection were set at a magnification of 300×, and the inspection area that was automatically scanned and analysed by the programme was $A_0 = 25$ mm^2.

With the aforementioned inspection setup, all observable defects with sizes larger than 1 μm^2 were registered. The reliability of the measurements will naturally increase with the defect size. In that regard, block maximum sampling is beneficial. In each inspection area, various defect types such as sulfides, oxides and nitrates were registered. The largest observable defect of each type in each inspection area was sampled. Often, a sulfide was the largest observable defect in the entire inspection area.

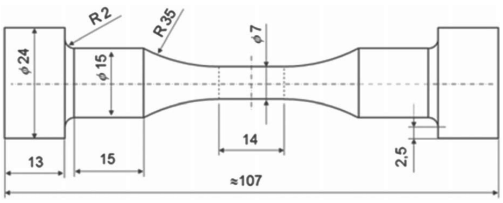

Fig. 1 Dimensions of the fatigue test bar.

Sampling from fracture surfaces

Forty-five axial fatigue tests for the fatigue specimen were performed using a RUMUL Testronic (Russenberger Prüfmaschinen AG Gewerbestrasse 10 CH-8212 Neuhausen am Rheinfall Schweiz) fatigue test machine. The fatigue tests were performed at resonant frequencies below 200 Hz. The tests were performed at a loading ratio of $R = -1$. Run-out specimens were broken at increased stress amplitudes, and every fracture surface was studied. The gauge volume of the specimen was about $V_g = 540$ mm^3.

The inspection of the fracture surfaces of the fatigue specimen was performed with a SEM microscope. The fracture surfaces were cut off of the test bars and labelled and cleaned with an ultrasound cleaning device. SEM pictures were taken of the fracture surface of the fatigue specimen, and measurements were performed as well as a chemical composition analysis of the inclusions found at the nucleation sites. The chemical composition analysis of the fracture surface inclusions was performed with an Electronic Data Systems. An example of an inclusion that caused fatigue failure in the specimen is given in Fig. 2.

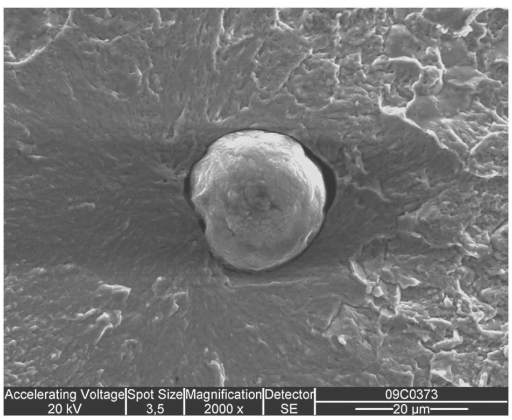

Fig. 2 A scanning electron microscope picture of an inclusion found on the surface of the fatigue test bar fracture surfaces.

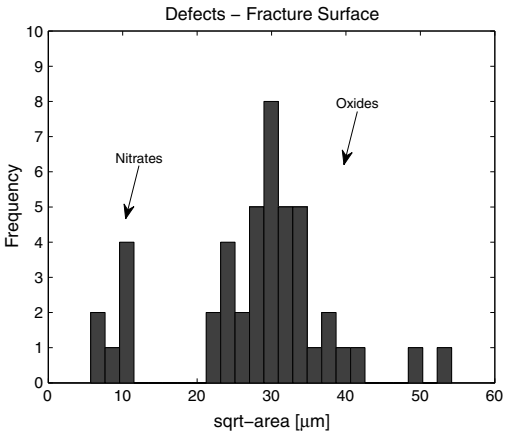

Fig. 3 Histogram of defects sampled from fracture surfaces of the fatigue specimen.

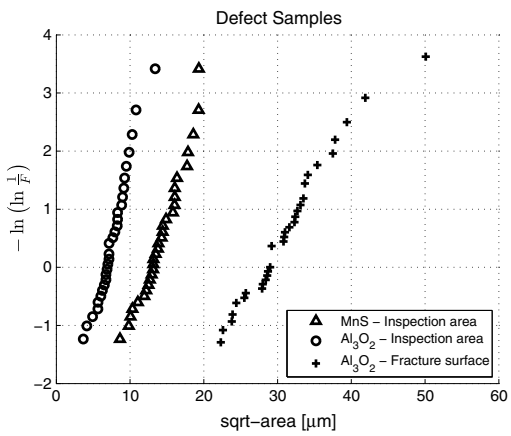

Fig. 4 Probability plot of defects sampled from inspection areas and fracture surfaces of fatigue specimen.

The type of defect found at the fracture surface in 38 of 45 specimens was oxides, while nitrates were found the remaining specimen. However, the nitrates were significantly smaller than the typical oxides found in the majority specimen and occurred on specimen exposed to particularly high stresses. It appears that other factors than the defect size become significant at high stresses for this material. The defects are presented in a histogram in Fig. 3 (where the nitrates are grouped together to the left).

Predicting the largest defects

Recall that several defect types were observed on the inspection areas. However, only two defect types are considered here: (i) manganese sulfides (MnS) and (ii) aluminium oxides (Al_3O_2). These two are chosen primarily because both occurred regularly on the inspection areas. Also, the MnS defects were often the largest ones on the inspection areas, while the Al_3O_2 defects were found on the fracture surfaces of the laboratory specimens. (The seven specimens where nitrates were found on the fracture surfaces are excluded from the analysis). The defects that are used in the analysis are summarized in a probability plot in Fig. 4.

The defect samples obtained from inspection areas are analysed according to the step-by-step procedure presented at the end of Theory and Method section and the standard practice for comparison. (The modified sampling strategy of considering each defect type separately is adopted for the standard practice as well. In this manner, the model performances may be evaluated more clearly.) Accordingly, the samples are fitted to Eq. (1); the maximum likelihood estimates of the parameters are summarized in Table 1.

Table 1 The maximum likelihood estimates of the parameters in Eq. (1)

	Present method			Standard practice		
	γ	a	b^*	γ	a	b^*
MnS	1.06	98.4	233	0.500[a]	12.9	2.64
Al_3O_2	0.616	10.8	3.81	0.500[a]	6.81	1.98

[a]By definition according to the $\sqrt{area}$ formulation.

Table 2 The estimated inspection volumes for each defect type according to the present method and the standard practice

	Present method V_0[mm^3]	Standard practice V_0[mm^3]	Difference %
MnS	0.207	0.358	−42.2
Al_3O_2	0.135	0.198	−31.8

It will be seen from the discussion in the succeeding text that the most relevant parameter is γ as it affects many aspects of the present model. In fact, certain aspects of the present model and the standard practice coincide for particular values of γ.

The next step is to estimate the corresponding inspection volumes according to Eq. (8). Here again, the present method and the standard practice yield slightly different estimates as summarized in Table 2.

Note that the inspection volume estimates based on the standard practice, that is, Eq. (3), are consistently larger and the difference seems to grow with γ.

Once the value of the inspection volumes, V_0, is available, the 'actual' sample sets may be estimated by

correcting the observed sample sets (cf. Eq. (9)). The results for the two defect types are presented in Figs 5 and 6. First, the amount of correction is determined by the value of γ. In fact, note that there is no correction when $\gamma = 1$ as the last term on the left-hand side in Eq. (9) cancels out. In fact, Eqs. (2) and (6), which are key assumptions for the standard practice and the present model, respectively, are equivalent formulations for $\gamma = 1$.

Accordingly, the correction for MnS defects is negligible. However, there is a slight correction for Al $_3O_2$ defects, which may prove significant when considering that the 'actual' sample set may be utilized as basis for considerable extrapolation in order to perform predictions.

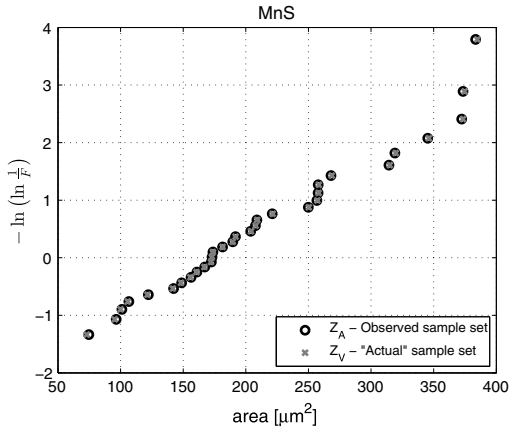

Fig. 5 Probability plot of the observed and the 'actual' sample set of MnS defects obtained from inspection areas.

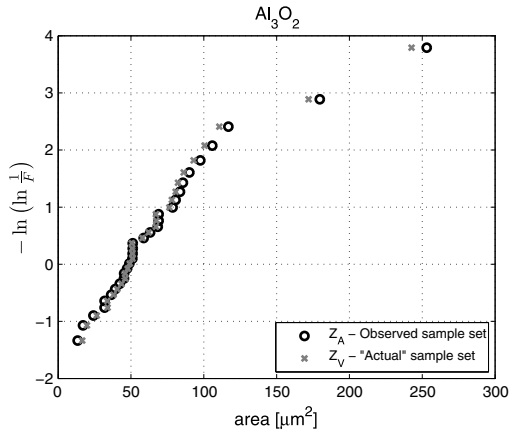

Fig. 6 Probability plot of the observed and the 'actual' sample set of Al $_3O_2$ defects obtained from inspection areas.

Table 3 The estimated inspection volumes for each defect type according to the present method and the standard practice

	μ	η	ρ
MnS	4.84	0.508	18.5
Al $_3O_2$	1.79	1.15	195

The largest defects expected to occur in an arbitrary volume are predicted by the extreme value distribution in Eq. (11). The 'actual' sample set, $\{Z_{V,i}, i = 1, \ldots, k\}$, is utilized to estimate the model parameters, which are summarized in Table 3.

The final step is to utilize Eq. (15) with the model parameters to estimate the largest defect size expected to occur in an arbitrary volume, V, with probability α. The results are presented in the next section.

Results

The present model and the standard practice are utilized to predict the defect sizes observed on the fracture surfaces of the laboratory specimen. Recall that the gauge volume of the specimen was about $V_g = 540$ mm^3. Essentially, Eq. (11), in the case of the present model, and Eq. (1), in the case of the standard practice, are extrapolated from the inspection volumes to the gauge volumes, $V_0 \rightarrow V_g$; models are extrapolated to volumes many thousand times larger than the inspection volumes. (Recall that the standard practice corresponds to the common Gumbel distribution with the $\sqrt{area}$ formulation.)

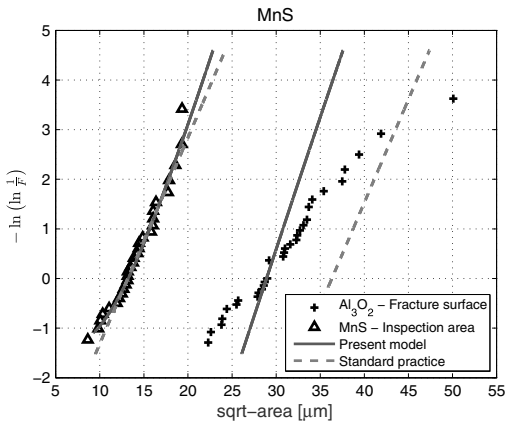

Fig. 7 Probability plots of the sample set from inspection areas (MnS) and observations from the fracture surfaces (Al $_3O_2$). Models are fitted to the sample set obtained from the inspection areas and then extrapolated towards larger volumes.

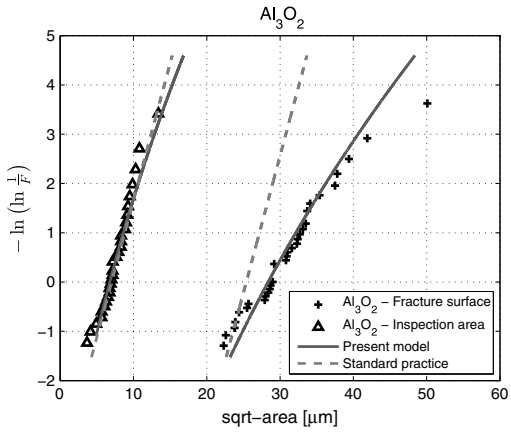

Fig. 8 Probability plots of the sample set from inspection areas (Al $_3O_2$) and observations from the fracture surfaces (Al $_3O_2$). Models are fitted to the sample set obtained from the inspection areas and then extrapolated towards larger volumes.

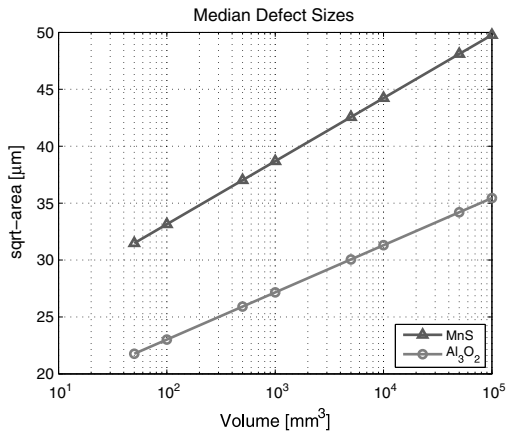

Fig. 9 The median size of the largest defect at a given volume as predicted by the standard practice model.

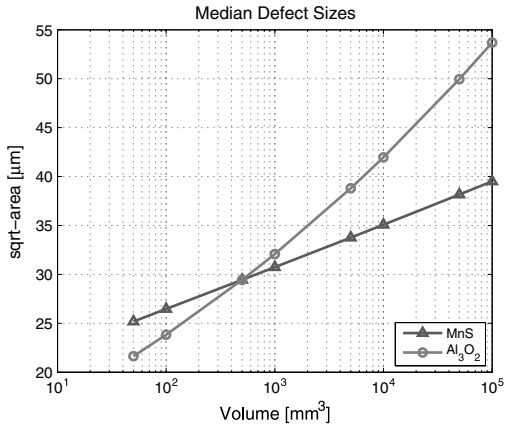

Fig. 10 The median size of the largest defect at a given volume according to the present model.

Consider the MnS defects first; the results are presented in Fig. 7. Note that both models fit the sample data obtained from inspection areas well and are initially remarkably similar. In practice, none of the models could have been rejected by means of formal hypotheses test. However, the difference becomes apparent when they are extrapolated to the gauge volume. And as expected, none of the models describe the defects from fracture surfaces particularly well because after all, they are not MnS defects.

The results for the Al $_3O_2$ defects are presented in Fig. 8. Similar to previous case, the models are initially similar but deviate significantly when extrapolated. In contrast to the standard practice in this case, the present model adequately describes the defects observed on the fracture surfaces of fatigue specimen. It should be emphasized that this is achieved by merely extrapolating the model from the sample set obtained from the inspection areas. That is, the present model successfully predicts the largest defects expected to occur in a relatively large volume, based on samples obtained from inspection areas.

Regardless, the most important achievement of the model is not the accuracy but rather its capability to capture significant trends. For instance, the experimental data suggest that MnS defects dominate the inspection areas but are overtaken by the Al $_3O_2$ defects at larger volumes. According to the standard practice model, this is not possible. In fact, it predicts the contrary that the difference will increase at larger volumes. This is demonstrated in Fig. 9 where the median size of the largest defect at a given volume according to the standard practice is presented.

However, a different trend emerges if the same plot is prepared for the present model; see Fig. 10. The present model predicts that Al $_3O_2$ will catch up and then outpace the MnS defects at some point. Curiously, the point of intersection is just below the gauge volume of the fatigue specimen. This suggests that if the fatigue specimen was made noticeably smaller, say half their sizes, the MnS defects would still be the dominant defect type observed on the fracture surfaces.

DISCUSSION AND CONCLUDING REMARKS

First, it should be mentioned that there are in fact sampling techniques such as 3D X-ray tomography that allow

direct sampling, that is, sampling the representative defect size rather than the observed size. Unfortunately, these techniques often have a set of challenges on their own: cost, availability, resolutions and allowable specimen size to mention a few. Thus, indirect sampling from polished surfaces is often the viable approach.

Nonetheless, a comprehensive statistical approach for analysing defects samples is presented. The primary intention is to highlight some of the obvious shortcoming of the standard practice[1] and then suggests a set of improvements that address some of them. The main challenge has been to preserve the main advantage of the standard practice: the simplicity and practical applicability. This goal is arguably partially achieved.

A significant contribution of this paper may be the analysis of defects sampled from inspection areas. A descriptive statistical model that may be considered as a generalization of the standard practice is presented: a relatively simple analytical method for converting the observed defect sample set into the 'actual' sample set, and the inspection area into the corresponding inspection volume is derived. Curiously, it was seen that the standard practice, which is essentially a heuristic 'black box' approach, is sometimes a special case of the present model. Furthermore, the outcome of these models in most common cases will not deviate much, and the benefit of applying the correction to the observed sample set is not always obvious.

The major contribution is the predictive statistical modelling approach described in this paper. An alternative approach that deviates, not only from the standard practice but also from most of the mainstream literature, is suggested. Abandoning the use of the classical extreme value distributions for defect analysis is an issue extensively studied by one of the authors, for example, Ref.[21] The proposed alternative extreme value distribution that is based on an underlying log-normal distribution assumption is not the only solution but still a reasonable one. It is clear that some work is still needed on this issue.

Note that the proposed method does not introduce any arbitrary restrictions on the size of the inspection areas, A_0 or the sample size k. However, some fundamental principles apply. First, larger A_0 will yield more reliable extreme value predictions (due to reduced extrapolation). Second, larger k will result in better parameter estimates.

The most promising feature of the presented model was its ability to predict an experimental observation that the standard practice missed, as presented in Application Example section. Namely, the fact that sulfides dominate observable defects during sampling, oxides will overtake the sulfides in size at sufficiently large volumes. The fact that the standard practice, even with the modified sampling strategy, missed this trend is concerning. In worst case, the standard practice will lead to erroneous predictions and conclusion regarding overall trends.

Finally, the paper may be summarized as follows:

- A comprehensive statistical modelling approach is presented.
- Relatively simple analytical expressions for converting the observed defect sample set to the 'actual' defect sample set, and the inspection area into the corresponding inspection volume is derived.
- An alternative extreme value distribution is presented in order to make consistent predictions.
- The present method appears to make reasonable predictions and also outperforms the standard practice while remaining practically applicable.

REFERENCES

1 ASTM. (2003) E2283-08: Standard practice for extreme value analysis of nonmetallic inclusion in steel and other microstructural features.
2 Murakami, Y. (2002) *Metal Fatigue: effects of Small Defects and Nonmetallic Inclusions*. Elsevier Science Ltd, Oxford, UK.
3 Anderson, C. W., Coles, S. G. (2002) The largest inclusion in a piece of steel. *Extremes*, **5**, 237–252.
4 Shi, G., Atkinson, H. V., Sellars, C. M., Anderson, C. W. (1999) Application of the generalized Pareto distribution to the estimation of the size of the maximum inclusion in clean steels. *Acta Mater.*, **47**, 1455–1468.
5 Atkinson, H. V., Shi, G. (2003) Characterization of inclusions in clean steels: a review including the statistics of extremes methods. *Prog. Mater. Sci.*, **48**, 457–520.
6 Beretta, S., Murakami, Y. (2001) Largest-extreme-value distribution analysis of multiple inclusion types in determining steel cleanliness. *Metall. Mater. Trans. B*, **32B**, 517–523.
7 Wicksell, S. D. (1925) The corpuscle problem: a mathematical study of a biometric problem. *Biometrica*, **17**, 84–89.
8 Baddeley, A., Jensen, E. B. V. editors (2005). Stereology for statisticians. Monographs on statistics and applied probability, 103.
9 Anderson, C. W., de Maré, J., Rootzén, H. (2005) Methods for estimating the sizes of large inclusion in clean steels. *Acta Mater.*, **53**, 2295–2304.
10 Takahashi, R., Sibuya, M. (1996) The maximum size of planar section of random spheres and its application in metallurgy. *Ann. Inst. Stat. Math.*, **48**, 127–144.
11 Takahashi, R., Sibuya, M. (1998) Prediction of the maximum size in Wicksell's corpuscle problem. *Ann. Inst. Stat. Math.*, **50**, 361–377.
12 Takahashi, R., Sibuya, M. (2001) Prediction of the maximum size in Wicksell's corpuscle problem, ii. *Ann. Inst. Stat. Math.*, **53**, 647–660.
13 Takahashi, R., Sibuya, M. (2002) Metal fatigue, Wicksell transform and extreme values. *Appl. Stoch. Models Bus. Ind.*, **18**, 301–312.
14 Takahashi, R., Sibuya, M. (2002) Maximum size prediction in Wicksell's corpuscle problem for the exponential tail data. *Extremes*, **5**, 55–70.
15 Cetin, A., Naess, A. (2012) Toward a proper statistical description of defects. *Int. J. Fatigue*, **38**, 100–107.

16 Meeker, M. Q., Escobar, L. A. (1998) *Statistical Methods for Reliability Data*. Wiley.
17 Cetin, A., Naess, A. (2012) Statistical characterisation of inclusions in metals: from 2D to 3D. *Mater. Sci. Technol.*, **28**, 965–970.
18 Wakefield, G. R., Sharp, G. R. (1996) Effect of casting technique on fatigue properties of hot isostatically pressed Al-10 Mg castings. *Mater. Sci. Technol.*, **12**, 518–522.
19 Yi, J. Z., Lee, P. D., Lindley, T. C., Fukui, T. (2006) Statistical modeling of microstructure and defect population effects on the fatigue performance of cast A356-T6 automotive components. *Mat. Sci. Eng. A*, **432**, 59–68.
20 Cetin, A., Härkegård, G., Naess, A. (2013) The fatigue limit: an analytical solution to a Monte Carlo problem. *Int. J. Fatigue*, **55**, 194–201.
21 Cetin, A., Härkegård, G., Naess, A. (2013) A physically based extreme value characterization of material fatigue. *Int. J. Fatigue*, **47**, 216–221.

Aalto-DD 191/2017
VTT SCIENCE 166

Small defects are often the cause of fatigue crack initiation and failure. Since the initiation and growth of small cracks is the longest portion of the fatigue life of a machine component it is also the area where the largest increase in performance and quality can be achieved through better understanding and modeling of the material. The prediction of the defect size along with the measurement and analysis of the small crack growth due to fatigue loading is examined in this thesis. The results provide knowledge and guidance to improve the quality and efficiency of engineering structures. The new methods and test results support and improve the modeling and prediction of machine components used in more demanding applications and loading situations.

ISBN 978-952-60-7649-2 (printed)
ISBN 978-952-60-7648-5 (pdf)
ISSN-L 1799-4934
ISSN 1799-4934 (printed)
ISSN 1799-4942 (pdf)

978-951-38-8579-3 (printed)
978-951-38-8578-6 (pdf)
2242-119X
2242-119X (printed)
2242-1203 (pdf)

Aalto University
School of Engineering
Department of Mechanical Engineering
www.aalto.fi

BUSINESS + ECONOMY

ART + DESIGN + ARCHITECTURE

SCIENCE + TECHNOLOGY

CROSSOVER

DOCTORAL DISSERTATIONS